Aspects of the Topological Kondo Effect

Jesada Temaismithi

Balliol College

University of Oxford

A thesis submitted for the degree of

Doctor of Philosophy

Hilary 2017

Aspects of the Topological Kondo Effect

Jesada Temaismithi
Balliol College, Oxford

A thesis submitted for the degree of
Doctor of Philosophy
at the University of Oxford, Hilary 2017

Abstract

We investigate theoretically the topological Kondo effect (TKE) and related non-Fermi-liquid (NFL) phenomena in correlated mesoscopic devices containing Majorana fermions. Using the numerical renormalisation group (NRG), we confirm and extend results obtained by conformal field theory (CFT) and we calculate numerically exact conductance curves for several different devices over large temperature ranges, which could be compared directly to future experiments. Our calculations uncover a wide range of physics in these mesoscopic devices and we derive several effective models to explain this behaviour.

We first consider the prototypical model proposed by Béri and Cooper [B. Béri and N. R. Cooper. *Phys. Rev. Lett.*, 109, 156803 (2012).] in which a non-local spin-1/2 is coupled to spin-1 conduction electrons. This model was proposed as the minimal model for the TKE, arising as the low-energy effective model of a superconducting grain connected to three leads containing Majorana fermions at the ends. We study the model in detail, confirming asymptotic CFT results and calculating the full conductance curves. We show that the NFL physics is robust to asymmetric Majorana–lead couplings, and uncover a duality between weak- and strong-coupling regimes using Abelian bosonisation. We also show how inter-Majorana couplings destabilise the NFL behaviour.

We next consider the device beyond the effective spin-1/2 model, working instead with an Anderson-type model where charge fluctuations can be taken into account. We consider various possibilities for the energy levels on the superconducting grain and calculate and compare the behaviour in each case. We show that the NFL physics is robust to charge fluctuations, and is not restricted only to the regime of a non-degenerate ground state on the superconductor with large charging energy. We also derive various low-energy effective models for the different charging states.

Finally, we investigate the device with a fourth lead attached. This gives rise to an effective two-channel Kondo model, but the device geometry means that the conductance is distinct from that studied previously. We also consider the full Anderson model, showing again that the conductance results are robust to charge fluctuations.

Acknowledgements

First, I would like to thank Dr Martin Galpin, my supervisor, who has helped me tremendously especially at the beginning and push me to the end. I acknowledge the Thai Government for the three years of financial support and thank Prof David Logan for liaising with them.

Other members of the Logan–Galpin group were also helpful, in particular, Andrew Mitchell, who taught me the Numerical Renormalisation Group and helped me get started. I greatly appreciate the hospitality of the people from Theoretical Condensed Matter, notably Neil Robinson, with whom I have enjoyed several discussions be it physics or others, Prof Steven Simon, who has recommended a number of articles in the area of Topological Matter at the beginning of my DPhil career, many of which I enjoyed immensely, and Prof John Chalker, who has helped provide me with the access to the Theoretical Physics building and arranged meetings with external guest speakers. Furthermore, teaching at Somerville College and working with Prof Jonathan Burton has been a joy and a very memorable experience.

The experience at Oxford would not have been the same without friends at Balliol, in particular, Midori Amano Patino, Natasha Ng, Alex Vai, and Laia Josa Culleré. In addition to the great times we had and the considerable amount of support, I have been influenced so much by you over the years. Thank you.

Finally, a big thanks to mum, dad, and my brother for the love and for just being there listening and talking to me. It may be difficult to understand exactly what I have been doing every day away from home, but I do appreciate their understanding and the devotion of their time for me.

Declaration

I am the sole author of this thesis and have produced this thesis without making use of anything else other than those specified; Other materials derived from articles or textbooks are properly acknowledged.

Jesada Temaismithi

Contents

1

Introduction

Scientists used to believe that matter is composed of a smallest unit, hence the term "atom". Later on, however, we found that atoms are actually composed of protons, neutrons, and electrons. Protons and neutrons are yet another type of composite particles where the former comprises two up quarks and one down quark resulting in the charge of $+e$ whereas the latter comprises one up quark and two down quarks resulting in a neutral particle. Nevertheless, most of chemistry, material science, and condensed-matter physics can be formed from the consideration of atoms as merely composed of protons, neutrons, and electrons, and how they interact with each other; their internal structures are irrelevant and materials properties are entirely different from those of their constituents. The idea of "emergent phenomena" [1], that new properties of a macroscopic system emerge out of a collection of microscopic entities and cannot be understood in terms of the fundamental laws that govern those entities themselves, is described in Philip Anderson's article – "More Is Different" [2]. And with that, being interested in the various properties of matter, we shall content ourselves in particular to the study of electrons and their interactions which give rise to an array of emergent phenomena.

An emergent phenomenon that is of interest to us and is central to the study of this project is the Majorana bound state, which in fact is hypothesised to exist as an elementary particle, a physical fermion, as well. Majorana fermions are particles that are their own antiparticles [3, 4, 5, 6]. Its existence was discovered when physicists were trying to use quantum mechanics to study relativistic

particles. It started with Klein and Gordon who proposed a relativistic wave equation by effectively squaring the Schrödinger equation [7]. (A more quantitative summary will be presented in the next chapter.) However, the solutions to the Klein-Gordon equation are problematic: not only do they not lead to positive definite probability density, the solutions with both positive and negative energies exist and the physical interpretation of the latter is problematic. Dirac then came up with his equation which solved the first problem [8] and he later solved the second problem by reinterpreting the negative energies as that of the antiparticles with opposite charge [9, 10], hence predicting the existence of positrons. The following year, Weyl showed that a simpler form of solutions exist for massless fermions; instead of a four-component field, the solution becomes two-component fields [11]. Pauli then proposed the existence of neutrinos two year later [12]. At the time it was believed that neutrinos are massless neutral particles; hence, their properties should be the same as those of Weyl fermions. However, since neutrinos are neutral, at the time, Majorana thought that it was possible that antineutrinos could be the neutrinos themselves and he came up with solutions to the Dirac equation which are real and describe particles which are their own antiparticles [3], that is $\gamma^\dagger = \gamma$ in second quantisation.

Whilst the existence of a Majorana fermion as an elementary physical particle is yet to be seen, it is also possible that Majorana fermions may exist as emergent quasiparticles in condensed matter systems. Since Majorana fermions are their own antiparticles, it is natural to search for them in superconducting systems where the quasiparticles are a combination of both electrons and holes which are antiparticles of each other. The most common type of pairing in superconductors however is of s-wave type; Cooper pairs are formed from electrons with opposite spins as can be seen from the form of the Boguliubov quasiparticle operator: $b = uc^\dagger_\uparrow + vc_\downarrow$ [13]. Since obviously $b^\dagger \neq b$, these Cooper pairs are not Majorana fermions. Thus, we need to look for effectively spinless superconducting systems in which the pairing mechanism is triplet and that is a p-wave superconductivity in one dimensional systems or a $p + ip$ superconductivity in two dimensional systems [5, 14]. Over the past few years, a number of possible candidates have been proposed as practical realisations of these Majorana fermions. In one-dimensional systems, which can be understood based on a simple model proposed by Kitaev

[15], since the electrons carry the spin $\frac{1}{2}$, the main task is to come up with a way to freeze out one of the spin species so that the system appears spinless, though stabilising such a system is yet an experimental challenge. Possible candidates in this category include the two dimensional topological insulators [16, 17] which grew out of Fu and Kane's proposals [18, 19] that the p-wave pairing may occur on the surfaces of a strong topological insulator under the proximity-induced superconductivity [20, 21, 22] (being in contact with an ordinary s-wave superconductor), conventional one dimensional semiconducting wires with appreciable spin–orbit coupling and a magnetic field [23, 24], or three dimensional topological insulator nanowires [25]. More details of the one-dimensional system will be given in Section 2.2. Candidates for the two-dimensional systems are split into two groups. The first group is the systems where the $p + \mathrm{i}p$ pairing is a result of the material's internal dynamics and the classic examples are the fractional quantum Hall state with $\nu = 5/2$ [26, 27] and the layered spinful triplet superconductor Sr_2RuO_4 [28, 29]. The second group once again falls into the case where we have to engineer the spinless $p + \mathrm{i}p$ superconductivity by forming appropriate heterostructures with various kinds of two dimensional electrons, though this approach once again suffers the same difficulty as in the one dimensional case in removing the spin degeneracy of the electrons. The classic examples in this group are the three dimensional topological insulators such as Bi_2Se_3 [30, 31, 32, 33, 34] and the conventional two dimensional electron systems which are either semiconductor based [35] or based on a quantum anomalous Hall state [36, 37]. We mention on the passing that in the two-dimensional $p + \mathrm{i}p$ superconductor, Majorana fermions appear in vortices in the superconducting pairing potential, and even when the gap is closed, they may appear upon varying chemical potential or electrostatic potential [5].

Not only are Majorana fermions of academic interest, but they also possess interesting properties that may have important technological applications as well. First of all, Majorana fermions are non-Abelian anyons [38]. In three spatial dimensions and one time dimension, (3+1)D, particles are classified into two categories, the result which comes from particle exchanges. If we consider all possible trajectories that take N indistinguishable particles from their initial spatial positions at some time to the same final spatial positions at later time, it turns out

that all these different trajectories fall into different topological classes which correspond to the elements of the permutation group S_N, whose elements detemine how the initial positions of these particles are permuted into the final positions. Since there are only two one-dimensional irreducible representations, the trivial representation and the sign representation, particles are classified into two categories, namely, bosons and fermions. The higher-dimensional representations of the permutation group can still be classified as bosons or fermions with an additional quantum number [39]. On the contrary, in two spatial dimensions, since a path which involves looping of a particle around the other cannot be deformed to a point without cutting through that other particle, the winding of a particle around the other is well defined and when two particles are exchanged twice, which is equivalent to one being looped around the other, they do not necessarily come back to the same state. For a system of two identical particles, upon exchange, its wavefunction may change by an arbitrary phase factor, $\psi \rightarrow \mathrm{e}^{\mathrm{i}\theta}\psi$, where the special case $\theta = 0$ corresponds to bosons and $\theta = \pi$ corresponds to fermions, and others with arbitrary values of θ are called anyons with statistics θ [39]. However, when we consider the general case of N particles, the classes of the trajectories correspond to the elements of the braid group $\mathcal{B}_N$, which is a non-Abelian group. Therefore, particles in this category obey non-Abelian braiding statistics – Majorana fermions are an example of such particles. Furthermore, since any single Dirac fermion can be mathematically decomposed into two Majorana fermions, which correspond to the real and the imaginary part of the original fermion, we can also form a Dirac fermion from two Majorana fermions. If a Dirac fermion is formed out of a pair of spatially separated Majorana fermions, this type of delocalised fermionic state will be robust against local perturbations which cause decoherence. The combination of non-Abelian statistics and the braid operations make Majorana fermions attractive as a basis for performing low-decoherence topological quantum computation [39, 40].

The term topological phase is usually associated with any system with robust degenerate ground states whose quasiparticle excitations are anyons, but its precise definition is given by Nayak et al [39]: a system is in a topological phase if all observables are invariant under smooth deformation of the space-time manifold at low temperature, or equivalently, that all observable properties are

independent of the choice of space-time coordinates. The term "at low temperature" is used in the sense that the invariance is only broken by terms that vanish as $\sim \max\left(\mathrm{e}^{-\Delta/T}, \mathrm{e}^{-|x|/\xi}\right)$ for some non-zero energy gap Δ and finite correlation length ξ, and for this reason, in general, topological phases have an energy gap separating the ground states from the excited states. In our context, Majorana fermions are proposed to exist on a topological superconductor, which can be engineered by proximity-coupling a long thin one-dimensional semiconducting wire with a strong spin–orbit coupling to an s-wave superconductor and exposing it to a magnetic field that is sufficiently strong (relative to the energy gap Δ and the chemical potential μ, in particular, $|g\mu_B B| > \sqrt{\Delta^2 + \mu^2}$) [5, 23, 24].

Further interest in Majorana fermions has stemmed from proposals of the so-called "topological Kondo effect" [41]. To put this in context, we first briefly review the conventional Kondo effect and related physical behaviour.

Historically, it was the existence of the electric resistance minimum found in non-magnetic metals with magnetic impurities that attracted physicists to the Kondo model [42]. The resistance of pure metals usually decreases as temperature is lowered due to the depopulation of phonon modes which can scatter conduction electrons. Upon further cooling, the resistivity reaches a constant value; while phonon scattering decreases with temperature and becomes insignificant at low temperature, lattice defects give rise to a finite resistivity. However, when a magnetic impurity is introduced, instead of becoming constant, the resistivity increases again upon cooling. In 1964, Jun Kondo applied perturbation theory to what was then called the s–d exchange model, now know as the Kondo model – a very simple model consisting of free conduction electrons and a local spin coupling between the spin of the magnetic impurity and that of the conduction electrons – and found that indeed due to the presence of such an interaction the resistance minimum exists [43]. However, Kondo used perturbation theory, which was unable to explain the physics of the model at temperature scale far below the resistance minimum. Later, this model has been studied extensively by a variety of different methods such as Anderson's "poor man's scaling" [44], Wilson's Numerical Renormalisation Group [45, 46, 47, 48], Fermi Liquid Theory [49], Bethe Ansatz [50, 51], and Conformal Field Theory [52, 53], and has also been generalised to other models such as the Anderson model [54] where the

imputiry spin is replaced by an energy level, or the multichannel Kondo model [55] where the conduction electrons of different kinds or channels are allowed. A quantitative and more extensive summary of the Numerical Renormalisation Group, which is the main tool used to study physical properties of the system in this project, will be presented in the next chapter. Later in the 2000s, the Kondo model was brought to attention to the science once again when it was shown that it can also be used to describe electron tunnelling processes in a quantum dot [56], leading to the experimental realisation of the two-channel Kondo effect and its Non-Fermi liquid properties [57, 58]. And once again, the Kondo model is seen to arise in these mesoscopic devices.

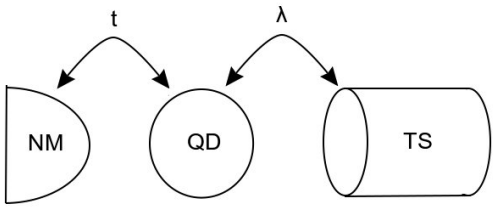

Figure 1.1: Schematic diagram of a simple device in which the Kondo physics, based on a quantum dot (QD), is combined by the Majorana fermions which are proposed to exist on the surface of a topological superconductor (TS), in connection with a normal metal lead (NM).

More recently, it was proposed that the Kondo physics if combined with Majorana fermions [59, 60, 61] will lead to interesting dc transport [62, 63, 64] or ac properties in quantum RC circuits [65, 66]. The most basic device is shown in Figure 1.1 where the a normal metal lead is coupled to a quantum dot, effectively realising a Kondo model, which is then connected to a Majorana fermion on the surface of a topological superconductor. A few other devices that utilise the connection of the Majorana fermions on a superconductor, which is also related closely to the Kondo physics have also been proposed. For example, the device that is central to this project is the simplest one in which a topological Kondo effect can be observed, proposed by Béri and Cooper [41]. This device is also being experimentally explored [67, 68]. They proposed a superconducting island that supports four Majorana fermions as is shown in Figure 1.2. Each of the three

Majoranas is locally coupled to a spinless conduction electron lead, shown as the solid lines on the figure. The Hamiltonian of the device then consists of the three spinless electron leads, the charging energy of the superconducting island, and the three local Majorana–lead couplings. In order to understand the transport properties of this device, Béri and Cooper performed a Schrieffer-Wolff transformation [69] and argued that in the regime where the temperature and voltages are much smaller than the energy gap and the superconducting charging energy, the physics of the device can be described by a low-energy effective Hamiltonian that is equivalent to a Kondo Hamiltonian of a spin-$\frac{1}{2}$ impurity with spin-1 conduction electrons. The three spin-1 states are formed from three spinless electron leads and the two spin-$\frac{1}{2}$ impurity states are formed from the two pairs of Majorana fermions with a specific parity. Since the Majorana fermions are nonlocal, the degeneracy is a topological degeneracy; hence, the phenomenon is named the "topological Kondo effect". Béri and Cooper then performed the renormalisation group analysis by using the poor man's scaling procedure [44] and showed that there is a renormalisation group flow towards the isotropic coupling and argued that the Kondo temperature is $T_{\mathrm{K}} \sim \mathrm{e}^{-\rho\lambda}$, where ρ is the density of states of the leads at Fermi level and λ is the typical size of the coupling constants. In order to understand the nature of the stable fixed point at low temperature of the model, Béri and Cooper used the conformal field theory [52, 53] to study properties near the non-Fermi liquid fixed point and confirm that the results agree with those of previous studies [70, 71], in which Abelian bosonisation was used to argue that this particular type of Kondo model is equivalent to the Kondo model in which a spin-$\frac{1}{2}$ impurity is coupled to four spin-$\frac{1}{2}$ conduction electron leads, the four-channel Kondo model. Whilst that is the case for the thermodynamics, that is certainly not the case in the dynamics [72]. Furthermore, the Non-Fermi liquid fixed point of the topological Kondo effect is in fact robust against the anisotropy of the Majorana–lead couplings, unlike the typical Kondo effect realised in quantum dots in which Non-Fermi liquid fixed point is stable at low temperature only if the channel isotropy is achieved, rendering this device a possibility for the multichannel Kondo effect to be experimentally constructed. Béri and Cooper also used the conformal field theory to calculate the zero-temperature value and also the asymptotic behaviours (both at small and large temperature) of the

off-diagonal conductance between two conduction leads. Finally, they ended the paper by generalising the device to a superconducting island hosting M Majorana fermions and argued that since the Majorana operators generate a Clifford algebra [3] with the spinor representation of the SO(M) Lie algebra, we have the SO(M) Kondo problem.

In addition to the device proposed by Béri and Cooper, there is also an array of semilar devices being proposed. One such device was studied by Zazunov et al [73] where the Hamiltonian that governs the proposed system involves real antisymmetric matrices, $\mathbf{\Omega}$ and $\mathbf{t}$, which contain information about the coupling between the different Majoranas for the former, and between the Majoranas and the conduction leads for the latter. Their main goal is to study the parity effects in the tunnelling conductance of the model with a few different topologyies of the junction. Altland and Egger [74] and later Zazunov et al [75] studied a multiterminal Coulomb–Majorana junction, in which N helical nanowires are set on top of a superconductor which hosts $2N$ Majorana fermions at the end of each wire, $M \leq 2N$ of which are tunnel coupled to the normal part of the conduction wires, which act as helical Luttinger liquids. Altland and Egger studied how the charging energy of the island affect the low-energy behaviour of the model including the renormalisation group flow whereas Zazunov showed that the model indeed corresponds to the two-channel Kondo model with SO(M) symmetry group and hence the observation of Non-Fermi liquid behaviour of the system. Finally, there are also studies by Tsvelik [76] and Crampé and Trombettoni [77] which are based on a system composed of three quantum Ising spin chains that are connected to each other in a Δ junction. The system is shown to be equivalent to the two-channel Kondo model with the presence of the Majorana fermions since they are equivalent to the quantum Ising chains through Jordan–Wigner transformation [76].

There have also been a number of studies that appear after the proposal of the topological Kondo effect. With regard to this particular setup of the Majorana device, Béri himself studied this SO(M) Kondo problem in more details by mapping it to a quantum Brownian motion model [78]. He calculated the asymptotic behaviours of the conductance tensors and also sketched a phase diagram of the topological Kondo effect in terms of the bare parameters of the model. Finally,

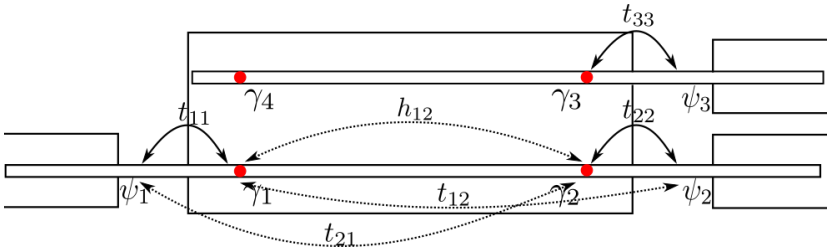

Figure 1.2: The minimal setup for the Majorana device which realises the topological Kondo effect. The central rectangle is a superconducting island which hosts the four Majorana fermions (red circles), three of which are locally tunnel coupled (solid lines) to the three conduction leads (the exterior rectangles). The device is proposed and studied by Béri and Cooper [41]. Later Galpin et al [72] also took into account the exponentially small nonlocal couplings (dotted lines) between the Majoranas and the conduction leads (t_{ij}) and among the Majoranas themselves (h_{ij}) and use the Numerical Renormalisation Group to study the device.

he highlighted the device with $M = 4$ and argued that this could be a possible experimental realisation of the two-channel Kondo model in which the Non-Fermi liquid fixed point is stable. Altland et al formed the Bethe ansatz solutions for the thermodynamics of the SO(M) Kondo model [79], then later applied the Abelian bosonisation technique to study the charge transport, spin dynamics, and multipoint correlations of the model near the low-temperature fixed point [80]. Eriksson et al applied quantum Brownian motion and bosonisation to calculate the scaling dimension of the leading irrelevant perturbation, which implies the power-law scaling of the conductance [81]. Eriksson et al also studied the local density of states and showed that the Kondo physics in this model can also be probed in tunnelling experiments. Plugge et al applied a few techniques such as bosonisation and renormalisation group to to study the process of "quasiparticle poisoning" by the presence of other low-lying fermionic quasiparticle states in the device [82]. Finally, the topological Kondo effect has also been proposed to be observable in optical trap systems [68].

It is the objective of this thesis to confirm the original predictions of Béri and Cooper, and to study the device in more details. Using the Numerical Renormalisation Group, we calculate numerically exact thermodynamics of the system and the full temperature dependent conductance curve, so that it can be useful

for the experimentalists who can fabricate the device. Furthermore, we are interested in the effects of the non-local couplings, both those between the leads and the Majorana fermions and those between the Majorana themselves (represented by dotted lines in Figure 1.2), and how these could affect the robustness of the Non-Fermi liquid properties at low temperature. After fully studying the spin model, we tackle the problem by a different approach. Instead of using the spin Hamiltonian which is an effective model, we model the superconductor as a dot with orbitals or energy levels available for electrons. In this sense, the model is equivalent to the Anderson generalisation of the Kondo model. We use the Numerical Renormalisation Group to study both thermodynamics and the conductance of the general Majorana device.

Much of the work from this study has been published [72]. Progress from several other studies is also being made [67, 68, 74, 75, 79, 80, 81, 82]. Specifically, Béri [78] has generalised the setup of the Majorana device to include M arbitrary number of leads attached to the superconducting island, where he has once again used conformal field theory to calculate the zero-temperature value and the asymptotic behaviour of the conductance as a function of M, and sketch the phase diagram of the topological Kondo effect. Later we will also follow this line of study by adding another conduction lead to the minimal Majorana device so that $M = 4$ and use Numerical Renormalisation Group to study both the system's thermodynamics and the conductance.

This thesis is structured in the following manner:

The second chapter presents all the necessary background information, starting from the most important ingredient in the Majorana Device – the Majorana fermions. We then provide a brief review of the toy model in which Majorana fermions can be realised in a condensed matter system and an overview of the Majorana device as is proposed by Béri and Cooper. Since the model can be understood in the context of the Kondo model, we give a detailed summary including the quantitative description of the Kondo model, the main tool that is heavily used in this project – the Numerical Renormalisation Group – and also a summary of the physical properties that are calculated and discussed repeatedly in this work.

The study of the low-temperature effective spin model of the minimal (three conduction electron leads) Majorana device is split into chapter 3 and 4, where we study the model with high symmetry requirements – the isotropic and the axial symmetry – in the former, and study the model which includes the exponentially small perturbations and the model without symmetry requirements in the latter. We study the Non-Fermi liquid properties of the system through the calculations of thermodynamic properties, in particular, the impurity entropy and the spin susceptibility, and the t-matrices and the linear conductance tensors which are dynamic properties. The materials in chapter 3 and half of that in chapter 4 have been published [72].

In chapter 5, we study the Majorana device without the low-energy transformation by implementing a suitable modelling of the charging energy part of the Hamiltonian of the device. The device with three different configurations of the superconducting island is then studied in details and we have confirmed that the low-temperature behaviour in the large-energy gap limit of the device is indeed the spin behaviour that we have found and studied earlier in the previous two chapters. In fact, the Non-Fermi liquid nature of the device can still be observed at low temperature independent of the configuration of the superconductor.

We then include an additional conduction electron lead to the device and study both its low-temperature effective spin model and also its equivalent level model in chapter 6. Here since the required computing resources are much higher, we only restrict ourselves to the study of the isotropic model in order to investigate mainly the Non-Fermi liquid properties of the model and compare them to the three-lead case. We leave the inclusion of anisotropy and other exponentially small perturbations for further studies.

Finally, we conclude the thesis with a brief summary at the end.

2

Background

In this chapter, we provide a brief review of all the essential ingredients that form the thesis. We begin by discussing the history and the proposal of the existence of Majorana fermions. Then we discuss the mesoscopic device of interest which incorporates the Majorana fermion quasiparticles. It turns out that under a certain set of conditions, the Hamiltonian that governs the behaviour of this device can be mapped onto a Kondo Hamiltonian; hence, we discuss it in the following section. Since the main tool that is used to study and investigate a physical system in this thesis is the Numerical Renormalisation Group, we discuss the general concept of the Renormalisation Group technique prior to that by providing two discrete examples, then discuss the Numerical Renormalisation Group in details, including its application to the physical properties calculations – such as thermodynamics, scattering t matrix, and the linear conductance – at the end, where we have also included known properties of the Kondo model.

2.1 Majorana Fermions

In quantum mechanics, a quantum state of a quantum mechanical system evolves in time according to the Schrödinger equation

$$H\psi = \mathrm{i}\hbar\frac{\partial}{\partial t}\psi, \tag{2.1.1}$$

where H is the Hamiltonian of the system. For a non-relativistic free particle, since its energy is $E = \frac{p^2}{2m}$, the quantised Hamiltonian operator becomes

$$H = -\frac{\hbar^2}{2m}\nabla^2. \tag{2.1.2}$$

For a relativistic particle, the form of the energy expression is more complicated $E = \sqrt{p^2c^2 + m^2c^4}$. In order to avoid the cumbersome expression involving the square root upon quantisation, we operate H onto the Schrödinger equation once again, and quantise the square of the energy [7]:

$$H^2\psi = \left(-\hbar^2c^2\nabla^2 + m^2c^4\right)\psi = -\hbar^2\frac{\partial^2}{\partial t^2}\psi, \tag{2.1.3}$$

$$\left(\nabla^2 - \frac{1}{c^2}\frac{\partial^2}{\partial t^2}\right)\psi = \left(\frac{mc}{\hbar}\right)^2\psi. \tag{2.1.4}$$

It was Dirac who in 1928 managed to come up with the "square-root" of the Klein–Gordon equation:

$$\mathrm{i}\left(\gamma^1\frac{\partial}{\partial x} + \gamma^2\frac{\partial}{\partial y} + \gamma^3\frac{\partial}{\partial z} + \frac{1}{c}\gamma^0\frac{\partial}{\partial t}\right)\psi = \frac{mc}{\hbar}\psi, \tag{2.1.5}$$

where γ^i are the gamma matrices, which in Dirac representation are given in terms of Pauli matrices σ_i as the following 4×4 matrices:

$$\begin{aligned} \gamma^0 &= \begin{pmatrix} I_2 & 0 \\ 0 & -I_2 \end{pmatrix}, \quad \gamma^1 = \begin{pmatrix} 0 & \sigma_x \\ -\sigma_x & 0 \end{pmatrix}, \\ \gamma^2 &= \begin{pmatrix} 0 & \sigma_y \\ -\sigma_y & 0 \end{pmatrix}, \quad \gamma^3 = \begin{pmatrix} 0 & \sigma_z \\ -\sigma_z & 0 \end{pmatrix}. \end{aligned} \tag{2.1.6}$$

Upon taking the square of the operator in the Dirac equation (2.1.5), we indeed obtain the Klein–Gordon equation (2.1.4), since the cross terms vanish due to the anti-commutation relation of the gamma matrices: $\{\gamma^\mu, \gamma^\nu\} = 2\eta^{\mu\nu}$, where $\eta^{\mu\nu}$ is the Minkowski metric tensor $(+---)$. In the covariant form, the Dirac equation (2.1.5) becomes

$$\left(\mathrm{i}\hbar\gamma^\mu\partial_\mu - mc\right)\psi = 0, \tag{2.1.7}$$

where the repeated index μ is summed over. Since the gamma matrices are complex, in general we expect ψ to be complex as well. If a field ψ creates

a particle A, its complex conjugate ψ^* creates its anti-particle $\bar{A}$ and destroy the particle A. If a particle is to be its own anti-particle, then it must be that $\psi^* = \psi$, i.e., that the field is real, or later in the operator context, that $\psi^\dagger = \psi$. It was Majorana [3] who found another representation of the gamma matrices, the Majorana representation, in which all four matrices are purely imaginary:

$$\begin{aligned} \widetilde{\gamma}^0 &= \begin{pmatrix} 0 & \sigma_y \\ \sigma_y & 0 \end{pmatrix}, \quad \widetilde{\gamma}^1 = \begin{pmatrix} \mathrm{i}\sigma_z & 0 \\ 0 & \mathrm{i}\sigma_z \end{pmatrix}, \\ \widetilde{\gamma}^2 &= \begin{pmatrix} 0 & -\sigma_y \\ \sigma_y & 0 \end{pmatrix}, \quad \widetilde{\gamma}^3 = \begin{pmatrix} -\mathrm{i}\sigma_x & 0 \\ 0 & -\mathrm{i}\sigma_x \end{pmatrix}, \end{aligned} \tag{2.1.8}$$

resulting in the Dirac equation (2.1.7) being real, and it is possible to have a real ψ as a solution. We therefore refer to it as a Majorana fermion (MF), a particle that is its own anti-particle. It is still unclear whether a MF exists as an elementary particle, but many physicists are optimistic that in certain condensed matter systems, a MF may exist as a quasiparticle excitation [3, 32, 38, 83, 84]. This fact is particularly appealing to many physicists because the MF has non-Abelian exchange statistics and, when is spatially delocalised, can be tolerant to local perturbations rendering it useful for a quantum information storage, leading to the idea of topological quantum computation [39, 85].

2.2 Majorana Fermion in a 1D Condensed Matter System

We now review a simple one-dimensional (1D) toy model of a condensed matter system that hosts MFs, which is believed to be realisable due to the superconducting proximity effect, by following standard review articles [5, 6, 14].

Kitaev [15] considered a one-dimensional spinless tight-binding chain with p-wave superconducting pairing described by the Hamiltonian

$$H = -\mu \sum_{i=1}^{N} a_i^\dagger a_i - \frac{1}{2} \sum_{i=1}^{N-1} \left(t a_i^\dagger a_{i+1} + \Delta \mathrm{e}^{\mathrm{i}\phi} a_i a_{i+1} + \text{adj.} \right), \tag{2.2.1}$$

where μ is the chemical potential, $t \geqslant 0$ the nearest-neighbour hopping parameter, $\Delta \geqslant 0$ the superconducting gap, ϕ the superconducting phase, a_i the annihilation

operators for a spinless electron at site i, and adj. denotes the Hermitian adjoint. The pairing is p-wave since it couples electrons of the same spin, in contrast to the standard s-wave pairing which couples those of opposite spins. The interesting physics of this model can be observed when the spinless fermion operator a_i is decomposed into its real and imaginary parts

$$a_i = \frac{\mathrm{e}^{-\mathrm{i}\phi/2}}{2}\left(\gamma_{R,i} + \mathrm{i}\gamma_{L,i}\right), \tag{2.2.2}$$

where $\gamma_{\alpha,i}$ are Majorana operators of type $\alpha \in \{L, R\}$ at site i and we include the superconducting phase term for convenience. The fact that they are Majorana operators can be seen upon inverting the above relation to obtain

$$\gamma_{L,i} = \mathrm{i}\left(\mathrm{e}^{-\mathrm{i}\phi/2}a_i^\dagger - \mathrm{e}^{\mathrm{i}\phi/2}a_i\right), \tag{2.2.3}$$

$$\gamma_{R,i} = \quad \mathrm{e}^{-\mathrm{i}\phi/2}a_i^\dagger + \mathrm{e}^{\mathrm{i}\phi/2}a_i, \tag{2.2.4}$$

which clearly shows that the canonical Majorana fermion relations are satisfied:

$$\gamma_{\alpha,i}^\dagger = \gamma_{\alpha,i}, \tag{2.2.5}$$

$$\{\gamma_{\alpha,i}, \gamma_{\beta,j}\} = 2\delta_{\alpha\beta}\delta_{ij}. \tag{2.2.6}$$

In this basis, H becomes

$$H = -\frac{\mu}{2}\sum_{i=1}^{N}\left(1 + \mathrm{i}\gamma_{R,i}\gamma_{L,i}\right) - \frac{\mathrm{i}}{4}\sum_{i=1}^{N-1}\left[\left(\Delta + t\right)\gamma_{R,i}\gamma_{L,i+1} + \left(\Delta - t\right)\gamma_{L,i}\gamma_{R,i+1}\right]. \tag{2.2.7}$$

Despite the complexity of the model Hamiltonian, its physics can be seen most easily in two special cases.

In the first case, when $\mu < 0$ and $t = \Delta = 0$, the second term of the Hamiltonian disappears altogether, leaving only the couplings between the two L and R Majoranas on the same site. In order to diagonalise the Hamiltonian, we combine the two Majoranas on each site (top panel of Figure 2.1), effectively going back to the original ordinary fermion a_i. The Majoranas of the same site are bound together and the chain rests in the topologically trivial phase. The Hamiltonian then becomes $H_1 = -\mu\sum_i a_i^\dagger a_i$, which implies that the unique ground state corresponds to the vacuum of a_i fermions and the spectrum is gapped since addition of a a_i fermion costs a finite amount of energy μ.

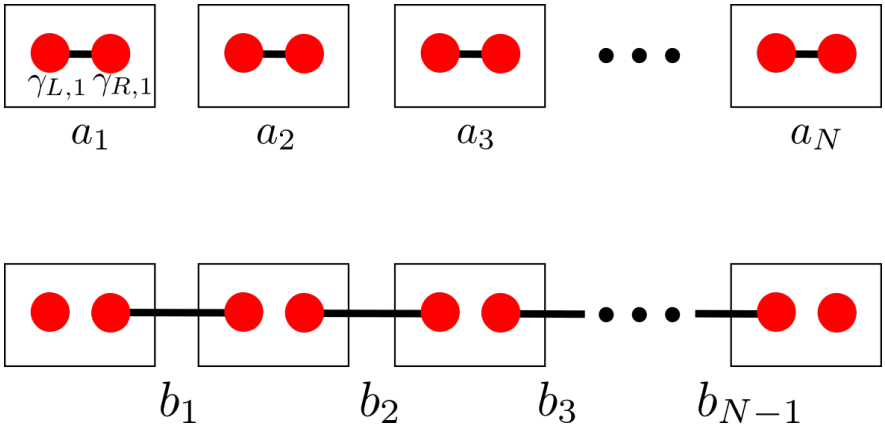

Figure 2.1: Diagramatic representation of the 's tight binding chain. (top) When $\mu < 0$ and $t = \Delta = 0$, the two Majoranas on the same site i, $\gamma_{L/R,i}$ are paired, resulting in a non-degenerate ground state with an energy gap. (bottom) When $\mu = 0$ and $t = \Delta \neq 0$, the Majoranas on a different site, $\gamma_{R,i}$ and $\gamma_{L,i+1}$, are paired and the ground state is doubly degenerate.

In the second case, when $\mu = 0$ and $t = \Delta \neq 0$, the remaining term corresponds to the coupling between the Majorana R at site i and the Majorana L at the adjacent site $i + 1$, and the topological phase appears. In terms of the ordinary fermion operators, $b_i = \frac{1}{2}(\gamma_{L,i+1} + \mathrm{i}\gamma_{R,i})$, the Hamiltonian reads $H_2 = t\sum_i \left(b_i^\dagger b_i - \frac{1}{2}\right)$. In the bulk, similar to before, addition of a b_i fermion costs a finite amount of energy t and the gap persists. However, the two Majorana localised at the end of the chain, $\gamma_{L,1}$ and $\gamma_{R,N}$, are completely absent from H_2; thus, the chain now supports zero-energy Majorana modes, which are realised from the these two Majorana fermions, seen by writing them as an ordinary, but non-local, fermion, $f = \frac{1}{2}(\gamma_{L,1} + \gamma_{R,N})$. The fact that this f fermion does not appear in H_2 implies that addition of this fermion to the system costs no energy, and the ground state is doubly degenerate: if the vacuum $|0\rangle$ is a ground state (even occupation), so is $f^\dagger |0\rangle$ with opposite parity (odd occupation); in contrast to the conventional superconductor where a unique ground state exists as condensates of Cooper pairs which are always of even parity.

The appearance of the delocalised Majorana zero modes and the ground-state degeneracy is a consequence of the fact that the chain forms a topological phase, which is not smoothly connected to the trivial phase. Due to this topological

origin, the existence of the topological phase does not rely on the fine tuning of the parameters μ, t, and Δ of the model [14]. In general, so long as the system is still in the topological phase, the two Majorana modes are not simply the $\gamma_{L,1}$ and $\gamma_{R,N}$ localised at the end of the chain, but their wavefunctions decay exponentially into the bulk of the chain on a length scale ξ given by the superconducting coherence length. The overlaps of the wavefunctions results in the split of the degeneracy on the energy scale of $\mathrm{e}^{-\ell/\xi}$, where ℓ is the length of the chain. Therefore, in a system whose $\ell \gg \xi$, the splitting is exponentially suppressed compared to other relevant energy scales of the system and the degeneracy is effectively realised.

These Majorana edge states will be utilised in a mesoscopic device of interest in this project whose details are described in the next section.

2.3 Béri–Cooper Majorana Device

Following Béri and Cooper [41, 72], we are interested in a mesoscopic device consisting of a superconducting island which supports four localised Majorana modes, three of which are coupled to spinless conduction electron leads (Figure 2.2). The system can be described by the following Hamiltonian

$$H = H_{\text{leads}} + H_{\text{c}} + H_{\text{M}} + H_{\text{t}}, \tag{2.3.1}$$

where the terms

$$H_{\text{leads}} = \sum_{ki} \varepsilon_k a_{ki}^\dagger a_{ki}, \tag{2.3.2}$$

$$H_{\text{c}} = E_{\text{c}} \left(N - \frac{q}{e} \right)^2, \tag{2.3.3}$$

$$H_{\text{M}} = \sum_{ij} \mathrm{i} h_{ij} \gamma_i \gamma_j, \tag{2.3.4}$$

$$H_{\text{t}} = \sum_{ij} t_{ij} \gamma_i \psi_j \mathrm{e}^{\mathrm{i}\phi/2} + \text{adj.} \tag{2.3.5}$$

H_{leads} represents the spinless conduction electron lead i with momentum k and dispersion relation ε_k. H_{c} is the charging energy of the superconducting island with N electrons and q is the gate charge. H_{M} is the exponentially-small coupling between Majorana fermions at the end of the leads. H_{t} describes the coupling

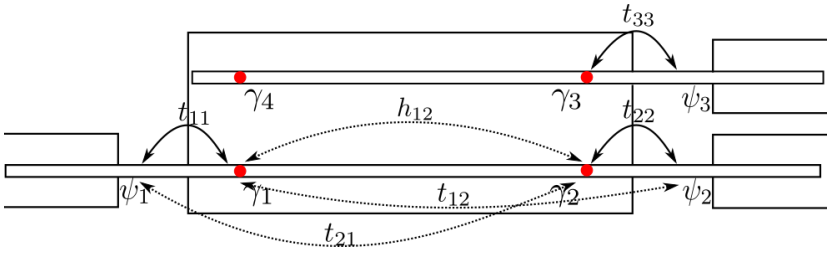

Figure 2.2: The minimal setup for the Majorana device which realises the topological Kondo effect. The central rectangle is a superconducting island with the charging energy $H_{\rm c}$. The island hosts four Majorana fermions (red circles), three of which are locally tunnel coupled, via $H_{\rm t}$, to the three conduction leads (the exterior rectangles). $H_{\rm t}$ includes both the local coupling (solid lines) and also the non-local coupling (dotted lines) between the conduction electron leads and the Majoranas. The effect of the local coupling has already been studied by Béri and Cooper [41]. In this thesis, we also study the effect of the non-local coupling.

between the Majorana mode i on the superconducting island and the conduction electron lead j, where the operators ψ_j correspond to the conduction electrons at the end of the lead j,

$$\psi_j = \frac{1}{\sqrt{N_{\rm orb}}} \sum_k a_{kj}, \tag{2.3.6}$$

and the phase operator $\mathrm{e}^{\mathrm{i}\phi/2}$ raises the number of electrons on the superconductor by one charge unit: $[N, \mathrm{e}^{\pm\mathrm{i}\phi/2}] = \pm\mathrm{e}^{\pm\mathrm{i}\phi/2}$. This tunnelling Hamiltonian can be obtained by writting the usual tunnelling Hamiltonian between the electrons on the superconducting island, $\psi_S(x)$, and the electrons on the regular conduction leads, ψ_j, as $\sim \psi_S(x_j)\psi_j + \text{adj.}$, where x_j is the tunnelling point. The superconducting electron operator can be expressed as $\psi_S(x) = \mathrm{e}^{\mathrm{i}\phi/2}\{\sum_j \xi_j(x)\gamma_j + \psi_{>,S}(x)\}$, where $\xi_j(x)$ are the Majorana wave functions and $\psi_{>,S}(x)$ is the piece of the electron operator with positive-energy BCS excitations [62]. The tunnelling Hamiltonian is then obtained by neglecting $\psi_{>,S}(x)$, which can be done below the energy scale of the superconducting gap [62].

We shall see later on that under a certain set of conditions, the Hamiltonian (2.3.1) above can be mapped onto an impurity Hamiltonian, namely, the Kondo Hamiltonian, which we now introduce in the next section.

2.4 Kondo Model

A problem of interest to condensed matter scientists in the 1930s was the electric resistance minimum found in non-magnetic metals with magnetic impurities. The resistance of pure metals decreases when temperature is lowered due to the depopulation of phonon modes which can scatter conduction electrons. Upon further cooling, the resistivity reaches a constant value: while phonon scattering decreases with temperature and becomes insignificant at low temperature, lattice defects give rise to a finite resistivity. However, when a magnetic impurity is introduced, instead of becoming constant, the resistivity increases again upon cooling [42].

It took thirty years before this was explained by Jun Kondo [43], who applied perturbation theory to the s–d exchange model, now known as the Kondo model:

$$\begin{aligned} H &= H_{\text{lead}} + J\,\mathbf{S}\cdot\mathbf{s} \\ &= \sum_{k\sigma} \varepsilon_k a^\dagger_{k\sigma} a_{k\sigma} + J\left\{\frac{1}{2}\left(S^+ s^- + S^- s^+\right) + S^z s^z\right\}, \end{aligned} \tag{2.4.1}$$

where $a_{k\sigma}$ are the operators for the conduction electrons of spin σ, $\sigma \in \{\uparrow,\downarrow\}$, the upper-case operators S^z, S^+, S^- are the z-component spin-projection, spin-raising, and spin-lowering operators for the impurity, and the analogous lower-case operators s^z, s^+, s^- are the local spin operators at the impurity site of the conduction electrons. Specifically, $\mathbf{s} = \sum_{\sigma\sigma'} \frac{1}{2} a^\dagger_\sigma \boldsymbol{\sigma}_{\sigma\sigma'} a_{\sigma'}$, where $a_\sigma = \frac{1}{\sqrt{N_{\text{orb}}}} \sum_k a_{k\sigma}$ are the operators for the conduction electrons at the impurity site and $\boldsymbol{\sigma} = (\sigma_x, \sigma_y, \sigma_z)$ are the Pauli matrices. The raising and lowering operators are related to the spin-projection operators by $S^\pm = S^x \pm \mathrm{i}S^y$. Essentially, the Kondo model (2.4.1) consists of two terms: the first term is the Hamiltonian of non-interacting conduction electrons and the second term represents the interaction – the spin coupling – between the conduction electrons and the impurity. If J is positive, the interaction is said to be antiferromagnetic, i.e., the two spins prefer to be antialigned. Kondo found that the spin contribution of the resistivity is $\rho_{\text{spin}} = -bc\ln(T/T_{\text{F}})$, where b is a constant, c is the impurity concentration, and T_{F} is the Fermi temperature. Together with the phonon contribution of aT^5, where a is a constant, the resistivity minimum is found to be at the temperature of

$T_{\min} = \left(\frac{bc}{5a}\right)^{1/5}$. Though the resistivity minimum problem was solved by Kondo, it can be seen from the spin contribution to the resistivity expression that it diverges at very low temperature. Such a problem occurs when the high-order terms become as important as the low-order terms, and the perturbation theory breaks down. Thus, other non-perturbative techniques, one of which – the Numerical Renormalisation Group – will be discussed in details, are required to study the impurity problem.

A variant of the Kondo model was proposed in 1980 by Nozières and Blandin [55] in order to take into account the orbital structure of the impurity. This is now known as the multichannel Kondo Model or specifically the n-channel Kondo Model, and its Hamiltonian can be written as

$$H = \sum_{ki\sigma} \varepsilon_k a^\dagger_{ki\sigma} a_{ki\sigma} + J \sum_i \mathbf{S} \cdot \mathbf{s}_i, \tag{2.4.2}$$

where $i \in \{1, ..., n\}$ is the channel index. The low-temperature behaviour of this model can be categorised into 3 groups depending on the relative size of the impurity spin S and the number of channels of the conduction electrons n. Details of these models will be provided in Section 2.5.2 after we have discussed the Renormalisation Group method and understood the fixed point structure of the standard one-channel Kondo model.

Now that we have described the standard Kondo model, in the next section, we discuss one of the techniques that is used to solve the problem, the Renormalisation Group, via two examples. Later, we discuss the Numerical Renormalisation Group technique, which a very powerful tool as it is non-perturbative but the renomalisation then has to be carried out numerically.

2.5 Renormalisation Group

Before describing the Renormalisation Group (RG) method, let us consider, as an analogy, the relationship between fluid mechanics and the fluid's composition. At the microscopic level, a fluid is composed of small particles that interact with one another and the interactions are described by quantum mechanics. Nevertheless, in order to understand the dynamics of a fluid, it is not necessary to understand its

microscopic details. Fluid mechanics, whilst being able to describe the dynamics, does not refer to the internal quantum structure of the fluid; the microscopic details are included in the parameters such as viscosity. Therefore, in order to describe the long-length behaviour of a fluid, we do not need to know the motion or the fluctuations on small length scales; only average behaviour at larger length scales needs to be considered. The process of averaging out the fluctuations on small length scales is known also as integrating out short-wavelength fluctuations.

The low-energy behaviour of condensed-matter systems is usually of interest since, in addition to the practicalities in a sense that, for example, we frequently deal with metals at room temperature not at its melting point, it tends to be universal, i.e., there is a set of common low-temperature behaviours among models with different microscopic details. Hence, the idea of RG will also be applied to integrate out, analogous to short-wavelength fluctuations, high-energy excitations of a theory, so that low-energy properties of a system can be understood.

In order to illustrate the RG principles, we discuss two explicit examples: the spin decimation as applied to the one-dimensional Ising model and the poor man's scaling to the Kondo model.

2.5.1 Real-Space Spin Decimation

We first discuss the RG method that is done in real space of the one-dimensional Ising model by following Pathria [86]. The model Hamiltonian is

$$H = -J \sum_{i=1}^{N} s_i s_{i+1}, \tag{2.5.1}$$

where $J > 0$ is the coupling constant and $s_i \in \{\pm\}$ is the spin at site i. The partition function of the system is then

$$Q = \sum_{\{s_i\}} \mathrm{e}^{-\beta H} = \sum_{\{s_i\}} \prod_{i=1}^{N} \exp\left\{K_0 + K_1 s_i s_{i+1}\right\}, \tag{2.5.2}$$

where $K_0 = 0, K_1 = \beta J$, and $\beta = 1/k_{\mathrm{B}}T$. The parameter K_0 is included for reasons that will later become clear. The RG idea here is to decimate half of the

spins from the chain by carrying out the sum over them. Assuming N even, we rewrite the summand above as

$$\prod_{i=1}^{N} \exp\left\{K_0 + K_1 s_i s_{i+1}\right\} = \prod_{j=1}^{\frac{1}{2}N} \exp\left\{2K_0 + K_1(s_{2j-1}s_{2j} + s_{2j}s_{2j+1})\right\}. \tag{2.5.3}$$

The sum over all the even spins s_{2j} can then be carried out to give

$$\prod_{j=1}^{\frac{1}{2}N} \exp(2K_0) \cdot 2\cosh\left\{K_1(s_{2j-1} + s_{2j+1})\right\}. \tag{2.5.4}$$

Denoting the odd spins $s_{2j-1} =: s'_j$, we attempt to rewrite the transformed partition function in its original form. In particular, we substitute the summand (2.5.4) into the partition function (2.5.2) and force it to be equal to the same partition function but with the transformed parameters K'_0 and K'_1:

$$Q = \sum_{\{s'_j\}} \prod_{j=1}^{\frac{1}{2}N} \exp(2K_0) \cdot 2\cosh\left\{K_1(s'_j + s'_{j+1})\right\} \stackrel{!}{=} \sum_{\{s'_j\}} \prod_{j=1}^{N'} \exp\left\{K'_0 + K'_1 s'_j s'_{j+1}, \right\} \tag{2.5.5}$$

which is required to be true for all choices of s'_j and s'_{j+1}. Specifically, we take $s'_j = s'_{j+1} = 1$ and $s'_j = -s'_{j+1} = 1$ to obtain

$$\exp(2K_0) \cdot 2\cosh(2K_1) = \exp(K'_0 + K'_1), \quad 2\exp(2K_0) = \exp(K'_0 - K'_1), \tag{2.5.6}$$

which can be inverted to give

$$K'_0 = 2K_0 + \ln(2\sqrt{\cosh 2K_1}), \quad K'_1 = \frac{1}{2}\ln(\cosh 2K_1). \tag{2.5.7}$$

Here it becomes clear why the parameter K_0 needs to be included: in an attempt to sum over half of the spins in the chain and rewrite the Hamiltonian in its original form, two unique conditions (2.5.6) need to be satisfied and thus, requiring two free parameters.

The thermodynamics of the Ising spin chain can be understood by considering the free energy. Setting $K_0 = 0$, the partition function of the system before and after the spin decimation are

$$Q = Q(K_1) = \mathrm{e}^{N'K'_0} Q(K'_1), \tag{2.5.8}$$

where $Q(K_1) = \sum_{\{s_i\}} \prod_i \mathrm{e}^{K_1 s_i s_{i+1}}$. Since $N' = \frac{1}{2}N$, we calculate the free energy per spin, $f(K_1) = -\frac{1}{N} k_\mathrm{B} T \ln Q(K_1)$ to be

$$f(K_1) = -\frac{1}{2} k_\mathrm{B} T K_0' + \frac{1}{2} f(K_1'). \tag{2.5.9}$$

In the limit $T \to \infty$, both K_1 and K_1' vanish and we obtain the high-temperature free energy

$$f(0) = -k_\mathrm{B} T K_0' = -k_\mathrm{B} T \ln 2. \tag{2.5.10}$$

This can be understood by considering the entropy $s = -\frac{\partial f}{\partial T} = k_\mathrm{B} \ln 2$, which suggests the two possible spin states; at high-temperature limit, each spin in the Ising chain becomes completely independent from one another. This also illustrates the significance of the parameter K_0'. In the limit $T \to 0$, $K_1 \to \infty$ and $K_1' \simeq \frac{1}{2} \ln \left(\frac{1}{2} \mathrm{e}^{2K_1} \right) \simeq K_1$. Using the equations (2.5.7) and (2.5.9), we find the free energy to be

$$f(K_1) \simeq -k_\mathrm{B} T \ln(2\sqrt{\cosh 2K_1}) \simeq -k_\mathrm{B} T K_1 = -J, \tag{2.5.11}$$

which is to be expected as it is indeed the energy per spin at low temperature when all the spins are aligned. In fact, for this particular model, the functional equation (2.5.9) does have a solution and we can solve for a general expression for the free energy

$$f(K_1) = -k_\mathrm{B} T \ln(2 \cosh K_1). \tag{2.5.12}$$

We can see from the discussion above that the RG transformation – in this case, the spin decimation or the sum over half of the spins – takes the parameter $J = K_1/\beta$ in the Hamiltonian (2.5.1) to J' via $K_1' = R(K_1)$, where the specific form of the transformation R is given by the equation (2.5.7). The RG transformation in general may have what we refer to as a *fixed point*, K^*, where

$$R(K^*) = K^*. \tag{2.5.13}$$

As can be seen from previously, the fixed points of the model are $K_\mathrm{I}^* = 0$ and $K_\mathrm{II}^* = \infty$. K_I^* is referred to as a *stable* fixed point since any values of K_1 near 0 results in K_1' that is smaller and approaches 0. On the contrary, the other fixed point K_II^* is *unstable* because any values of $K_1 \neq 0$ results in K_1 that goes towards K_I^*. Therefore, a generic one-dimensional Ising model with finite J appears disordered when viewed on a long enough length scale, or when enough spins are decimated.

2.5.2 Energy-Space Poor Man's Scaling

A perturbative RG procedure that is relevant to the impurity problem is Anderson's poor man's scaling [44]. We review the method as is presented by Hewson [69] by following the outline given in details by Altland and Simons [87]. We begin by considering the Kondo Hamiltonian (2.4.1) but lowering its symmetry by allowing anisotropy between the coupling constants of the z component and the x, y components. Expanding out the conduction electron spin operators s^i in terms of the creation and annihilation operators, the Hamiltonian of the anisotropic Kondo model then takes the form

$$H = \sum_{k\sigma} \varepsilon_k a^\dagger_{k\sigma} a_{k\sigma} + \frac{1}{2} \sum_{kk'} \left\{ J_+ S^+ a^\dagger_{k\downarrow} a_{k'\uparrow} + J_- S^- a^\dagger_{k\uparrow} a_{k'\downarrow} + J_z S^z \left(a^\dagger_{k\uparrow} a_{k'\uparrow} - a^\dagger_{k\downarrow} a_{k'\downarrow} \right) \right\}. \tag{2.5.14}$$

Assuming that the conduction band of a constant density of states ρ_0 is of bandwidth $2D$ centred at $\varepsilon_k = 0$, we divide the band into the high-energy electron/hole states occupying the energy shell $D/b < |\varepsilon_k| < D$ and the remaining states $0 < |\varepsilon_k| < D/b$, where $b > 1$. We attempt to derive a low-energy effective Hamiltonian by considering virtual excitations to the high-energy states as perturbations. In particular, we split the Hilbert space of the system into three subspaces: $\{\psi_0\}$ with no electrons/holes in the upper/lower band edges, $\{\psi_1\}$ with at least one electron in the upper band edge, and $\psi_{\bar{1}}$ with at least one hole in the lower band edge. Applying the projection operator $P_i, i \in \{0, 1, \bar{1}\}$ to the Schrödinger equation, $H\psi = E\psi$, inserting the identity operator $1 = \sum_j P_j$, using the fact that $P_j^2 = P_j$:

$$P_i (E\psi) = P_i (H\psi) = P_i H \sum_j P_j^2 \psi = \sum_j P_i H P_j \psi_j, \tag{2.5.15}$$

where ψ_j is the wavefunction in the subspace j, and arriving eventually at a set of equations

$$E\psi_i = \sum_j H_{ij} \psi_j, \tag{2.5.16}$$

where $H_{ij} \coloneqq P_i H P_j$ can be interpreted as the components of H that takes the states from subspace j to subspace i. We then solve the equations (2.5.16) for $\psi_{\bar{1}}$

and ψ_1 and substitute them into the equation for ψ_0, namely,

$$E\psi_0 = H_{0\bar{1}}\psi_{\bar{1}} + H_{00}\psi_0 + H_{01}\psi_1 \tag{2.5.17}$$

$$= \left[H_{0\bar{1}}\left(E - H_{\bar{1}\bar{1}}\right)^{-1} H_{\bar{1}0} + H_{00} + H_{01}\left(E - H_{11}\right)^{-1} H_{10}\right]\psi_0. \tag{2.5.18}$$

Focussing on the term that scatters an electron into the upper band edge, we identify H_{10} to be

$$H_{10} = \frac{1}{2}\sum_{k_s,k_f}\left\{J_+ S^+ a^\dagger_{k_f\downarrow}a_{k_s\uparrow} + J_- S^- a^\dagger_{k_f\uparrow}a_{k_s\downarrow} + J_z S^z\left(a^\dagger_{k_f\uparrow}a_{k_s\uparrow} - a^\dagger_{k_f\downarrow}a_{k_s\downarrow}\right)\right\}, \tag{2.5.19}$$

where k_f span the range of energies within the band edge and k_s span the range of lower energies. Then, there are eight possible processes that are allowed for the $H_{01}\times H_{10}$ term, i.e., those that take the states from within $\{\psi_0\}$ to $\{\psi_1\}$ and back to $\{\psi_0\}$, four of which are

$$J_z S^z a^\dagger_{k'_s\uparrow}a_{k_f\uparrow} \times J_z S^z a^\dagger_{k_f\uparrow}a_{k_s\uparrow} \tag{2.5.20}$$

$$J_- S^- a^\dagger_{k'_s\uparrow}a_{k_f\downarrow} \times J_+ S^+ a^\dagger_{k_f\downarrow}a_{k_s\uparrow} \tag{2.5.21}$$

$$J_z S^z a^\dagger_{k'_s\uparrow}a_{k_f\uparrow} \times J_- S^- a^\dagger_{k_f\uparrow}a_{k_s\downarrow} \tag{2.5.22}$$

$$-J_z S^z a^\dagger_{k'_s\downarrow}a_{k_f\downarrow} \times J_+ S^+ a^\dagger_{k_f\downarrow}a_{k_s\uparrow}, \tag{2.5.23}$$

and the other four are related by symmetry. The first two pairs preserve the spin of the electrons whilst the latter two involve a spin-flip process. There are also contributions of the same type from the $H_{0\bar{1}}\times H_{\bar{1}0}$. Combining the sixteen contributions, we arrive at the renormalised coupling constants

$$J_\pm(b) = J_\pm - \frac{1}{2}J_z J_\pm \rho_0 D\left(1-\frac{1}{b}\right)\left(\frac{1}{E-D+\varepsilon_k} + \frac{1}{E-D-\varepsilon_{k'}}\right), \tag{2.5.24}$$

$$J_z(b) = J_z - \frac{1}{2}J_+ J_- \rho_0 D\left(1-\frac{1}{b}\right)\left(\frac{1}{E-D+\varepsilon_k} + \frac{1}{E-D-\varepsilon_{k'}}\right). \tag{2.5.25}$$

Since we are interested in the low-energy properties, $E \ll D$, and the typical internal excitation energy $\varepsilon_k \ll D$, the recursion relations can then be written as

$$\frac{\mathrm{d}J_\pm}{\mathrm{d}\ln D} = -\rho_0 J_z J_\pm, \tag{2.5.26}$$

$$\frac{\mathrm{d}J_z}{\mathrm{d}\ln D} = -\rho_0 J_+ J_-, \tag{2.5.27}$$

where $\mathrm{d}D = D\left(1 - \frac{1}{b}\right)$, $b \to 1$, and the scaling trajectory follows the relation

$$J_z^2 - J_\pm^2 = \text{const.} \tag{2.5.28}$$

For the ferromagnetic model with $J_z < 0$, if $|J_z| > J_\pm$, as the bandwidth is reduced, $J_\pm \to 0$. If $|J_z| < J_\pm$, and also for the antiferromagnetic model with $J_z > 0$, J_z and $J_\pm$ gets larger and larger until the perturbation method used here is no longer valid.

For simplicity, we now consider the isotropic antiferromagnetic Kondo model with $J_z = J_\pm =: J > 0$. The scaling equations (2.5.26) and (2.5.27) become

$$\frac{\mathrm{d}K}{\mathrm{d}\ln D} = -K^2, \tag{2.5.29}$$

where $K = \rho_0 J$ is the dimensionless coupling constant. There are two fixed points for this model: the weak-coupling (WC) fixed point $K^*_{\mathrm{WC}} = 0$ and the strong-coupling (SC) fixed point $K^*_{\mathrm{SC}} = \infty$. The weak-coupling fixed point is unstable and corresponds to the model at high temperature where the impurity is effectively decoupled from the conduction electrons. As the bandwidth is reduced and with it high-energy excitations integrated out, the system flows to the strong-coupling fixed point, which is stable and corresponds to the model at low temperature where the conduction electrons and the impurity effectively form a spin singlet state and we usually refer to it as the impurity spin being *screened*. In addition, if we integrate the scaling equation (2.5.29) from the initial bandwidth D and the coupling constant K to the renormalised values $\widetilde{D}$ and $\widetilde{K}$

$$\int_K^{\widetilde{K}} -\frac{\mathrm{d}K}{K^2} = \int_D^{\widetilde{D}} \mathrm{d}\ln D \tag{2.5.30}$$

$$\frac{1}{\widetilde{K}} - \frac{1}{K} = \ln\frac{\widetilde{D}}{D} \tag{2.5.31}$$

$$D\,\mathrm{e}^{-1/K} = \widetilde{D}\,\mathrm{e}^{-1/\widetilde{K}}. \tag{2.5.32}$$

We thus obtain a scaling invariant which is usually referred to as the Kondo temperature T_{K}, defined via

$$k_{\mathrm{B}} T_{\mathrm{K}} = D\,\mathrm{e}^{-1/K} \tag{2.5.33}$$

which is a single parameter that characterises the RG flow.

In the case of the antiferromagnetic multichannel Kondo model (2.4.2), the scaling equations (2.5.26) and (2.5.27) are modified [88] to

$$\frac{\mathrm{d}K_\perp}{\mathrm{d}\ln D} = -K_\perp K_z + \frac{n}{4}(K_\perp^2 + K_z^2)K_\perp, \tag{2.5.34}$$

$$\frac{\mathrm{d}K_z}{\mathrm{d}\ln D} = -K_\perp^2 + \frac{n}{2}K_\perp^2 K_z, \tag{2.5.35}$$

where the transverse coupling constants are set to equal $K_\perp \coloneqq K_+ = K_-$ for simplicity, and the third-order terms are included in order to obtain the leading dependence on n, the number of channel. In the isotropic limit, $K_z = K_\perp$, the scaling equations (2.5.34) and (2.5.35) collapse to

$$\frac{\mathrm{d}K}{\mathrm{d}\ln D} = -K^2 + \frac{n}{2}K^3, \tag{2.5.36}$$

which leads to the modified Kondo temperature

$$k_\mathrm{B}T_\mathrm{K} = DK^{n/2}\,\mathrm{e}^{-1/K}. \tag{2.5.37}$$

Furthermore, upon setting the scaling equation (2.5.36) to zero, it might seem that there exists also another fixed point $K^*_\mathrm{IC} = 2/n$. This is obtained by assuming that the second-order term is of the same magnitude as the third-order term and, except in the case where n is large [55], the perturbation theory is no longer justified. Nevertheless, results from NRG calculations have been used to show the existence of this intermediate fixed point [89].

As mentioned before, the low-temperature behaviour of the multichannel Kondo model depends on the relative size of the impurity spin S and the number of channels of the conduction electrons n and can be split into 3 cases. This can be understood by considering the strong-coupling behaviour of the model, where the n channels of spin-$\frac{1}{2}$ conduction electrons together with the spin S impurity form an effective spin of the size $|S - n/2|$. We thus categorise the multichannel Kondo model into three different cases: the underscreened model with $S > \frac{n}{2}$, the exactly screened model with $S = \frac{n}{2}$, and the overscreened model with $S < \frac{n}{2}$. It turns out that for the exactly screened and underscreened cases, the behaviour is similar to that of the single-channel model: K^*_WC is unstable; K^*_SC is stable; K^*_IC

does not exist. However, in the case of overscreened model, both K^*_{WC} and K^*_{SC} are unstable; K^*_{IC} exists, is stable, and has properties that cannot be explained by Fermi-liquid theory and is therefore known as the Non-Fermi liquid (NFL) fixed point [55, 89].

2.5.3 Numerical Renormalisation Group

The principal method that is used in this project is a particular implementation of RG, the Numerical Renormalisation Group (NRG) [45, 46, 48]. The main idea of NRG is the same as RG in the sense that by carrying out the NRG procedure, the low-temperature behaviour of a system of interest is found. However, contrary to the poor man's scaling, which is perturbative, NRG is not. The general procedure of NRG is the following:

1. Logarithmic discretisation of the conduction band
2. Mapping to a semi-infinite chain
3. Iterative diagonalisation of the Hamiltonian of the chain
4. Calculation of physical properties

Before we discuss the NRG procedure, we briefly discuss the general form of a quantum impurity Hamiltonian, which usually consists of three parts:

$$H = H_{\mathrm{imp}} + H_{\mathrm{band}} + H_{\mathrm{imp\text{–}band}}, \tag{2.5.38}$$

where H_{imp} is Hamiltonian of the impurity, for example, the second term of the Kondo Hamiltonian (2.4.1), H_{band} the conduction band, and $H_{\mathrm{imp\text{–}band}}$ the interaction between them. In particular, the latter two Hamiltonian take the following forms:

$$H_{\mathrm{band}} = \sum_{k\sigma} \varepsilon_k a^\dagger_{k\sigma} a_{k\sigma}. \tag{2.5.39}$$

$$H_{\mathrm{imp\text{–}band}} = \sum_{k\sigma} V_k \left(f^\dagger_\sigma a_{k\sigma} + a^\dagger_{k\sigma} f_\sigma \right), \tag{2.5.40}$$

where the operators $a_{k\sigma}$ are for the electrons in the conduction band with spin σ, momentum k, and energy ε_k, the operators f_σ for the impurity, and the parameter V_k the coupling constant between the impurity and the band.

In this thesis, we make standard assumptions in NRG for metallic bands, that the conduction electron band is uniform and extends from $-D$ to D, choose D as the energy unit, i.e., setting $D = 1$, and ignore the momentum dependence of V_k, i.e., $V_k = V$, the Hamiltonian can then be rewritten in the continuous form as [48]

$$H = H_{\text{imp}} + \sum_\sigma \int_{-1}^{1} \mathrm{d}\varepsilon\, \varepsilon\, a^\dagger_{\varepsilon\sigma} a_{\varepsilon\sigma} + \sum_\sigma \int_{-1}^{1} \mathrm{d}\varepsilon \sqrt{\frac{\Delta_0}{\pi}} \left(f^\dagger_\sigma a_{k\sigma} + a^\dagger_{k\sigma} f_\sigma \right), \quad (2.5.41)$$

where $\Delta_0 = \pi V^2$ is the hybridisation function, a is a continuum conduction electron operator which satisfies the standard commutation relations: $\{a^\dagger_{\varepsilon\sigma}, a_{\varepsilon'\sigma'}\} = \delta(\varepsilon - \varepsilon')\delta_{\sigma\sigma'}$.

Now we proceed to the first step of the NRG procedure, the logarithmic discretisation of the conduction band. With the parameter $\Lambda > 1$, we define a set of intervals marked by the following points

$$x_n = \pm\Lambda^{-n}, n \in \mathbb{N}. \quad (2.5.42)$$

The width of each interval is therefore

$$d_n = \Lambda^{-n}(1 - \Lambda^{-1}). \quad (2.5.43)$$

Within each interval, we define a complete set of orthonormal functions

$$\psi^\pm_{np}(\varepsilon) = \begin{cases} \frac{1}{\sqrt{d_n}} \mathrm{e}^{\pm \mathrm{i}\omega_n p \varepsilon}, & \text{for } x_{n+1} < \pm\varepsilon < x_n, \\ 0 & \text{outside this interval,} \end{cases} \quad (2.5.44)$$

with the Fourier harmonic index $p \in \mathbb{Z}$ and the fundamental Fourier frequencies $\omega_n = \frac{2\pi}{d_n}$. We then expand the conduction electron operators $a_{\varepsilon\sigma}$ in this basis as

$$a_{\varepsilon\sigma} = \sum_{np} \left[a_{np\sigma} \psi^+_{np}(\varepsilon) + b_{np\sigma} \psi^-_{np}(\varepsilon) \right], \quad (2.5.45)$$

where the inverse transformation is given by

$$a_{np\sigma} = \int_{-1}^{1} \mathrm{d}\varepsilon \, \left[\psi_{np}^{+}(\varepsilon)\right]^{*} a_{\varepsilon\sigma}, \tag{2.5.46}$$

$$b_{np\sigma} = \int_{-1}^{1} \mathrm{d}\varepsilon \, \left[\psi_{np}^{-}(\varepsilon)\right]^{*} a_{\varepsilon\sigma}. \tag{2.5.47}$$

The operators $a_{np\sigma}$ and $b_{np\sigma}$ as written above are now discrete electron operators satisfying the standard commutation relations $\{a_{np\sigma}^{\dagger}, a_{n'p'\sigma'}\} = \delta_{nn'}\delta_{pp'}\delta_{\sigma\sigma'}$. We now convert the general Hamiltonian, equation (2.5.41), into one with these discrete operators. The conduction electron term then becomes

$$\begin{aligned}\int_{-1}^{1} \mathrm{d}\varepsilon \, \varepsilon \, a_{\varepsilon\sigma}^{\dagger} a_{\varepsilon\sigma} = &\sum_{np} \left(\xi_n^{+} a_{np\sigma}^{\dagger} a_{np\sigma} + \xi_n^{-} b_{np\sigma}^{\dagger} b_{np\sigma}\right) \\ &+ \sum_{n,p\neq p'} \left[\alpha_n^{+}(p,p') a_{np\sigma}^{\dagger} a_{np'\sigma} - \alpha_n^{-}(p,p') b_{np\sigma}^{\dagger} b_{np'\sigma}\right].\end{aligned} \tag{2.5.48}$$

The first term is diagonal in p and the energies are given by

$$\xi_n^{\pm} = \frac{1}{2}\Lambda^{-n}\left(1 + \Lambda^{-1}\right). \tag{2.5.49}$$

The coupling constants between states with different p are given by

$$\alpha_n^{\pm}(p,p') = \frac{1-\Lambda^{-1}}{2\pi\mathrm{i}} \frac{\Lambda^{-n}}{p'-p} \exp\left(\frac{2\pi\mathrm{i}(p'-p)}{1-\Lambda^{-1}}\right). \tag{2.5.50}$$

The hybridisation term is also transformed to

$$\int_{-1}^{1} \mathrm{d}\varepsilon \sqrt{\frac{\Delta_0}{\pi}} f_{\sigma}^{\dagger} a_{k\sigma} = \frac{1}{\sqrt{\pi}} f_{\sigma}^{\dagger} \sum_{n} \left(\gamma_n^{+} a_{n0\sigma} + \gamma_n^{-} b_{n0\sigma}\right), \tag{2.5.51}$$

with the coefficients

$$\gamma_n^{\pm} = \left(\frac{\Delta_0}{2}\right)^{1/2} \left(\frac{1-\Lambda^{-1}}{\Lambda^{n}}\right)^{1/2}. \tag{2.5.52}$$

Clearly, the impurity operator $f_{\sigma}^{\dagger}$ is coupled only to the conduction electron operators with $p = 0$: $a_{n0\sigma}$ and $b_{n0\sigma}$. Therefore, we argue that since the coupling constants between states with different p, $\alpha_n^{\pm}(p,p')$, equation (2.5.50), contains the prefactor $(1-\Lambda^{-1})$, which vanishes in the continuous limit, $\Lambda \to 1$, we shall ignore all the $p \neq 0$ states. In practice, this approximation still produces accurate results even for Λ as large as 2 [45, 46, 48].

The Hamiltonian (2.5.41) is then turned into the discretised form:

$$H \approx H_{\text{imp}} + \sum_{n\sigma} \left(\xi_n^+ a_{n\sigma}^\dagger a_{n\sigma} + \xi_n^- b_{n\sigma}^\dagger b_{n\sigma}\right) \tag{2.5.53}$$
$$+ \frac{1}{\sqrt{\pi}} \sum_\sigma \left(f_\sigma^\dagger \sum_n \left(\gamma_n^+ a_{n\sigma} + \gamma_n^- b_{n\sigma}\right) + \sum_n \left(\gamma_n^+ a_{n\sigma}^\dagger + \gamma_n^- b_{n\sigma}^\dagger\right) f_\sigma \right),$$

where we have now relabelled the operators $a_{n\sigma} \coloneqq a_{n0\sigma}$ and dropped completely the index p.

Before we continue with the next step in the NRG procedure, we mention a problem that arises from the discretisation of the model. It turns out that the discretisation introduces oscillations into the thermodynamic expectation values. A standard method that is used to alleviate this problem is to perform the "z averaging" [90]. By introducing a small shift in the discretisation point

$$x_n = \begin{cases} 1, & n = 0, \\ \Lambda^{-n+z}, & n \geqslant 1, \end{cases} \tag{2.5.54}$$

where $z \in [0, 1)$, these artificial oscillations can be removed by averaging the thermodynamic quantities over calculations with different values of z. Note however that the continuum recovered by this method is still different from the true continuum limit $\Lambda \to 1$. In addition, in order to accelerate the convergence to the continuum limit, it is conventional to multiply Δ_0 by a correction factor A_Λ [47, 48, 91], which takes the value of

$$A_\Lambda = \frac{1}{2}\frac{\Lambda + 1}{\Lambda - 1} \ln \Lambda. \tag{2.5.55}$$

The next step is to map the discretised Hamiltonian (2.5.53) onto a semi-infinite chain. The third term of the Hamiltonian is a coupling between the impurity operator $f_\sigma^\dagger$ to another conduction electron degree of freedom, which we now call $c_{0\sigma}^\dagger$ defined as

$$c_{0\sigma} \coloneqq \frac{1}{\sqrt{\xi_0}} \sum_n \left(\gamma_n^+ a_{n\sigma} + \gamma_n^- b_{n\sigma}\right). \tag{2.5.56}$$

The normalisation constant ξ_0 can be written as

$$\xi_0 = \sum_n \left[\left(\gamma_n^+\right)^2 + \left(\gamma_n^-\right)^2\right] = \Delta_0. \tag{2.5.57}$$

The hybridisation term then becomes

$$\frac{1}{\sqrt{\pi}} f_\sigma^\dagger \sum_n \left(\gamma_n^+ a_{n\sigma} + \gamma_n^- b_{n\sigma}\right) = \sqrt{\frac{\xi_0}{\pi}} f_\sigma^\dagger c_{0\sigma}. \tag{2.5.58}$$

Here the operator $c_{0\sigma}$ corresponds to the first site of the conduction electron chain. This operator is not orthogonal to the $a_{n\sigma}$ and $b_{n\sigma}$, but we can use a standard tridiagonalisation procedure to generate the orthogonal set of operators $c_{n\sigma}$ via an orthogonal transformation,

$$c_{n\sigma} = \sum_{m=0}^{\infty} \left(u_{nm} a_{m\sigma} + v_{nm} b_{m\sigma}\right), \tag{2.5.59}$$

whose inverse is

$$a_{n\sigma} = \sum_{m=0}^{\infty} u_{mn} c_{m\sigma}, \qquad b_{n\sigma} = \sum_{m=0}^{\infty} v_{mn} c_{m\sigma}. \tag{2.5.60}$$

The Hamiltonian (2.5.53) can then be transformed into the semi-infinite chain as required:

$$H = H_{\text{imp}} + \sqrt{\frac{\xi_0}{\pi}} \sum_\sigma \left(f_\sigma^\dagger c_{0\sigma} + c_{0\sigma}^\dagger f_\sigma\right) + \sum_{\sigma,n=0}^{\infty} t_n \left(c_{n\sigma}^\dagger c_{n+1\sigma} + c_{n+1\sigma}^\dagger c_{n\sigma}\right), \tag{2.5.61}$$

where the operators $c_{n\sigma}^\dagger$ now represent the nth site of the conduction electron chain. The zeroth coefficients can be read off directly from the definition of the operators $c_{0\sigma}$, equation (2.5.56):

$$u_{0m} = \frac{\gamma_m^+}{\sqrt{\xi_0}}, \qquad v_{0m} = \frac{\gamma_m^-}{\sqrt{\xi_0}}. \tag{2.5.62}$$

The recursion relations for the remaining parameters can be derived and are initialised at $n = 0$ by

$$\begin{aligned} t_0^2 &= \frac{1}{\xi_0} \sum_m \left[\left(\xi_m^+ \gamma_m^+\right)^2 + \left(\xi_m^- \gamma_m^-\right)^2\right], \\ u_{1m} &= \frac{\xi_m^+ u_{0m}}{t_0}, \qquad v_{1m} = \frac{\xi_m^- v_{0m}}{t_0}. \end{aligned} \tag{2.5.63}$$

For $n \geqslant 1$, the recursion relations are the following

$$\begin{aligned} t_n^2 &= \sum_m \left[\left(\xi_m^+ u_{nm}\right)^2 + \left(\xi_m^- v_{nm}\right)^2 \right] - t_{n-1}^2, \\ u_{n+1,m} &= \frac{1}{t_n}\left(\xi_m^+ u_{nm} - t_{n-1} u_{n-1,m}\right), \\ v_{n+1,m} &= \frac{1}{t_n}\left(\xi_m^- v_{nm} - t_{n-1} v_{n-1,m}\right). \end{aligned} \tag{2.5.64}$$

Wilson [45] has solved for the expression of t_n analytically:

$$t_n = \frac{1}{2}(1+\Lambda^{-1})\frac{1-\Lambda^{-n-1}}{\sqrt{1-\Lambda^{-2n-1}}\sqrt{1-\Lambda^{-2n-3}}}\Lambda^{-n/2}. \tag{2.5.65}$$

In the limit of large n, $t_n \to \frac{1}{2}(1+\Lambda^{-1})\Lambda^{-n/2}$, clearly decrease exponentially in n. The $n=0$ conduction electron site is usually interpreted as the electron shell localised physically closest to the impurity. This shell is then coupled to the next shell $n=1$ which is farther away from the impurity on the energy scale that is of $\sqrt{\Lambda}$ smaller than before, and so on.

We now arrive at the next step of the NRG procedure – the iterative diagonalisation. This is also the step where RG transformation takes place: $H(K) \xrightarrow{R} H(K')$. The Hamiltonian (2.5.61) can be viewed as a series of Hamiltonians $H_N, N \in \mathbb{N}$, which approaches H in the limit $N \to \infty$:

$$H_N = \Lambda^{(N-1)/2}\left\{ H_{\text{imp}} + \sqrt{\frac{\xi_0}{\pi}}\sum_\sigma \left(f_\sigma^\dagger c_{0\sigma} + c_{0\sigma}^\dagger f_\sigma \right) + \sum_{\sigma,n=0}^{N-1} t_n \left(c_{n\sigma}^\dagger c_{n+1\sigma} + c_{n+1\sigma}^\dagger c_{n\sigma} \right) \right\}, \tag{2.5.66}$$

with $H = \lim_{N\to\infty} \Lambda^{-(N-1)/2} H_N$. The factor of $\Lambda^{(N-1)/2}$ is introduced into the equation (2.5.66) in order to cancel the N dependence of t_{N-1} (equation (2.5.65)) Therefore, two successive Hamiltonians are related by

$$H_{N+1} = \Lambda^{1/2} H_N + \Lambda^{N/2} \sum_\sigma t_N \left(c_{N\sigma}^\dagger c_{N+1\sigma} + c_{N+1\sigma}^\dagger c_{N\sigma} \right), \tag{2.5.67}$$

where the sequence starts at

$$H_0 = \Lambda^{-1/2}\left\{ H_{\text{imp}} + \sqrt{\frac{\xi_0}{\pi}}\sum_\sigma \left(f_\sigma^\dagger c_{0\sigma} + c_{0\sigma}^\dagger f_\sigma \right) \right\}. \tag{2.5.68}$$

The equation (2.5.67) can then be interpreted as a RG transformation R in the sense that $H_{N+1} = R(H_N)$. Unlike in the Sections 2.5.1 and 2.5.2 where fixed points are characterised by a set of parameters $\{K\}$ where $R(H(\{K^*\})) = H(\{K^*\})$, there exists no such representation where a set of parameters $\{K^*\}$ can be identified in NRG. Instead, we characterise H_N by its enegy eigenvalues $E_N(r)$ and their eigenstates $|r\rangle_N$:

$$H_N |r\rangle_N = E_N(r) |r\rangle_N , \quad r \in \{1, \ldots, N_s\}, \tag{2.5.69}$$

where N_s is the dimension of H_N. In order to iteratively diagonalise H_N, we assume that the eigenstates and their eigenvalues have been determined for a given N. A basis state for H_{N+1}, labelled as $|r; s\rangle_{N+1}$, is constructed by taking a direct product of the eigenstates of H_N with a suitable basis of the added site $|s(N+1)\rangle$:

$$|r; s\rangle_{N+1} := |r\rangle_N \otimes |s(N+1)\rangle . \tag{2.5.70}$$

The Hamiltonian matrix elements of H_{N+1} are then

$$H_{N+1}(rs, r's') = {}_{N+1}\langle r; s \,|\, H_{N+1} \,|\, r'; s'\rangle_{N+1}. \tag{2.5.71}$$

The Hamiltonian H_{N+1} can then be diagonalised to give the new set of eigenstates $|r\rangle_{N+1}$ with eigenvalues $E_{N+1}(r)$. This new set of eigenstates are related to the product states via the unitary matrix U:

$$|r\rangle_{N+1} = \sum_{r's'} U(r, r's') \, |r'; s'\rangle_{N+1} . \tag{2.5.72}$$

Furthermore, it is convenient to set the energy of the ground state to zero.

Since the basis states of H_{N+1} is constructed from the direct product with a basis set of the added site as written in the equation (2.5.70), the dimension of the Hilbert space grows exponentially by a factor of the dimension of the space of the added site in each NRG step, rendering it impractical to perform diagonalisation numerically. The standard solution to this problem is to truncate the eigenspace by keeping only the N_s lowest-energy eigenstates. The dimension of the eigenspace is therefore fixed to N_s and the NRG computation time grows linearly with the number of NRG steps required. The appropriate number of eigenstates required depends on the model and this is conventionally checked by

varying N_s until the low-energy RG flow is no longer affected. Since in each NRG step, the addition of a new site is a perturbation of the order $\Lambda^{-1/2}$, this becomes very small and the truncation works well for large values of Λ. The smaller the chosen Λ is, the higher number of N_s is required. It is therefore essential to determine the optimised value of Λ and N_s for a particular model Hamiltonian. By choosing $\Lambda \to 1$, we are closer to the continuum limit, but at the same time, large value of N_s is required by the truncation to work efficiently. As mentioned before, it has been shown that accurate results can be obtained even for Λ as large as 2 [45, 46, 48]; hence, in this project, we choose $\Lambda = 3$ and vary the N_s until we obtain the results that are no longer dependent on the number of states kept.

Whilst the RG flow behaviour of a model can already be studied from how the low-lying energy levels behave as a function of NRG iterations, NRG is also powerful for providing information about the physical properties. Their calculations are reviewed in the next section.

2.6 Physical Properties

2.6.1 Thermodynamics

At each NRG iteration N, an average value of a thermodynamic quantity at temperature T can be calculated through

$$\langle \cdots \rangle^{(N)} = \frac{1}{Z^{(N)}} \sum_r \mathrm{e}^{-\beta E_N(r)} \, {}_N\langle r \,|\cdots|\, r\rangle_N, \tag{2.6.1}$$

where the partition function

$$Z^{(N)} = \sum_r \mathrm{e}^{-\beta E_N(r)}. \tag{2.6.2}$$

Since the Hamiltonian H_N is scaled by the factor of $\Lambda^{(N-1)/2}$ in the equation (2.5.66), the states with $E_N(r)/\Lambda^{(N-1)/2} \gg k_\mathrm{B}T$ are exponentially suppressed due to the Boltzmann factor and do not significantly contribute to the sum. We can therefore define the quantity

$$\bar{\beta} \coloneqq \frac{\beta_N}{\Lambda^{(N-1)/2}} \sim 1, \tag{2.6.3}$$

where the inverse temperature $\beta_N = (k_\mathrm{B}T_N)^{-1}$. In practice, $\bar{\beta}$ is chosen to be from 0.5 to 1 and at Nth iteration of the NRG procedure, the temperature is then defined through it, i.e., $k_\mathrm{B}T_N \coloneqq \Lambda^{(N-1)/2}/\bar{\beta}$

The simplest thermodynamic quantities that can be calculated by NRG are the impurity contribution to the entropy S_imp, heat capacity C_imp, and the magnetic susceptibility χ_imp. Given a thermodynamic system and the energies of all the microstates, the free energy F and the internal energy U – in the units where $k_\mathrm{B} = 1$ – are given by

$$F = -T \ln Z \tag{2.6.4}$$

and

$$U = \langle H \rangle = -\frac{1}{Z}\frac{\partial Z}{\partial \beta}, \tag{2.6.5}$$

where $Z = \sum_r \mathrm{e}^{-\beta E(r)}$ is the partition function. The entropy and the heat capacity can then be calculated from via their temperature derivatives:

$$S = -\frac{\partial F}{\partial T} = \beta \langle H \rangle + \ln Z \tag{2.6.6}$$

and

$$C = \frac{\partial U}{\partial T} = \beta^2 \left(\left\langle H^2 \right\rangle - \langle H \rangle^2 \right). \tag{2.6.7}$$

The impurity contribution to these properties are calculated by subtracting away the contribution from the free conduction electrons, e.g., $S_\mathrm{imp} \coloneqq S - S_0$. As an explicit example, at the NRG iteration N, the impurity contribution to the entropy at temperature T_N is calculated from

$$S_\mathrm{imp}(T_N) = S^{(N)} - S_0^{(N)} = \beta_N \left(\left\langle H^{(N)} \right\rangle - \left\langle H_0^{(N)} \right\rangle \right) + \ln \frac{Z^{(N)}}{Z_0^{(N)}}. \tag{2.6.8}$$

The magnetic susceptibility can be calculated in a similar fashion:

$$\chi = \frac{\partial M}{\partial B} = \frac{\partial}{\partial B}\left(\frac{1}{\beta Z}\frac{\partial Z}{\partial B} \right) = \beta \left(\left\langle M^2 \right\rangle - \langle M \rangle^2 \right), \tag{2.6.9}$$

where M is the magnetic moment, which is the sum of the S_z of all spins. The impurity contribution is then $\chi_\mathrm{imp} = \chi - \chi_0$.

For the isotropic one-channel Kondo model, at high temperature, $S_\mathrm{imp} \to \ln 2$ going towards the weak-coupling fixed point due to the doubly degeneracy of

the free spin-$\frac{1}{2}$ impurity, and $T\chi_{\text{imp}} = \frac{1}{3}S(S+1) = \frac{1}{4}$ following Curie's law. At low temperature, due to the strong coupling between the impurity and the conduction electron degree of freedom, the impurity is screened and $S_{\text{imp}} \to 0$ and χ_{imp} becomes constant.

As for the multichannel Kondo model, as is mentioned in Section 2.4, the model is classified into 3 different categories, whose low-temperature behaviours are very interesting. Imagining the posibility of having the impurity spin S being screened by the n channels of spin-$\frac{1}{2}$ conduction electrons, we categorise the model into the case where the spin is exactly screened $S = \frac{n}{2}$, underscreened $S > \frac{n}{2}$, and overscreened $S < \frac{n}{2}$. In the exactly screened case, as the name suggests, $S_{\text{imp}} \to 0$. In the underscreened case, there remains a residual effective spin $S' = S - \frac{n}{2}$ and thus, $S_{\text{imp}} \to \ln[S'(S'+1)]$. And for the most interesting case of all, the overscreened case, the low-temperature impurity entropy at the NFL fixed point, as calculated from Bethe-ansatz solution [92] and conformal field theory (CFT) [93], follows the expression:

$$S_{\text{imp}}(T \to 0) = \ln\left\{\frac{\sin[\pi(2S+1)/(n+2)]}{\sin[\pi/(n+2)]}\right\}, \tag{2.6.10}$$

which suggests non-integer ground-state degeneracy. Near this NFL fixed point, if n is the number of channels, the asymptotic behaviour of the impurity entropy is found to

$$S_{\text{imp}}(T) - S_{\text{imp}}(0) \sim \begin{cases} T^{2\Delta}, & \text{for } n > 2, \\ aT\left(1 - b\ln T\right), & \text{for } n = 2, \end{cases} \tag{2.6.11}$$

where a, b are some constants, $\Delta = 2/(2+n)$, and $1+\Delta$ is the known scaling dimension of the leading irrelevant boundary operator at the overscreened fixed point [52]. Since the heat capacity is related to the entropy by the relation $C = T\frac{\mathrm{d}S}{\mathrm{d}T}$, they have the same asymptotic behaviour. Furthermore, the asymptotic behaviour of the magnetic susceptibility near the NFL fixed point is the same

$$T\chi_{\text{imp}}(T) \sim\sim \begin{cases} T^{2\Delta}, & \text{for } n > 2, \\ cT\left(1 - d\ln T\right), & \text{for } n = 2, \end{cases} \tag{2.6.12}$$

where c, d are some constants.

2.6.2 Scattering t Matrix

The zero-temperature scattering t matrix is define through the equation:

$$G_{kk',i}(\omega) = \frac{\delta_{kk'}}{z-\epsilon_k} + \left(\frac{1}{z-\epsilon_k}\right)\tau_{kk',i}(\omega)\left(\frac{1}{z-\epsilon'_k}\right), \tag{2.6.13}$$

where $G_{kk',j}(\omega)$ is the retarded Green function, $z = \omega + \mathrm{i}\delta$ with $\delta \to 0^+$, and the Fourier transform of $G_{kk',i}(\omega)$ is $G_{kk',i}(t) = -\mathrm{i}\theta(t)\langle\{a_{ki}(t), a^\dagger_{k'i}(0)\}\rangle$. Physically, the t matrix can be understood by considering its relationship with the Green function. The Green function quantifies the scattering of an electron with a wavevector k and spin i at $t = 0$ to the state with a wavevector k' at later time t. As is seen from the equation (2.6.13), the Green function consists of two terms: the first term arises from the non-interacting part of the Hamiltonian, H_{leads}, and the second term is related to the interaction. Therefore, the t matrix is related to the scattering amplitude that arises from the interacting part of the Hamiltonian. Denoting in general the retarded correlation function $-\mathrm{i}\theta(t)\langle\{A(t), B(0)\}\rangle$ by $\langle\langle A; B\rangle\rangle_\omega$, we can derive the general equations of motion by taking the time-derivative and Fourier transforming them:

$$z\langle\langle A; B\rangle\rangle_\omega = \langle\{A, B\}\rangle + \langle\langle [A, H]\,; B\rangle\rangle_\omega \tag{2.6.14}$$

$$= \langle\{A, B\}\rangle + \langle\langle A; [H, B]\rangle\rangle_\omega. \tag{2.6.15}$$

Applying this to the general Hamiltonian $H = H_{\text{leads}} + H_{\text{int}}$, we can write the retarded Green function above $G_{kk',i}(\omega)$ as

$$\langle\langle a_{ki}; a^\dagger_{k'i}\rangle\rangle_\omega = \frac{\delta_{kk'}}{z-\epsilon_k} + \frac{\langle\{[a_{ki}, H_{\text{int}}]\,, a^\dagger_{k'i}\}\rangle + \langle\langle [a_{ki}, H_{\text{int}}]\,; [a_{k'i}, H_{\text{int}}]^\dagger\rangle\rangle_\omega}{(z-\epsilon_k)(z-\epsilon'_k)}. \tag{2.6.16}$$

Therefore, the t matrix can be read off as

$$\tau_{kk',i}(\omega) = \langle\{[a_{ki}, H_{\text{int}}]\,, a^\dagger_{k'i}\}\rangle + \langle\langle [a_{ki}, H_{\text{int}}]\,; [a_{k'i}, H_{\text{int}}]^\dagger\rangle\rangle_\omega. \tag{2.6.17}$$

For convenience, we shall focus on the dimensionless t matrix defined as

$$t_i(\omega) \coloneqq -\pi\rho\,\mathrm{Im}\sum_k \tau_{kk,i}(\omega). \tag{2.6.18}$$

In calculating the t matrix via NRG, we use the FDM–NRG method [94, 95]. Due to the discretisation, we obtain a discrete set of delta functions. We then use the standard method of Ref. [94, 95] to broaden the poles.

The zero-frequency value of the zero-temperature scattering t matrix of the overscreened Kondo model with n channels of conduction electrons and spin-s impurity has been previously calculated from CFT [96]:

$$t(0) = \frac{1}{2}\left(1 - \frac{\cos[\pi(2s+1)/(2+n)]}{\cos[\pi/(2+n)]}\right). \tag{2.6.19}$$

In addition, the asymptotic behaviour near the NFL fixed point is found to be

$$t(\omega) - t(0) \sim -|\omega|^{\Delta}. \tag{2.6.20}$$

2.6.3 Linear Conductance

The other important dynamic quantity is the linear differential conductance in an ac field. We assume that at $t = -\infty$, the system is in equilibrium with all the leads at a common chemical potential $\mu = 0$. Then, also at $t = -\infty$, we adiabatically switch on the chemical potential of lead j which is time dependent: $\mu_j(t) = eV_j \cos(\omega t)$. Assuming that the current $I_i(t,\omega) \coloneqq e\left\langle \frac{\mathrm{d}}{\mathrm{d}t} N_i \right\rangle$, where N_i is the number operator of lead i, has reached an oscillatory steady state by $t = 0$, we define a dimensionless ac conductance tensor as

$$\left(\frac{e^2}{h}\right) G_{ij}(\omega;T) \coloneqq \lim_{V_j \to 0} \frac{\partial I_i(t=0;\omega)}{\partial V_j}. \tag{2.6.21}$$

One may obtain the static conductance in response to a dc voltage by taking the limit $\omega \to 0$: $G_{ij}^{\mathrm{dc}}(T) = \lim_{\omega\to 0} G_{ij}(\omega;T)$.

We use the Kubo formalism [97] to obtain an expression for the linear conductance that can be calculated by NRG. If we have a system that is described by a time-independent Hamiltonian H with a time-dependent perturbation that is adiabatically switched on $H'(t) = \mathrm{e}^{\eta t} B F(t)$, with $\eta \to 0^+$, where B is an operator which describes how the field couples to the system and $F(t)$ is a time-dependent scalar, the change in the expectation value of an observable A, $\Delta\langle A(t)\rangle \coloneqq \mathrm{Tr}[\rho(t)A - \rho_{\mathrm{eq}}A]$, where $\rho(t)$ and ρ_{eq} are the density matrices in the

presence and absence of the perturbation, respectively, is given in Appendix B of Hewson [69]:

$$\Delta \langle A(t) \rangle = \frac{1}{\mathrm{i}\hbar} \mathrm{Tr} \int_{-\infty}^{t} \mathrm{e}^{\eta t'} [B, \rho_{\mathrm{eq}}] A(t - t') F(t') \, \mathrm{d}t', \tag{2.6.22}$$

where $A(t-t') = \mathrm{e}^{\mathrm{i}H(t-t')/\hbar} A \mathrm{e}^{-\mathrm{i}H(t-t')/\hbar}$ is the observable in the interaction picture. In the context of our mesoscopic device, the perturbation which arises from the chemical potential of lead j is of the form

$$H'(t) = \mu_j(t) N_j = e \cos(\omega t) V_j N_j, \tag{2.6.23}$$

where e is the magnitude of the electron charge, ω the frequency of the ac bias voltage, and N_j the number operator of lead j. The current into lead i, $I_i(t) = \left\langle \frac{\mathrm{d}}{\mathrm{d}t} e N_i(t) \right\rangle = e \left\langle \dot{N}_i(t) \right\rangle$ can then be calculated by substituting $A = e\dot{N}_i(t)$ and $B = N_j$ into the Kubo formula, equation (2.6.22):

$$I_i(t;\omega) = \frac{e^2 V_j}{\mathrm{i}\hbar} \mathrm{Tr} \int_{-\infty}^{t} \mathrm{e}^{\eta t'} [N_j, \rho_{\mathrm{eq}}] \dot{N}_i(t - t') \cos(\omega t') \, \mathrm{d}t'. \tag{2.6.24}$$

With the change of variable $t - t' \to t''$ and the definition of the conductivity tensor

$$\sigma_{ij}(\omega) = \frac{\mathrm{i}}{\hbar} \mathrm{Tr} \int_{0}^{\infty} \mathrm{e}^{\mathrm{i}(\omega + \mathrm{i}\eta)t} [N_j, \rho_{\mathrm{eq}}] \dot{N}_i(t) \, \mathrm{d}t, \tag{2.6.25}$$

the current can be rewritten as

$$I_i(t;\omega) = -\frac{e^2 V_j}{2} \left[\mathrm{e}^{-\mathrm{i}\omega t} \sigma_{ij}(\omega) + \mathrm{e}^{\mathrm{i}\omega t} \sigma_{ij}(-\omega) \right] \tag{2.6.26}$$

Finally, with the definition of the spectral function $K_{ij}(\omega)$ which can be expressed as real and imaginary part:

$$K_{ij}(\omega) = -\frac{\mathrm{i}}{\hbar} \int_{0}^{\infty} \mathrm{e}^{\mathrm{i}(\omega + \mathrm{i}\eta)t} \left\langle [\dot{N}_j, \dot{N}_i(t)] \right\rangle \, \mathrm{d}t \tag{2.6.27}$$

$$= K'_{ij}(\omega) + \mathrm{i} K''_{ij}(\omega), \tag{2.6.28}$$

we obtain

$$G_{ij}(t;\omega) = \left(\frac{h}{e^2} \right) \frac{\partial I_i(t;\omega)}{\partial V_j} \tag{2.6.29}$$

$$= 2\pi \left[\cos(\omega t) \frac{\hbar^2 K''_{ij}(\omega)}{\hbar\omega} - \sin(\omega t) \frac{\hbar^2 \left(K'_{ij}(\omega) - K'_{ij}(0) \right)}{\hbar\omega} \right]. \tag{2.6.30}$$

The static dc conductance can be obtained by taking the limit $\omega \to 0$:

$$G_{ij}^{\mathrm{dc}} = \lim_{\omega\to 0} G_{ij}(t;\omega) = -2\pi \lim_{\omega\to 0} \frac{\hbar^2 K_{ij}''(\omega)}{\hbar\omega}. \tag{2.6.31}$$

In comparison with the value at $t = 0$,

$$G_{ij}(\omega) \coloneqq G_{ij}(t=0;\omega) = -2\pi \frac{\hbar^2 K_{ij}''(\omega)}{\hbar\omega}, \tag{2.6.32}$$

we therefore indeed have that

$$G_{ij}^{\mathrm{dc}} = \lim_{\omega\to 0} G_{ij}(\omega). \tag{2.6.33}$$

Finally, by Lehmann resolving $K_{ij}''(\omega)$, one finds that $\mathrm{sgn}[K_{ii}''(\omega)] = \mathrm{sgn}[\omega]$ and as a result, $G_{ii}(\omega) \leqslant 0$. Essentially, in the dc limit, when we apply a positive bias to lead i there is then a current flowing out from that lead and we expect the conductance to be negative.

Now that we have reviewed all the essential ingredients that will be used throughout this thesis, we study the behaviour of the mesoscopic device mentioned earlier by applying NRG to study first its low-energy effective model in the next chapter, and later on, the full model.

3

The Isotropic and the Axially Symmetric Spin Models

In this chapter, we consider the Majorana device as described previously in Section 2.3. Since we are mainly interested in the low-temperature behaviour of the model, following Béri [41], we first derive the low-energy effective model by projecting it into a subspace of a particular charging state. It turns out that the effective model is the Kondo model with a spin-$\frac{1}{2}$ impurity coupled to spin-1 conduction electrons. In order to reduce the complexity of the model, we first impose the full symmetry condition by requiring the coupling constants to all be equal and study the isotropic Kondo model by NRG. We investigate both the model's static thermodynamic properties – the impurity entropy and spin susceptibility – and also the dynamic properties – t matrix and linear conductance. Finally, we lift the isotropic symmetry requirement and find that the low-temperature Fermi liquid behaviour is robust. The work in this chapter has already been published [72].

3.1 Low-Energy Effective Model

Given the Hamiltonian (2.3.1) that is introduced in Section 2.3,

$$H = H_{\text{leads}} + H_{\text{c}} + H_{\text{M}} + H_{\text{t}}, \tag{3.1.1}$$

we are particularly interested in energy scales that are much lower than the charging energy E_c. Assuming that the system is tuned to the middle of a Coulomb blockade valley [15, 27] where $\langle H_\mathrm{c}\rangle = 0$ for some N, Béri [41] derived a low-energy effective Hamiltonian, by following the method that is outlined in Section 2.5.2: consider virtual excitations to the adjacent charging states $N-1$ and $N+1$ as perturbations. Here, we split the Hilbert space into three subspaces: $\{\psi_0\}$ for the charging state N, $\{\psi_1\}$ for $N+1$, and $\{\psi_{\bar{1}}\}$ for $N-1$. The low-energy effective Hamiltonian can be read off from the equation (2.5.18) as

$$H_\mathrm{eff} = H_{0\bar{1}}\left(E - H_{\bar{1}\bar{1}}\right)^{-1} H_{\bar{1}0} + H_{00} + H_{01}\left(E - H_{11}\right)^{-1} H_{10}. \tag{3.1.2}$$

As before, H_{ij} is interpreted as the components of H that takes the states from subspace j to subspace i. Therefore, $H_{10} = H_{0\bar{1}} = \sum_{ij} t_{ij}\gamma_i\psi_j \mathrm{e}^{\mathrm{i}\phi/2}$ adds an electron to the superconductor whereas $H_{01} = H_{\bar{1}0} = H_{10}^\dagger$ removes an electron from the superconductor. Furthermore, since the subspace with $N-1$ and $N+1$ are not connected, $H_{\bar{1}1} = H_{1\bar{1}} = 0$. Finally, H_{00} is the part of the Hamiltonian that does not change the number of electrons on the superconductor: $H_{00} = H_\mathrm{leads} + H_\mathrm{M}$.

Consider now explicitly the third term and noting that the commutation relation $\left[H_{11}, \mathrm{e}^{\mathrm{i}\phi/2}\right] = E_\mathrm{c}\mathrm{e}^{\mathrm{i}\phi/2}$ is of the form $[H, A] = cA$, we can then use the identity $\frac{1}{E-H}A = A\frac{1}{E-(H+c)}$ [98]. Therefore,

$$H_{01}\left(E - H_{11}\right)^{-1} H_{10} = \sum_{ij} t_{ij}^* \mathrm{e}^{-\mathrm{i}\phi/2}\psi_j^\dagger\gamma_i \left(E - H_{11}\right)^{-1} \sum_{kl} t_{kl}\gamma_k\psi_l \mathrm{e}^{\mathrm{i}\phi/2} \tag{3.1.3}$$

$$= \sum_{ijkl} t_{ij}^* t_{kl} \mathrm{e}^{-\mathrm{i}\phi/2}\psi_j^\dagger\gamma_i\gamma_k\psi_l \mathrm{e}^{\mathrm{i}\phi/2}\left(E - (H_{11} + E_\mathrm{c})\right)^{-1} \tag{3.1.4}$$

$$\approx \sum_{ijkl} \frac{t_{ij}^* t_{kl}}{-E_\mathrm{c}}\gamma_i\gamma_k\psi_j^\dagger\psi_l \tag{3.1.5}$$

$$= \sum_{ijkl} \frac{t_{ij}^* t_{kl}}{E_\mathrm{c}}\gamma_k\gamma_i\psi_j^\dagger\psi_l - \sum_{ijl} \frac{2t_{ij}^* t_{il}}{E_\mathrm{c}}\psi_j^\dagger\psi_l, \tag{3.1.6}$$

where we have made the approximation that E_c is much larger than the energy scale of interest. The terms $\psi_j^\dagger\psi_l$ (without the Majorana operators) of the equation (3.1.6) are potential scattering terms, do not renormalise, and will not be

considered. Similarly,

$$H_{0\bar{1}}\left(E - H_{\bar{1}\bar{1}}\right)^{-1} H_{\bar{1}0} \approx \sum_{ijkl} \frac{t_{ij}^* t_{kl}}{-E_\mathrm{c}} \gamma_k \gamma_i \psi_l \psi_j^\dagger \tag{3.1.7}$$

$$= \sum_{ijkl} \frac{t_{ij}^* t_{kl}}{E_\mathrm{c}} \gamma_k \gamma_i \psi_j^\dagger \psi_l - \sum_{ijk} \frac{t_{ij}^* t_{kj}}{E_\mathrm{c}} \gamma_k \gamma_i. \tag{3.1.8}$$

We shall ignore and absorb the second term of the equation (3.1.8) into the Majorana-coupling terms H_M. The first terms of the two equations are the same and can be combined, though we shall neglect the terms where $i = k$ since these are again potential scattering terms. Thus, the low-energy effective Hamiltonian becomes

$$H_\mathrm{eff} = H_\mathrm{leads} + H_\mathrm{M} + \sum_{\substack{ijkl \\ i \neq k}} \frac{2 t_{ij}^* t_{kl}}{E_\mathrm{c}} \gamma_k \gamma_i \psi_j^\dagger \psi_l. \tag{3.1.9}$$

We shall now show that the last two terms can be written in terms of the spin operators. First, we consider a Kondo model of a spin-$\frac{1}{2}$ impurity coupled to spin-1 conduction electrons [41, 70, 71]:

$$H_\mathrm{K} = \sum_\alpha J_{\alpha\alpha} S_\alpha I_\alpha, \tag{3.1.10}$$

where S_α is a spin-$\frac{1}{2}$ object and can be realised from the Majorana bilinears as mentioned in Section 2.1, $S_\alpha = \frac{1}{2}\sigma_\alpha = -\frac{\mathrm{i}}{4}\sum_{ij} \epsilon_{\alpha ij} \gamma_i \gamma_j$, and I_α is a spin-1 object formed from the lead electrons, $I_\alpha = -\mathrm{i}\sum_{ij} \epsilon_{\alpha ij} \psi_i^\dagger \psi_j$, where σ_α are the Pauli matrices and $\epsilon_{\alpha ij}$ is the antisymmetric Levi–Civita tensor. Consider explicitly the $\alpha = 1$ component of H_K:

$$J_{11} S_1 I_1 = \frac{1}{2} J_{11} \gamma_2 \gamma_3 \left(\psi_3^\dagger \psi_2 - \psi_2^\dagger \psi_3\right) = \frac{J_{11}}{2} \left(\gamma_2 \gamma_3 \psi_3^\dagger \psi_2 + \gamma_3 \gamma_2 \psi_2^\dagger \psi_3\right). \tag{3.1.11}$$

Now consider only the first term in the parenthesis, this can be generated from the last term of the effective Hamiltonian (3.1.9) when the indices $i = j = 3$, $k = l = 2$, which leads to the coupling $\sim t_{22} t_{33}$, and also when $i = l = 2$, $j = k = 3$, leading to the coupling $\sim t_{23}^2$. The former is the local coupling between the Majoranas and the lead electrons whereas the latter is the long-range coupling between the Majorana and the other lead electrons. Since the Majoranas are well localised, the overlap between the wavefunctions of the non-local Majoranas are

small and the coupling constants $t_{ij,i\neq j}$ are exponentially small, $t_{23} \ll t_{22}, t_{33}$ and can be ignored. We therefore conclude that indeed the spin Hamiltonian (3.1.10) is a result of some of the last term of the effective Hamiltonian (3.1.9) and the spin coupling constants $J_{\alpha\alpha}$ can be expressed as

$$J_{\alpha\alpha} \approx \sum_{ij} |\epsilon_{\alpha ij}| \frac{2t_{ii}t_{jj}}{E_{\mathrm{c}}}, \tag{3.1.12}$$

where as mentioned before, the exponentially small long-range couplings when $i = l, j = k$ are ignored. Furthermore, other exponentially small non-local couplings t_{ij}, h_{ij}, where $i \neq j$ generate the term

$$\delta H = \sum_{\substack{\alpha\beta \\ \alpha\neq\beta}} J_{\alpha\beta} S_\alpha I_\beta + \sum_{\alpha\beta} J'_{\alpha\beta} S_\alpha I^{(2)}_\beta + \sum_\alpha h_\alpha S_\alpha, \tag{3.1.13}$$

where $I^{(2)}_\alpha = \sum_{ij} \psi^\dagger_i \left[J^{(2)}_\alpha\right]_{ij} \psi_j$ are the five components of a spin-2 density and $J^{(2)}_\alpha$ are elementary symmetric real matrices. The coupling constants $J_{\alpha\beta} \sim J'_{\alpha\beta} \sim \frac{t_{ij}t_{jj}}{E_{\mathrm{c}}}$, and $h_\alpha \sim \epsilon_{\alpha ij} h_{ij}$. Therefore, our effective low-energy Hamiltonian becomes

$$H_{\mathrm{eff}} = H_{\mathrm{leads}} + H_{\mathrm{K}} + H_{\mathrm{M}} + \delta H. \tag{3.1.14}$$

3.2 Isotropic Spin Model

In order to understand the basic universal physics of the model, we shall begin by ignoring all the exponentially small terms in the equation (3.1.14): δH, which arises from the non-local coupling between the Majorana and the lead electrons and H_{M}, which describes the non-local coupling between two Majorana fermions. Furthermore, we impose the full symmetry condition and consider the isotropic spin coupling of the Hamiltonian H_{K}, equation (3.1.10): $J_{11} = J_{22} = J_{33} =: J$. This condition corresponds physically to the device in which the local couplings between all the conduction leads and the Majoranas are equal. Therefore, the effective Hamiltonian of interest is reduced to

$$H^{\mathrm{iso}}_{\mathrm{eff}} = \sum_{ki} \varepsilon_k a^\dagger_{ki} a_{ki} + J \sum_\alpha S_\alpha I_\alpha. \tag{3.2.1}$$

We then perform the following transformation to the lead operators:

$$c_{k,-1} = \frac{1}{\sqrt{2}}(a_{k1} + \mathrm{i}a_{k2}), \tag{3.2.2}$$

$$c_{k,0} = a_{k3}, \tag{3.2.3}$$

$$c_{k,+1} = \frac{-1}{\sqrt{2}}(a_{k1} - \mathrm{i}a_{k2}). \tag{3.2.4}$$

The electron orbitals localised at the end of each wire become $f_j = \frac{1}{\sqrt{N_{\mathrm{orb}}}} \sum_k c_{k,j}$, analogous to the equation (2.3.6). By changing the spin-1 operators I_α to their raising and lowering equivalents $I^\pm = I_x \pm \mathrm{i}I_y$ and expressing them in terms of these transformed lead operators,

$$I^+ = \sqrt{2}\left(f_0^\dagger f_{-1} - f_{+1}^\dagger f_0\right), \tag{3.2.5}$$

$$I^- = \sqrt{2}\left(f_0^\dagger f_{+1} - f_{-1}^\dagger f_0\right), \tag{3.2.6}$$

$$I_z = f_{+1}^\dagger f_{+1} - f_{-1}^\dagger f_{-1}, \tag{3.2.7}$$

the effective Hamiltonian becomes

$$\begin{aligned} H_{\mathrm{eff}}^{\mathrm{iso}} = \sum_{kj} \varepsilon_k c_{k,j}^\dagger c_{k,j} + J\Big\{ & S_z\left(f_{+1}^\dagger f_{+1} - f_{-1}^\dagger f_{-1}\right) \\ & + \frac{1}{\sqrt{2}}\left[S^+\left(f_0^\dagger f_{+1} + f_{-1}^\dagger f_0\right) + S^-\left(f_{+1}^\dagger f_0 + f_0^\dagger f_{-1}\right)\right]\Big\}, \end{aligned} \tag{3.2.8}$$

where, analogous to the spin-1 operators I_α, the spin-$\frac{1}{2}$ operators S_α are also expressed in their raising and lowering forms $S^\pm = S_x + \mathrm{i}S_y$.

From the standard NRG code for a Kondo model with a spin–$\frac{1}{2}$ impurity coupled to spin-$\frac{1}{2}$ conduction electrons, we therefore replace the spin-$\frac{1}{2}$ lead electron operators $s_z(0)$, $s^+(0)$, and $s^-(0)$ by the spin-1 operators, equation (3.2.5)–(3.2.7). The two quantum numbers which are used in block diagonalisation processes are then the total charge, $Q = 2(n_{+1} + n_0 + n_{-1} - \frac{3}{2})$, where the factor of $\frac{3}{2}$ is added so that the maximum and minimum number of charge is symmetric about 0, and the total z-component of the spins, $2S_{z,\mathrm{tot}} = 2(S_z + n_{+1} - n_{-1})$, where the factor of 2 is added so that the number is an integer, and the operators $n_j = f_j^\dagger f_j$.

3.2.1 Kondo Scale and Thermodynamics

Before we discuss any specific physical properties of the model, we discuss the Kondo temperature T_{K}, which is the universal temperature that sets the scale of the universal flow of *all* the physical properties. Since Fabrizio and Gogolin [70] and Sengupta and Kim [71] argued a Kondo model with spin-$\frac{1}{2}$ impurity coupled to spin-1 conduction electrons is equivalent to the 4CK model, we might expect the same dependence of the Kondo temperature as a function of the coupling strength J, equation (2.5.37) with $n = 4$:

$$T_{\mathrm{K}}/D = c\,(\rho J)^2\,\mathrm{e}^{-1/\rho J}. \tag{3.2.9}$$

Numerically, we define T_{K} to be the temperature at which the impurity entropy, as defined in Section 2.6.1, is halfway between the WC and NFL fixed points: $S_{\mathrm{imp}}(T_{\mathrm{K}}) = \frac{1}{2}(\ln 2 + \ln\sqrt{3}) \approx 0.62$. As is shown in Figure 3.1, the results from NRG confirms that exactly.

The RG flow behaviour of this model can be observed clearly from the impurity entropy S_{imp} as a function of temperature (Figure 3.2 (left)). The universal RG flow is the same as that of 4CK model: a crossover from the WC fixed point at high temperature with $S_{\mathrm{imp}} = \ln 2 \approx 0.69$, since the spin-$\frac{1}{2}$ is doubly degenerate, to the NFL fixed point with $S_{\mathrm{imp}} = \ln\sqrt{3} \approx 0.55$, coinciding with the residual entropy value expected of an overscreened multichannel Kondo model, equation(2.6.10) with $n = 4$. Near the NFL fixed point, when $T \ll T_{\mathrm{K}}$, the impurity entropy follows the asymptotic form: $S_{\mathrm{imp}}(T) - S_{\mathrm{imp}}(0) \sim (T/T_{\mathrm{K}})^{2/3}$, exactly the expected behaviour of the NFL fixed point of the 4CK model, equation (2.6.11) with $n = 4$.

The equivalent universal flow behaviour is also observed in the impurity spin susceptibility $T\chi_{\mathrm{imp}}$ (Figure 3.2 (right)), also defined in Section 2.6.1: a crossover from the WC fixed point at high temperature with $T\chi = C = \frac{1}{3}S(S+1) = \frac{1}{4}$, where C is the Curie constant and $S = \frac{1}{2}$ is the spin of the impurity, following Curie's law, to the NFL fixed point with $T\chi = 0$. The same asymptotic relation near the NFL fixed point are the same as that of the impurity entropy, $T\chi_{\mathrm{imp}}(T) \sim (T/T_{\mathrm{K}})^{2/3}$, and these have already been identified [41, 72] and are in full agreement with the numerical results presented here.

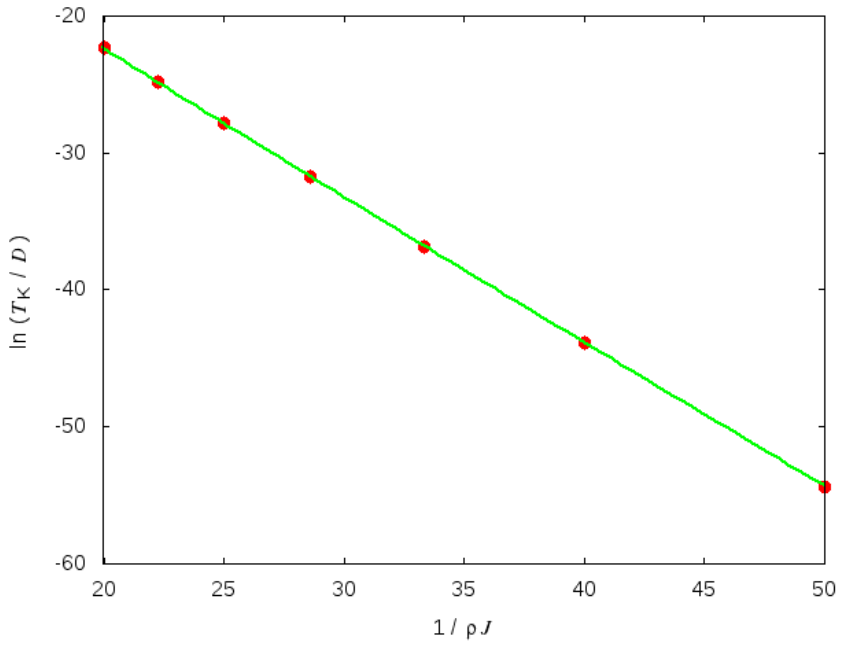

Figure 3.1: The dependence of the Kondo temperature T_K on $1/\rho J$ for the isotropic spin model. The red dots are data calculated from NRG whereas the green line is the analytical expression from the poor man's scaling, equation (3.2.9).

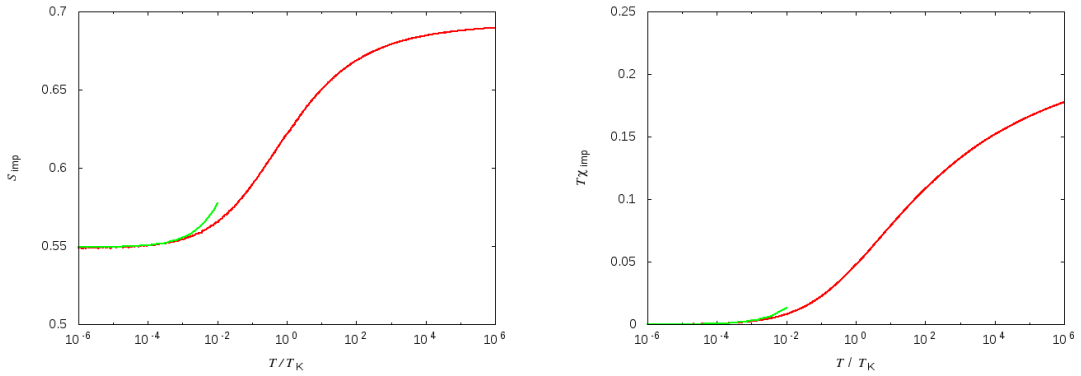

Figure 3.2: The universal temperature dependence of the thermodynamics for the isotropic spin model. (left) The impurity entropy S_imp (red line) showing the RG flow from the WC fixed point $S_\mathrm{imp} = \ln 2 \approx 0.69$ to the NFL fixed point $S_\mathrm{imp} = \ln\sqrt{3} \approx 0.55$, with the asymptote near the NFL fixed point of $(T/T_\mathrm{K})^{2/3}$ (green line). (right) The impurity spin susceptibility $T\chi_\mathrm{imp}$ (red line) following the same crossover with the same asymptote (green line).

3.2.2 Dynamics: Scattering t Matrix

In this section, we study the universal RG flow of the scattering t matrix and the zero-bias differential conductance. The t matrix can be calculated by using the equation (2.6.17) in the general formulation in section 2.6.2, but we need to first calculate the commutation relations

$$[c_{k,j}, H_{\text{int}}] = \frac{1}{\sqrt{N_{\text{orb}}}} X_j, \tag{3.2.10}$$

where

$$X_{-1} = J\left(\frac{1}{\sqrt{2}} S^+ f_0 - S^z f_{-1}\right), \tag{3.2.11}$$

$$X_0 = \frac{J}{\sqrt{2}}\left(S^+ f_{+1} + S^- f_{-1}\right), \tag{3.2.12}$$

$$X_{+1} = J\left(\frac{1}{\sqrt{2}} S^- f_0 + S^z f_{+1}\right). \tag{3.2.13}$$

Substituting these relations into the equation (2.6.17), we find the expression for the t matrix:

$$\tau_j(\omega) = \sum k\tau_{kk,j}(\omega) = jJ\langle S_z\rangle + \langle\langle X_j; X_j^\dagger\rangle\rangle_\omega. \tag{3.2.14}$$

As defined previously in equation (2.6.18), the dimensionless quantity of interest is $t_i(\omega) = -\pi\rho\,\text{Im}\tau_i(\omega)$.

Although the expressions above for t matrices are written in terms of X_j operators which involve the localised transformed operators f_k, they are also valid for t matrices in the original physical basis. The reasoning is as follows: Since the original lead operator a_{k3} and the transformed lead operator $c_{k,0}$ are the same, the t matrix for the physical lead 3 is the same as that for the transformed spin $i = 0$. However, since the model under consideration is isotropic, the t matrices for all three spin species are the same; hence, so are those for all three leads. This is confirmed in our NRG result (not shown) and we shall show only the results calculated from the spin $j = -1$. Figure 3.3 shows the zero-temperature scattering t matrix as a function of frequency ω. The universal RG flow from the WC fixed point where $t_i = 0$ to the NFL fixed point where $t_i = \frac{1}{2}$ is clearly observed. Note here that this zero-frequency value $t_i(0) = \frac{1}{2}$ is different from the value CFT predicted for the 4CK model, equation(2.6.19) with $n = 4$ and $s = \frac{1}{2}$:

$t_i^{4\mathrm{CK}}(0) = \frac{3-\sqrt{3}}{6} \approx 0.21$. This is not unexpected because the actual conduction channels of the two models are different [72]: whereas there are 4 channels of spin-$\frac{1}{2}$ electrons in one model, there is a single channel of spin-1 electrons in the other.

In addition, we analyse the asymptotic behaviour of the model both at high and low frequency. The behaviour at high frequency $|\omega| \gg T_\mathrm{K}$, near the WC fixed point, can be explained by the perturbative scattering of conduction electrons from the spin-$\frac{1}{2}$ impurity local moment, and takes the form [99]

$$t_i(\omega) \overset{|\omega|\gg T_\mathrm{K}}{\sim} \frac{1}{a + \ln^2(b|\omega|/T_\mathrm{K})}, \tag{3.2.15}$$

with some constants a and b. The behaviour near the NFL fixed point at low frequency $|\omega| \ll T_\mathrm{K}$ is as predicted by CFT [96], equation (2.6.20), for 4CK model:

$$t_i(\omega) - t_i(0) \overset{|\omega|\ll T_\mathrm{K}}{\sim} -\left(\frac{|\omega|}{T_\mathrm{K}}\right)^{\frac{1}{3}}. \tag{3.2.16}$$

3.2.3 Dynamics: Linear Conductance

Finally, we study the dynamic property that can be probed experimentally, the linear conductance. Since the local couplings t_{ii} are isotropic, the Hamiltonian under consideration is symmetric with respect to the interchange of the leads and the three conduction leads are equivalent; hence, there are only two distinct conductance tensors: $G_{ii}(\omega)$ and $G_{ij}(\omega)$ when $i \neq j$.

According to the equation (2.6.32), the conductance is related to the spectral function by $G_{ij}(\omega) = -2\pi\frac{\hbar^2 K''_{ij}(\omega)}{\hbar\omega}$, whereas $K_{ij}(\omega)$ is related to the time derivatives of the lead operators $\dot{N}_i$ through equation (2.6.27). Therefore, we need to calculate them first. Furthermore, when working with NRG, the lead operators that we use are the transformed lead operators $c_{k,j}$ equation(3.2.2–3.2.4). Unlike in the case of the t matrix where the result for the spin $j = -1$ is equivalent to that in the physical basis, here we need to explicitly relate the conductance tensors of the two bases.

If we represent the number operators in the physical basis by $N_i = a^\dagger_{ki} a_{ki}$ and those in the transformed basis by $\mathcal{N}_j = c^\dagger_{k,j} c_{k,j}$, we can show that $\mathcal{N}_{-1} + \mathcal{N}_1 =$

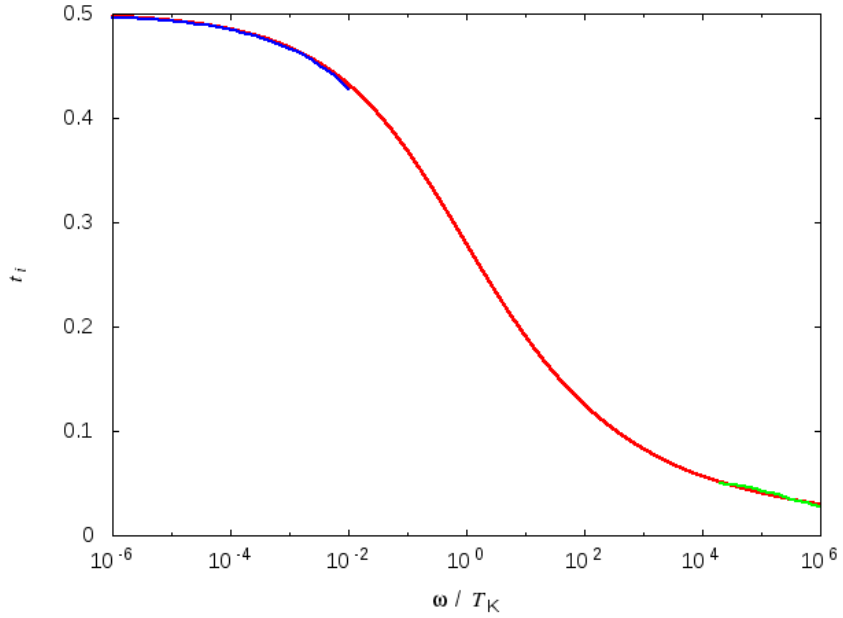

Figure 3.3: The frequency dependence of the zero-temperature scattering t matrices t_i for the isotropic spin model, calculated from NRG (red line) with the high-temperature asymptote of equation(3.2.15) (green line), and the low-temperature NFL asymptote, equation (3.2.16) (blue line).

$N_1 + N_2$ and $\mathcal{N}_0 = N_3$. Therefore,

$$\mathcal{G}_{00}(\omega) = G_{33}(\omega), \tag{3.2.17}$$

$$\mathcal{G}_{-10}(\omega) + \mathcal{G}_{10}(\omega) = G_{13}(\omega) + G_{23}(\omega). \tag{3.2.18}$$

Due to current conservation, we also have that

$$G_{13}(\omega) + G_{23}(\omega) + G_{33}(\omega) = 0, \tag{3.2.19}$$

$$\mathcal{G}_{-10}(\omega) + \mathcal{G}_{00}(\omega) + \mathcal{G}_{10}(\omega) = 0. \tag{3.2.20}$$

Imposing the isotropy condition, $\mathcal{G}_{ik}(\omega) = \mathcal{G}_{jk}(\omega)$ and $G_{ik}(\omega) = G_{jk}(\omega)$ when $i, j \neq k$ and combining it with the two results above, we conclude that

$$G_{ik}(\omega) = -\frac{1}{2}G_{ii}(\omega) = -\frac{1}{2}\mathcal{G}_{ii}(\omega) = \mathcal{G}_{ik}(\omega). \tag{3.2.21}$$

Both the diagonal and off-diagonal conductance tensors are conserved by the basis transformation.

The last ingredient we need for the NRG calculation is the expression for the time derivatives of the lead operators $\dot{N}_i$, which can be calculated by using the equation $\mathrm{i}\hbar\dot{N}_i = [N_i, H]$:

$$\mathrm{i}\hbar\dot{\mathcal{N}}_{-1} = \frac{J}{\sqrt{2}}\left(S^+ f_{-1}^\dagger f_0 - S^- f_0^\dagger f_{-1}\right), \tag{3.2.22}$$

$$\mathrm{i}\hbar\dot{\mathcal{N}}_{+1} = \frac{J}{\sqrt{2}}\left(S^- f_{+1}^\dagger f_0 - S^+ f_0^\dagger f_{+1}\right), \tag{3.2.23}$$

$$\mathrm{i}\hbar\dot{\mathcal{N}}_0 = -\mathrm{i}\hbar\left(\dot{\mathcal{N}}_{-1} + \dot{\mathcal{N}}_{+1}\right), \tag{3.2.24}$$

where the last equation arises physically from the current conservation. We can therefore use these operators to calculate $K_{ij}(\omega)$ and subsequently to calculate $G_{ij}(\omega)$ using the standard FDM-NRG method [94, 95].

Arbitrarily, we choose to calculate the off-diagonal conductance $\mathcal{G}_{-10}(\omega)$ and the diagonal conductance $G_{-1-1}(\omega)$. As mentioned in Section 2.6.3, the diagonal conductance is expected to be negative. Together with the equation (3.2.21), we expect the off-diagonal conductance to be positive. This is indeed observed to be the case, as shown in Figure 3.4. The zero-frequency values are observed to be $G_{ik}(\omega) = \frac{2}{3}$ and $G_{ii}(\omega) = -\frac{4}{3}$. The relationship between the two clearly holds at zero-frequency, but in general, the equation (3.2.21), $G_{ik}(\omega) = -\frac{1}{2}G_{ii}(\omega)$, can be confirmed: $G_{00}(\omega)$ scaled by a factor of $-\frac{1}{2}$ superposes onto $G_{10}(\omega)$. Since we have confirmed the relationship between the two conductance tensors, we now focus only on the positive off-diagonal conductance $G_{ik}(\omega), i \neq k$. As in the case of t matrix, the behaviour at high frequency $|\omega| \gg T_\mathrm{K}$, near the WC fixed point, takes the form

$$G_{ik}(\omega; T=0) \overset{|\omega|\gg T_\mathrm{K}}{\sim} \frac{1}{a' + \ln^2(b'|\omega|/T_\mathrm{K})}, \tag{3.2.25}$$

with some constants a' and b', which is characteristic of spin-flip scattering of conduction electrons from a free spin-$\frac{1}{2}$ impurity local moment. The behaviour at low frequency $|\omega| \ll T_\mathrm{K}$, near the NFL fixed point if of the form

$$G_{ik}(\omega; T=0) - G_{ik}(0,0) \overset{|\omega|\ll T_\mathrm{K}}{\sim} -\left(\frac{|\omega|}{T_\mathrm{K}}\right)^{\frac{2}{3}}, \tag{3.2.26}$$

clearly different from the asymptote of the t matrix $(|\omega|/T_\mathrm{K})^{1/3}$, equation (3.2.16). The explanation for the different power is given by Béri through CFT [41, 72].

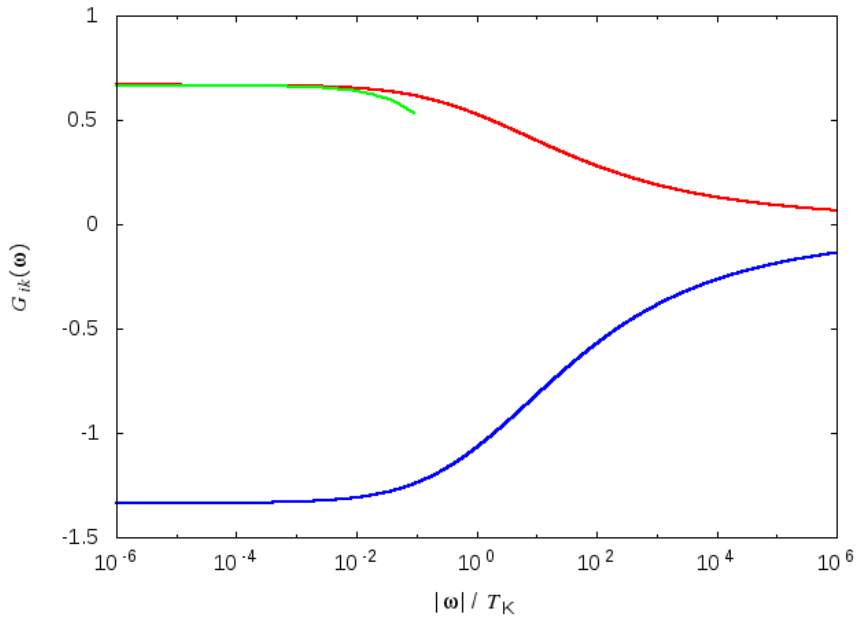

Figure 3.4: The frequency dependence of the zero-temperature conductance tensors G_{ik} for the isotropic spin model, calculated from NRG, both for the non-diagonal component $G_{ik}, i \neq k$ which is positive (red line) and the diagonal component G_{ii} which is negative (blue line). As expected, $G_{ik}(|\omega|/T_K) = -\frac{1}{2}G_{ii}(|\omega|/T_K)$, equation(3.2.21). Near the NFL fixed point, the asymptotic behaviour for $G_{ik}(|\omega|/T_K)$ is of the form $(|\omega|/T_K)^{2/3}$ (green line) predicted by CFT, equation (3.2.26).

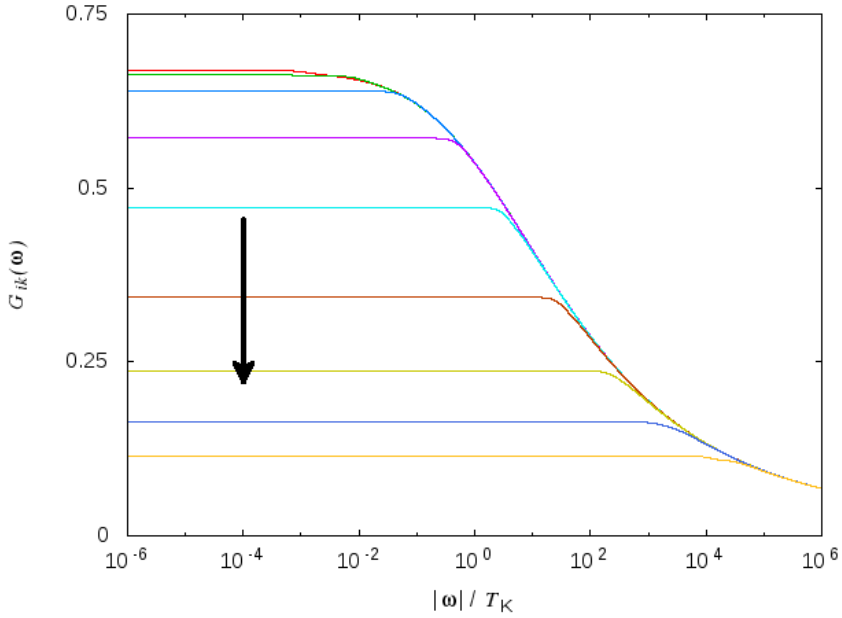

Figure 3.5: The frequency dependence of the conductance tensors $G_{ik}, i \neq k$ for the isotropic spin model at the temperature range of $10^{-4} \leqslant T/T_K \leqslant 10^4$. The temperature is increased along the direction of the black arrow.

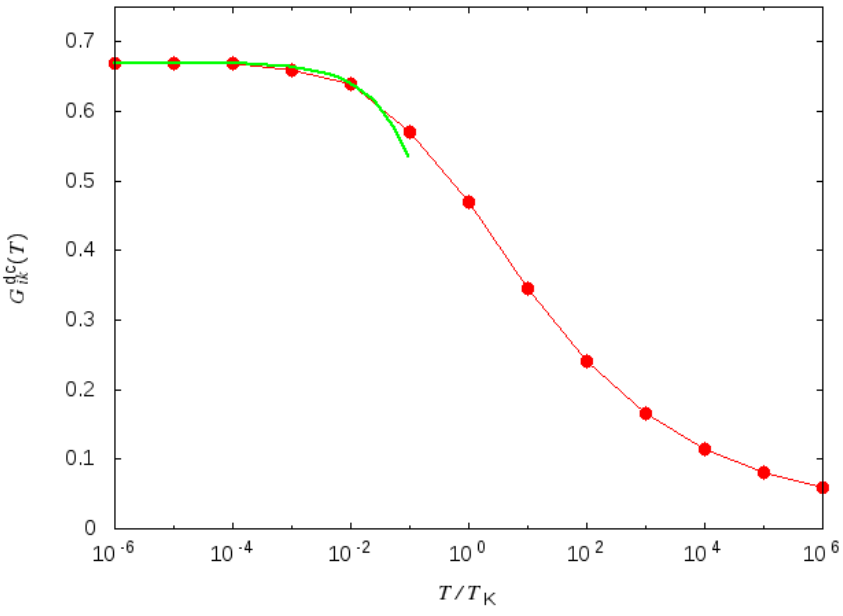

Figure 3.6: The temperature dependence of the dc conductance tensors $G_{ik}^{\mathrm{dc}}(T), i \neq k$ for the isotropic spin model which is calculated by taking the limit as $\omega \to 0$ of $G_{ik}(\omega; T)$ (red dots; the line is merely a guide line). The asymptotic behaviour near the NFL fixed point is of the form $(T/T_K)^{2/3}$ (green line), consistent with the CFT prediction.

By using perturbation theory arond the NFL fixed point, the scaling dimension of the leading irrelevant operators is $\frac{4}{3}$; CFT thus predicts the asymptote of $\omega^{4/3-1}$ for the t matrix. However, all the first-order contributions to the conductance vanish by symmetry; therefore, the asymptote for the conductance becomes $\omega^{2/3}$ due to the second-order terms.

We close this section by looking at the temperature dependence of the linear conductance, which is shown in Figure 3.5 at the temperature range of $10^{-4} \leqslant T/T_{\mathrm{K}} \leqslant 10^{4}$. The frequency dependence of the conductance tensor follows the same zero-temperature curve, however, plateaus off sooner. The higher the temperature, the sooner it reaches the zero-frequency value. From it, we can extract the static conductance by taking the limit $\omega \to 0$, equation (2.6.33). The temperature dependence of the static conductance is shown in Figure 3.6 where we observe that the behaviour is the same as that the frequency dependence of the zero-temperature conductance. In particular, we show in Figure 3.7 that near the NFL fixed point at low temperature, the asymptote agrees with the prediction by CFT [41]:

$$G_{ik}^{\mathrm{dc}}(T) - G_{ik}^{\mathrm{dc}}(0) \overset{T \ll T_{\mathrm{K}}}{\sim} - \left(\frac{T}{T_{\mathrm{K}}}\right)^{\frac{2}{3}}. \tag{3.2.27}$$

Now that we have fully understood the basic properties of the isotropic model, in the next section, we relax some symmetry constraints and study their consequences.

3.3 Axially-Symmetric Model

In this section, we continue to study the spin part of the Hamiltonian (3.1.10), but start considering some of the perturbation terms in δH. In particular, we constraint the system to a case where the coupling $t_{11} = t_{22}$ and imaginary coupling $t_{12} = -t_{21}$, which leads to the axial symmetry around axis 3 and allows the calculations to be done with real matrix elements. Finally, we allow the transverse and the longitudinal spin coupling constants to be different. The Hamiltonian of interest then is

$$H_{\mathrm{eff}}^{\mathrm{axial}} = \sum_{ki} \varepsilon_k a_{ki}^{\dagger} a_{ki} + J_z S_z I_z + J_{\perp} \sum_{\alpha \in \{x,y\}} S_\alpha I_\alpha. \tag{3.3.1}$$

Performing the lead operator transformations (3.2.2)–(3.2.4) as before, and explicitly expressing the spin-1 operators I_α in terms of the localised lead electron operators f_j, (3.2.5)–(3.2.7), the Hamiltonian of the axially-symmetric spin model can then be written as

$$\begin{aligned} H_{\text{eff}}^{\text{axial}} = &\sum_{kj} \varepsilon_k c_{k,j}^\dagger c_{k,j} + J_z S_z \left(f_{+1}^\dagger f_{+1} - f_{-1}^\dagger f_{-1} \right) \\ &+ \frac{J_\perp}{\sqrt{2}} \left[S^+ \left(f_0^\dagger f_{+1} + f_{-1}^\dagger f_0 \right) + S^- \left(f_{+1}^\dagger f_0 + f_0^\dagger f_{-1} \right) \right]. \end{aligned} \tag{3.3.2}$$

3.3.1 Kondo Temperature for Small K_z

As usual, we begin by investigating the Kondo temperature. Béri [41] has shown that for this model, the scaling equations up to the second-order of the coupling constants are exactly the same as that of the single-channel Kondo model,

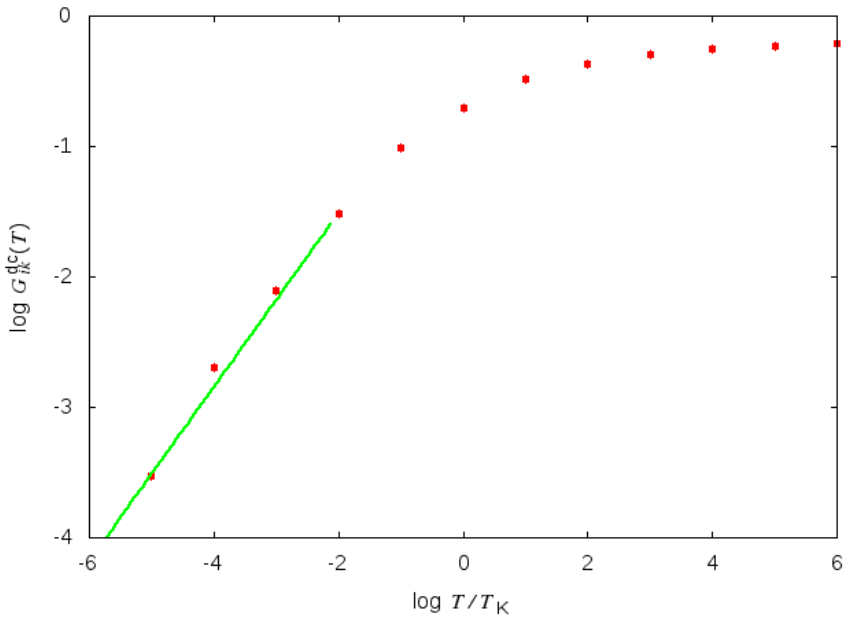

Figure 3.7: The log–log plot of the temperature dependence of the dc conductance tensors $G_{ik}^{\text{dc}}(T)$ for the isotropic spin model. The plot is linear with the slope of $\frac{2}{3}$ confirming the asymptotic behaviour in equation (3.2.27).

equations (2.5.26)–(2.5.27):

$$\frac{\mathrm{d}K_\perp}{\mathrm{d}\ln D} = -K_\perp K_z, \quad \frac{\mathrm{d}K_z}{\mathrm{d}\ln D} = -K_\perp^2. \tag{3.3.3}$$

These scaling equations can then be solved in the limit of small coupling constants to give [100, 101]:

$$T_\mathrm{K}/D \overset{K_z \ll 1}{\simeq} c\,\mathrm{e}^{-\alpha/K_z}, \tag{3.3.4}$$

where

$$\alpha = \begin{cases} \frac{1}{\gamma}\tan^{-1}\gamma, & K_z \leqslant K_\perp, \\ \frac{1}{\gamma}\tanh^{-1}\gamma, & K_z \geqslant K_\perp, \end{cases} \tag{3.3.5}$$

with

$$\gamma^2 = \left|1 - \left(\frac{K_\perp}{K_z}\right)^2\right|. \tag{3.3.6}$$

Figure 3.8 (left) shows the K_z dependence of T_K calculated from NRG at four different values of $K_\perp \in \{0.02, 0.1, 0.2, 1\}$. For small $K_z \ll 1$, the results agree very well with the equation (3.3.4).

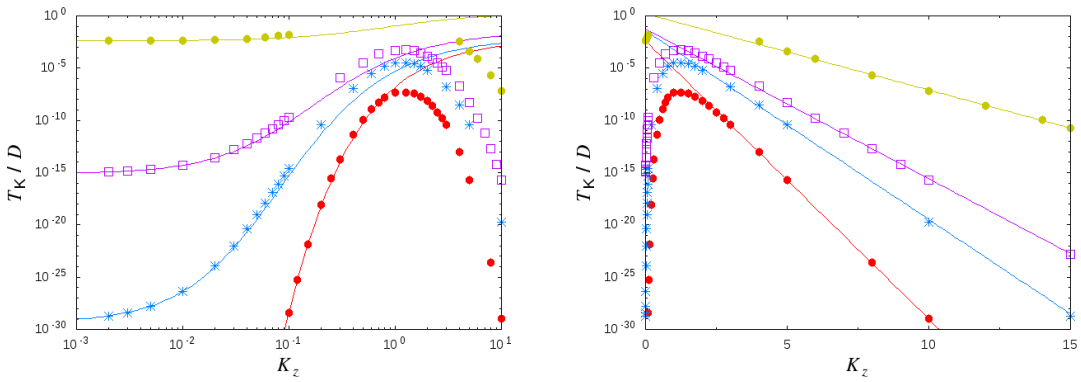

Figure 3.8: The dependence of the Kondo temperature T_K on the coupling constant $K_z = \rho J_z$ at the different values of $K_\perp = \rho J_\perp = 0.02, 0.1, 0.2, 1$ (red circles, blue crosses, purple squares, and green circles, respectively) for the axially-symmetric spin model (3.3.2). (left) The log–log plot highlights the agreement of the T_K (for small K_z) calculated from NRG with the equation (3.3.4) (red line, blue line, purple line, and green line), which is obtained by analytically solving the scaling equations 3.3.3 in the limit $K_z \ll 1$. (right) The log–linear plot shows the exponential decay in the T_K as a function of K_z (for large K_z), equation (3.3.7).

3.3.2 Kondo Temperature for Large K_z and Bosonisation

When K_z is large, the perturbative scaling equations (3.3.3) are no longer valid. However, the results from NRG clearly show the exponential behaviour:

$$T_{\mathrm{K}} \overset{K_z \gg 1}{\sim} \mathrm{e}^{-f(K_\perp)\cdot K_z}. \tag{3.3.7}$$

This can be understood by applying a bosonisation [102, 103, 104] as first used by Schiller and De Leo for a different model [105] to the axially-symmetric Kondo Hamiltonian (3.3.2).

First of all, since the Kondo interaction is local and the dispersion relation is spherically symmetric, we may expand the electron operators in spherical harmonics and find that only the s-wave harmonic interacts with the impurity. Therefore, the three-dimensional problem impurity problem is reduced to an effective one-dimensional problem defined on half-line, $x > 0$ with the impurity at the beginning of the line $x = 0$ [52]. Furthermore, working near the Fermi level, we linearise the dispersion relation by expanding it to the first-order in k, near the Fermi points $k_0 = \pm k_{\mathrm{F}}$, and setting the Fermi energy $\varepsilon_{\mathrm{F}} = 0$:

$$\varepsilon_k = \frac{\hbar^2 k^2}{2m} \simeq \pm \frac{\hbar^2 k_{\mathrm{F}}}{m}(k - k_{\mathrm{F}}) \approx \pm \hbar v_{\mathrm{F}}(k - k_{\mathrm{F}}), \tag{3.3.8}$$

where the Fermi velocity $v_{\mathrm{F}} = \hbar k_{\mathrm{F}}/m$. Then we rewrite the fermion operator $c_{k,j}$ in the position representation:

$$c_{k,j} = \frac{1}{\sqrt{N_{\mathrm{orb}}}} \int' \mathrm{d}x\, \mathrm{e}^{\mathrm{i}kx}\, \psi_j(x), \tag{3.3.9}$$

where the $\int'$ denotes the half line $x > 0$. Therefore, the lead Hamiltonian becomes

$$\begin{aligned} H_{\mathrm{leads}} &= \sum_{k,j} \varepsilon_k c^\dagger_{k,j} c_{k,j} \\ &= \frac{1}{N_{\mathrm{orb}}} \sum_{k,j} \varepsilon_k \int' \mathrm{d}x'\, \mathrm{d}x\, \mathrm{e}^{-\mathrm{i}k(x'-x)} \psi^\dagger_j(x') \psi_j(x) \\ &\simeq \frac{1}{N_{\mathrm{orb}}} \int' \mathrm{d}x'\, \mathrm{d}x \sum_{k,j} \Big\{ \hbar v_{\mathrm{F}}(k - k_{\mathrm{F}}) \mathrm{e}^{-\mathrm{i}(k-k_{\mathrm{F}})(x'-x)} \psi^\dagger_j(x')\, \psi_j(x) \\ &\qquad - \hbar v_{\mathrm{F}}(k - k_{\mathrm{F}})\, \mathrm{e}^{+\mathrm{i}(k-k_{\mathrm{F}})(x'-x)} \psi^\dagger_j(x')\, \psi_j(x) \Big\}. \end{aligned}$$

We then combine the "left-moving" and the "right-moving" fields (related to one another by $x \leftrightarrow -x$) into a single term, by extending the variable x to $(-\infty, \infty)$, hence dropping the prime from the integral. Relabelling the variable $k \coloneqq k - k_{\mathrm{F}}$, we arrive at

$$\begin{aligned} H_{\mathrm{leads}} &= \frac{1}{N_{\mathrm{orb}}} \int \mathrm{d}x' \, \mathrm{d}x \sum_{k,j} \hbar v_{\mathrm{F}} k \, \mathrm{e}^{-\mathrm{i}k(x'-x)} \psi_j^\dagger(x') \, \psi_j(x) \\ &= \frac{1}{N_{\mathrm{orb}}} \int \mathrm{d}x' \, \mathrm{d}x \sum_{k,j} \hbar v_{\mathrm{F}} \left(-\mathrm{i}\partial_x \, \mathrm{e}^{-\mathrm{i}k(x'-x)} \right) \psi_j^\dagger(x') \, \psi_j(x) \\ &= \frac{1}{N_{\mathrm{orb}}} \int \mathrm{d}x' \, \mathrm{d}x \sum_{k,j} \mathrm{i}\hbar v_{\mathrm{F}} \cdot \mathrm{e}^{-\mathrm{i}k(x'-x)} \psi_j^\dagger(x') \, \partial_x \, \psi_j(x) \\ &= \mathrm{i}\hbar v_{\mathrm{F}} \sum_j \int \mathrm{d}x' \, \mathrm{d}x \, \delta(x - x') \psi_j^\dagger(x') \, \partial_x \, \psi_j(x) \\ &= \mathrm{i}\hbar v_{\mathrm{F}} \sum_j \int \mathrm{d}x \, \psi_j^\dagger(x) \, \partial_x \, \psi_j(x). \end{aligned} \tag{3.3.10}$$

Therefore, the Kondo Hamiltonian in the continuum limit takes the form

$$\begin{aligned} H = \mathrm{i}\hbar v_{\mathrm{F}} \sum_j \int \mathrm{d}x \, \psi_j^\dagger(x) \, \partial_x \, \psi_j(x) + J_z a S_z \left(\psi_{+1}^\dagger(0) \psi_{+1}(0) - \psi_{-1}^\dagger(0) \psi_{-1}(0) \right) \\ + \frac{J_\perp a}{\sqrt{2}} \left[S^+ \left(\psi_0^\dagger(0) \psi_{+1}(0) + \psi_{-1}^\dagger(0) \psi_0(0) \right) + S^- \left(\psi_{+1}^\dagger(0) \psi_0(0) + \psi_0^\dagger(0) \psi_{-1}(0) \right) \right]. \end{aligned} \tag{3.3.11}$$

Then we use the standard formulation expressing the boson fields $\phi_j(x)$ in terms of the fermion fields $\psi_j(x)$ via [102, 103, 104]

$$\psi_j(x) = P_j \frac{1}{\sqrt{2\pi\alpha}} \mathrm{e}^{-\mathrm{i}\phi_j(x)}, \tag{3.3.12}$$

where the boson fields obey

$$[\phi_j(x), \phi_k(y)] = -\mathrm{i}\pi\delta_{jk} \, \mathrm{sgn}(x - y), \tag{3.3.13}$$

with the ultraviolet momentum cutoff $\alpha^{-1} = \pi/a$. The operators P_j are the phase factors to ensure the fermion anticommutation relations. The Hamiltonian

in terms of the boson fields then becomes

$$\begin{aligned} H = \frac{\hbar v_{\mathrm{F}}}{4\pi} \sum_j \int \mathrm{d}x \left[\partial_x \phi_j(x)\right]^2 + \frac{\delta_z a}{\pi^2 \rho} S_z \left[\partial_x \psi_{+1}(0) - \partial_x \psi_{-1}(0)\right] \\ + \frac{J_\perp}{2\sqrt{2}} \left\{ S^+ \left(\mathrm{e}^{\mathrm{i}[\phi_0(0) - \phi_{+1}(0)]} + \mathrm{e}^{\mathrm{i}[\phi_{-1}(0) - \phi_0(0)]} \right) \right. \\ \left. + S^- \left(\mathrm{e}^{\mathrm{i}[\phi_{+1}(0) - \phi_0(0)]} + \mathrm{e}^{\mathrm{i}[\phi_0(0) - \phi_{-1}(0)]} \right) \right\}, \end{aligned} \tag{3.3.14}$$

where the phase shift associated with J_z in the absence of $J_\perp$ is given by [105]

$$\delta_z = \tan^{-1}\left(\frac{\pi \rho J_z}{2}\right). \tag{3.3.15}$$

Next, we form linear combinations of the three boson fields $\phi_j(x)$ as [70]

$$\phi(x) = \frac{1}{\sqrt{3}} \left[\phi_{+1}(x) + \phi_0(x) + \phi_{-1}(x)\right], \tag{3.3.16}$$

$$\phi_s(x) = \frac{1}{\sqrt{2}} \left[\phi_{+1}(x) - \phi_{-1}(x)\right], \tag{3.3.17}$$

$$\phi_f(x) = \frac{1}{\sqrt{6}} \left[\phi_{+1}(x) - 2\phi_0(x) + \phi_{-1}(x)\right], \tag{3.3.18}$$

resulting in the Hamiltonian

$$\begin{aligned} H = \frac{\hbar v_{\mathrm{F}}}{4\pi} \sum_n \int \mathrm{d}x \left[\partial_x \phi_n(x)\right]^2 + \sqrt{2}\, \delta_z \, \frac{a}{\pi^2 \rho} \, S_z \partial_x \psi_s(0) \\ + \frac{J_\perp}{2\sqrt{2}} \left\{ S^+ \left(\mathrm{e}^{-\frac{\mathrm{i}}{\sqrt{2}}[\phi_s(0) + \sqrt{3}\phi_f(0)]} + \mathrm{e}^{-\frac{\mathrm{i}}{\sqrt{2}}[\phi_s(0) - \sqrt{3}\phi_f(0)]} \right) \right. \\ \left. + S^- \left(\mathrm{e}^{+\frac{\mathrm{i}}{\sqrt{2}}[\phi_s(0) + \sqrt{3}\phi_f(0)]} + \mathrm{e}^{+\frac{\mathrm{i}}{\sqrt{2}}[\phi_s(0) - \sqrt{3}\phi_f(0)]} \right) \right\}. \end{aligned} \tag{3.3.19}$$

Then we perform a canonical transformation $H \to UHU^\dagger$, with $U = \mathrm{e}^{\mathrm{i}\sqrt{2}\phi_s(0) S_z}$. Using the commutation relation (3.3.13) which implies that $[\partial_x \psi_s(0), \mathrm{e}^{k\psi_s(0)}] = -2\mathrm{i}\pi k \delta(0) \mathrm{e}^{k\psi_s(0)}$, we obtain the results:

$$U \;\; \partial_x \phi_s(0) \;\; U^\dagger = \;\; \partial_x \phi_s(0) \;\; - 2\sqrt{2}\pi\delta(0) S_z \partial_x \psi_s(0), \tag{3.3.20}$$

$$U \; \left[\partial_x \phi_s(0)\right]^2 U^\dagger = \left[\partial_x \phi_s(0)\right]^2 - 4\sqrt{2}\pi\delta(0) S_z \partial_x \psi_s(0). \tag{3.3.21}$$

In addition, the commutation relation $[S^z, S^+] = S^+$ implies that $\mathrm{e}^{kS^z} S^+ = S^+ \, \mathrm{e}^{k(S^z+1)}$, and results in the transformation

$$U S^+ U^\dagger = S^+ \, \mathrm{e}^{\frac{\mathrm{i}}{\sqrt{2}} \cdot 2\phi_s(0)}. \tag{3.3.22}$$

Ignoring the constant term that is generated from (3.3.20), using the relation $\hbar v_{\mathrm{F}} = a/2\pi\rho$, and performing the final transformation $\psi_s(x) \to -\psi_s(x)$, the transformed Hamiltonian reads

$$\begin{aligned} H = \frac{\hbar v_{\mathrm{F}}}{4\pi} \sum_n \int \mathrm{d}x \, [\partial_x \, \phi_n(x)]^2 + \sqrt{2} \left(\frac{\pi}{2} - \delta_z\right) \frac{a}{\pi^2 \rho} \, S_z \partial_x \psi_s(0) \\ + \frac{J_\perp}{2\sqrt{2}} \Big\{ S^+ \left(\mathrm{e}^{-\frac{\mathrm{i}}{\sqrt{2}}[\phi_s(0) + \sqrt{3}\phi_f(0)]} + \mathrm{e}^{-\frac{\mathrm{i}}{\sqrt{2}}[\phi_s(0) - \sqrt{3}\phi_f(0)]} \right) \\ + S^- \left(\mathrm{e}^{+\frac{\mathrm{i}}{\sqrt{2}}[\phi_s(0) + \sqrt{3}\phi_f(0)]} + \mathrm{e}^{+\frac{\mathrm{i}}{\sqrt{2}}[\phi_s(0) - \sqrt{3}\phi_f(0)]} \right) \Big\} . \end{aligned} \tag{3.3.23}$$

Since the resulting Hamiltonian (3.3.23) is, except for the δ_z part, identical to the one prior to the transformation, equation (3.3.19), the transformation can be viewed as a duality between the strong and the weak coupling with fixed $K_\perp$, and the parameter K_z follows

$$\begin{aligned} \delta_z' &= \frac{\pi}{2} - \delta_z \\ \tan^{-1} \frac{\pi K_z'}{2} &= \frac{\pi}{2} - \tan^{-1} \frac{\pi K_z}{2} \\ K_z' &= \frac{2}{\pi} \cot \left(\tan^{-1} \frac{\pi K_z}{2} \right) \\ K_z' &= \left(\frac{2}{\pi} \right)^2 \frac{1}{K_z}. \end{aligned} \tag{3.3.24}$$

Therefore, we expect the model with fixed small $K_\perp$ and K_z to have the same physics as that with $K_z' = \xi/K_z$, where $\xi = \left(\frac{2}{\pi}\right)^2$. Furthermore, if we define the quantity

$$\nu = \ln \frac{K_z}{\sqrt{\xi}}, \tag{3.3.25}$$

clearly, the duality holds between two Hamiltonians (with fixed $K_\perp$) in which one has the longitudinal coupling $\sqrt{\xi}\mathrm{e}^{\nu}$ whereas the other $\sqrt{\xi}\mathrm{e}^{-\nu}$, which suggests that the physics is insensitive to the sign of ν. If we assume that $\ln T_{\mathrm{K}}$ can be expanded as a power series in ν, it should therefore be of even power:

$$\ln T_{\mathrm{K}}/D \;\simeq\; \mu \, \nu^2 = \mu \left(\ln K_z - \frac{1}{2} \ln \xi \right)^2 , \tag{3.3.26}$$

where μ is a constant. This agrees very well with the results from NRG (Figure 3.9), though we have slightly adjusted the constant $\xi = 0.37$.

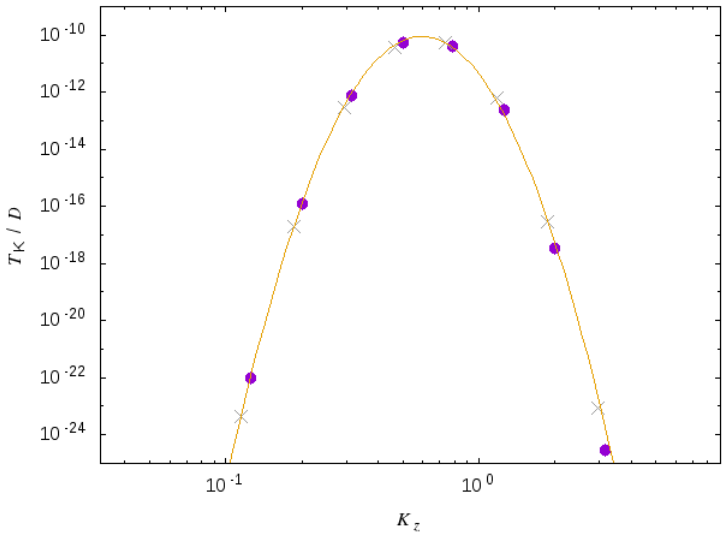

Figure 3.9: The Kondo temperature of the axially symmetric model with fixed $K_\perp = 0.001$, highlighting the duality between the model with K_z (circles) and $K_z' = \xi/K_z$ (crosses), in comparison to the equation (3.3.26) (line), where here we have adjusted the constant $\xi = 0.37$.

Finally, in the limit of small $K_\perp \ll K_z \ll 1$, we can also use the results obtained from poor man's scaling earlier, equation (3.3.4), by expanding α in the limit of small $x = K_\perp/K_z$

$$\gamma = \sqrt{1-x^2} \simeq 1 - \frac{1}{2}x^2, \tag{3.3.27}$$

$$\alpha = \frac{1}{\gamma}\tanh^{-1}\gamma = \frac{1}{2\gamma}\ln\frac{1+\gamma}{1-\gamma} \simeq \frac{1}{2}\ln\frac{4}{x^2} \sim -\ln x \sim -\ln K_\perp, \tag{3.3.28}$$

$$T_\mathrm{K} = c\,\mathrm{e}^{-\alpha/K_z} \sim \mathrm{e}^{(\ln K_\perp)/K_z}. \tag{3.3.29}$$

Together with the duality relation, we expect T_K when $K_z \gg 1$ then to be

$$T_\mathrm{K} \sim \mathrm{e}^{\frac{1}{\xi}\ln K_\perp \cdot K_z}, \tag{3.3.30}$$

which is indeed the relation (3.3.7) found numerically from the NRG results.

Note also that whilst the relation above certainly holds for large K_z, according to the right panel of Figure 3.8, which once again shows the K_z dependence of T_K calculated from NRG at four different values of $K_\perp \in \{0.02, 0.1, 0.2, 1\}$ but on

a log–linear scale, such a condition holds relatively loosely. For instance, when $K_\perp = 0.02$ (red circles in Figure 3.8 (right panel)), the relation (3.3.7) is seen to hold for K_z as small as 3.

We note also that whilst the fixed points of this Kondo model with spin-1 conduction electrons are very similar to those of the 4-channel Kondo model, there is a clear difference between the RG flows of the two models. In the 4-channel case, when the coupling constant K_z is antiferromagnetic and is sufficiently large, the ground state is the free spin state which is the same as in the case of the ferromagnetic model. Therefore, there are two Kosterlitz–Thouless lines separating between the ferromagnetic and antiferromagnetic domains [105]. However, in our case with spin-1 conduction electrons, due to the presence of the duality between the small and large K_z, such a transition is not present and the low-temperature NFL behaviour persists for all values of coupling constants.

Finally, we have calculated the thermodynamics of the axially symmetric model and, as is shown in Figure 3.10, found its qualitative behaviour to be the same as that of the model with full isotropic symmetry, i.e., at high temperature, the entropy approaches $\ln 2$, which is the value of at the WC fixed point. As temperature is decreased, the entropy decreases down to the value of $\ln\sqrt{3}$, the value at the NFL fixed point. This shows that the NFL fixed point is robust against the spin anisotropy in the Kondo context, or equivalently the channel anisotropy in the physical setup. Experimentally, this implies that the Non-Fermi liquid behaviour that can be experimentally probed in this device does not require the fine of the tunnel couplings among all the conduction leads.

3.3.3 Dynamics

Due to the reduced symmetry, we no longer have a single representative t matrix as in the isotropic case. Axial symmetry implies that two of the spin species $j = \pm 1$ are equivalent to each other, resulting in $t_{+1}(\omega) = t_{-1}(\omega) \neq t_0(\omega)$ (Figure 3.11). At high frequency, they take the usual form near the WC fixed point, equation (3.2.15), with different constants a and b. At low frequency, both curves collapse onto the same universal as obtained previously from the isotropic model, Figure (3.3), reinforcing the robustness of the NFL fixed point against the spin

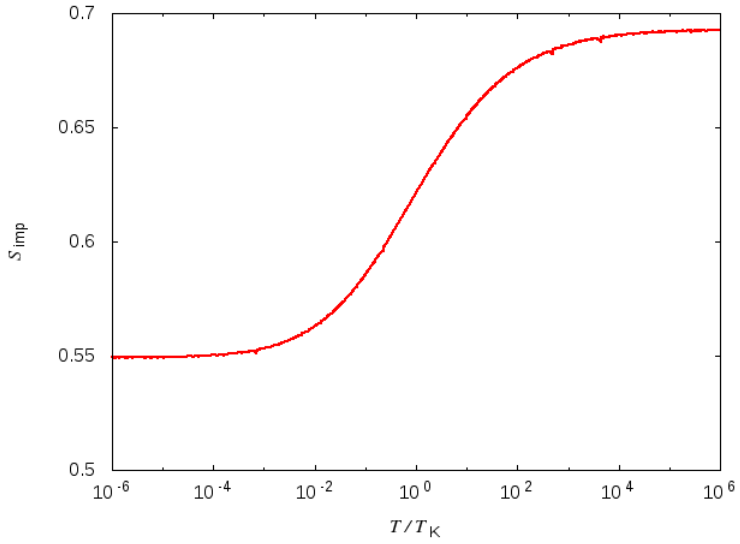

Figure 3.10: The temperature dependence of the thermodynamics for the axially symmetric spin model. The curve is the universal impurity entropy curve that is obtained earlier for the isotropic model, the left panel of Figure 3.2, showing that the Non-Fermi liquid behaviour is robust against the spin anisotropy.

anisotropy. The same behaviour is also found for the zero-temperature conductance tensor, G_{ik}, of the model. As shown in Figure 3.12, at high frequency, the behaviour is that of the model at the WC fixed point, and gradually flows to the NFL fixed at low frequency whilst the curve superposes onto that of the isotropic model.

In this chapter, we studied the basic properties of the Majorana device by ignoring all the exponentially suppresed couplings. We found that the Hamiltonian which governs the low-energy behaviour of the model is a spin model, in particular, it is a Kondo model with a spin-$\frac{1}{2}$ impurity coupled to spin-1 conduction electrons. Whilst its low-temperature thermodynamics provides an evidence that the stable fixed point of this model is the same as that of the 4-channel spin-$\frac{1}{2}$ Kondo model, characteristed by the zero-temperature impurity entropy $S_{\rm imp}(0) = \ln\sqrt{3}$ and its asymptote $\sim T^{2/3}$, their RG flows are different. Whilst here are two parameter regimes in the 4-channel model which has a decoupled local-moment ground state – the ferromagnetic model with $|J_\perp| < |J_z|$ and the

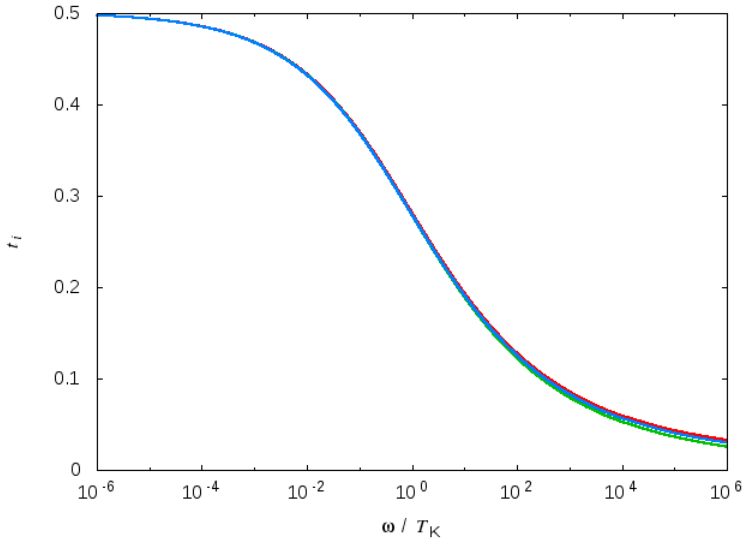

Figure 3.11: The frequency dependence of the zero-temperature scattering t matrices $t_{+1}(\omega) = t_{-1}(\omega)$ (red line) and $t_0(\omega)$ (green line) of the axially symmetric spin model in comparison with that of the isotropic model (blue line). At low frequency, both curves collapse onto the same universal curve, approaching the NFL fixed point with the $(|\omega|/T_K)^{1/3}$ asymptote, equation (3.2.16).

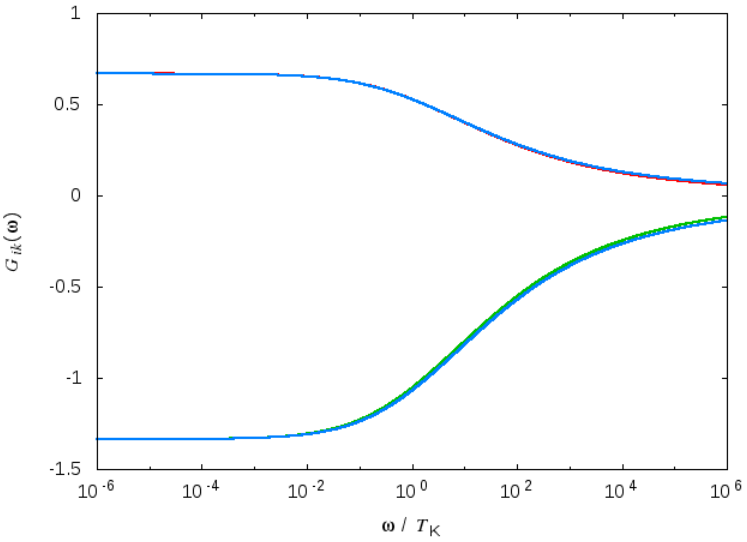

Figure 3.12: The frequency dependence of the zero-temperature conductance tensor G_{ik} of the axially symmetric model: both the non-diagonal component G_{ik} (red line) and the diagonal component G_{ii} (green line), in comparison with those of the isotropic model (blue lines). At low frequency, both curves collapse onto the same universal curves, approaching the NFL fixed point with the $(|\omega|/T_K)^{2/3}$ asymptote, equation (3.2.26). Once again, the low-temperature NFL behaviour is robust against the anisotropy.

anti-ferromagnetic model with large enough J_z – only the former region exists in the spin-1 conduction electron model; the whole of the anti-ferromagnetic region only has a stable low-temperature NFL fixed point. In the next chapter, we shall investigate the effects of including some of the exponentially small coupling terms that we ignored here and also completely lifts the symmetry constraint of the model.

4

The Spin Model with Lower Symmetry

In this chapter, we continue to study the low-temperature effective spin model that is derived from the Hamiltonian of the Majorana device. We split the chapter into two parts. In the first part, we study the effects of the exponentially small perturbations that arise from non-local couplings between the Majoranas, or those between the Majorana and the conduction electrons on different leads, in the form of the effective channel anisotropy and Zeeman field. Note that the term anisotropy used here is not the anisotropy between the couplings of the different physical conduction leads. As will be explained in details later, the anisotropy in this part is the anisotropy between the couplings of the spin-$\frac{1}{2}$ impurity and the different spin species of the spin-1 conduction electrons. We shall find that these two perturbations produce the same physics: they destablise the NFL behaviour of the model and at low temperature the behaviour of the system becomes that of the Fermi liquid at the SC fixed point. Parts of the materials in this section have also been published [72]. In the second part, neglecting these small perturbations, we look back at the Kondo spin model without imposing any symmetry conditions. We will show that the NFL physics is stable against this type of anistropy and the physics of the model is that found previously in the axially symmetric model.

4.1 Inclusion of the Perturbations

In the first half of this chapter, we study the low-energy effective spin model, equation (3.1.14), that was derived in Section 3.1 of the previous chapter:

$$H_{\text{eff}} = H_{\text{leads}} + H_{\text{K}} + H_{\text{M}} + \delta H, \tag{4.1.1}$$

where $H_{\text{leads}} = \sum_{ki} \varepsilon_k a_{ki}^\dagger a_{ki}$, equation (2.3.2), is the free conduction electron lead term, $H_{\text{K}} = \sum_\alpha J_{\alpha\alpha} S_\alpha I_\alpha$, equation (3.1.10), is the Kondo spin term, $H_{\text{M}} = \sum_{ij} \mathrm{i} h_{ij} \gamma_i \gamma_j$, equation (2.3.4), is the magnetic Zeeman term arising from non-local couplings between the Majorana fermions, and

$$\delta H = \sum_{\substack{\alpha\beta \\ \alpha\neq\beta}} J_{\alpha\beta} S_\alpha I_\beta + \sum_{\alpha\beta} J'_{\alpha\beta} S_\alpha I_\beta^{(2)} + \sum_\alpha h_\alpha S_\alpha, \tag{4.1.2}$$

equation(3.1.13), are other perturbative terms which arise from long-range couplings between the Majorana fermions with the conduction electrons on different leads. We have studied extensively the effect of the Kondo spin term alone with some symmetry constraints in the previous chapter but will now include the exponentially small non-local perturbations; therefore, there are a number of free parameters to work with. Since we have now understood from the previous chapter that the NFL fixed point is robust against the channel anisotropy in the physical setup, i.e., the coupling constants between the Majorana j and the conduction electrons on lead j are not equal, or equivalently in Kondo language, it is robust against the spin anisotropy, i.e., the longititudinal coupling constant J_z is not the same as the transverse one $J_\perp$, in this chapter, we shall investigate another type of anisotropy. First of all, we once again enforce the isotropic symmetry condition on the Kondo spin part H_{K}, which is given as part of equation (3.2.8), which for reasons that will be subsequently explained, is rewritten as

$$\begin{aligned} H_{\text{K}}^{\text{iso}} = J\Big\{ & S_z \left(f_{+1}^\dagger f_{+1} - f_0^\dagger f_0 \right) + \frac{1}{\sqrt{2}} \left(S^+ f_0^\dagger f_{+1} + S^- f_{+1}^\dagger f_0 \right) + \\ & S_z \left(f_0^\dagger f_0 - f_{-1}^\dagger f_{-1} \right) + \frac{1}{\sqrt{2}} \left(S^+ f_{-1}^\dagger f_0 + S^- f_0^\dagger f_{-1} \right) \Big\}. \end{aligned} \tag{4.1.3}$$

Effectively, we have broken this Kondo model into two standard spin-$\frac{1}{2}$ Kondo models with spin-$\frac{1}{2}$ conduction electrons: the first part (the top line) is a Kondo

model where the conduction electrons with spin $\uparrow$ are represented by the electrons in channel $j = +1$ and $\downarrow$ by $j = 0$ and the second part (the bottom line) is also the same type of Kondo model but with spin $\uparrow$ are represented by the electrons in channel $j = 0$ and $\downarrow$ by $j = -1$.

We will now consider the effect of δH. First of all, since we can realise a spin-$\frac{1}{2}$ out of a product of Majoranas, we combine H_{M} and the last term of δH. To keep the problem simple, we keep only the S_z term and simply call the coefficient in front of it h; this is the effective Zeeman term. Secondly, the first two terms in δH will add different contributions to the different terms in equation (4.1.3). Once again, in order to keep the problem tractable, we consider a simple case near the isotropic limit, where the coupling of the two parts of the Kondo model is only slightly different and we parameterise the difference by a small positive parameter δ, added to the first part of the equation (4.1.3). Together with the conduction leads H_{leads}, the Hamiltonian of interest in this part of the chapter takes the form

$$\begin{aligned} H_{\mathrm{eff}} = &\sum_{kj} \varepsilon_k c^\dagger_{k,j} c_{k,j} + hS_z \\ &+ \Big\{ (J+\delta) \left[S_z \left(f^\dagger_{+1} f_{+1} - f^\dagger_0 f_0 \right) + \frac{1}{\sqrt{2}} \left(S^+ f^\dagger_0 f_{+1} + S^- f^\dagger_{+1} f_0 \right) \right] \\ &\quad + J \left[S_z \left(f^\dagger_0 f_0 - f^\dagger_{-1} f_{-1} \right) + \frac{1}{\sqrt{2}} \left(S^+ f^\dagger_{-1} f_0 + S^- f^\dagger_0 f_{-1} \right) \right] \Big\}. \end{aligned} \tag{4.1.4}$$

4.2 Channel Anisotropy

We begin by considering only the effect of the channel anisotropy (positive $\delta \neq 0$) by setting the effective Zeeman field $h = 0$. As usual, we investigate first the thermodynamics of the model: the impurity entropy, S_{imp}.

4.2.1 Thermodynamics and Crossover to Fermi-Liquid

Consider first the case where the anisotropy is very weak ($\delta/D = 10^{-8}$, red line of Figure 4.1). At high temperature, the behaviour of the model is the same as that of the isotropic spin model: the RG flows from the WC fixed point, characterised by $S_{\mathrm{imp}} = \ln 2$, to the NFL fixed point with $S_{\mathrm{imp}} = \ln \sqrt{3}$, with the

same $(T/T_{\mathrm{K}})^{2/3}$ asymptotic behaviour (the two lines superpose exactly onto each other). However, at low temperature, there is an additional RG flow to a fixed point with $S_{\mathrm{imp}} = 0$, characteristic value at the SC fixed point where the system behaves as a standard Fermi liquid.

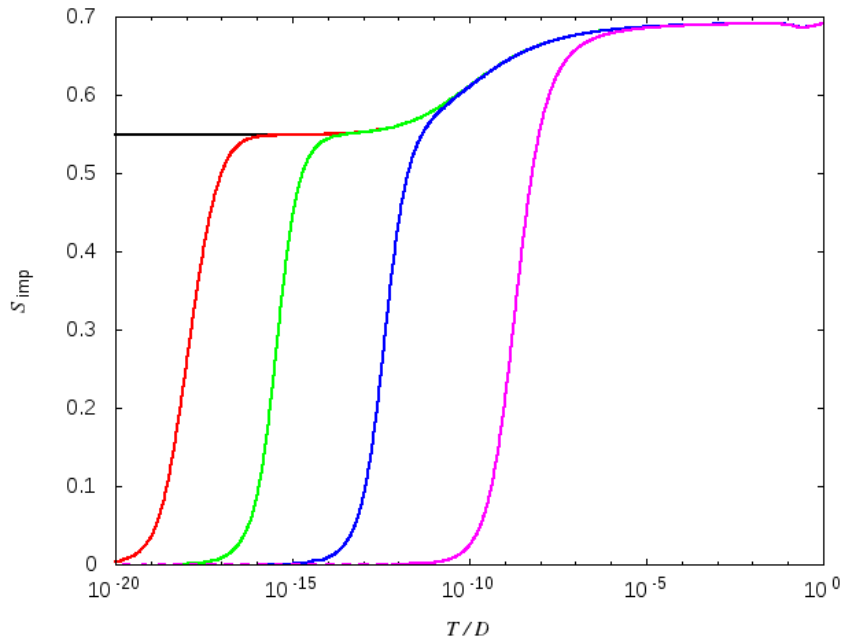

Figure 4.1: The impurity entropy for the spin model with the δ anisotropy. Here, the coupling constant $J/D = 0.1$ whilst the small anisotropy $\delta/D = 10^{-8}, 10^{-6}, 10^{-4}$, and 10^{-2} (red, green, blue, and magenta lines, respectively), in comparison to the isotropic case (black line). In addition to the usual RG flow from the WC fixed point $S_{\mathrm{imp}} = \ln 2$ to the NFL fixed point $S_{\mathrm{imp}} = \ln\sqrt{3}$ (no anisotropy; black line), we have also found the crossover to the SC fixed point $S_{\mathrm{imp}} = 0$.

This additional RG flow can be understood by considering this spin model with spin-1 conduction electrons as a model with two channels of spin-$\frac{1}{2}$ conduction electrons as mentioned in the previous section and can be explained by using the standard argument that is used to explain the instability of the NFL fixed point against the channel anisotropy in the two-channel Kondo model. Since the coupling constant $J + \delta > J$, the former renormalises to infinity much faster than the latter and the system is driven to the SC fixed point where the impurity spin is screened by channel $j = 0, +1$, resulting in zero impurity entropy; the channel

$j = -1$ simply decouples [72]; had the parameter $\delta < 0$, channel $j = +1$ would decouple instead, though resulting in the same thermodynamics nonetheless.

Upon increasing the magnitude of the perturbation δ, the coupling constant $J + \delta$ renormalises even faster and the RG flows to the SC fixed point sooner. This crossover to the Fermi-liquid regime, when there is a good scale separation between to flow from the WC fixed point and the flow towards the SC fixed point, has been found to follow the power law [72, 80]

$$T_{\mathrm{FL}}^{*} \sim T_{\mathrm{K}} \times \left| \frac{\delta}{D} \right|^{3/2} . \tag{4.2.1}$$

Here we conveniently choose the Fermi-liquid crossover scale, $T_{\mathrm{FL}}^{*} = \frac{1}{2} \ln \sqrt{3}$, halfway between the NFL and the SC fixed points. This relation is confirmed by our NRG results as shown in Figure 4.2: we observe a good agreement between the crossover temperature scale extracted from NRG and the power law above in the region where temperature is low enough that there is a good separation between the initial RG flow and the latter, i.e., $T_{\mathrm{FL}}^{*} \ll T_{\mathrm{K}}$. If the perturbation δ is large enough, the RG flows directly from the WC to the SC fixed point.

Clearly, these non-local couplings perturb the system in such a way that the NFL fixed point is no longer stable at low temperature and it becomes more difficult to experimentally observe the NFL physics. However, as is seen from Figure 4.1 (e.g., red line), that there is a parameter regime in which there is a good separation between the three different regions ($T_{\mathrm{FL}}^{*} \ll T_{\mathrm{K}}$). Since it is the coupling J that controls the Kondo scale and the δ parameter that controls T_{FL}^{*}, the scale separation can be achieved if $\delta \ll J$. Experimentally, this means that we need to engineer a device whose non-local couplings to the Majoranas are much smaller than the local couplings between the Majoranas and the leads. The NFL physics can then be observed at the intermediate temperature range. In addition, we can also use the power law, equation (4.2.1), to characterise for the subsequent flow (NFL $\rightarrow$ SC fixed point) and hence, the topological Kondo effect, as well.

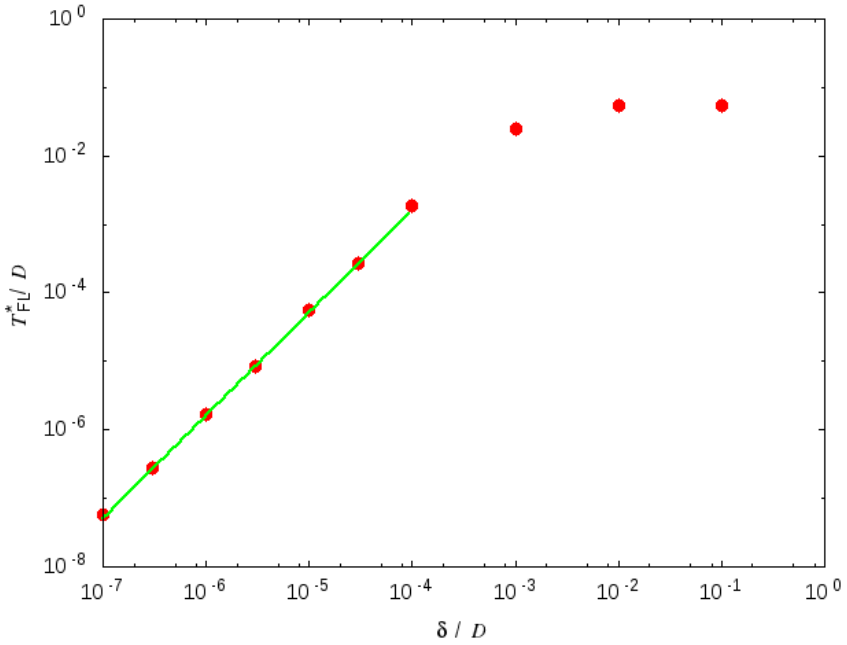

Figure 4.2: The Fermi-liquid crossover temperature scale for the spin model with the δ anisotropy. The red circles are data obtained from NRG, which agree very well with the power law $|\delta/D|^{3/2}$ (green line) which follows from dimensional scaling arguments in CFT, at low enough temperature where there is a good scale separation, i.e., $T^*_{\mathrm{FL}} \ll T_{\mathrm{K}}$.

4.2.2 Dynamics

Similar to the case of the model with the axial spin symmetry (Section 3.3), the three t matrices are not equal. Specifically, since it is the channel symmetry that is broken, the differences between the t matrix of the three channels become even more obvious, as is shown in Figure 4.3. The behaviour of the t-matrices can be understood by splitting them into three regions. At very high frequencies, all three t-matrices approach zero, the WC fixed point values. When the frequency is lowered, there is a RG flow from WC to NFL fixed as before. Note that in this case, it is t_0 (Figure 4.3, blue line) that is exactly the same as that of the isotropic model – recall the transformation (3.2.3) – and we have also observed that $t_0(\omega) = \frac{1}{2}[t_{-1}(\omega) + t_{+1}(\omega)]$. Furthermore, when there is a good

scale separation, i.e., $T_{\mathrm{FL}}^{*} \ll |\omega| \ll T_{\mathrm{K}}$, we found the asymptotic behaviour of

$$t_i(\omega) \sim \begin{cases} \frac{1}{2} \pm p_i \left(|\omega|/T_{\mathrm{FL}}^{*}\right)^{-1/3}, & i = \pm 1, \\ \frac{1}{2} + p_i \left(|\omega|/T_{\mathrm{FL}}^{*}\right)^{-2/3}, & i = 0, \end{cases} \tag{4.2.2}$$

where p_i are some constants.

At lower frequencies, $\omega \ll T_{\mathrm{FL}}^{*}$, the subsequent RG flows from the NFL to the SC (Fermi-liquid) fixed point – $t_i(\omega) \to 1$ – for the channel $i = +1$ and 0 (Figure 4.3, green and blue lines) where the renormalisation of the coupling constant grows very fast whereas the channel $i = -1$ gets decoupled (Figure 4.3, red line) and $t_{-1} \to 0$. Near the SC fixed point, we found the standard asymptotes

$$t_i(\omega) \sim \begin{cases} 1 - q_i(|\omega|/T_{\mathrm{FL}}^{*})^2, & i = 0, +1, \\ 0 + q_i(|\omega|/T_{\mathrm{FL}}^{*})^2, & i = -1, \end{cases} \tag{4.2.3}$$

where q_i are some constants.

The off-diagonal conductance $G_{10}(\omega)$ (Figure 4.4) also shows the RG flows from the WC, then approaches the NFL fixed point at high frequencies, before the subsequent crossover to the SC fixed point at lower frequencies, where the conductance vanishes. This can be understood [72] by considering an electron tunnelling due to the voltage applied at channel $i = 0$ from, say, channel $i = 0$ to $+1$ which at the same time flips the spin impurity from $\uparrow$ to $\downarrow$ due to the conservation of S_z. This therefore prevents the further electron transport since the impurity is now in the $\downarrow$ state. A flow of electrons can be facilitated only by the coupling of the channel $i = -1$, where the electron can then flow from the channel $i = 0$ to -1 and by doing so flips the impurity spin back to $\uparrow$. Finally, the asymptotic relations of the off-diagonal conductance near the NFL and SC fixed points are expectedly found to be

$$G_{10}(\omega) \sim \begin{cases} \frac{2}{3} - p'(|\omega|/T_{\mathrm{FL}}^{*})^{-4/3}, & T_{\mathrm{FL}}^{*} \ll |\omega| \ll T_{\mathrm{K}}, \\ 0 + q'(|\omega|/T_{\mathrm{FL}}^{*})^2, & |\omega| \ll T_{\mathrm{FL}}^{*}, \end{cases} \tag{4.2.4}$$

where p' and q' are constants.

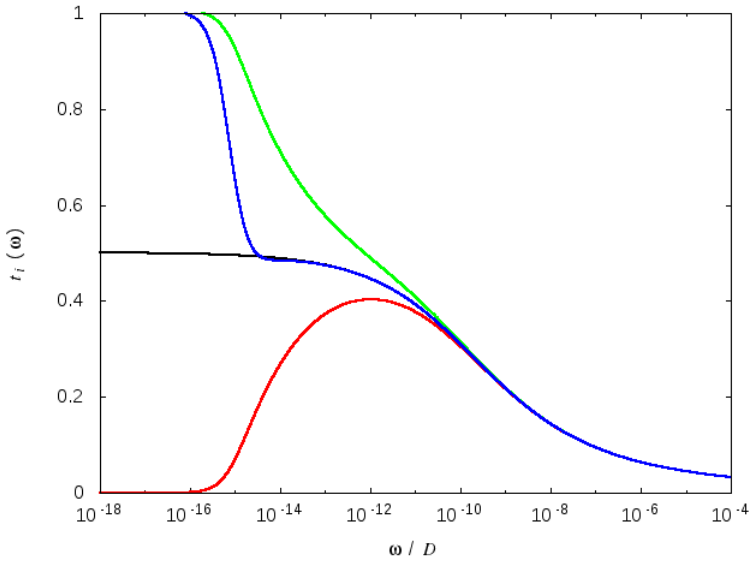

Figure 4.3: The zero-temperature scattering t matrices of the the spin model with δ anisotropy, $\delta/D = 10^{-6}$, resulting in $t_{+1}(\omega)$ (green line) and $t_0(\omega)$ (blue line) flow to the SC fixed point ($t = 1$) at low temperature whereas $t_{-1}(\omega)$ (red line) decouples ($t = 0$). The t matrix of the isotropic spin model (black line) is included for reference.

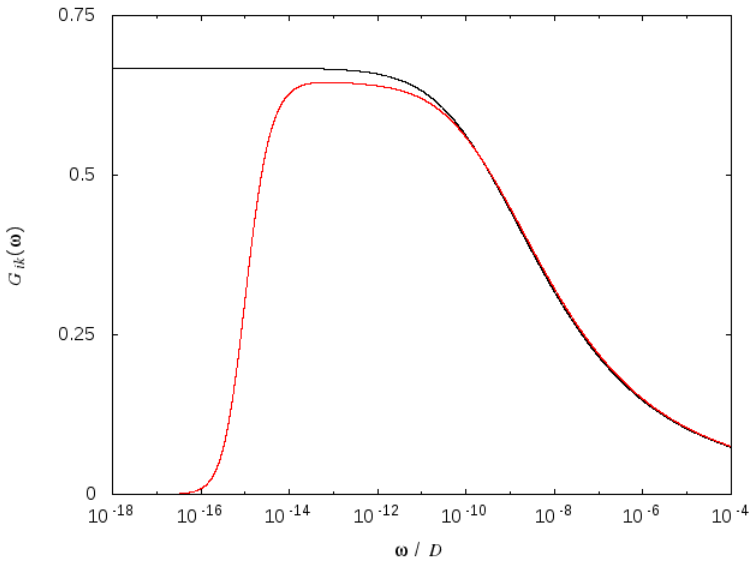

Figure 4.4: The zero-temperature non-diagonal conductance tensor G_{ik} of the spin model with δ anisotropy, $\delta/D = 10^{-6}$. At intermediate temperature range, it approaches the NFL behaviour ($G = \frac{2}{3}$). At low temperature, the crossover to Fermi-liquid regime ($G = 0$) is observed. The conductance of the isotropic spin model (black line) is included for reference.

4.3 Zeeman Field

In this part of the chapter, we consider the effect that arises from the effective Zeeman field by setting the anisotropy parameter $\delta = 0$. It turns out that the effect of turning on the Zeeman field on the *thermodynamics* of the model is largely the same as including the channel anisotropy [72]. As in shown in Figure 4.5, the NFL fixed point with the characteristic $S_{\text{imp}} = \ln\sqrt{3}$ is not stable and RG flows to the SC fixed point with $S_{\text{imp}} = 0$ at very low temperature. A rough physical argument can be made: by turning on the Zeeman field, according to the equation (4.1.4), the impurity spin $S_z = \uparrow$ becomes energetically unfavourable and the impurity ground state is the $S_z = \uparrow$ state – the impurity entropy therefore vanishes. A better argument which takes into account the fact that the impurity problem is a many-body phenomena is given in the context of RG: since the field breaks the spin symmetry of the model and the NFL fixed point is unstable to this symmetry breaking, at low temperature, the RG flow towards the SC fixed point which is when a particular spin state is favoured, resulting in the vanishing impurity entropy. Interestingly, the order of magnitude of the field required to push the system to Fermi liquid is much smaller than that of the anisotropy parameter δ. Furthermore, the entropy curves of this crossover if scaled by T^*_{FL} superpose exactly on top of each other, showing that the RG crossover to the SC fixed point is universal.

Regarding the dynamics of the model, since it is easier to understand conductance, we shall discuss it first. Figure 4.6 shows as expected that the inclusion of the field destroys the conductance at low energy scales. In this case, the behaviour of the system can be understood by realising that at low energy scales, the field freezes the spin state of the impurity rendering it impossible to support the transport of the conduction electrons which requires the spin flip of the impurity. Whilst in the channel anisotropy discussed in the previous section, transport of a single electron blocks further transport of the system, in this case, the Zeeman field directly freezes the impurity spin state and annihilates the conductance of the system.

Finally, we present the scattering t-matrices of the system under the influence of the Zeeman field (Figure 4.7). At first sight, this appears to be radically differ-

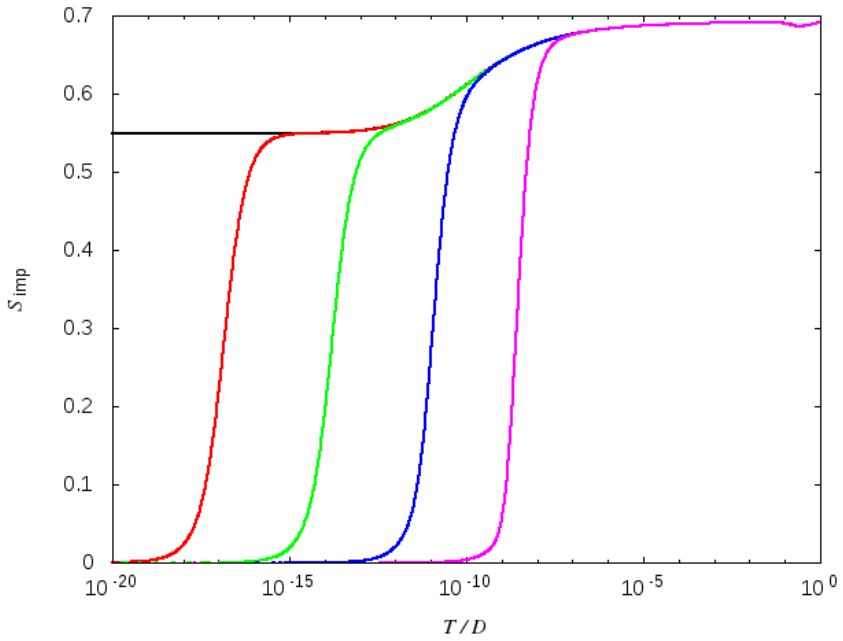

Figure 4.5: The impurity entropy for the spin model with the Zeeman field turned on. Here, the coupling constant $J/D = 0.1$ whilst the field $h_z/D = 10^{-14}, 10^{-12}, 10^{-10}$, and 10^{-8} (red, green, blue, brown, and yellow lines, respectively), in comparison to the case with no field (black line). Similar to the channel anisotropy case, Figure 4.1, there is a crossover from the NFL fixed point $S_{\text{imp}} = \ln\sqrt{3}$ to the SC fixed point $S_{\text{imp}} = 0$.

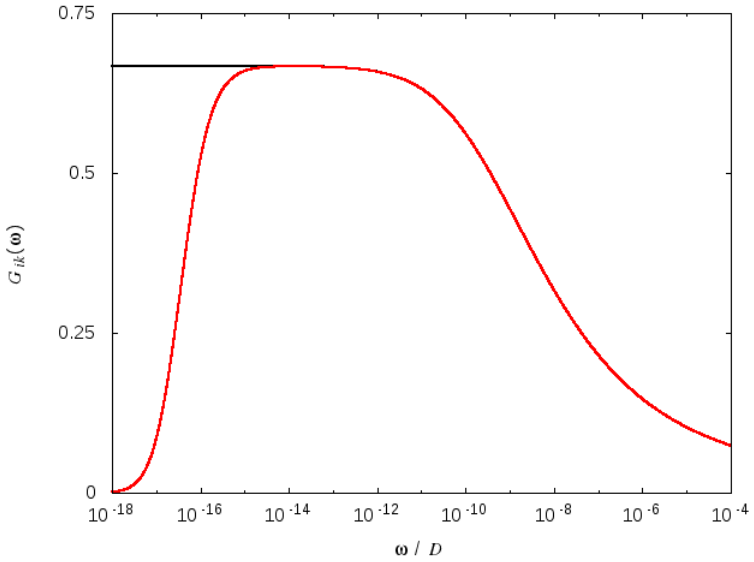

Figure 4.6: The zero-temperature conductance tensor G_{ik} of the isotropic spin model with the Zeeman field $h/D = 10^{-14}$ (red line). Similar to that of the channel anisotropic model, it approaches the NFL value $G = \frac{2}{3}$ at intermediate frequency range and crosses over to the Fermi-liquid regime with $G = 0$ at low frequencies. The conductance of the isotropic spin model (black line) is included for reference.

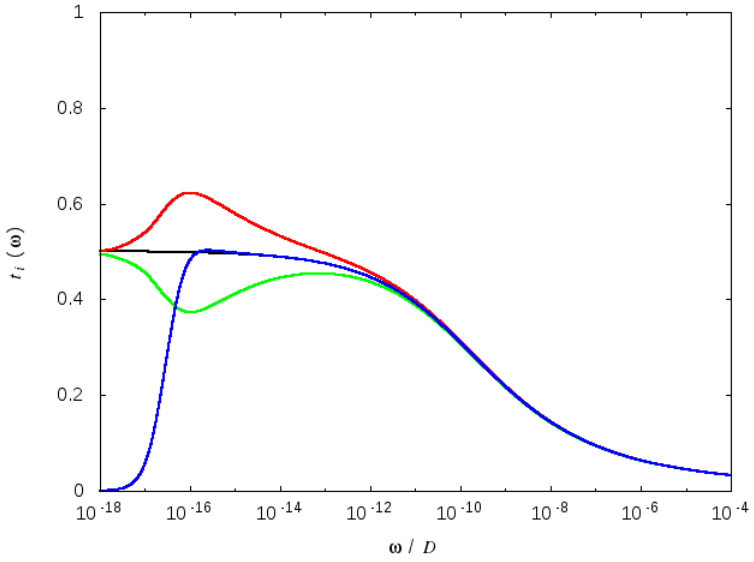

Figure 4.7: The zero-temperature scattering t matrices of the isotropic spin model with the Zeeman field $h/D = 10^{-14}$: $t_{+1}(\omega)$ (green line), $t_0(\omega)$ (blue line), and $t_{-1}(\omega)$ (red line), in comparison to the case without the field (black line). Though they look drastically different from those of the channel anistropic case (Figure 4.3), they are related to each other via the equations (4.3.1) and (4.3.3).

ent from the t-matrices of the channel anisotropic system (Figure 4.3). However, an insight can be gained by considering the S-matrices of the system S_k which are related to the t-matrices via

$$2\pi \mathrm{i}\rho\tau_k(\omega) = 1 - S_k\mathcal{G}(\omega), \tag{4.3.1}$$

where S_k is the Fermi-liquid S-matrix containing phase shift information, which in the case of the model with anisotropy, $S_k^\delta \propto -k$ [106], and $\mathcal{G}(\omega)$ is some frequency-dependent function universal to both $k = \pm 1$ species. By inverting the relation and combining the proportionality constant of S_k^δ into the function $\mathcal{G}^\delta(\omega)$, we have

$$\mathcal{G}^\delta(\omega) = \pi \mathrm{i}\rho\,[\tau_{+1}(\omega) - \tau_{-1}(\omega)]. \tag{4.3.2}$$

Figure 4.8 and 4.9 (red lines) show the real and the imaginary part of the function $\mathcal{G}(\omega)$ of the channel anisotropic spin model.

The presence of the Zeeman field introduces an imaginary factor into the S matrices of the system, i.e., $S_k^h \propto \mathrm{i}k$ [106]. The factor i in the equation (4.3.2) hence disappears and we expect the relation between the two systems as

$$\mathcal{G}^\delta(\omega) = \mathrm{i}\mathcal{G}^h(\omega), \tag{4.3.3}$$

which is indeed shown to be the case in Figure 4.8 and 4.9. Note also that the zero-frequency values of the t matrices of the spinful channels $k = \pm 1$ are found to be $\frac{1}{2}$, which is also what is expected in the case of 2-channel Kondo model under a magnetic field [106, 107].

Effectively, the Zeeman field perturbs the system in the same way as the channel anisotropy does to the physics of the system, i.e., it destablises the NFL fixed point and pushes the system towards the SC fixed point where Fermi liquid behaviour is observed.

4.4 Lifting Symmetry Constraints

In the second half of this chapter, we shall study only the main Kondo spin part of the Hamiltonian, equation (3.1.10), ignoring all the small perturbations that have previously been considered in the first half of the chapter. This time, however,

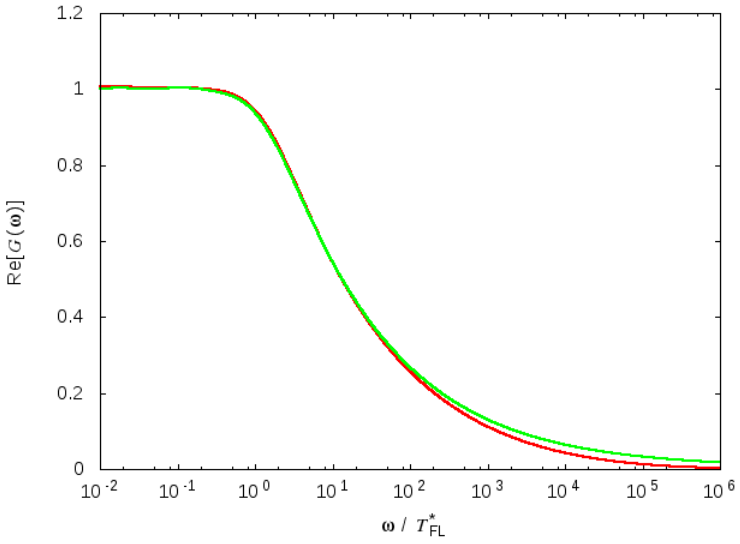

Figure 4.8: The real part of the frequency dependent of the function $\mathcal{G}(\omega/T^*_{\rm FL})$ as defined in the equation (4.3.1) for the spin model in the presence of the δ anisotropy (red line) and the imaginary part of the same function for the model with Zeeman field turned on (green line). The two functions are related to each other by the equation (4.3.3).

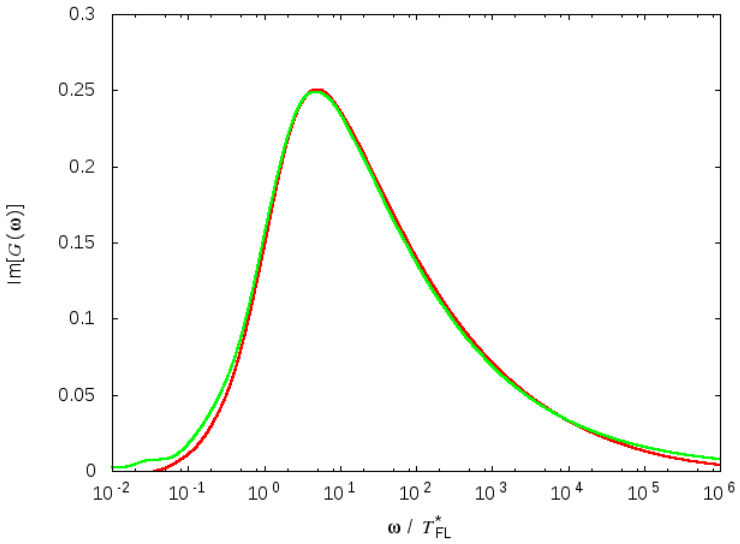

Figure 4.9: The imaginary part of the function $\mathcal{G}(\omega/T^*_{\rm FL})$ for the δ anisotropy case (red line) and the real part for the Zeeman field case (green line).

we shall not impose any symmetry constraints on the system and work with the following Hamiltonian

$$H_{\text{eff}} = \sum_{ki} \varepsilon_k a_{ki}^\dagger a_{ki} + \sum_{\alpha\in\{x,y,z\}} J_{\alpha\alpha} S_\alpha I_\alpha. \tag{4.4.1}$$

Béri has studied this model before using the Conformal Field Theory and the poor man's scaling procedure [41]. In the weak coupling limit, he proposed that the RG flow follows the scaling equation

$$\frac{\mathrm{d}J_\alpha}{\mathrm{d}l} = -\rho J_\beta J_\gamma, \tag{4.4.2}$$

and its permutations, where $\alpha, \beta, \gamma \in \{1, 2, 3\}$ are distinct, $l = \ln D$, D is the bandwidth, and ρ is the density of states of the conduction electrons. In this section, we seek to extensively study the spin model in general without any symmetry constraints and seek to confirm that these scaling equations indeed hold and that the NFL fixed point is stable against this type of anisotropy. Since the Hamiltonian needs to be entered manually into the NRG code, for convenience we choose to represent the spin-1 operators as $I_\alpha = -\mathrm{i}\sum_{ij} \varepsilon_{\alpha ij} \psi_i^\dagger \psi_j$ so that the matrix elements of the Hamiltonian are relatively simple, instead of representing it by the original spin-1 operators. The compensation, however, is that we have to perform the computation using complex numbers. Therefore, the NRG is code is rewritten so that all the numbers are changed to complex double precision floating point numbers, the matrix elements of the Hamiltonian in the basis of $\psi_i^\dagger \psi_j$ are entered into the code, and without the symmetry requirements as imposed in the previous chapter, the total spin $S_{z,\text{tot}} = S_z + \left(f_{+1}^\dagger f_{+1} - f_{-1}^\dagger f_{-1}\right)$ is no longer conserved and has to be removed from the code. Since the computation becomes more costly as the dimension of the matrices to be diagonalised is increased, we focus only on the thermodynamics of the system and use it to characterise the flow and the behaviour of the model.

We ran NRG calculations for various combinations of $J_\alpha/D \in [0.01, 10]$ and have found that indeed the NRG flow of the impurity entropy does always go from the WC fixed point, $S_{\text{imp}} = \ln 2$, at high temperature to the NFL fixed point, $S_{\text{imp}} = \ln\sqrt{3}$ at low temperature (Figure 4.10). The RG flow also scales on top of the universal curve obtained previously (left panel of Figure 3.2).

Figure 4.11 shows the Kondo temperature as a function of one of the coupling constants J_2 at four different values of $J_1/D = 0.01, 0.05, 0.1, 0.5$ and fixed $J_3/D = 0.1$. Indeed much of the behaviour found in the axially symmetric model (Section 3.3) is retained here. At weak coupling, the Kondo temperature grows as a function of J_2 – we will look into this more closely whether and how well this agrees with the results from the scaling equations above. At strong coupling, the Kondo temperature decays exponentially, $T_\mathrm{K} \propto \mathrm{e}^{-J_2}$, resulting in the duality-like behaviour found in the axially symmetric model.

In order to look more closely at the weak coupling regime of the model, we are going to compare the Kondo temperature obtained from the NRG calculations to those obtained from solving the RG scaling equations (4.4.2) above. We use Mathematica to solve the scaling equations, where we have fixed $J_3/D = 0.01$ and vary $J_1/D \in [0.1, 0.5]$, $J_2/D \in [0.1, 5]$ with $\Delta J_\alpha/D = 0.01$. We initiated the parameter $l_0 = 0$ and arbitrarily choose the Kondo temperature to be the energy scale $l_\mathrm{K} = \ln T_\mathrm{K}$ at which the coupling $J_3(l_\mathrm{K})/D$ is renormalised to 5. We have also multiplied l_K by another arbitrary constant so that it can be compared directly to the Kondo temperature obtained from NRG. Figure 4.12 (left panel) shows the contour plot of the log of the Kondo temperature as a function of the coupling constants J_1/D and J_2/D whilst the other coupling constant $J_3/D = 0.01$ is fixed. According to the scaling equations (4.4.2), due to the presence of the negative sign, the parameters J_α always increases as the parameter l decreases. Since $\frac{\mathrm{d}J_3}{\mathrm{d}l} \propto J_\alpha$, the larger the initial values of J_α are, the faster J_3 renormalises; thus, the less negative l becomes. The Kondo temperature then increases (becomes less negative) quickly as J_1, J_2 increase to the regime beyond where the scaling equations are valid.

It is also very clear that these results are very different from those obtained from NRG calculations (Figure 4.12, right panel) in the region of large $J_2/D > 1$. Whilst the Kondo temperature increases as J_2 increases upon solving the scaling equations, NRG shows that Kondo temperature in fact decreases as J_2 increases. This is also consistent with results found for the axially symmetric model found in the previous chapter and also earlier in this section where we have observed the duality-like behaviour (Figure 4.11, left panel), particularly that the turning point is near $J_2/D \approx 1$. The discrepancy arises from the fact that the scaling equations

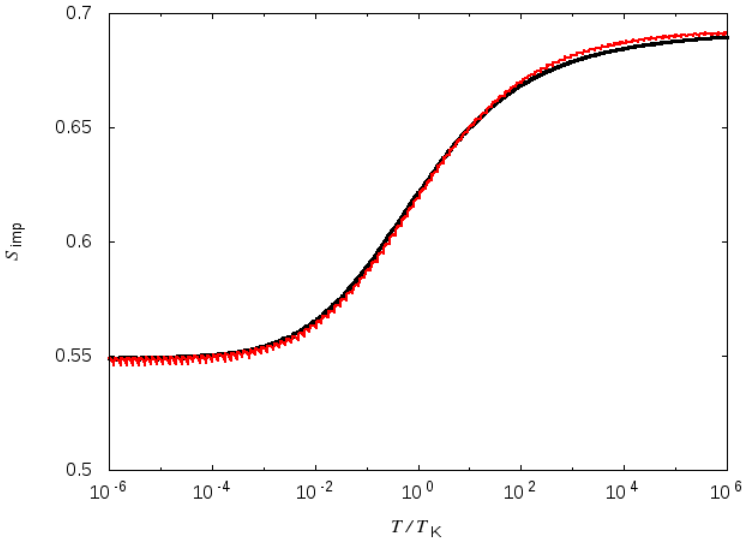

Figure 4.10: The temperature dependence of the impurity entropy of the spin model when no symmetry constraints are enforced. The results from NRG calculations (red) scales on top of the universal impurity entropy curve of the isotropic spin model (red line of the left panel of Figure 3.2, shown as the black line here).

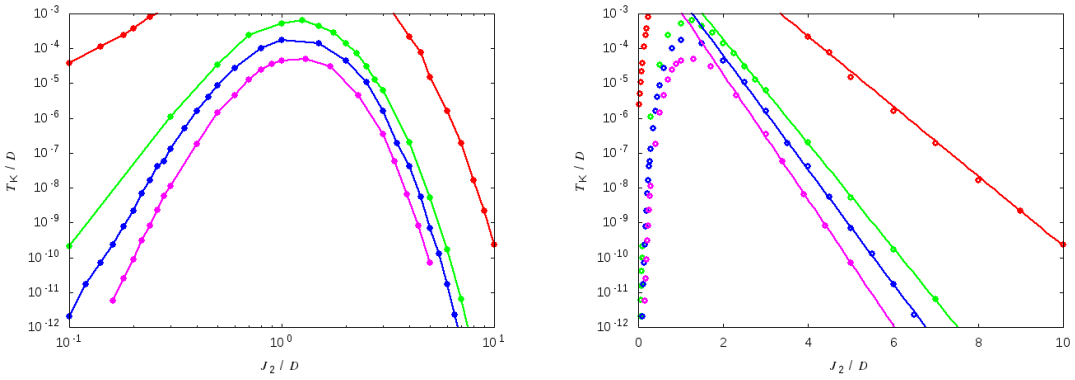

Figure 4.11: The dependence of the Kondo temperature T_K on the coupling constant J_2 where we have fixed $J_3/D = 0.1$ and varied $J_1/D = 0.01, 0.05, 0.1, 0.5$ (red circles, blue crosses, purple squares, and green circles, respectively) for the spin model without any symmetry constraints (4.4.1). (left) The log–log plot; (right) The log–linear plot. The behaviour similar to the duality found previously in the axially symmetric model, Figure 3.8, is also observed here. Furthermore, for large J, the Kondo temperature decays exponentially as a function of one of the coupling constants, exactly the same as is the axially symmetric case, equation (3.3.7).

(4.4.2) are only valid in the small coupling regime; hence, the results obtained by solving them are no longer valid and the top half of the plot is incorrect.

The similarities between the results obtained from these two methods can, nevertheless, be seen more clearly when we look at the plot on a log scale where the region of $J_2/D > 1$ is shown on an equal footing to that of $J_2/D < 1$, or if we simply zoom in to the region of small $J_2/D \leq 1$ on the linear scale. In the former, the log scale (Figure 4.13), the bottom half of the plot – $J_2/D < 1$ – agree very well with the results obtained from NRG. In the latter, the linear scale (Figure 4.14), where we show only on the region of $J_2/D \leq 1$, the results from the two methods obviously agree very well with each other.

We close this chapter off by remarking that we have now fully studied the spin model. This model supports the NFL behaviour at low temperature, which is robust against the presence of the anisotropy between the local couplings of the leads and the Majorana fermions. In addition, this model exhibits the duality between the region of weak coupling $J < 1$ and strong coupling $J > 1$, consistent with the behaviour found for the axially symmetric model which is studied in the previous chapter. The presence of other exponentially small perturbations, for instance, the non-local couplings between the Majoranas, on the contrary, destablises the NFL behaviour and pushes the system towards strong-coupling Fermi-liquid regime. Whilst this may pose some challenges into experimentally observing the NFL behaviour, it is still possible to do so when there is a good separation between the two energy scales.

In the next chapter, we shall study the Majorana device fully, without performing the low-energy transformation, including as well a consideration of the structure of the device.

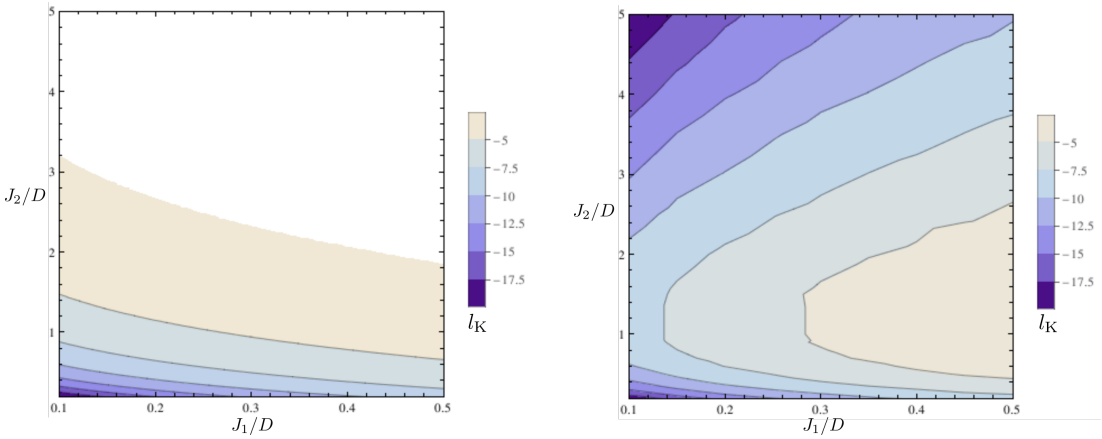

Figure 4.12: The contour plot of the log of the Kondo temperature ($l_K = \ln T_K$) as a function of the coupling constants $J_1/D \in [0.1, 0.5]$ and $J_2/D \in [0.2, 5.0]$ with fixed $J_3/D = 0.01$. (left panel) The plot is obtained by solving the weak-coupling RG scaling equations (4.4.2) and the Kondo temperature is defined to be the energy scale l_K at which $J_3(l_K)/D = 5$. As the coupling constant is increased either along J_1 or J_2, the log of the Kondo temperature increases as well (becomes less negative). (right panel) The plot is obtained from NRG calculations. In this case, since the Kondo temperature increases with the coupling constants when they are smaller than 1 but decreases once they are greater than 1 (See Figure 4.11), the turning point of the contour lines occur at $J_2/D \approx 1$.

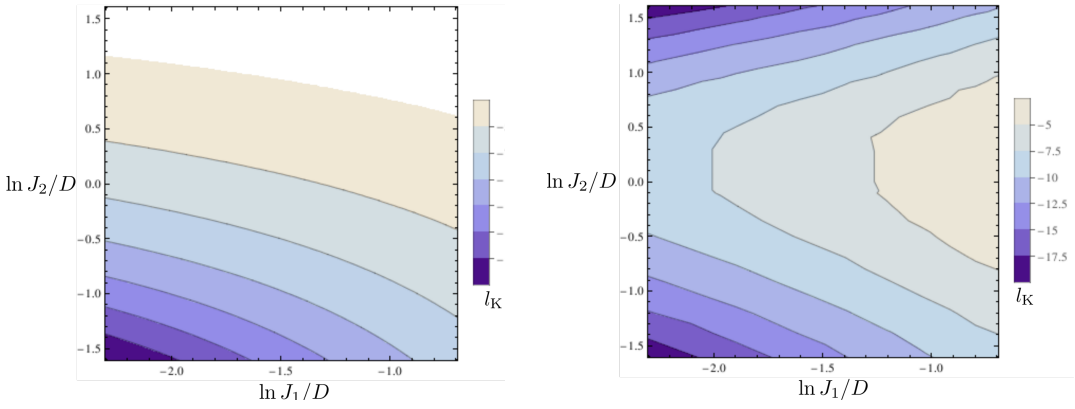

Figure 4.13: The contour plot of the log of the Kondo temperature ($l_K = \ln T_K$) as a function of the coupling constants on a log scale $\ln J_1/D$ and $\ln J_2/D$ with fixed $J_3/D = 0.01$. (left panel) The plot is obtained by solving the scaling equations. (right panel) The plot is obtained from NRG calculations.

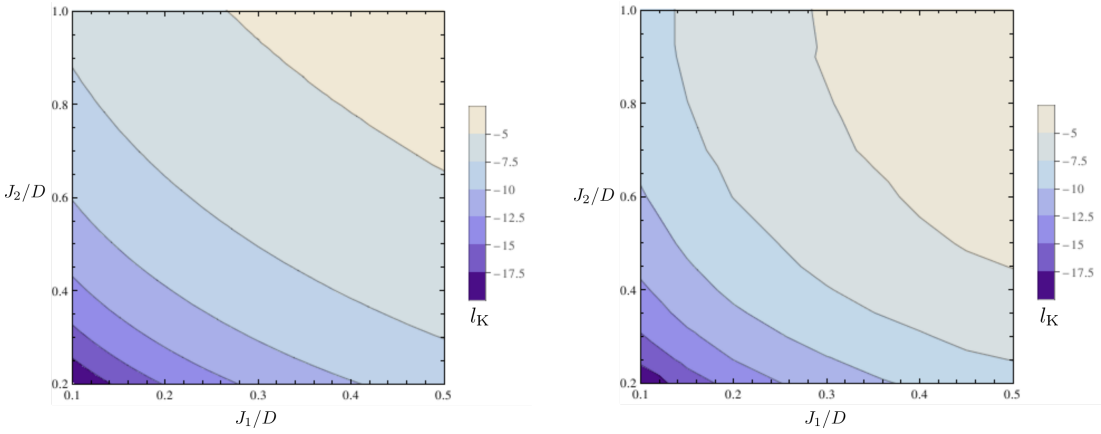

Figure 4.14: The contour plot of the log of the Kondo temperature ($l_K = \ln T_K$) zoomed in near the region of $J_1/D \leq 1.0$. (left panel) Results from solving the scaling equations. (right panel) Results obtained from NRG calculations. It is clear that for small $J_2/D < 0.6$, the two plots agree very well with each other.

5

Beyond the Low-Temperature Effective Model

In the previous two chapters, we were interested in the low-temperature behaviour of the Majorana device and in order to simplify the model, we derived a low-energy effective model by projecting it onto the ground-state subspace, the subspace where the superconductor is tuned to some N charged state and $\langle H_c \rangle = 0$. We found that the effective low-energy Hamiltonian is a Kondo spin-$\frac{1}{2}$ Hamiltonian coupled to the spin-1 conduction electrons and we study its thermodynamics and zero-temperature conductance tensors. In this chapter, we shall not perform such a projection but attempt to study the model in full. Since the charging energy Hamiltonian contains the variable N, the number of charges on the superconducting island, which is an arbitrary number, NRG cannot directly handle this Hamiltonian right away. We shall therefore assume that the level spacings are sufficiently large that only a few charge states need to be considered and start by studying the simplest configuration of the superconductor – having only two charge states. Afterwards, we add more states so that the energy configuration is the same as that which can be generated from the charging energy Hamiltonian directly and study how its physics is changed.

5.1 Hamiltonian of the Majorana Device

In Section 2.3, we discuss the Majorana device of interest in this project and write down the Hamiltonian (2.3.1)

$$H = H_{\text{leads}} + H_{\text{c}} + H_{\text{M}} + H_{\text{t}}, \tag{5.1.1}$$

stating that our device consists of a mesoscopic superconducting island with the charging energy term $H_{\text{c}} = E_c \left(N - \frac{q}{e}\right)^2$ with four Majorana bound states present, three of which are coupled to conduction electron H_{leads} via the tunnelling term $H_{\text{t}} = \sum_{ij} t_{ij} \gamma_i \psi_j \mathrm{e}^{\mathrm{i}\phi/2} + \text{adj.}$, in addition to being able to lightly couple with each other via H_{M}. In the previous two chapters, we worked in the low-temperature and low-coupling regime, so that we could perform a low-energy transformation to the Hamiltonian above and work with the effective spin model (3.1.14). In this chapter, we shall consider the structure of the superconducting island as well.

In order to be able to implement the NRG calculation of this model, we need to rewrite H_{t} by converting all the operators, if not already, into the standard Dirac fermions operators: we replace the exponential operator $\mathrm{e}^{\mathrm{i}\phi/2}$ which creates an electron on the superconductor by a canonical creation operator $d^\dagger$ and form two Dirac fermions from the four Majorana γ_i via

$$f = \frac{1}{2}\left(\gamma_1 + \mathrm{i}\gamma_2\right), \tag{5.1.2}$$

$$f' = \frac{1}{2}\left(\gamma_3 + \mathrm{i}\gamma_4\right), \tag{5.1.3}$$

resulting in the Hamiltonian

$$H_{\text{t}} = d^\dagger \left\{ t_1 \left[\left(f + f^\dagger\right) \psi_1 - \mathrm{i}\left(f - f^\dagger\right) \psi_2 \right] + t_3 \left(f' + f'^\dagger\right) \psi_3 \right\} + \text{adj.} \tag{5.1.4}$$

We ignore the non-diagonal exponentially-small couplings and assume equal couplings between lead 1 and lead 2, $t_1 = t_2$, in order to avoid working with a complex Hamiltonian. Performing a set of transformations equivalent to (3.2.2)–(3.2.4),

$$\phi_1 = \frac{1}{\sqrt{2}}(\psi_1 + \mathrm{i}\psi_2), \tag{5.1.5}$$

$$\phi_2 = \frac{1}{\sqrt{2}}(\psi_1 - \mathrm{i}\psi_2), \tag{5.1.6}$$

$$\phi_3 = \psi_3, \tag{5.1.7}$$

we will therefore be working with the following tunnelling Hamiltonian

$$H_{\mathrm{t}} = d^{\dagger}\left\{\sqrt{2}t_1\left(f^{\dagger}\phi_1 + f\phi_2\right) + t_3\left(f' + f'^{\dagger}\right)\phi_3\right\} + \mathrm{adj.} \tag{5.1.8}$$

Similarly, we remodel the Hamiltonian that represents the superconductor so that it can be implemented in the NRG codes. Our approach is to consider the energy spectrum of this physical system and then we will come up with a Hamiltonian that is capable of producing this very same energy spectrum. It is known that electrons are paired in the form of Cooper pairs in the ground state of a conventional superconductor, i.e., that the ground state of a superconductor has even number of electrons, whereas the excitations with odd number of electrons cost energy; the system is gapped with its energy spectrum shown in the top left panel of Figure 5.1. In the presence of Majorana fermions, however, as is mentioned in Section 2.2, there exists a zero-energy mode which supports a zero-energy excitation. Since the states with odd and even number of electrons are now on the equal footing energetically, the conventional energy gap Δ disappears, resulting in the energy spectrum that is shown in the top right panel of Figure 5.1. Finally, it is the charging energy $H_{\mathrm{c}} = E_c\left(N - \frac{q}{e}\right)^2$ that lifts the

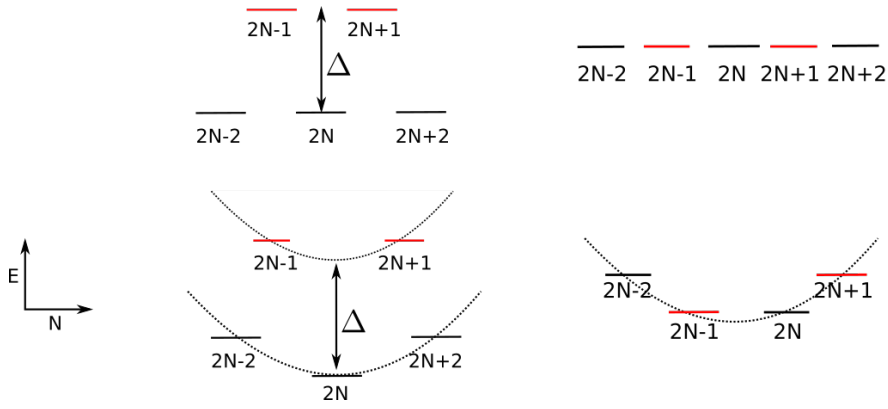

Figure 5.1: Following Ref. [62], energy spectrum of a superconductor as a function of its number of electrons. Whereas the figures on the top (bottom) are the spectrum for the superconductors without (with) charging energy, the figures on left (right) are those for when there are not (are) Majorana fermions present.

degeneracy among the different charge states [62]. The details of the energy spectrum, however, depends on the value of the gate charge q, which can be tuned via the gate voltage across the capacitor that is connected to the superconducting island. For instance, if $q = N_0 e$, where N_0 is an integer, the ground state which is the N_0-charge state is non-degenerate. However, if $q = \frac{N_0}{2}e$, at half integer, the ground states – the $\frac{N_0 \pm 1}{2}$-charge states – are now degenerate; its energy spectrum then takes the same form as that of the bottom right panel of Figure 5.1. Note also that it is the charging energy that breaks the degeneracy of all the different charge states on the superconductor, rendering N, the number of charges on the dot, a meaningful quantum number which we shall use as a principal number to classify the superconducting states.

Finally, in order to further simplify the form of the possible Hamiltonian for the superconductor, we assume that only a few charge states of the superconducting island are energetically accessible, and model the charging energy H_{c} by write down a simplified Hamiltonian H_{SI}. Neglecting the exponentially small couplings, we now drop H_{M} and for the rest of the chapter will be working with the following Hamiltonian

$$H = H_{\mathrm{leads}} + H_{\mathrm{SI}} + H_{\mathrm{t}}. \tag{5.1.9}$$

5.2 The Simplest Case: Two Charge States

We first consider the simplest case possible: the case in which the only two states that are energetically accessible to the system are the states N and $N+1$. (In the bottom right panel of Figure 5.1, this is the case where only the two lowest energy states – the charge states $2N-1$ and $2N$ – are considered, though the two need not be degenerate in general.) In this case, effectively the superconductor can be viewed as a single orbital with two charge states available. Note that whilst earlier in Chapter 3, we derive the effective spin model by assuming that the charge state N is the ground state and consider the transitions to the two other charge states $N-1$ and $N+1$ as perturbations, we study a system with only two charge states here. The assumption that the charging energy E_{c} is much greater than the energy scale of interest (Section 3.1) then corresponds to the case where

the difference in energy between the two charge states N and $N+1$ are larger than other parameters in the model.

Since the superconducting island can now be treated as a single orbital, its Hamiltonian can be written simply as

$$H_{\mathrm{SI}}^{\mathrm{2CS}} = \varepsilon\, n, \tag{5.2.1}$$

where $n = d^\dagger d$ is the number operator of the electron in that orbital and ε is the energy cost for that electron. Arbitrarily, we choose $\varepsilon < 0$ and the ground state configuration of the superconducting island is the occupied state. Furthermore, since the energy difference between the two superconducting states is $|\varepsilon|$, we refer to it as the energy gap. The Hilbert space of this system can be constructed by taking the direct product of the superconducting orbital, as is represented by the electron operator d, with the two Majorana pairs, represented by the electron operators f and f', each of which can either be empty or occupied, resulting in a total number of 8 states. However, Fu made the following argument for a system with a single Majorana mode [62]: Recall that the ground states of the superconductor are composed of two sectors, one with even number of electrons called $|e\rangle$, the other with odd number of electrons called $|o\rangle$, which are related to each other by $f|e\rangle = 0$ and $|o\rangle = f^\dagger|e\rangle$ and are represented as

$$|e,\phi\rangle = \sum_{n=2N} a_n e^{\mathrm{i}\phi N}\,|2N\rangle\,, \tag{5.2.2}$$

$$|o,\phi\rangle = \sum_{n=2N+1} a_n e^{\mathrm{i}\phi(N+1/2)}\,|2N+1\rangle\,. \tag{5.2.3}$$

This therefore imposes that the occupation of Majorana mode $f^\dagger f = \frac{1}{2}(\mathrm{i}\gamma_1\gamma_2 + 1)$ is fixed by the number of electrons on the superconductor mod 2, $\mathrm{i}\gamma_1\gamma_2 = (-1)^n$, i.e., whether the Majorana mode is occupied depends on whether the number of electrons on the superconductor is even or odd. Therefore, the conclusion is that the actual Hilbert space is smaller than that generated from the direct product. In our case, with two Majorana modes, represented by the operators f and f', the constraint is generalised so that the parity of the two Majorana modes must be the same as the parity of the superconducting electron. For example, if the parity of the Majorana is even, either the two Majorana modes are both empty

or both occupied, the number of the electrons on the superconductor must be even as well, or in this case, the single orbital $n = d^\dagger d$ must be empty.

In order to remove the states with incorrect parity, for example, the state in which the superconducting orbital is empty (even) but the two Majorana modes are only singly occupied (odd), we add the following fictitious energy cost to the Hamiltonian in the initialisation step of the NRG:

$$\begin{aligned} H^{\text{fic}} = x \Big\{ &(1-n)\left[n_{M1}(1-n_{M2}) + (1-n_{M1})n_{M2}\right] \\ &+ n \ \left[(1-n_{M1})(1-n_{M2}) + n_{M1}n_{M2}\right] \Big\}, \end{aligned} \tag{5.2.4}$$

where the state in the first line is the state with the empty superconducting orbital and odd Majorana parity and vice versa for the second line, and we have chosen the energy penalty $x/D = 10^3$. In the example mentioned above, the superconducting orbital is empty $n = 0$ whereas the two Majorana modes are only singly occupied, $n_{M1} = 0, n_{M2} = 1$ or $n_{M1} = 1, n_{M2} = 0$, which corresponds to the state in the first line. These two states will get an additional energy cost of x and will be projected out in the first iteration of NRG.

5.2.1 Decoupled Limit

When the superconducting island is decoupled from the leads, the system of interest then consists of a simple two-level subsystem with an energy gap of ε which is connected to the Majoranas and the three independent free-electron leads. The entropy of the superconducting sector can be straightforwardly calculated from the thermodynamic relation

$$S_{\text{SI}} = -\frac{\partial F}{\partial T} = \frac{\partial}{\partial T} T \ln Q = \ln\left(1 + \mathrm{e}^{-\varepsilon/T}\right) + \frac{\varepsilon}{T}\frac{\mathrm{e}^{-\varepsilon/T}}{1+\mathrm{e}^{-\varepsilon/T}}. \tag{5.2.5}$$

At low temperature, the empty state is energetically unfavourable and the ground state is the occupied state; thus, $S_{\text{SI}} \to 0$ as expected. At high temperature, both states are accessible and indeed $S_{\text{SI}} \to \ln 2$.

In order to discuss this system in the context of impurity problem, we use the previously defined $S_{\text{imp}} = S - S_0$ where S is that of the full system and S_0 is that of free conduction electron leads. Since the system is composed of the superconducting island, the Majoranas, and the free conduction leads, subtracting

away the contributions from the leads, $S_{\text{imp}} = S_{\text{SI}} + S_{\text{M}}$. Now we consider the ground state that is formed from the direct product between the superconducting orbital and the two Majorana fermion orbitals, $|n_{SI}\rangle \otimes |n_{M1}, n_{M2}\rangle$. Since the coupling constant $t = 0$, the Majoranas completely disappear and the Hamiltonian of the system, taken away the lead contributions, is simply $H_{\text{SI}} = \varepsilon n_{\text{SI}}$; the Majorana sector, however, still remains in the Hilbert space. Since $\varepsilon < 0$, the ground state of the superconducting orbital is occupied, $n_{\text{SI}} = 1$, and $S_{\text{SI}} = 0$. Furthermore, since the parity of the superconducting sector is odd, the parity constraint forces the parity of the Majorana sector to be odd as well. There are two such states, $|n_{M1}, n_{M2}\rangle \in \{|1,0\rangle, |0,1\rangle\}$ with odd parity; therefore, at low temperature, $S_{\text{M}} = \ln 2$. We finally conclude that $S_{\text{imp}} = \ln 2$ at low temperature.

As mentioned before, both odd and even parity states of the superconductor are accessible at high temperature. The odd parity superconducting state is associated with two odd parity Majorana fermion states, and vice versa for the even parity superconducting state. Therefore, $S_{\text{M}} = \ln 2$ and $S_{\text{imp}} = \ln 4$. Figure 5.2 shows that the impurity entropy of the system in the decoupled limit calculated from NRG agree exactly with the analytical relation above, with the two limiting values also confirmed as discussed and the crossover between the two limits occurs at the energy scale of $T \sim |\varepsilon|$.

5.2.2 Large-Energy Gap Limit

As mentioned before, when the energy gap between the two superconducting states is larger than other parameters in the model, we would expect the low-energy behaviour of the system to be the same as that found for the effective spin model being studied in the previous two chapters. Figure 5.3 shows the impurity entropy of the superconducting system with a large energy gap $|\varepsilon|/D = 10$ assuming isotropic coupling constants $t_1 = t_3$. Since the energy gap is large, the empty superconducting state becomes energetically unfavourable and hence inaccessible; the ground state of the superconducting sector of the system is the occupied state. At high temperature, we found the impurity entropy to be that of the WC fixed point value $S_{\text{imp}} = \ln 2$ as expected; whereas in the spin model, this arises from the degenerate spin doublet state, in this case, the value reflects solely

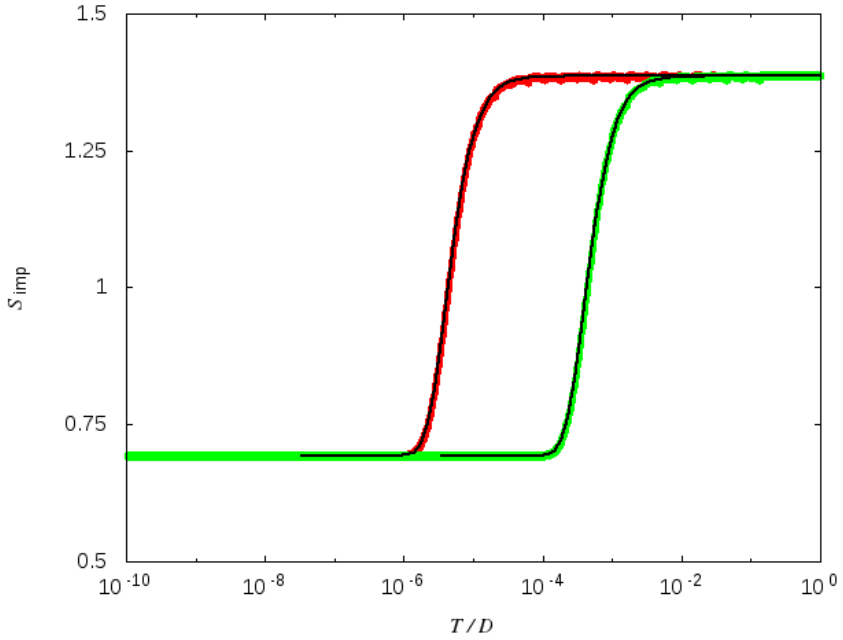

Figure 5.2: Impurity entropy as a function of temperature of the Majorana device in the decoupled limit. The results from NRG is shown, in the case of $-\varepsilon/D = 10^{-5}$ (red) and 10^{-3} (green) against the analytical results (black lines) from the equation (5.2.5).

the degeneracy in the Majorana sector. When the coupling constant is turned on, the impurity entropy flows to the NFL fixed point value $S_{\text{imp}} = \ln\sqrt{3}$, which is exactly the behaviour of the low-temperature effective spin model studied in the previous chapters. Furthermore, the results found in this large-energy gap limit superimpose exactly onto the universal impurity entropy curve of the spin model. Finally, the other feature that we found for this Majorana device in the large-energy gap limit which is very similar to the behaviour of the effective spin model is the duality behaviour found in the strong-coupling regime.

In section 3.1, we have already shown in equation (3.1.12) that when the charging energy is large, the effective spin coupling constant $J_{\alpha\alpha}$ is related to the tunnelling coupling constant t_{ij} via

$$J \sim \frac{t^2}{|\varepsilon|}, \tag{5.2.6}$$

in the isotropic limit. Together with equation (3.2.9), which states that the Kondo

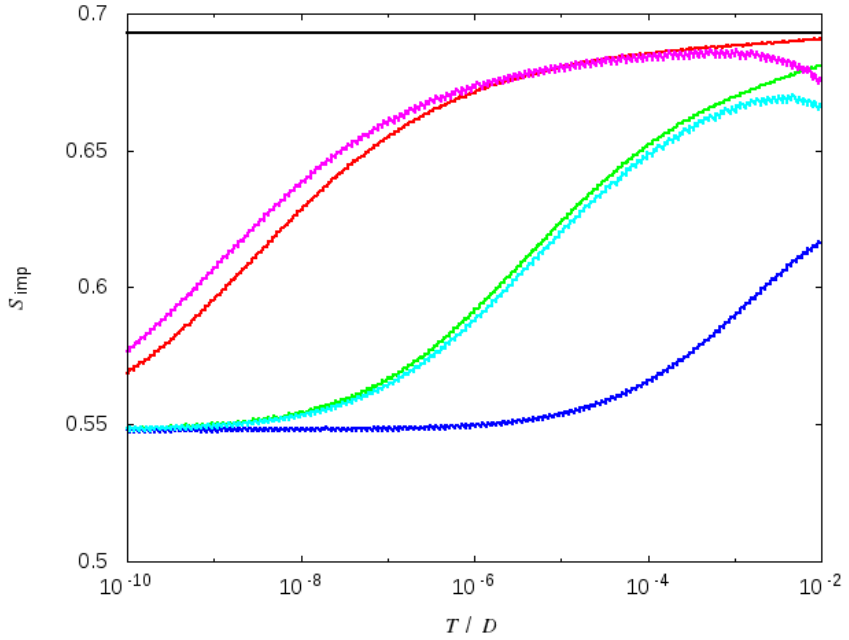

Figure 5.3: Impurity entropy as a function of temperature of the Majorana device in the large-energy gap limit, $|\varepsilon|/D = 10$. The coupling constants are assumed to be isotropic $t_1/D = t_3/D = 0.8$(red), 1(green), 3(blue), 4(cyan), and 5(magenta). The decoupled limit $t = 0$ is also included for reference (black line). The entropy flows from the WC limit $S_{\text{imp}} = \ln 2$ at high temperature to the NFL value $S_{\text{imp}} = \ln\sqrt{3}$. These curves are exactly the same as the universal entropy curve of the spin model.

temperature $T_{\text{K}} \sim J^2 \mathrm{e}^{-c_1/J}$, we therefore expected

$$T_{\text{K}}/D \sim t^4\, \mathrm{e}^{-c_2/t^2}. \tag{5.2.7}$$

Figure 5.4 shows that the Kondo temperature calculated from NRG (red circles) as a function of the coupling constant t agree very well with the relation above (green line). In addition, we could also study the dependence of the Kondo temperature on the size of the energy gap, which for the same reason is predicted to be

$$T_{\text{K}}/D \sim \frac{1}{|\varepsilon|^2}\, \mathrm{e}^{-c_3|\varepsilon|}. \tag{5.2.8}$$

This is confirmed in Figure 5.5 where we have obtained the Kondo temperature from NRG for when the energy gap $|\varepsilon|/D \in [1, 10]$ is large and the coupling

constants of $t/D = 0.5$ and 0.7 – the NRG results agree very well with the analytical relation (5.2.8).

Since we have discovered in section 3.3.2 that there is a duality between the model with the spin coupling constant $J \leftrightarrow \frac{1}{J}$ when the coupling constant is large, we also expect the Kondo temperature relation (5.2.7) to follow the same behaviour, i.e.,

$$T_{\mathrm{K}}/D \sim \frac{1}{t^4}\,\mathrm{e}^{-c_4 t^2} \tag{5.2.9}$$

to hold when the tunnelling coupling constant t is large. This is confirmed in Figure 5.4 (blue line) where we have shown that the expression above agrees with the data calculated from NRG when the energy gap $|\varepsilon|/D = 10$.

Now we study another physical property that can be experimentally probed, the conductance tensor. Just as in section 3.2.3, we need the expressions for the time derivatives of the lead operators, which we determine first in the transformed basis $N_i = \phi_i^\dagger \phi_i$ as

$$\mathrm{i}\hbar\dot{N}_1 = \sqrt{2}t_1\left(-d^\dagger f^\dagger \phi_1 + \phi_1^\dagger f d\right), \tag{5.2.10}$$

$$\mathrm{i}\hbar\dot{N}_2 = \sqrt{2}t_1\left(-d^\dagger f \phi_2 + \phi_2^\dagger f^\dagger d\right), \tag{5.2.11}$$

$$\mathrm{i}\hbar\dot{N}_3 = \quad t_3\left(-d^\dagger (f' + f'^\dagger)\phi_3 + \phi_3^\dagger (f' + f'^\dagger) d\right). \tag{5.2.12}$$

In order to be able to interpret the results, we need to work with the operators in the physical basis $\mathcal{N}_i = \psi_i^\dagger \psi_i$, which can be expressed in the transformed basis as

$$\mathcal{N}_1 = \psi_1^\dagger \psi_1 = \frac{1}{2}\left(N_1 + \phi_1^\dagger \phi_2 + \phi_2^\dagger \phi_1 + N_2\right), \tag{5.2.13}$$

$$\mathcal{N}_2 = \psi_2^\dagger \psi_2 = \frac{1}{2}\left(N_1 - \phi_1^\dagger \phi_2 - \phi_2^\dagger \phi_1 + N_2\right), \tag{5.2.14}$$

$$\mathcal{N}_3 = N_3, \tag{5.2.15}$$

where we clearly observe as well that $N_1 + N_2 = \mathcal{N}_1 + \mathcal{N}_2$ as a result of the transformation (5.1.5)–(5.1.6). The expressions for the time-derivative operators are then

$$\begin{aligned}\mathrm{i}\hbar\dot{\mathcal{N}}_{1,2} = \frac{1}{2}\sqrt{2}t_1\Big\{ &- d^\dagger\left(f^\dagger\phi_1 + f\phi_2\right) + \left(\phi_1^\dagger f + \phi_2^\dagger f^\dagger\right) d \\ &\mp d^\dagger\left(f^\dagger\phi_2 + f\phi_1\right) \pm \left(\phi_2^\dagger f + \phi_1^\dagger f^\dagger\right) d\Big\}.\end{aligned} \tag{5.2.16}$$

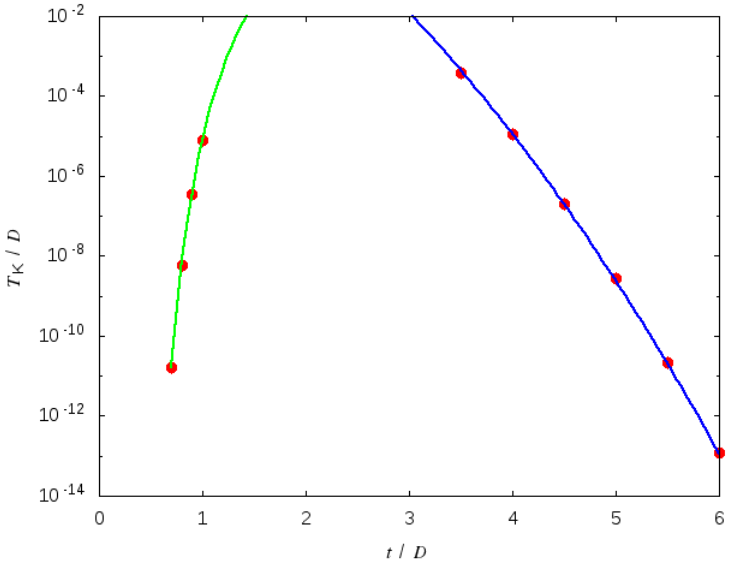

Figure 5.4: The dependence of the Kondo temperature T_{K} on the coupling constant t in the large-energy gap limit $|\varepsilon|/D = 10$ of the Majorana device. The red dots are data calculated from NRG whereas the green line is the analytical relation obtained from the low-energy transformation at weak-coupling limit, equation (5.2.7), and the blue line is that at strong-coupling limit, equation (5.2.9).

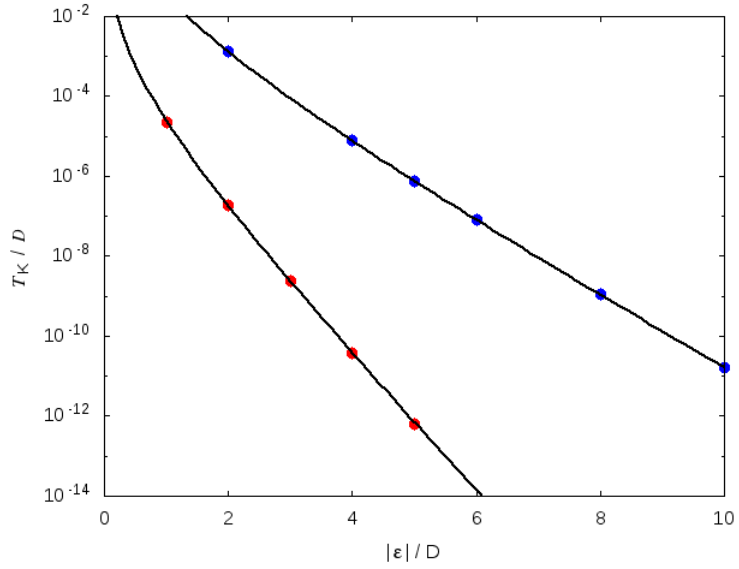

Figure 5.5: The dependence of the Kondo temperature T_{K} on the energy gap $|\varepsilon|$ in the large-energy gap limit $|\varepsilon|/D \in [1, 10]$ of the Majorana device when the coupling constants are $t/D = 0.5$ (red dots) and 0.7 (blue dots). The NRG results (dots) agree very well with the analytical relation (5.2.8) (black lines).

Figure 5.6 shows the frequency dependence of the zero-temperature conductance tensor in the large-energy gap limit. As anticipated, the results found for the device in this limit (red line) collapse onto the universal curve of the isotropic spin model (black line), showing the RG flow from the WC fixed point at high temperature to the NFL fixed point at low temperature, and once again confirming that when the energy gap between the states on the superconductor is large, the model behaves effectively as a spin model studied in the previous chapter. Indeed, the spin physics is robust against the inclusion of the charge fluctuation to the $N+1$ charge state in this two-charge state model and the low-energy effective model that we derived in Section 3.1 does correctly capture the low-energy physics of this model.

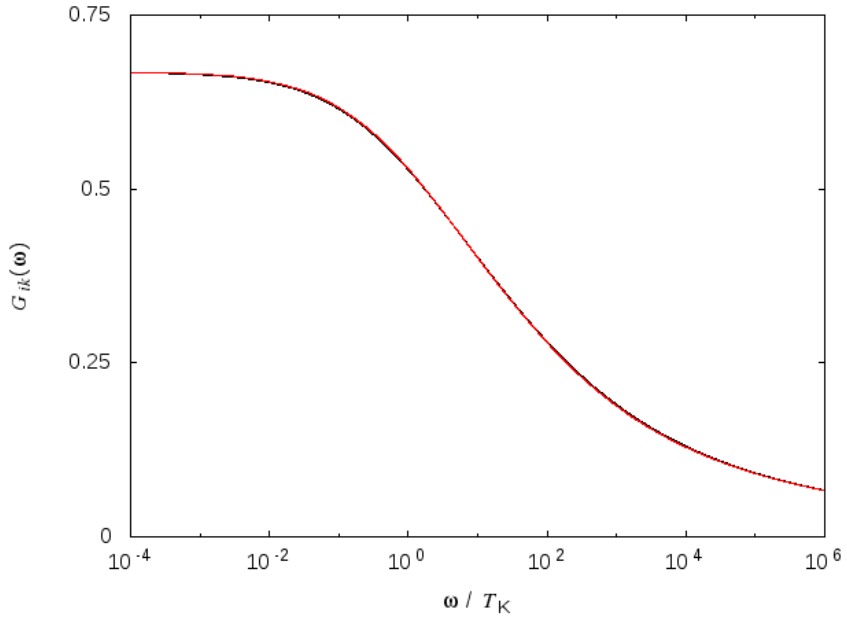

Figure 5.6: The zero-temperature conductance tensor of the Majorana device in the large-energy gap limit. In this limit, the conductance curve is the universal curve obtained earlier from the isotropic spin model (Figure 3.4).

We close this section by discussing one of the remarkable features of the topological Kondo effect: it can be turned off by decoupling one of the leads [41]. This can also be seen in the results from NRG calculation (Figure 5.7), where

we calculate the impurity entropy of the system when lead $k = 3$ is being slowly decoupled from the superconductor – $t_3 \to 0$. It can be seen very clearly that as t_3 is decreased, the RG flow towards the NFL fixed point occurs at a lower temperature scale. Once t_3 is small enough, which is still as large as $0.1D$, the Kondo temperature then becomes smaller than $10^{-14}D$. Certainly, removing lead $k = 3$ completely would effectively lift the topological Kondo effect. We can also see from the figure that the anisotropy in the coupling constants t_k does not change the qualitative RG flow pattern of the system; therefore, we will not look further into the anisotropy of this type.

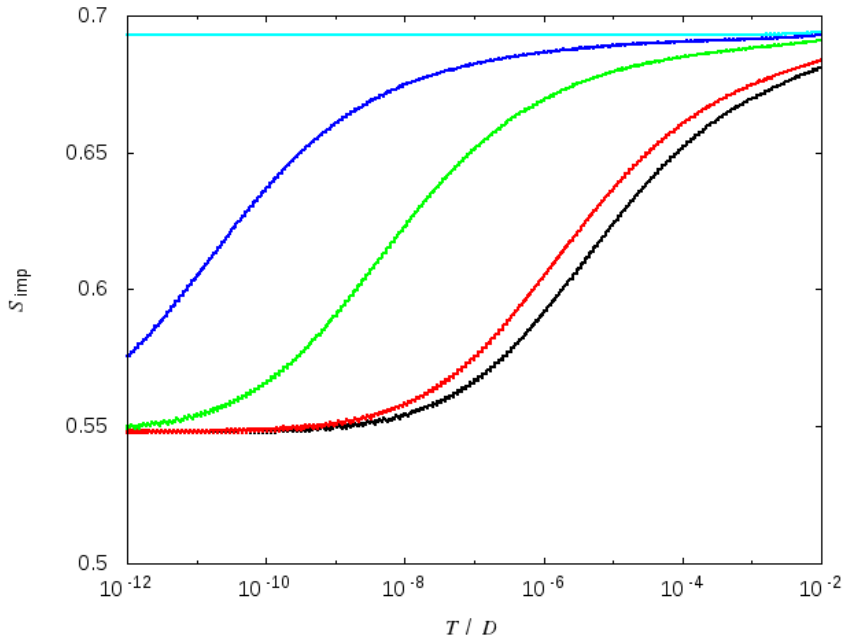

Figure 5.7: Impurity Entropy of the Majorana device as a function of temperature in the large-energy gap limit when lead $k = 3$ is being slowly decoupled from the superconducting island, i.e., $t_3/D = 0.9$ (red), 0.5 (green), 0.3 (blue), and 0 (cyan) whilst $t_1/D = 1$ is kept fixed. The result of the fully coupled case $t_3 = t_1 = 1$ is also included for reference (black). As t_3 is reduced, the Kondo scale quickly decreases until the RG flow to NFL fixed point can no longer be observed in the temperature range of interest.

5.2.3 Doubly Degenerate System

Now we turn our attention to the system where there is no energy gap between the empty and the occupied states on the superconductor, i.e., $\varepsilon = 0$. This superconductor energy configuration is the ground-state manifold of the energy configuration in the lower right panel of Figure 5.1 – the charge states $2N-1$ and $2N$ in the figure are represented by the two superconducting states in our model and the other charge states are of energies inaccessible to the system. Since this energy configuration is very different from what we have considered before, it is possible that different physics is observed.

We study the RG flow of this system by studying the impurity entropy (Figure 5.8). As can be seen, the qualitative features of the RG flow are indeed different from those other systems studied before. In the decoupled limit, (black line of Figure 5.8), the impurity entropy stays constant at $\ln 4$. This is due to the quadruply degeneracy of the system, half of which is from the superconducting sector which is doubly degenerate, and the other half is from the Majorana sector. As we have mentioned before, due to the parity constraint, the occupied superconducting state is allowed with only the odd Majorana configurations and vice versa. Since there are two Majorana states of each parity, the Majorana contribution to the impurity entropy is $\ln 2$. When the conduction electrons are coupled to the Majoranas on the superconductor, we can observe a new crossover from this $\ln 4$ fixed point to the NFL fixed point with the usual impurity entropy of $\ln \sqrt{3}$. Interetingly, despite the fact that now the superconducting state can either be occupied or empty at low temperature, the RG flow still goes towards the $\ln \sqrt{3}$ NFL fixed point. Therefore, we conclude that the NFL fixed point is remarkably robust against the charge fluctuation in the superconductor. Finally, we observe that the Kondo scale increases as the coupling constant is increased as before.

Once the coupling is large enough, the impurity entropy is observed to be $\ln 2$ at high temperature and eventually flows towards the NFL fixed point. Furthermore, we have found that the the impurity entropy curve obtained in this regime superposes exactly onto the universal curve which characterises the flow from the WC fixed point to the NFL fixed point in the spin model (the left panel of Figure

3.2). Whilst this parameter regime is very different from that which we know to generate the spin physics – zero energy gap with large t, instead of the previously large energy gap – the same physics reappears here.

We can understand the system in this large-t regime by perturbatively deriving an effective Hamiltonian. If the Hamiltonian of a system can be decomposed as $H = H_0 + \lambda H_1$, where H_0 is the part of the Hamiltonian whose eigenstates and eigenvalues are know and H_1 is a perturbation. The expression for the effective Hamiltonian up to the second order is given by [108]:

$$\begin{aligned} H_{\text{eff}} &= H_0 P_\alpha + P_\alpha H_1 P_\alpha \\ &\quad + \frac{1}{2} \sum_{\substack{ijk \\ \gamma \neq \alpha}} |i\alpha\rangle \langle i\alpha| H_1 |k\gamma\rangle \langle k\gamma| H_1 |j\alpha\rangle \langle j\alpha| \left(\frac{1}{E_{i\alpha} - E_{k\gamma}} + \frac{1}{E_{j\alpha} - E_{k\gamma}} \right), \end{aligned} \tag{5.2.17}$$

where α indicates the ground-state manifold, $P_\alpha = \sum_i |i\alpha\rangle \langle i\alpha|$ is the projection operator onto the manifold α, and $E_{i\alpha}$ is the energy of the state i of the manifold α.

Now, in the limit $\varepsilon = 0$, the Hamiltonian of the system is simply

$$H = H_{\text{leads}} + H_{\text{t}}, \tag{5.2.18}$$

where H_{t} is given in equation (5.1.8). With the coupling constants $t_1 = t_3 =: t$ being large, we shall take H_{t} to be H_0 and consider the infinite chain H_{leads} as a perturbation. Since the coupling strength decreases along the chain, to the first approximation, we shall consider only the first term of the infinite chain. Taking the basis states to be the direct product of the superconductor orbital d, the two Majorana fermion orbitals f and f', and the orbitals of the three lead electrons at the impurity site ϕ_i, we exactly diagonalise H_{t} and found the lowest-energy eigenstates to be

$$|\chi_1\rangle = \quad |1;10;010\rangle + k\,|1;01;001\rangle + k\,|0;00;110\rangle + |0;11;011\rangle\,, \tag{5.2.19}$$

$$|\chi_2\rangle = -\,|1;01;100\rangle + k\,|1;10;001\rangle + k\,|0;11;110\rangle + |0;00;101\rangle\,, \tag{5.2.20}$$

where $k = \frac{1}{2}(\sqrt{5} - 1)$, and the eigenstates are written in terms of the occupation number of the superconducting sector, Majorana sector, and the lead sector,

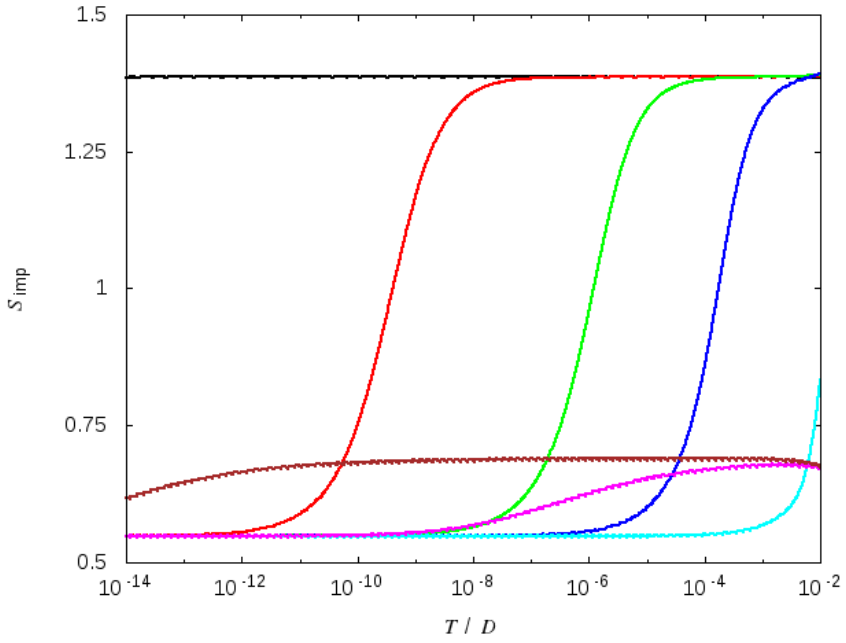

Figure 5.8: Impurity Entropy of the Majorana device as a function of temperature when the two superconducting states are degenerate ($\varepsilon = 0$). The coupling constant $t/D = 0.1$ (red), 0.2 (green), 0.3 (blue), 0.5 (cyan), 1 (magenta) and 2 (brown). The decoupled limit $t = 0$ (black), where the impurity entropy stays constant at the value of $\ln 4$ at all temperatures due to the double degeneracy both in the superconducting sector and in the Majorana sectors, is also added for reference. When the leads are weakly coupled to the superconducting island and is as large as $0.1D$, we can observe a RG flow to the NFL fixed point with $S_{\mathrm{imp}} = \ln\sqrt{3}$. As the coupling becomes stronger, the Kondo scale becomes larger until eventually it starts decreasing – in the same sense that the spin model studied in the previous chapters does. In this strong-coupling regime, the RG flow is the universal flow from the WC fixed point to the NFL fixed point that is found in the spin model.

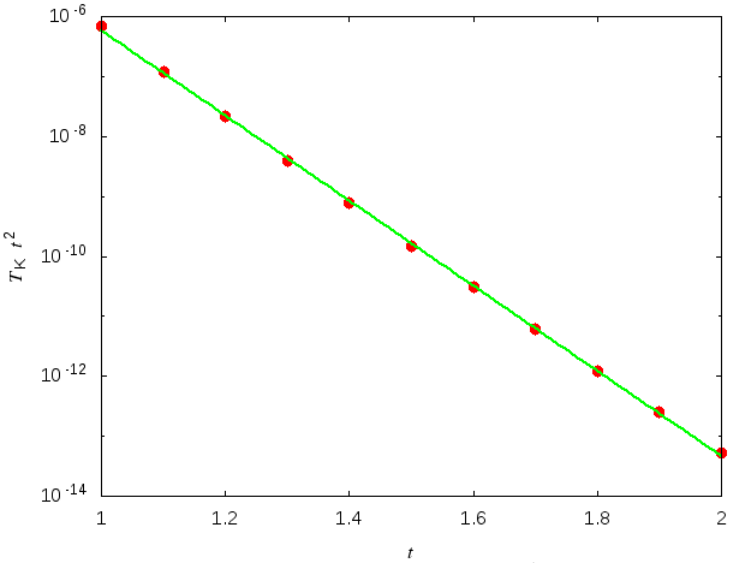

Figure 5.9: The linear relationship between $\ln T_{\rm K}\, t^2$ and t (red circles), where $T_{\rm K}$ is the Kondo temperature and t is the coupling constant between the Majorana and the leads, in the large-t regime $t/D \in [1, 2]$. The fact that this relationship is linear confirms the equation (5.2.28) (green line)), that indeed $T_{\rm K} \sim \frac{1}{t^2} {\rm e}^{-a_2 t}$.

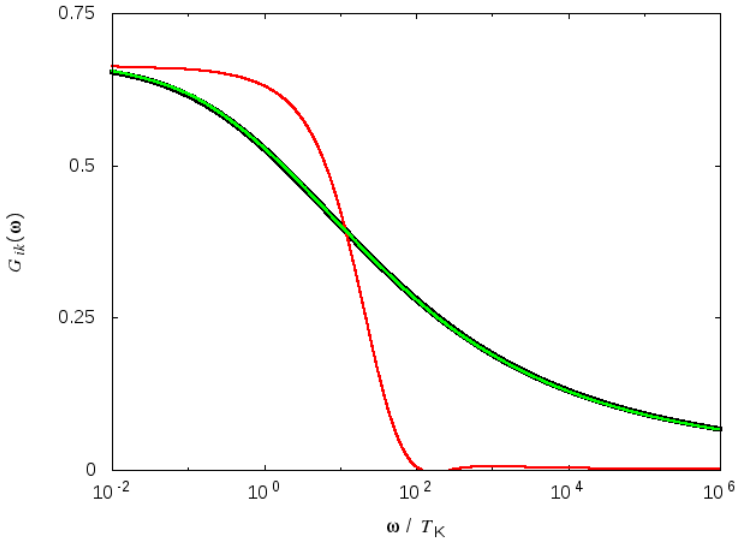

Figure 5.10: The frequency dependence of the zero-temperature non-diagonal linear conductance of the Majorana device both in the small-t regime (red line) and the large-t regime (green line). The results from the isotropic spin model (red line of Figure 3.4) is also shown here (black line) for reference. Clearly, the RG flow of the model in the strong-coupling regime is exactly the same as that of the effective spin model studied previously in Chapter 3.

respectively. The energy of the ground states is

$$\varepsilon_0 = -\frac{1}{2}(\sqrt{5}+1)\,t, \tag{5.2.21}$$

whilst the energy of the first excited states is

$$\varepsilon_1 = -\sqrt{2}\,t, \tag{5.2.22}$$

both of which are clearly directly proportional to t. At low enough temperature, all high-energy states are thermally inaccessible and the model can then be viewed as an effective doubly degenerate degree of freedom together with H_{leads}. It turns out to be convenient to use the discretised form of the lead Hamiltonian, which is given as a part of equation(2.5.61). Since t_n as is given by the equation (2.5.65) decays exponentially in the discretisation parameter Λ, we consider only the first term $n = 0$ and ignore the rest; therefore,

$$H_1 = \sum_i s\left(c_{0i}^\dagger c_{1i} + c_{1i}^\dagger c_0\right), \tag{5.2.23}$$

where s is the coupling constant in the semi-infinite chain, given by equation(2.5.64). Taking the basis states to be the direct product of the two-level system $\{\,\chi_i\,\}$ and the orbitals of the three lead electrons at the site $n = 1$, the non-diagonal part of the effective Hamiltonian is found to be

$$\begin{aligned} H_{\text{eff}}^{\text{xD}} = -\frac{s^2 p}{\Delta E}\Big\{ &|\chi_1;001\rangle\langle\chi_2;010| + |\chi_1;101\rangle\langle\chi_2;110| \\ &- |\chi_1;100\rangle\langle\chi_2;001| + |\chi_1;110\rangle\langle\chi_2;011|\Big\} + \text{adj.}, \end{aligned} \tag{5.2.24}$$

where p is a constant and $\Delta E = \varepsilon_1 - \varepsilon_0$ is the energy difference between the ground state and the first excited state. We note that the lead sector of the matrix elements on the first line can be represented by the operator $c_{13}^\dagger c_{12}$ since they both remove an electron from the third lead and create one on the second lead, and $c_{11}^\dagger c_{13}$ for the matrix elements on the second line. Furthermore, since the $\{\,\chi_i\,\}$ sector is a two-level system, we can define a lowering operator $S^- = |\chi_1\rangle\langle\chi_2|$. Hence, we rewrite the effective Hamiltonian as

$$H_{\text{eff}}^{\text{xD}} = -\frac{s^2 p}{\Delta E}\left\{S^-(c_{13}^\dagger c_{12} - c_{11}^\dagger c_{13}) + S^+(c_{12}^\dagger c_{13} - c_{13}^\dagger c_{11})\right\}. \tag{5.2.25}$$

Performing one last canonical transformation $c_{11} \to -c_{11}$, and recognising that the lead-sector operators in the left bracket is the spin-1 raising operator

$$L^+ = \sqrt{2}\begin{pmatrix} 0 & 1 & 0 \\ 0 & 0 & 1 \\ 0 & 0 & 0 \end{pmatrix} = \sqrt{2}\left(\psi_\uparrow^\dagger \psi_0 + \psi_0^\dagger \psi_\downarrow\right), \tag{5.2.26}$$

we conclude that the effective Hamiltonian is a spin flipping Hamiltonian

$$H_{\text{eff}}^{\text{xD}} = -\frac{s^2 p}{\sqrt{2}\Delta E}\left(S^- L^+ + S^+ L^-\right). \tag{5.2.27}$$

Since the difference in energy $\Delta E \sim t$, the effective coupling constant $J = \frac{s^2 p}{\sqrt{2}\Delta E} \sim \frac{1}{t}$ and we expect the Kondo temperature of this large-t regime to depend on the coupling strength t as

$$T_{\text{K}} \;\sim\; J^2 \mathrm{e}^{-a_1/J} \;\sim\; \frac{1}{t^2}\mathrm{e}^{-a_2 t}. \tag{5.2.28}$$

We extracted the Kondo temperature from NRG results and show that the relationship between $\ln T_{\text{K}}\, t^2$ and t is linear (Figure 5.9), confirming precisely the equation above.

Furthermore, we have also calculated the zero-temperature linear conductance tensor of this degenerate system (Figure 5.10). Clearly, in the large-t regime, the RG flow is exactly that of the spin model and therefore support the interpretation of the model as a spin coupling model that arises from the effective two-level system that is coupled to the three conduction leads above when we study the impurity entropy.

The small-t regime, which corresponds to the impurity entropy flowing from $\ln 4$ at high temperature to $\ln\sqrt{3}$ at low temperature, however, is different and can be experimentally distinguished from that in the strong-coupling regime by the measurement of the conductance.

5.2.4 Lifting the Constraints

Consider now the one-orbital system in general. We have seen so far that in one extreme where the leads are decoupled $t = 0$, there is a RG flow from the free-orbital regime with $S_{\text{imp}} = \ln 4$ towards occupied superconductor state with

$S_{\text{imp}} = \ln 2$, where the degeneracy comes from the Majorana sector, at the energy scale $T \sim |\varepsilon|$ due to the presence of the energy gap (Section 5.2.1). In the other extreme where the ground states are degenerate $\varepsilon = 0$, the coupling between the leads and the Majoranas t_i generates the RG flow towards the NFL regime, $S_{\text{imp}} \to \ln\sqrt{3}$, which can be from the free-orbital regime (Section 5.2.3) or the regime where the superconductor is occupied (Section 5.2.2). In general, therefore, we see a combination of the two types of behaviour.

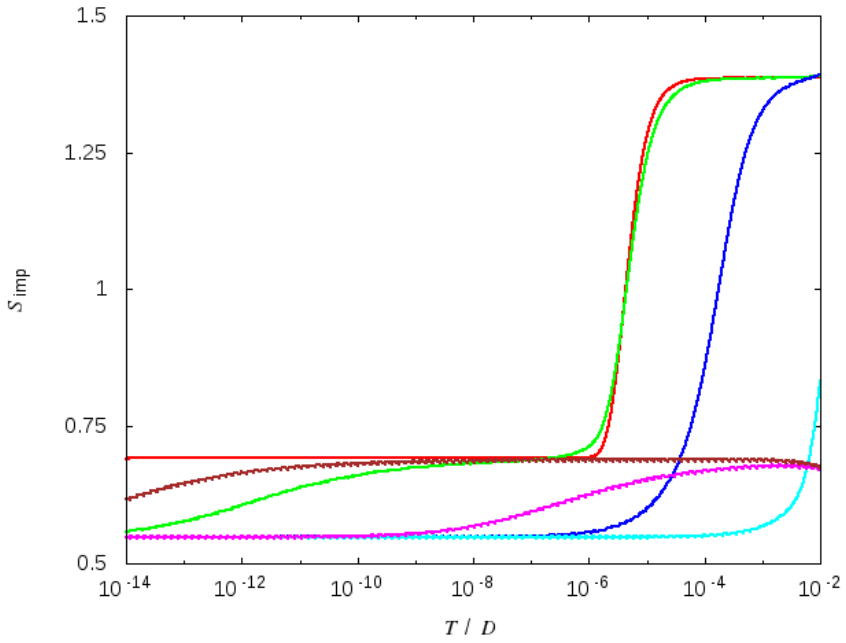

Figure 5.11: Impurity Entropy of the Majorana device as a function of temperature in the case where the energy gap is small: $\varepsilon/D = 10^{-5}$. The coupling constant $t/D = 0.1$ (red), 0.2 (green), 0.3 (blue), 0.5 (cyan), 1 (magenta) and 2 (brown). When t is small (e.g., $t/D = 0.1$), the system behaves as if the lead electrons are decoupled from the Majoranas (red circles of Figure 5.2). When t is very large, i.e., $t/D \geq 0.3$, the system behaves as if the states on the superconductor are degenerate (Figure 5.8). In the intermediate-t range, we observe both the RG flow from free-orbital regime to occupied-superconductor free-Majorana regime, and the subsequent flow to the NFL regime.

Let us consider first the case where the energy gap is very small, $|\varepsilon|/D = 10^{-5}$. Figure 5.11 shows the temperature dependence of the impurity entropy of this

system. When the coupling is very small, the impurity entropy is identical that of the decoupled system down to the lowest temperature scale (Figure 5.2). When the coupling constant t is moderately large ($0.3 \leq t/D \leq 0.5$), the system behaves in the same way the degenerate system does (Figure 5.8): the impurity entropy flows directly from $\ln 4$ to $\ln \sqrt{3}$ and the Kondo scale increases as the parameter t is increased; once t is much larger, the impurity entropy if found to be $\ln 2$ even at high temperature and flows towards the NFL value of $\ln \sqrt{3}$.

It is the intermediate-coupling regime that we observe both types of RG flows. In order to study the behaviour of this model without having to calculate its properties at a temperature range that is unreasonably low, we increase the coupling to $|\varepsilon|/D = 10^{-2}$, which is larger, but is still small compared to the parameter t, so that the initial RG flow to $S_{\text{imp}} = \ln 2$ occurs at higher temperature. We then calculate the impurity entropy (Figure 5.12, left panel), Kondo temperature, and its conductance (Figure 5.12, right panel), where we have found that both the impurity entropy and the zero-temperature conductance tensor of the model in this regime are exactly the same as that of the spin model – the two curves superpose exactly onto the results of the spin model – and also that $T_{\text{K}} \sim J^2 \, \mathrm{e}^{-a_3/J} \sim t^4 \, \mathrm{e}^{-a_4/t^2}$, despite the fact that here the energy gap $|\varepsilon|/D = 10^{-2}$ is not large at all compared to the coupling constant $t/D \sim 0.3$. Hence, the topological Kondo effect can still be observed even when the energy gap of the system is not large provided that the coupling between the superconducting island and the electron leads is sufficiently large.

We therefore conclude that in this one-orbital system, there are three types of RG flows: the flow from the free-orbital regime, characterised by $S_{\text{imp}} = \ln 4$, to the regime where the superconducting orbital is occupied and the Majorana degree of freedom is doubly degenerate with $S_{\text{imp}} = \ln 2$; the flow from either this latter regime or the regime where t is so strong that a doubly degenerate degree of freedom is formed from the superconducting orbital, the Majoranas, and the conduction electrons at the first site towards the NFL fixed point; and the direct flow from the free-orbital regime towards the NFL fixed point.

The first type of flow is controlled by the size of the energy gap parameter ε and occurs at the energy scale of $T \sim \varepsilon$. The second type of flow occurs from a doubly degenerate system when the coupling between the leads and the

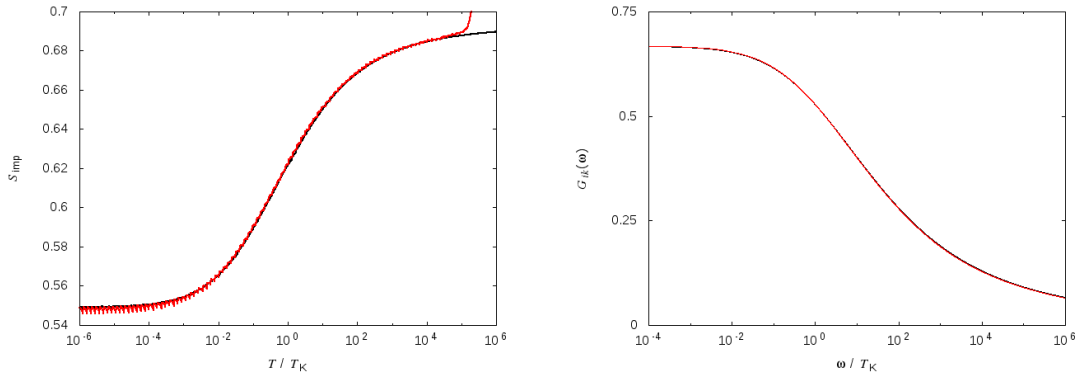

Figure 5.12: The physical properties for the Majorana device with a single superconductor orbital with the energy gap $|\varepsilon|/D = 0.01$ (red lines) in comparison with those of the spin model (black lines). (left) The impurity entropy S_{imp} showing the RG flow from $\ln 2$ to $\ln\sqrt{3}$. At very high temperature, we can observe the tail of the initial RG flow from $S_{\text{imp}} = \ln 4$. (right) The zero-temperature non-diagonal conductance tensor G_{ik} showing the corresponding RG flow.

Majoranas is strong enough; this is where the behaviour of the system is the same, regardless of whether the actual energy gap is large enough relative to the coupling constant, as the effective spin model studied in Chapter 3, which assumes a large energy gap. Finally, the third type of the flow occurs in the case of weak coupling and small- or no-gap system and is a direct crossover from the free-orbital regime to the NFL regime.

5.3 Three Charge States

We now proceed to consider the case in which in addition to the states N and $N+1$ being energetically accessible as is studied in the previous section, we also include the charge state $N+2$ as is shown in the left panel of Figure 5.13. As in the previous section, we choose the $N+1$ charge state to be the ground state. There are now two energy gaps and we call the energy difference from the ground state energy of the N charge state $|\varepsilon|$ and that of the $N+2$ charge state $|\varepsilon'|$, with $\varepsilon < 0$ as before. The energy difference between these two energy gaps are defined as $\Delta\varepsilon$.

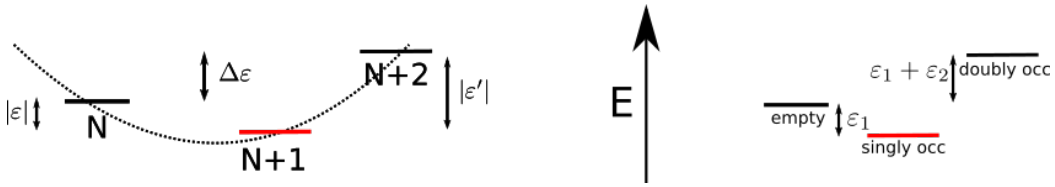

Figure 5.13: (left) Energy spectrum of a superconductor with three energetically accessible charge states. The energy difference from the ground state energy of the N charge state is labelled as $|\varepsilon|$ and that of the $N+2$ charge state as $|\varepsilon'|$. The energy difference between the two energy gaps is defined as $\Delta\varepsilon = |\varepsilon'| - |\varepsilon|$. (right) Energy spectrum of the two-orbital model. In comparison to the physical model, $\varepsilon_1 \coloneqq \varepsilon$, and the energy difference between the empty and the double occupied states is $\varepsilon_1 + \varepsilon_2 \coloneqq \Delta\varepsilon$.

This three-state system can be modelled as a system composed of two orbitals with the Hamiltonian

$$H_{\mathrm{SI}}^{\mathrm{3CS}} = \varepsilon_1 \, n_1 + \varepsilon_2 \, n_2, \tag{5.3.1}$$

where $n_i = d_i^\dagger d_i$ are the number operators for the orbital i and ε_i its energy. There are then a total of four states in the Hilbert space of the superconducting sector: empty, singly occupied (on orbital 1 or 2), and doubly occupied. Since we want only one singly occupied state, we choose to project the singly occupied state in which the electron occupies the second orbital n_2 away by adding an energy penalty to it, $E_{\mathrm{SO}}^{\mathrm{fic}} = x(1-n_1)n_2$. Its energy spectrum is shown in the right panel of Figure 5.13. From the Hamiltonian, the energy of the empty state is clearly zero. The energy of the singly occupied state is $\varepsilon_1 \coloneqq \varepsilon$ in the physical device. Finally, the energy difference between the empty and the double occupied state is $\varepsilon_1 + \varepsilon_2 \coloneqq \Delta\varepsilon$. For the rest of the section, we choose to discuss the results in terms of the original physical parameters ε and ε'. Furthermore, since each of these states must also be associated to a Majorana configuration with a correct parity, we remove the incorrect states by also adding an energy penalty in the form analogous to equation (5.2.4):

$$\begin{aligned} H^{\mathrm{fic}} = x \Big\{ &[(1-n_1)(1-n_2) + n_1 n_2]\,[n_{M1}(1-n_{M2}) + (1-n_{M1})n_{M2}] \\ &+ [n_1(1-n_2) + (1-n_1)n_2]\,[(1-n_{M1})(1-n_{M2}) + n_{M1}n_{M2}] \Big\}. \end{aligned} \tag{5.3.2}$$

5.3.1 Symmetric System

As can be seen in Figure 5.13, there are two free parameters: ε and ε'. We shall first investigate the system in which the ground state configuration is non-degenerate and we work in the symmetric limit, i.e., we set the two energy gaps to be equal, $\varepsilon = \varepsilon'$; hence, the two free parameters are now reduced down to one: the energy gap ε.

5.3.1.1 Decoupled Limit

As usual, we study the system in the decoupled limit where we can analytically solve the problem first. The impurity entropy of this system is found to be

$$S_{\text{imp}} = \ln 2 + \ln\left(2 + \mathrm{e}^{-\varepsilon/T}\right) + \frac{\varepsilon}{T}\frac{\mathrm{e}^{-\varepsilon/T}}{2 + \mathrm{e}^{-\varepsilon/T}}, \tag{5.3.3}$$

where as before, the $\ln 2$ term comes from the degeneracy in the Majorana sector. At high temperature, all three states on the superconductor are accessible, each of which is paired with two possible Majorana configurations, resulting in $S_{\text{imp}} = \ln 6$. At low temperature, both the empty and the doubly occupied states are no longer thermally accessible; hence, the configuration of the superconductor is fixed to singly occupied, is associated to the two odd Majorana configurations, and results in $S_{\text{imp}} = \ln 2$. As before, the crossover from the high-temperature regime to low-temperature regime occurs at $T \sim |\varepsilon|$

5.3.1.2 Large-Energy Gap Limit

We know from the study of the large-energy gap of the model with two charge states (Section 5.2.2) that the ground state of the superconductor is the (singly) occupied state and the second-order virtual transition to the empty state in this large-energy gap limit generates a spin model, equation (3.1.10), with the coupling constant $J \sim \frac{t^2}{\varepsilon}$ as is given in the equation (3.1.12). In this three-charge state system, the ground state is the same and the transition to the empty state should generate the spin model with the same coupling strength. However, in addition to the transition to the empty state, there is also a second-order virtual transition to the doubly occupied state, which should generate another spin model with

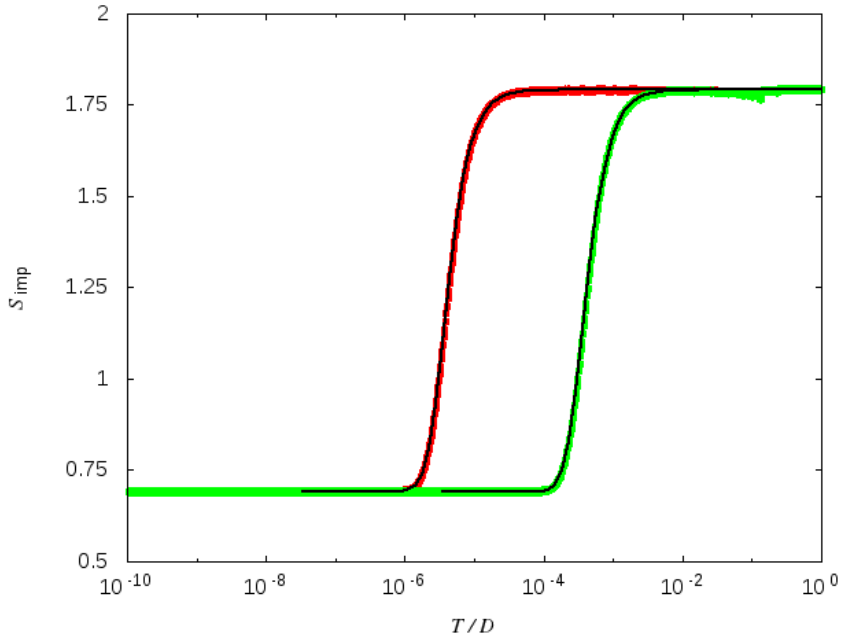

Figure 5.14: Temperature dependence of the Impurity entropy of the two-charge state Majorana device in the decoupled limit. The NRG results in the case of $-\varepsilon/D = 10^{-5}$ (red) and 10^{-3} (green) agree with the analytical results (black lines, equation (5.3.3)).

the same coupling $J \sim \frac{t^2}{\varepsilon}$. Since $H_{\mathrm{SI}}^{\mathrm{3CS}} = H_{\mathrm{SI}}^{\mathrm{2CS}} + \varepsilon_2\, n_2$, we expect the effective Hamiltonian to be $H_{\mathrm{eff}} = H_{\mathrm{K}} + H_{\mathrm{K}} = 2\,\frac{t^2}{\varepsilon} \sum_\alpha S_\alpha I_\alpha$. In order to easily compare the results with the two-charge state system, we shall study the model with the energy gap of $|\varepsilon|/D = 20$, exactly twice the size of the energy gap of the one-orbital system we studied before.

Figure 5.15 shows impurity entropy as a function of temperature of the three-charge state Majorana device in the large-energy gap limit, $|\varepsilon|/D = 20$, assuming as before isotropic coupling constants $t_1 = t_3$. In the small-t regime, the behaviour of the impurity entropy of the two-orbital system is qualitatively the same as that of the one-orbital system. The RG flow of this system can be effectively described by the spin model and goes from the free spin value of $\ln 2$ at high temperature to the NFL value of $\ln\sqrt{3}$ at low temperature. The curve obtained from this system is exactly the universal curve of the spin model (left panel of Figure 3.2). The left panel of Figure 5.16 also shows that the Kondo scale extracted from this

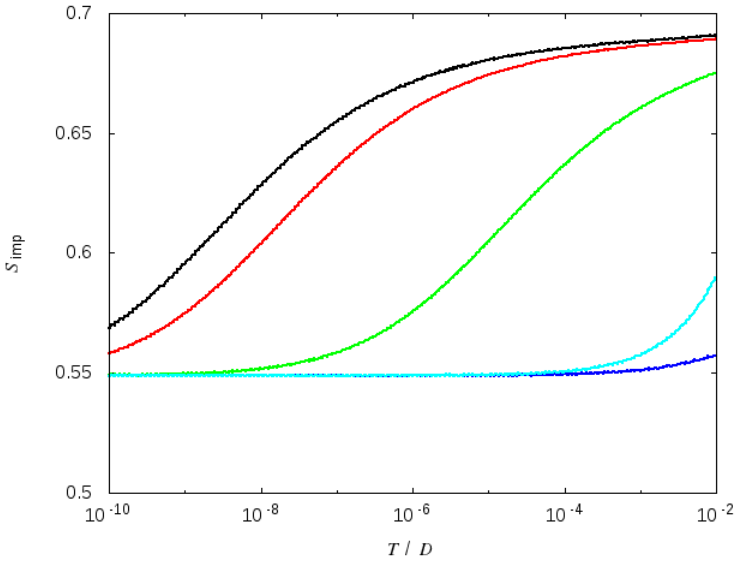

Figure 5.15: Temperature dependence of the Impurity entropy of the three-charge state Majorana device in the large-energy gap limit, $|\varepsilon|/D = 20$, with the coupling constants of 0.8 (red), 1 (green), 3 (blue), and 5 (cyan). The result of the two-charge state system with $|\varepsilon|/D = 10, t/D = 0.8$ is included for reference (black line). When the coupling is weak, the entropy flows from the free-spin value $S_{\text{imp}} = \ln 2$ at high temperature to the NFL value $S_{\text{imp}} = \ln\sqrt{3}$. Whilst these curves are exactly the same as the universal entropy curve of the spin model, the crossover scale does not occur exactly at the same temperature scale as that of the two-charge state system.

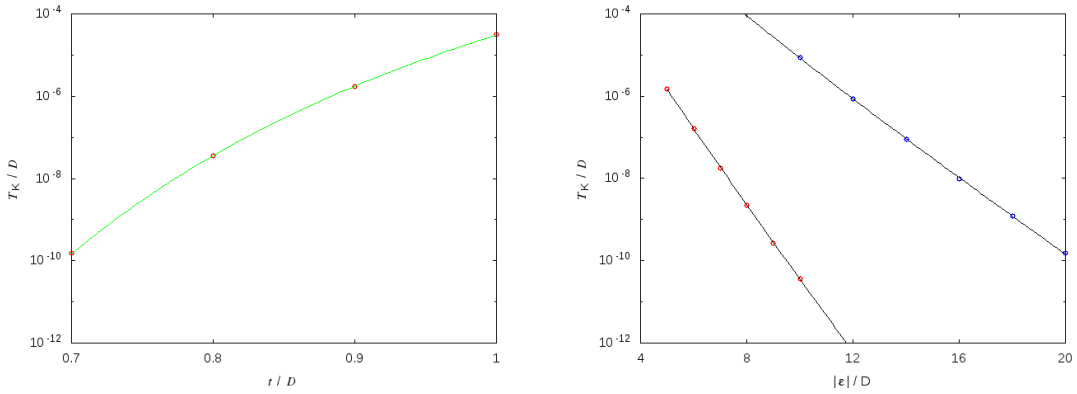

Figure 5.16: The dependence of the Kondo temperature T_{K}, in the large-energy gap and small-t limit of the three-charge state Majorana device on (left) the coupling constant t and (right) the energy gap $|\varepsilon|$. The results obtained here show the same dependence as in the case of the two-charge state device both on the coupling t (Figure 5.4, green line), $T_{\text{K}}/D \sim t^4\, \mathrm{e}^{-c_2/t^2}$, equation (5.2.7), and the gap ε (Figure 5.5), $T_{\text{K}}/D \sim \frac{1}{|\varepsilon|^2}\, \mathrm{e}^{-c_3|\varepsilon|}$, equation (5.2.8).

system does have the same dependence on the strength of the coupling constant t as that of the two-charge state system, equation (5.2.7).

Figure 5.15 also shows that the crossovers of the two systems at the same coupling strength and $\varepsilon^{3\mathrm{CS}} = 2\varepsilon^{3\mathrm{CS}}$ do not occur at the same exact temperature scale. In order to derive the effective spin coupling constant of $\frac{t^2}{\varepsilon}$, the assumption that the charging energy or the energy gap in this context is large is made (Section 3.1). It is possible that in this case the energy gaps $\varepsilon^{3\mathrm{CS}}/D = 20$ and $\varepsilon^{3\mathrm{CS}}/D = 10$ are not large enough for the relation between the two coupling constants, $J_{2\varepsilon}^{3\mathrm{CS}} = J_{\varepsilon}^{2\mathrm{CS}}$, hence the two Kondo scales, to be exact. We will come back to this when we study the dependence of the coupling constant on the energy gap.

We have also calculated the zero-temperature conductance tensor (Figure 5.17) and obtained the universal conductance curve of the spin model (red line of Figure 3.4) as expected, confirming the low-temperature effective behaviour of the spin model.

On the other hand, in the large-t regime, the behaviour of the three-charge state system is very different from that of the two-charge state system. It turns out that in this case, the duality behaviour – the mapping between $J \leftrightarrow \frac{1}{J}$ and – which is observed in both the spin model and the two-charge state model, is completely absent.

In addition to the dependence on the coupling constant t of the Kondo temperature, we have also studied its dependence on the energy gap. The right panel of Figure 5.16) shows indeed that the Kondo temperature has the same dependence on the energy gap ε as in the two-charge state system. In fact, it is the size of the energy gap that explains the discrepancy between the one-orbital and two-orbital device in this limit. As mentioned above in order to determine that the effective low-energy Hamiltonian is a Kondo spin Hamiltonian with the coupling constant proportional to $\frac{t^2}{\varepsilon}$, we assume that the energy gap ε is large. Therefore, we determine the impurity entropy (hence the Kondo temperature) of the two systems in the large-energy gap limit when coupling is fixed at $t/D = 1$ (Figure 5.18), setting the energy gap of the three-charge state system to always be twice of that of the two-charge state system, i.e., $\varepsilon^{3\mathrm{CS}} = 2\varepsilon^{2\mathrm{CS}}$. It is clear that the crossover of the three-charge state system always occurs at a slightly higher temperature than that of the three-charge state system. Nevertheless, if we calculate

the Kondo temperature of the two systems, we found that the ratio between the Kondo temperatures, $T_{\mathrm{K}}^{3\mathrm{CS}}/T_{\mathrm{K}}^{2\mathrm{CS}}$ decreases as the energy gaps increases. Specifically, we found that the ratios take the values of 3.70, 3.33, 3.03, and 2.86 for the case where $\varepsilon^{3\mathrm{CS}}/D$ is varied from 20, 30, 40, and 50, respectively. Whilst it is not clear that this ratio will eventually approach 1, we see that the assumption that the effective coupling strength can be added, $J^{3\mathrm{CS}} = J^{2\mathrm{CS}} + J^{2\mathrm{CS}} = 2J^{2\mathrm{CS}}$, becomes more reliable for larger values of the energy gaps. Perhaps calculations of Kondo temperature at even larger energy gaps ($\varepsilon/D > 50$) will generate more convincing results. In any case, we will come back to this addition of coupling constant once again when we study the asymmetric system in the large-energy gap limit (Section 5.3.2.2).

5.3.1.3 Triply Degenerate Limit

Another limit in which we can perform some analytical study of the model and compare its results to those from NRG is the vanishing energy-gap limit, $\varepsilon = 0$, even though this limit is not physically realisable in the Majorana device being studied since this triply degenerate energy configuration can not be achieved by tuning the background charge q in Equation (2.3.3).

Figure 5.19 shows the temperature dependence of the impurity entropy where we can observe a few different types of RG flow. When the coupling t is very small ($t/D < 0.1$), the entropy flows from the high-temperature value of $\ln 6$ to $\ln 2$ at low temperature. At high temperature, all the three occupation states of the superconductor, each associated with two Majorana configurations, are thermally accessible, resulting in the impurity entropy of $\ln 6$. At low temperature, since the coupling is very small, the flow to the NFL fixed point is not observed; however, there is still a flow to $S_{\mathrm{imp}} = \ln 2$. As in the case for the simple 2-site tight-binding model, the fact that the ground state at low temperature is the positive linear combination of the two sites reflects the fact that the energy of the system is minimised when electrons are allowed to spread over them, in this case, the low-temperature configuration of the superconductor is a particular linear combination of the three occupation states; the residual impurity entropy of $\ln 2$ is a result of the usual degeneracy in the Majorana sector. We observe here as

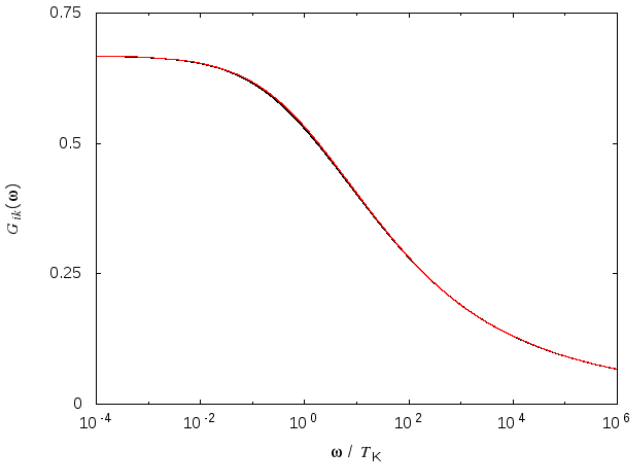

Figure 5.17: Frequency dependence of the zero-temperature conductance of the three-charge state Majorana device in the large-energy gap limit, $|\varepsilon|/D = 20$ and small coupling t (red line) which superposes directly onto the universal conductance curve of the isotropic spin model (black line here; red line of Figure 3.4)

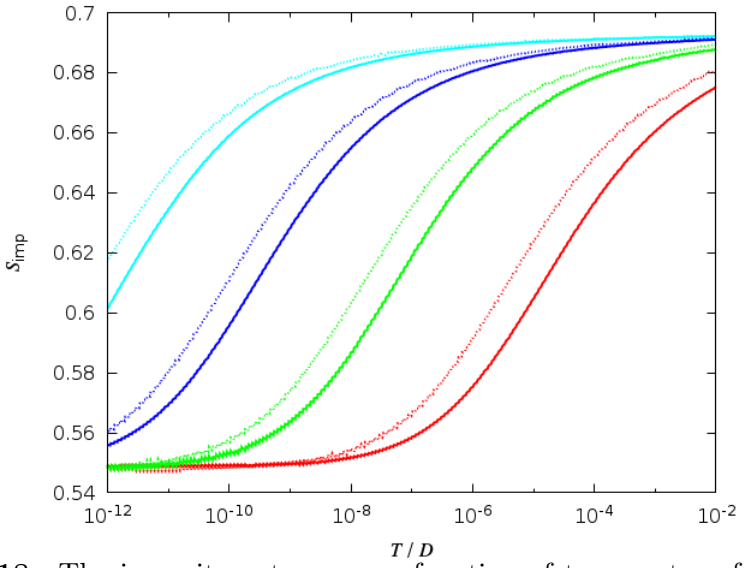

Figure 5.18: The impurity entropy as a function of temperature for the three-charge state Majorana device (solid line) in comparison to that of the two-charge state device (dotted line). The coupling constant is kept fixed at $t/D = 1$ whilst the energy gap of the the three-charge state system is $\varepsilon^{3CS}/D = 20, 30, 40, 50$ (red, green, blue, and cyan solid lines) and that of the two-charge state is $\varepsilon^{2CS}/D = 10, 15, 20, 25$ (red, green, blue, and cyan dotted lines); the energy gap of the three-charge state system is always twice that of the two-charge state, $\varepsilon^{3CS} = 2\varepsilon^{2CS}$. All the dotted lines can be superimposed on the solid lines if they are scaled by the factor of 3.70, 3.33, 3.03, and 2.86 for $\varepsilon^{2CS}/D = 10, 15, 20,$ and 25, respectively.

well that the flow occurs at the temperature scale $T^*/D \sim (t/D)^2$: for instance, by increasing the coupling constant t/D from 10^{-4} (red line of Figure 5.19) by a factor of 10^2 to 10^{-2} (green line), the Kondo temperature increases by a factor of 10^4 from $T_\mathrm{K}/D \sim 10^{-9}$ to 10^{-5}.

When the coupling becomes sufficiently strong ($t/D \sim 0.2$), we observe a further flow from $\ln 2$ to the NFL value $\ln\sqrt{3}$. Given these two limiting values of the impurity entropy, we suspect that this is the usual topological Kondo effect that can be described by the spin model studied previously. We thus compared the entropy curve to that of the spin model and found that indeed the RG flow in this regime is the universal RG flow characteristic of the topological Kondo effect (the left panel of Figure 3.2). Furthermore, we have also confirmed the usual Kondo temperature dependence on the coupling, $T_\mathrm{K}/D \sim t^4\,\mathrm{e}^{-c/t^2}$, thus concluding that we observe the topological Kondo effect in the intermediate-t regime of the triply degenerate limit of the three-charge state Majorana device.

Nevertheless, as is mentioned before, this three-charge state system differs from the two-charge state system in that the duality-like behaviour is no longer observed here and increasing the coupling does not further decreases the Kondo temperature. In order to understand this behaviour, we performed the derivation of an effective Hamiltonian for large t coupling as we did for the two-charge state system (Section 5.2.3). Take $H_0 \coloneqq H_\mathrm{t}$, equation (5.1.8), we exactly diagonalise it and found that the ground states are

$$
\begin{aligned}
|\chi_1\rangle &= |0;00;111\rangle - \alpha\,|1;10;011\rangle + \beta\,|1;01;110\rangle + \gamma\,|2;00;001\rangle + |2;11;010\rangle\,,\\
|\chi_2\rangle &= |0;11;111\rangle + \alpha\,|1;01;101\rangle - \beta\,|1;10;110\rangle - \gamma\,|2;11;001\rangle + |2;00;100\rangle\,,\\
|\chi_3\rangle &= |2;00;000\rangle + \alpha\,|1;10;010\rangle - \beta\,|1;01;001\rangle + \gamma\,|0;00;110\rangle + |0;11;011\rangle\,,\\
|\chi_4\rangle &= |2;11;000\rangle + \alpha\,|1;01;100\rangle + \beta\,|1;10;001\rangle - \gamma\,|0;11;110\rangle - |0;00;101\rangle\,,
\end{aligned}
$$

where $\alpha = \theta^3 - 4\theta$, $\beta = \theta^3 - 5\theta$, $\gamma = \theta^2 - 4$, $\theta = \sqrt{\frac{1}{2}(5+\sqrt{17})}$, and the eigenstates are written in terms of the occupation number of the superconducting sector, Majorana sector, and the lead sector, respectively. The energy of the ground states is $\varepsilon_0 = -t\theta$ whereas the lowest energy of the excited states is $\varepsilon_1 = -\sqrt{2}t$.

As before, we take the first term of the discretised H_leads to be the perturbation H_1 as is given in the equation (5.2.23) and found that the non-diagonal part of

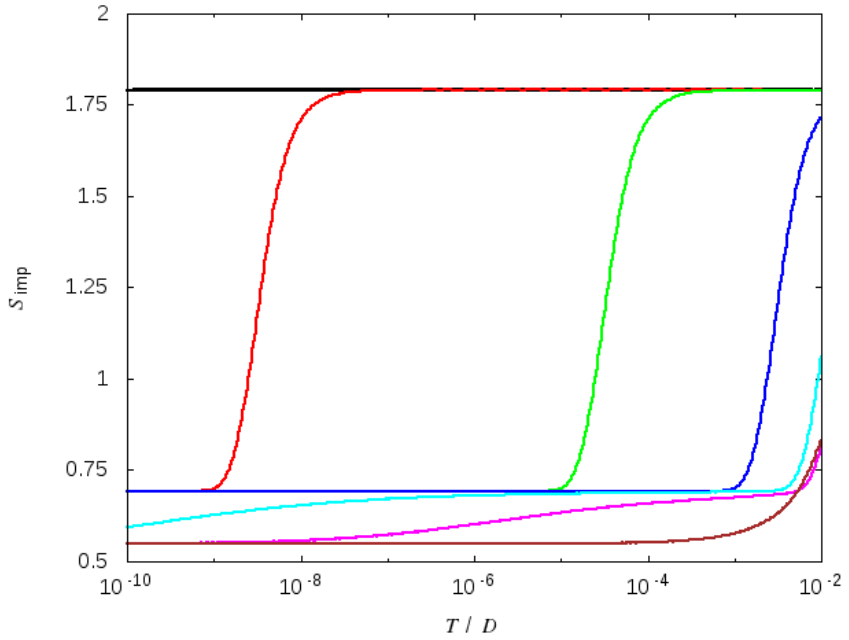

Figure 5.19: Temperature dependence of the impurity entropy of the three-charge state Majorana device in the zero-energy gap limit, where the ground-state configuration of the superconductor is triply degenerate. The coupling constants t/D are 10^{-4} (red), 0.01 (green), 0.1 (blue), 0.2 (cyan), 0.25 (magenta), and 0.5 (brown). There are three RG flow pattern observed here: the first one, when t is very small, is from the high-temperature $\ln 6$ as a result of the triply generate superconductor configuration and doubly generate Majorana configuration to the low-temperature $\ln 2$ where the superconductor sector configuration is fixed to a linear combination of the three occupation states and the residual entropy is a result of the Majorana; the second one, in the intermediate-t range, in addition to the first type of flow, the RG flows further to the low-temperature NFL $\ln\sqrt{3}$; the last type is a flow directly from $\ln 6$ to $\ln\sqrt{3}$ and occurs for very large t. In this case, increasing t does not further decrease the Kondo temperature.

the effective Hamiltonian is

$$\begin{aligned} H_{\text{eff}}^{\text{xD}} = -\frac{s^2 q}{\Delta E}\Big\{ & |\chi_1;001\rangle\langle\chi_2;010| + |\chi_1;101\rangle\langle\chi_2;110| \\ & - |\chi_1;100\rangle\langle\chi_2;001| + |\chi_1;110\rangle\langle\chi_2;011| \\ & + |\chi_3;001\rangle\langle\chi_4;010| + |\chi_3;101\rangle\langle\chi_4;110| \\ & - |\chi_3;100\rangle\langle\chi_4;001| + |\chi_3;110\rangle\langle\chi_4;011| \Big\} + \text{adj.}, \end{aligned} \tag{5.3.4}$$

where q is a constant and $\Delta E = \varepsilon_1 - \varepsilon_0 \sim t$. By defining a set of lowering operators, $S_1^- = |\chi_1\rangle\langle\chi_2|$ and $S_2^- = |\chi_3\rangle\langle\chi_4|$, recognising as before that the lead sector of the matrix elements above can be represented by the operators $c_{13}^\dagger c_{12}$ and $-c_{11}^\dagger c_{13}$, and replacing them by the spin-1 raising/lowering operators, e.g., $L^+ = \sqrt{2}\left(c_{11}^\dagger c_{13} + c_{13}^\dagger c_{12}\right)$, we obtain the effective Hamiltonian

$$H_{\text{eff}}^{\text{xD}} = -\frac{s^2 q}{\sqrt{2}\Delta E}\sum_i \left(S_i^- L^+ + S_i^+ L^-\right), \tag{5.3.5}$$

which is a spin Hamiltonian coupling two spin-$\frac{1}{2}$ impurities with spin-1 conduction electrons. Since this is different from the single impurity spin model, the bosonisation argument does not apply, we do not have such a small-J–large-J mapping, and the duality behaviour is not observed.

Note also another significant difference between the degenerate two-charge state (Figure 5.8) and three-charge state (Figure 5.19) systems. In the former, with the ground state coupled to only one excited state, the high-temperature charge-fluctuation character of the ground state with $S_{\text{imp}} = \ln 4$ is somewhat more stable: the coupling is required to be almost as strong as $t/D \sim 1$ before we could observe that $S_{\text{imp}} = \ln 2$ at high temperature. Hence, the topological Kondo effect is not observed in the small-t regime and can only observed at large-t ($t/D > 1$). In the three-charge state system with the ground state coupled to both of the excited states, however, the charge-fluctuation character disappears relatively easier – $S_{\text{imp}} \to \ln 2$ is observed at $T \sim 10^{-9}$ when the coupling $t/D \sim 10^{-4}$ – and topological Kondo effect can thus be observed at a much weaker coupling, $t/D \sim 0.1$. It appears therefore that the topological Kondo effect requires the degeneracy in the Majorana sector (each parity has two configurations), that the degeneracy in the superconducting sector be lifted (so that $S_{\text{imp}} = \ln 2$), and

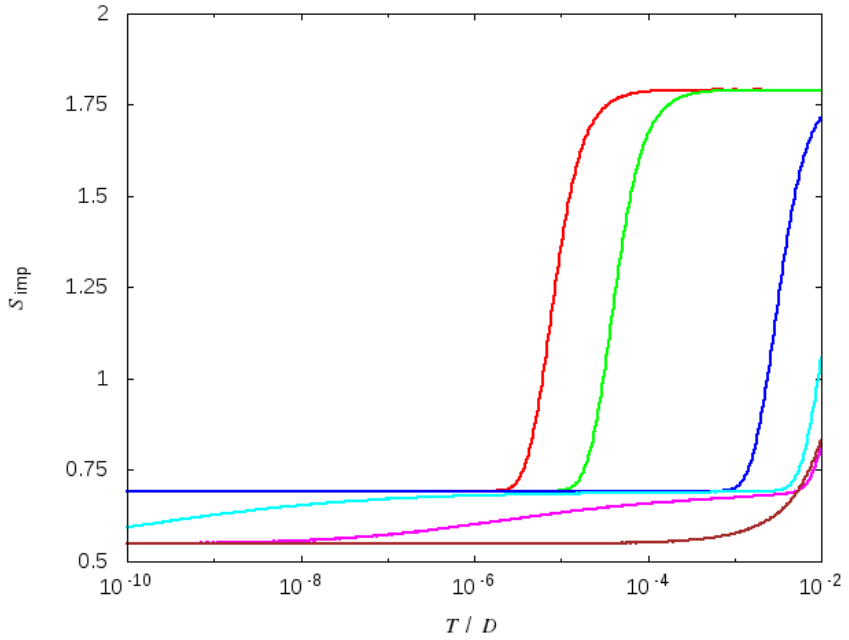

Figure 5.20: Temperature dependence of the impurity entropy of the three-charge state Majorana device when the energy gap is allowed to take a smaller value, here in particular, $|\varepsilon|/D = 2 \times 10^{-5}$. The coupling constants t/D are 10^{-4} (red), 0.01 (green), 0.1 (blue), 0.2 (cyan), 0.25 (magenta), and 0.5 (brown). Compared to the case of the degenerate three-charge state device (Figure 5.19), the only difference between the two systems is in the small-t region: whereas here the entropy quickly flows to $\ln 2$ due to the energy gap, the entropy of the degenerate system remains at $\ln 4$ until the coupling becomes sufficiently large. The physics of the strong coupled region remains the same.

a coupling between the superconductor and the spinless leads that is sufficiently strong that allows a transition to the excited state available in the superconductor sector.

5.3.1.4 Lifting the Constraints

We would like to close the study of the symmetric three-charge state model by lifting all the constraints previously imposed onto the model, in the same manner that we approached the two-charge state system. For instance, consider the case where the energy gap is non-zero but still small, say, $\varepsilon/D = 2 \times 10^{-5}$ (Figure

5.20). When the coupling is very small, the results are significantly different from those of the model in the degenerate limit (Figure 5.19). There, since the energy levels are degenerate, when t is not very large, the impurity entropy remains at $\ln 6$; once t is sufficiently large, there is a RG flow towards $\ln 2$ occuring at $T^*/D \sim (t/D)^2$. Here, however, due to the energy gap, the excited states become energetically inaccessible once $T < |\varepsilon|$ and the RG flow towards $\ln 2$ occurs right then. Therefore, the results of the model in general are different from the degenerate regime as long as $(t/D)^2 < |\varepsilon|/D$. If t is large enough that the flow towards $\ln 2$ occurs before $T \sim |\varepsilon|$, the energy gaps become irrelevant, and the system behaves in the same way the degenerate system does. As before, when $t/D \sim 0.1$, we can observe the NFL physics and its signature $S_{\text{imp}} \to \ln\sqrt{3}$.

Upon further increasing the size of the energy gap $|\varepsilon|$, the first RG flow ($S_{\text{imp}} = \ln 6 \to \ln 2$) occurs at a higher temperature scale, but at the same time, the Kondo scale slowly decreases and the second RG flow ($S_{\text{imp}} = \ln 2 \to \ln\sqrt{3}$) is observed at lower temperature. When the energy gap is sufficiently large, the Kondo temperature follow the relation (5.2.8), $T_{\text{K}}/D \sim \frac{1}{|\varepsilon|^2}\,\mathrm{e}^{-c_3|\varepsilon|}$, and the topological Kondo effect is observed in the same manner as in the degenerate limit.

We can therefore conclude that the symmetric three-charge state system share some similarities with the two-charge state system, but also has its own unique features. When the energy gap and the coupling are relatively small, there is a RG flow towards a "free spin-$\frac{1}{2}$" state ($S_{\text{imp}} \to \ln 2$) for both models, though given that the free orbital behaviour of the two models are different, the high-temperature impurity entropy take different values. The behaviour of the two models then become significantly different in the intermediate- and large-t regime. In the former, whilst the two-charge state system exhibits a direct RG flow from the free-orbital to the NFL regime, we observe in the three-charge state system a RG flow first from the free-orbital to the free spin-$\frac{1}{2}$ regime, then to the NFL regime which is the topological Kondo effect. In the latter, the $J \leftrightarrow \frac{1}{J}$ duality is observed only in the two-charge state system but not in the three-charge state system. Once the energy gap is large, nonetheless, both systems effectively behave as a Kondo spin and exhibits NFL physics at low-temperature, with the additional state only serves to increase the effective coupling in the three-charge state system,

with the same exception that the duality is observed only in the two-charge state system but not in the three-charge state system.

Next we shall lift the symmetry requirement that the two energy gaps ε and ε' be kept equal.

5.3.2 Asymmetric System

In order to be more realistic and to enable the model to describe the Majorana device for a general value of q/e, we now lift the symmetry constraint and allow the energies of the N and $N+2$ charge states – modelled by the empty and the doubly occupied states – to be different, i.e., we no longer enforce the condition $\varepsilon = \varepsilon'$. This exactly results in the energy spectrum as is shown in Figure 5.13. As before, we begin by considering the system in the decoupled limit first.

5.3.2.1 Decoupled Limit

Since we have already understood the effect of the first energy gap ε from the previous section, we shall arbitrarily fix it to be $-\varepsilon/D = 10^{-5}$. The reason why we pick the energy gap to be of this size is so that we can compare it to the symmetric case, where we observe the entropy flow from $\ln 6$ to $\ln 2$ at the temperature scale of $T/D \sim |\varepsilon|/D \sim 10^{-5}$ (Figure 5.14). Now we only have the second energy gap ε' to consider. We shall restrict ourselves only to the case where the energy of the doubly occupied state is greater than that of the empty state, i.e., $|\varepsilon| < |\varepsilon'|$. We will not consider the case where the energy of the doubly occupied state is lower than that of the singly occupied state either, for that is not physically realisable in the charging-energy Hamiltonian. Furthermore, instead of using the second energy gap $|\varepsilon'|$ as a free parameter, in this section, we shall directly parameterise the system by the energy difference between the two energy gaps, $\Delta\varepsilon = |\varepsilon'| - |\varepsilon| > 0$.

As is shown in Figure 5.13, the energy spectrum of the superconductor is that of a three-level system where the energy of the first level is set to zero, the second to $\varepsilon < 0$, and the third to $\Delta\varepsilon > 0$. The impurity of the whole system, including

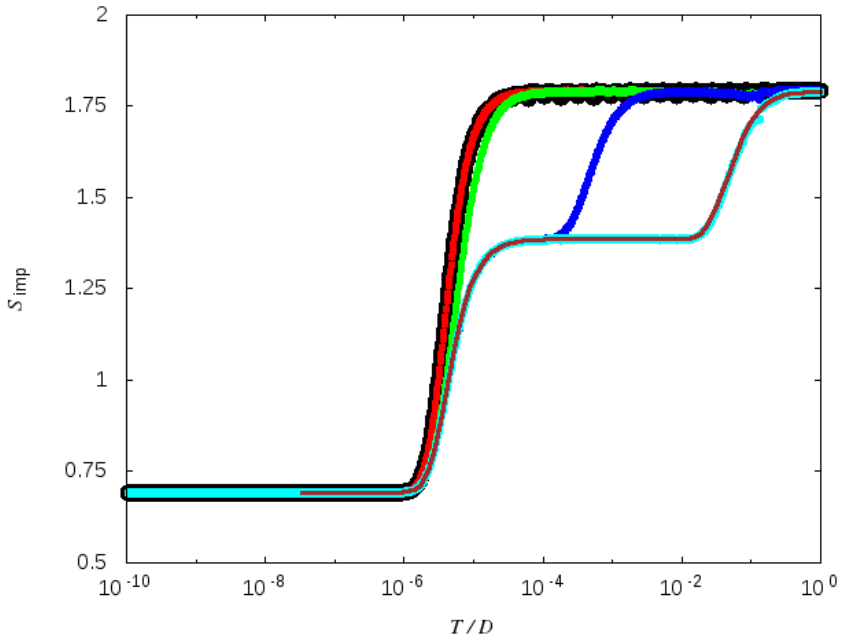

Figure 5.21: Temperature dependence of the impurity entropy of the asymmetric three-charge state Majorana device when the leads are decoupled, $t = 0$. The first energy gap is fixed $-\varepsilon/D = 10^{-5}$ and the second energy gap is parameterised as $|\varepsilon'| = |\varepsilon| + \Delta\varepsilon$, where $\Delta\varepsilon/D$ is varied from 10^{-7} (red), 10^{-5} (green), 10^{-3} (blue), to 10^{-1} (cyan). The impurity entropy of the symmetric system is added for reference (black dots, visually lying underneath the red dots). As expected, the NRG results agree with the analytical results, calculated from the equation (5.3.6), an example of which is shown on the figure (brown line for $\Delta\varepsilon/D = 10^{-1}$, visually lying on top of the cyan dots) as well. When the energy difference $\Delta\varepsilon$ is large enough, we could observe an additional RG flow of the entropy from $\ln 6$ to $\ln 4$ due to the fact that at the intermediate temperature scale, the only state being thermally inaccessible is the doubly occupied state. Eventually the entropy flows to the usual $\ln 2$.

the Majorana can then be calculated:

$$S_{\text{imp}} = \ln 2 + \ln\left(1 + \mathrm{e}^{-\varepsilon/T} + \mathrm{e}^{-\Delta\varepsilon/T}\right) + \frac{1}{T}\frac{\varepsilon \mathrm{e}^{-\varepsilon/T} + \Delta\varepsilon \mathrm{e}^{-\Delta\varepsilon/T}}{1 + \mathrm{e}^{-\varepsilon/T} + \mathrm{e}^{-\Delta\varepsilon/T}}, \tag{5.3.6}$$

which agrees very well with the results obtained from NRG calculations (Figure 5.21). The qualitative behaviour of the system is unaffected by the asymmetry if the energy difference $\Delta\varepsilon$ is much smaller than the first energy gap, i.e., $\Delta\varepsilon \ll |\varepsilon|$ (red line); in fact, even when the two energies are equal, the RG flow pattern remains essentially the same (green line). The entropy flows from $\ln 6$ – due to the fact that three charge states in the superconducting sector, each is associated with two Majorana states with the allowed parity, are energetically accessible – to the usual $\ln 2$ when the two energetically unfavourable states of the superconductor are projected out and the residual entropy is a result of the Majoranas. The flow occurs at the temperature scale of $T \sim |\varepsilon|$. However, once the energy difference is much greater than the first energy gap, $\Delta\varepsilon \gg |\varepsilon|$, an additional flow of the entropy from $\ln 6$ to $\ln 4$ is observed at $T \sim \Delta\varepsilon$. This is due to the fact that in the intermediate temperature range $|\varepsilon| < T < \Delta\varepsilon$, the temperature is large enough that the empty state is still thermally accessible but too small for the doubly occupied state to be accessible.

5.3.2.2 Large-Energy Gap Limit

Earlier in the symmetric case, we argue that due to the second-order virtual transitions, the model should behave like a spin model at low temperature in this limit (Section 5.3.1.2); we therefore expect the impurity entropy to be the non-Fermi liquid value of $\ln\sqrt{3}$. At high temperature, since the other two states on the superconductor are thermally inaccessible due to the large energy gaps, we expect the entropy to be $\ln 2$ due to the degeneracy of the Majoranas. This is indeed observed in the results calculated from NRG (left panel, Figure 5.22). Furthermore, we argued that the coupling strength of the effective spin model can be added $J^{3\text{CS}} = J^{2\text{CS}} + J'^{2\text{CS}}$. Since $J^{2\text{CS}} \sim \frac{t^2}{|\varepsilon|}$, whereas the effective coupling $J^{3\text{CS}} \sim 2\,\frac{t^2}{|\varepsilon|}$ in the symmetric case, it should be $\frac{t^2}{|\varepsilon|} + \frac{t^2}{|\varepsilon'|}$ in this asymmetric case. We put this hypothesis to test by analysing the Kondo temperature dependence on the two energy gaps.

In the limit where both energy gaps are large, the dependence of the Kondo temperature on the coupling constant follows the equation (3.2.9): $T_{\mathrm{K}} \sim J^2 \mathrm{e}^{-c/J}$. If it is the case that the effective coupling constant can be added, we expect the Kondo temperature of this asymmetric two-orbital model in the large-energy gap limit to be

$$T_{\mathrm{K}}/D \sim \left(\frac{1}{|\varepsilon|} + \frac{1}{|\varepsilon'|}\right)^2 \mathrm{e}^{-c/\left(\frac{1}{|\varepsilon|}+\frac{1}{|\varepsilon'|}\right)}. \tag{5.3.7}$$

We calculated the Kondo temperature of the three-charge state system when both of the energy gaps are large; we fix the first energy gap $|\varepsilon|/D = 50$ and the coupling constant $t/D = 1.2$, and vary the second energy gap $|\varepsilon'|/D \in [30, 90]$. We have found that indeed the Kondo temperature (calculated from NRG, shown as red dots in Figure 5.22) follows the equation (5.3.7) and thus confirming the hypothesis that the effective coupling can indeed be added.

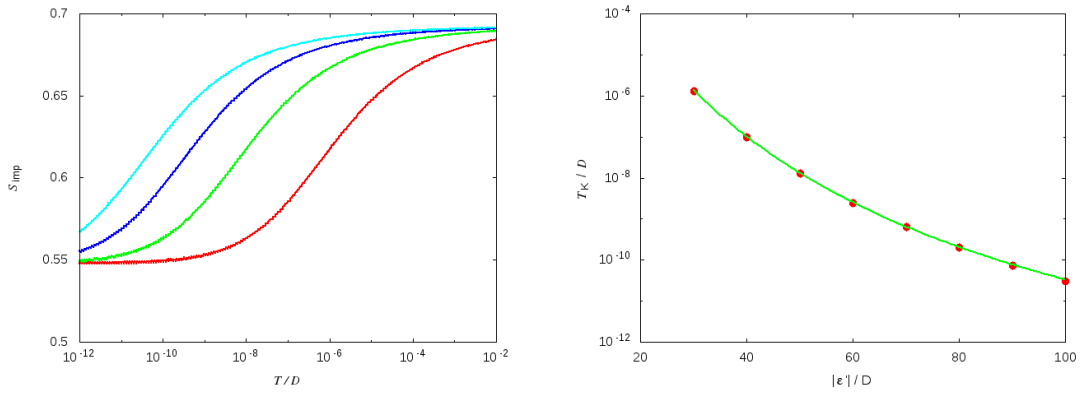

Figure 5.22: Thermodynamics of the asymmetric three-charge state Majorana device when both of the energy gaps are large, in particular, we fix the first energy gap to be $|\varepsilon|/D = 50$ and the coupling constant $t/D = 1.2$, whereas the second energy gap is varied: $|\varepsilon'|/D \in [30, 90]$. (left) The impurity entropy of the system as a function of temperature. Since the energy gaps are large, only the singly occupied state is thermally accessible even at high temperature and $S_{\mathrm{imp}} = \ln 2$. At low temperature, the model behaves like a spin model which shows NFL behaviour $S_{\mathrm{imp}} = \ln \sqrt{3}$. (right) The dependence of the Kondo temperature on the second energy gap $|\varepsilon'|$. The results from the NRG calculation (red dots) agree very well with the prediction from the equation (5.3.7) (green line).

5.3.2.3 Lifting the Constraints

We could now proceed to study the asymmetric three-charge state system where we impose no constraints on it. Recall the results of the study of the symmetric system with no constraints in Section 5.3.1.4. We found that in comparison to the generate system (Section 5.3.1.3), the system with no constraints behaves very similarly, the difference being only in the small-t regime where a RG flow towards $\ln 2$ at $T \sim |\varepsilon|$ occurs at $T \sim |\varepsilon|$ when $(t/D)^2 < |\varepsilon|/D$ due to the presence of the energy gaps. When the coupling t is large, the energy gaps become irrelevant, the RG flow towards $\ln 2$ is observed, and thus, the gapped and ungapped systems behave identically. Hence, in the presence of asymmetric gaps, we predict that once again, the asymmetric system should behave differently from the degenerate limit only when the coupling is small. If the coupling is large, the energy gaps are irrelevant to the problem and whether the gaps are symmetric or asymmetric should not affect the behaviour of the system.

We consider as an example a case where the first enery gap is set to $|\varepsilon|/D = 2 \times 10^{-5}$ so that it is equal to that of the symmetric system that we studied earlier (Section 5.3.1.4), and now set the second energy gap to $|\varepsilon'|/D = 10^{-8}$. Its impurity entropy as is shown in Figure 5.23 is indeed very similar to that of the symmetric model (Figure 5.20) and also the degenerate model (Figure 5.19). When the coupling is small, we observe an additional RG flow to $\ln 4$ of the impurity entropy at the temperature scale of $T \sim |\varepsilon|$; this is due to the presence of the second smaller energy gap, and the behaviour of this system is different from both the symmetric and the degenerate systems as expected. The RG may then flow to $\ln 2$ at lower $T \sim |\varepsilon'|$ when the empty state is no longer energetically accessible. When the coupling becomes stronger, the system is forced to flow to $\ln 2$ at a higher temperature scale and the flow may flow from $\ln 4$ if $|\varepsilon'|/D < (t/D)^2 < |\varepsilon|/D$, or may flow directly from $\ln 6$ if $(t/D)^2 > |\varepsilon|/D$. As mentioned before, if the coupling becomes very strong, it dominates the behaviour of the system; the energy gaps can effectively be neglected; the three-charge state systems, whether symmetric, asymmetric, or degenerate all behave in the same manner.

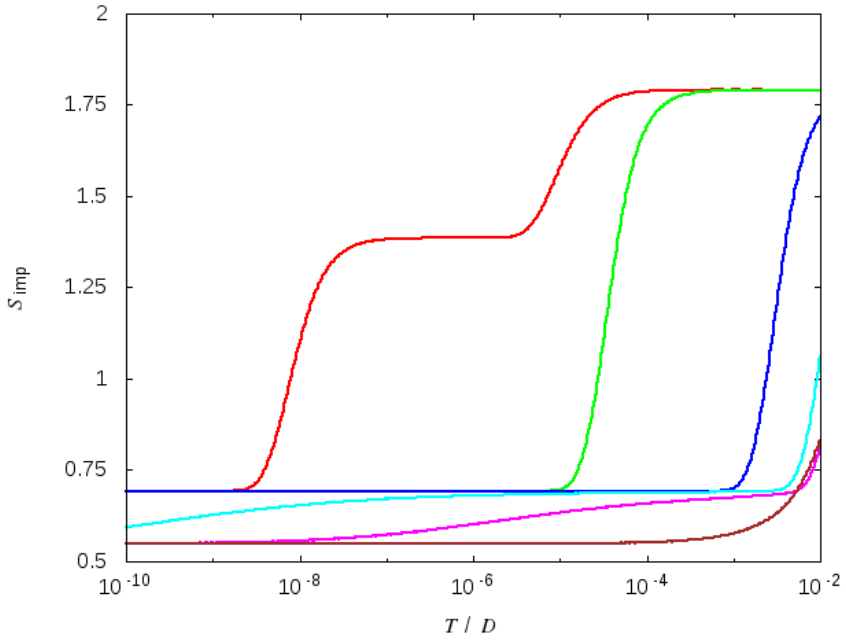

Figure 5.23: Temperature dependence of the impurity entropy of the asymmetric three-charge state Majorana device with the energy gap $|\varepsilon|/D = 2 \times 10^{-5}$. In this particular case, we choose the other smaller energy gap to be $|\varepsilon'|/D = 10^{-8}$. The coupling constants t/D are 10^{-4} (red), 0.01 (green), 0.1 (blue), 0.2 (cyan), 0.25 (magenta), and 0.5 (brown). Compared to the case of the symmetric three-charge state device (Figure 5.20), the only difference between the two systems is in the weak coupling region with $|\varepsilon'| < T < |\varepsilon|$, where there is an additional flow to $\ln 4$ due to the empty state becoming energetically inaccessible.

Now that we understand the behaviour of the three-charge state system, in the next section, we allow another charge state $N+3$ to be energetically accessible. In this way, it is possible to study a superconducting configuration where the ground states can be degenerate and virtual second-order transitions to first excited states are possible from both of the ground states.

5.4 Four Charge States

In the final section of the chapter, we consider the Majorana device in which the charge state $N+3$ is also energetically inaccessible – the energy spectrum is shown

in the left panel of Figure 5.24. The advantage of studying this superconductor configuration, compared to those that we have studied earlier, is that now it is possible to study the device in which there are now two states in the ground-state manifold ($N+1$ and $N+2$ charge states in the figure) and both of these states are allowed virtual second-order transitions to the first excited states (N and $N+3$ charge states), enabling us to fully capture the low-energy part of the energy spectrum of the Majorana device with charging energy (lower right panel of Figure 5.1). In particular, we can now model the situation where $N+1$ and $N+2$ charge states are degenerate but virtual excitations to N and $N+3$ charge states are included.

Before we write down the model Hamiltonian for this particular configuration of the superconducting island, we consider carefully the energy spectrum generated by the charging energy Hamiltonian, $H_{\mathrm{c}} = E_c \left(N - \frac{q}{e}\right)^2$. If the background charge is tuned to $q/e = N_0 + \frac{3}{2}$, we know that the ground states of the system are the $N+1$ and $N+2$ charge states, which are doubly degenerate. In order to parameterise the system away from this particular degenerate point, we define a parameter δ, i.e., $q/e = N_0 + \frac{3}{2} - \delta$ and $\delta \in [0, \frac{1}{2}]$. Since $H_{N+1} - H_N = 2E_{\mathrm{c}}(N - N_0 - 1 - \delta)$, if $\delta \neq 0$, the energy difference between the states in the ground-state manifold, i.e., the N_0+1 and N_0+2 charged states is

$$\Delta\varepsilon \coloneqq |H_{N_0+2} - H_{N_0+1}| = 2E_{\mathrm{c}}\,\delta. \tag{5.4.1}$$

Moreover, we can calculate the sizes of the energy gaps on both sides:

$$|\varepsilon| = 2E_{\mathrm{c}}(1+\delta), \tag{5.4.2}$$

$$|\varepsilon'| = 2E_{\mathrm{c}}(1-\delta). \tag{5.4.3}$$

This four-charge state system can be modelled as a system composed of three orbitals

$$H_{\mathrm{SI}}^{\mathrm{4CS}} = \varepsilon_1\, n_1 + \varepsilon_2\, n_3 + \varepsilon_3\, n_3, \tag{5.4.4}$$

where as before n_i are the number operators for the orbital i with energy ε_i. There are now eight possible configurations in the Hilbert space of the superconducting sector: empty, triply-degenerate singly occupied, triply-degenerate doubly occupied, and fully occupied. As before, we add energy penalty to the

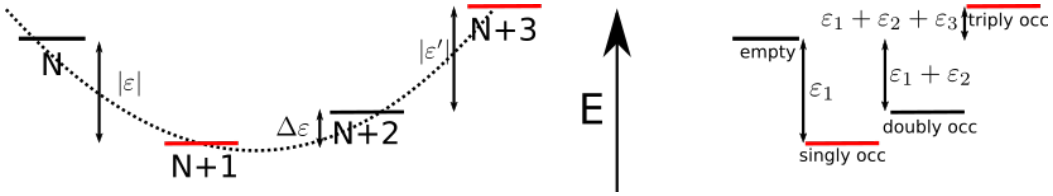

Figure 5.24: (left) Energy spectrum of a superconductor with four energetically accessible charge states. The energy difference between the two charge states in the ground-state manifold is $\Delta\varepsilon$. The sizes of the two energy gaps are labelled as $|\varepsilon|$ and $|\varepsilon'|$. (right) Energy spectrum of the three-orbital model. In comparison to the physical model, $\varepsilon_1 \coloneqq \varepsilon$, and the energy difference between the empty and the double occupied states is $\varepsilon_1 + \varepsilon_2 \coloneqq \Delta\varepsilon$.

pairs of states with the configurations of $(0,1,0),(0,0,1)$ and $(1,0,1),(0,1,1)$ to project out two of the three degenerate states so that we have a total of four non-degenerate occupation states remaining in the Hilbert space. Furthermore, we add the energy penalty to the states with incorrect Majorana configurations. Specifically, we add the following terms to the Hamiltonian

$$\begin{aligned} H^{\text{fic}} = x \Big\{ &[(1-n_1)(1-n_2)(1-n_3) + n_1 n_2 (1-n_3) + n_1 (1-n_2) n_3 + (1-n_1) n_2 n_3] \times \\ &[n_{M1}(1-n_{M2}) + (1-n_{M1}) n_{M2}] \\ + &[n_1(1-n_2)(1-n_3) + (1-n_1) n_2 (1-n_3) + (1-n_1)(1-n_2) n_3 + n_1 n_2 n_3] \times \\ &[(1-n_{M1})(1-n_{M2}) + n_{M1} n_{M2}] \Big\}. \end{aligned} \tag{5.4.5}$$

5.4.1 Symmetric System

To minimise the number of free parameters in the system, we begin by studying the symmetric system first, $\delta = 0$. This results in the energy difference $\Delta\varepsilon = 0$, rendering the $N+1$ and $N+2$ charge states to be degenerate. In addition, the sizes of the two energy gaps are equal $|\varepsilon| = |\varepsilon'|$. The energy spectrum of this system is the same as that portrayed in the lower right panel of Figure 5.1 (with a relabelling of the states).

5.4.1.1 Decoupled Limit

When the system is decoupled, the impurity entropy can be calculated:

$$S_{\text{imp}} = \ln 2 + \ln\left(2 + 2\,\mathrm{e}^{-\varepsilon/T}\right) + \frac{\varepsilon}{T}\frac{\mathrm{e}^{-\varepsilon/T}}{1+\mathrm{e}^{-\varepsilon/T}}, \tag{5.4.6}$$

and we can confirm that the results obtained from NRG agree with this formula (Figure 5.25). At high temperature, the impurity entropy takes the value of $\ln 8$ due to the four possible occupation states in the superconducting sector, each of which is associated with a doubly degeneracy in the Majorana sector. The entropy then flows to $\ln 4$ at low temperature since the empty and the triply occupied states are energetically unfavourable and are no longer thermodynamically accessible. The entropy crossover is observed at $T \sim |\varepsilon|$ as usual.

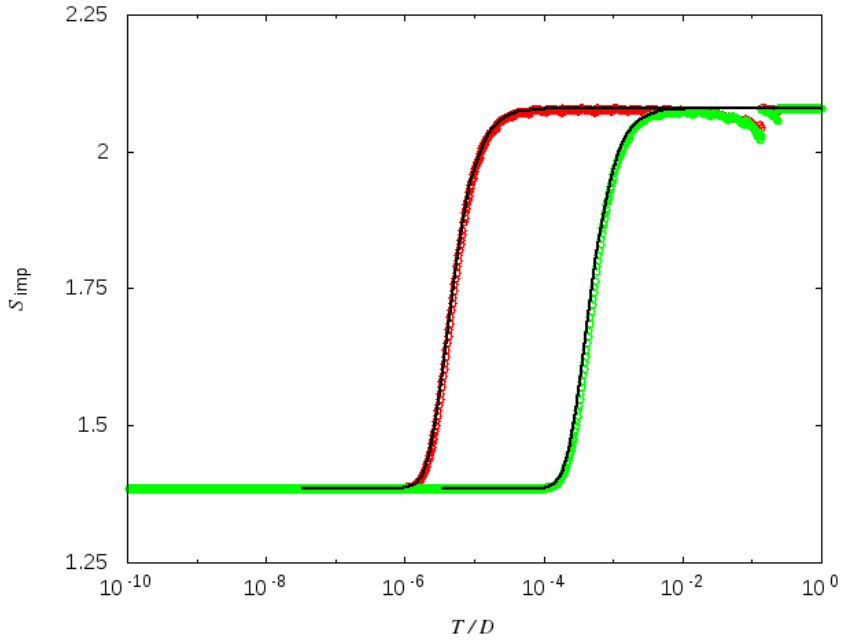

Figure 5.25: Temperature dependence of the Impurity entropy of the four-charge state Majorana device in the decoupled limit. The NRG results in the case of $-\varepsilon/D = 10^{-5}$ (red circles) and 10^{-3} (green circles) agree with the analytical results (black lines, equation (5.4.6)).

5.4.1.2 Large-Energy Gap Limit

We then proceed to the large-energy gap limit of the device, whose energy spectrum is similar to that of the three-charge state device (Section 5.3.1.2), except that the ground state in this case is doubly degenerate. When we studied the two-charge state device (Section 5.2.2), we applied the low-energy projection into the ground state subspace. We found that the virtual transitions from the ground state to the excited state in the large-energy gap limit, which are of second-order nature, generate an effective Kondo spin which at low temperature exhibits the NFL behaviour. When we studied the three-charge state device (Section 5.3.1.2), we argued that there exist virtual transitions from the ground state to two excited states; hence, in the large-energy gap limit, we obtain an effective Kondo spin with twice the coupling strength. In this case, since each of the ground states can be virtually excited to its excited states as well, i.e., $N+1 \to N$ and $N+2 \to N+3$, it is only natural to expect such a behaviour here. That, nevertheless, is not the case.

When we derive the low-energy effective Hamiltonian by projecting the full Hamiltonian onto the ground-state manifold as in the equation (5.2.17), we split the Hamiltonian (5.1.9) into $H_0 = H_{\mathrm{SI}} + H_{\mathrm{leads}}$, and $H_1 = H_{\mathrm{t}}$. In both the two-charge state and three-charge state models, the ground state of H_0 is non-degenerate. The first-order term $P_\alpha H_1 P_\alpha$ always vanishes because H_{t} involves either creating or annihilating an electron on the superconducting island, thus being outside the ground-state manifold. In the symmetric four-state case, since the ground-state manifold consists of two charge states, the first-order term is not zero and is more significant than the second-order term. The physics of this model should thus arise mainly from the first-order H_{t} which couples the degenerate ground states, rather than the second-order virtual transitions to the excited states; hence, its behaviour should be more similar to that of the degenerate two-charge state system rather than the large-energy gap limit of the two systems.

As can be seen in from the impurity entropy of the system as shown in Figure 5.26, that is indeed the case – the RG flow of the impurity entropy is similar to the case of the degenerate two-charge state system (Figure 5.8). When the coupling t is not too big, the impurity entropy starts off at the value of $\ln 4$ at

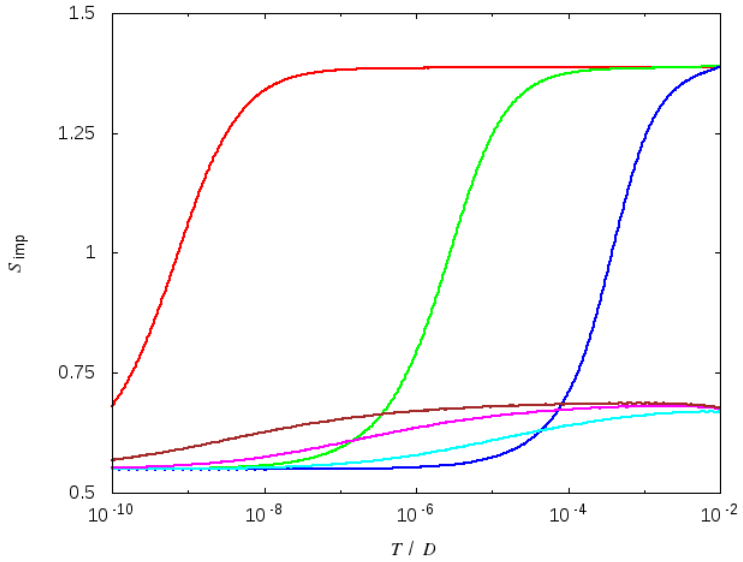

Figure 5.26: The temperature dependence of the Kondo temperature T_{K} in the large-energy gap limit $|\varepsilon|/D = 10$ of the four-charge state Majorana device when the coupling constants are $t/D = 0.1$ (red), 0.2 (green), 0.3 (blue), 0.8 (cyan), 1.0 (magenta), and 1.2 (brown). The results of the first three cases are not universal whereas those of the latter three are the universal curve of the spin model.

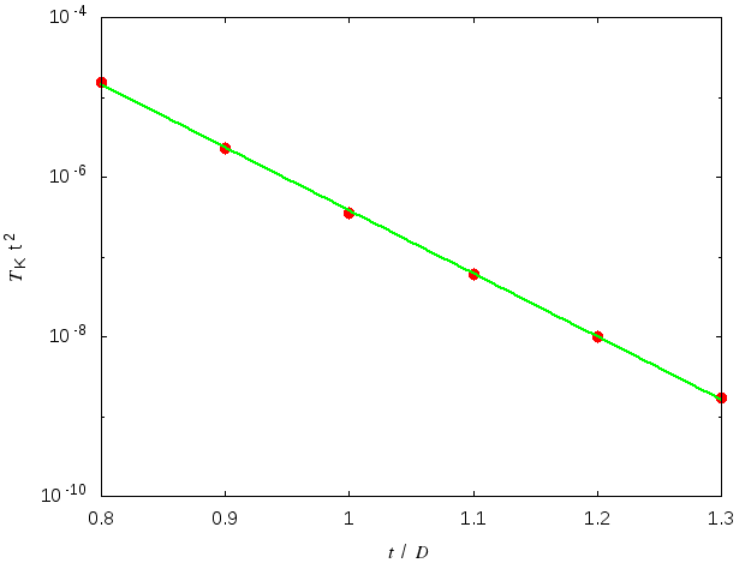

Figure 5.27: Dependence of the Kondo temperature on the coupling constant t for the four-charge state Majorana device in the large-energy gap limit. Whilst the impurity entropy and the conductance suggests that the physics in this region is the universal spin physics, the dependence of the Kondo temperature takes the form $T_{\mathrm{K}} \sim \frac{1}{t^2}\,\mathrm{e}^{-kt}$.

high temperature. A factor of two in the entropy is due to the degeneracy of the ground states; the empty and the triply occupied states are projected out, and there remain the singly and doubly occupied states. The other factor of two is as usual a result of the degenerate Majoranas. When the coupling is large enough, we observe the low-temperature NFL physics and the impurity entropy signature of $\ln\sqrt{3}$. The curves are rescaled in order to be checked if they give universal physics, but it is not visually conclusive whether these curves are universal. Later, we will come back to this when we discuss the linear conductance.

When the coupling t is much larger ($t/D \sim 0.1$ in this case), we observe that the impurity entropy is $\ln 2$ even at high temperature. As mentioned before (Section 5.2.3) that the tunnelling part of the Hamiltonian connects the two ground states, and a new set of doubly degenerate ground states $\{|\chi_i\rangle\}$, equation (5.2.19)–(5.2.20) is formed, and hence the $\ln 2$ entropy. When the temperature is lowered, there is a RG flow towards the NFL fixed point as expected. Furthermore in this region, the curves obtained from the NRG calculations are exactly the universal curves of the spin model and the Kondo temperature in this region follows the asymptote that one would expect for the degenerate two-charge state system, $T_{\mathrm{K}} \sim \mathrm{e}^{-kt}$, equation (5.2.28), as is shown in Figure 5.27.

Finally, we calculate also the frequency dependence of the zero-temperature off-diagonal linear conductance and compare the results to the known result of the spin model. According to Figure 5.28, the conductance calculations also show two types of RG flow for the model, both of which flow from $G_{ik}(\omega) = 0 \to \frac{2}{3}$, that which we have found in the case of two-charge state system system as well (Figure 5.10). In the large-t regime, we found that the conductance curves are universal and have confirmed that they are the same curve as that of the spin model with the asymptote $\omega^{2/3}$. On the contrary, in the small-t regime, the curves are not universal, as is shown in Figure 5.29.

We could study the system where the energy gaps are set to zero and we have a quadruply set of degenerate states. Nevertheless, since we already understand how the degeneracy affects the physics of the system from the previous two studies (in the two-charge state system and three-charge state system systems), together with the fact that this system is not realisable by the charging energy

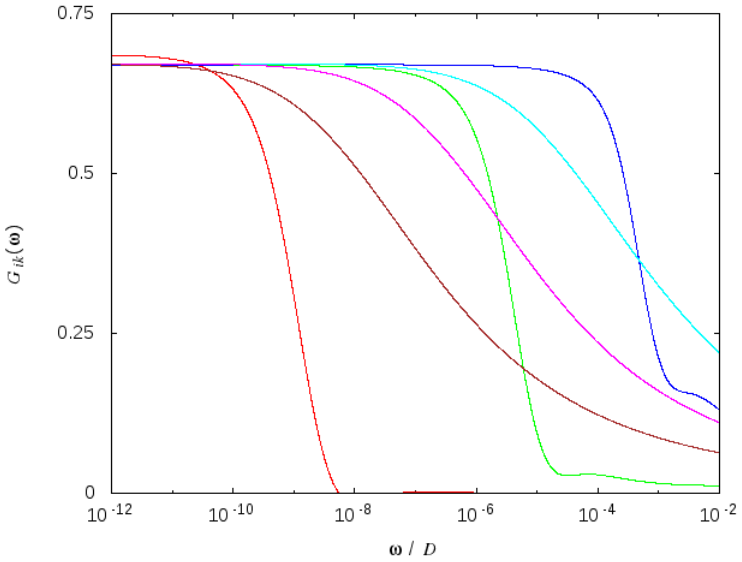

Figure 5.28: The frequency dependence of the zero-temperature linear conductance $G_{ik}(\omega)$ in the large-energy gap limit $|\varepsilon|/D = 10$ of the four-charge state Majorana device. The coupling constants are $t/D = 0.1$ (red), 0.2 (green), 0.3 (blue), 0.8 (cyan), 1.0 (magenta), and 1.2 (brown). Similar to the case of the impurity entropy, the first three conductance curves are not universal whereas the latter three are the universal conductance curve of the spin model.

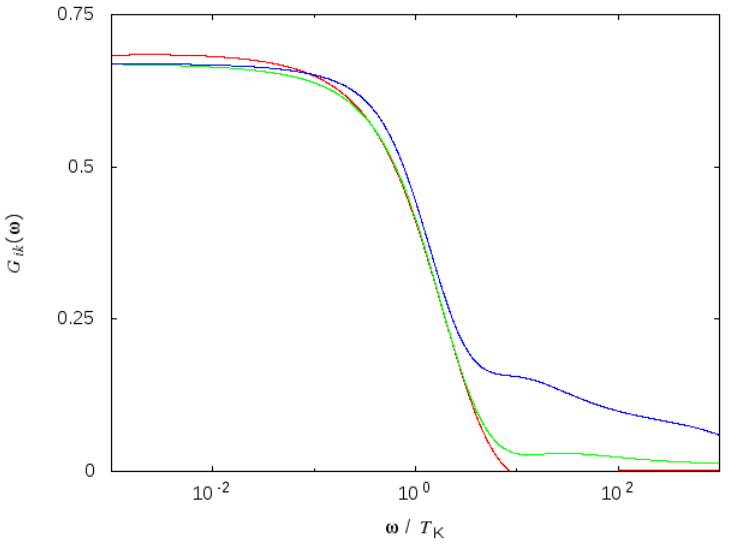

Figure 5.29: The frequency dependence, scaled by the appropriate Kondo temperature, of the linear conductance $G_{ik}(\omega/T_K)$ in the large-energy gap limit $|\varepsilon|/D = 10$ and coupling constant $t/D \in [0.1, 0.3]$ not too large, of the four-charge state Majorana device. As is clearly seen, the conductance curves in this regime does not collapse onto a single universal curve.

Hamiltonian, we will not pursue it and move on directly to study the system with energy gaps not necessarily large.

5.4.1.3 Lifting the Constraints

Finally, we remove the large-energy gap constraint previously imposed on the system. At high temperature, since all four states are thermally accessible, we expect that the impurity entropy starts off at the value of $\ln 8$, where the other factor of two comes from the degenerate Majorana states. Like in the three-charge state model (Section 5.3.1.4), there is then a competition between the coupling and the energy gap that renders the two excited states energetically inaccessible. The coupling is very small, $(t/D)^2 < |\varepsilon|/D$, the crossover occurs at the temperature scale $T \sim \varepsilon$. Upon further increasing the coupling t until $(t/D)^2 > |\varepsilon|/D$, the crossover occurs at higher temperature scale. As an explicit example, we consider the case where the energy gap is $-\varepsilon/D = 2 \times 10^{-5}$ (Figure 5.30). When $t/D = 10^{-3}$, $(t/D)^2 = 10^{-6} < |\varepsilon|/D$, and the crossover occurs at $T/D \sim |\varepsilon|/D \sim 10^{-5}$.

Upon further increasing the coupling t, the NFL behaviour of the system can be observed and we see the RG flow towards the NFL fixed point value of $\ln\sqrt{3}$ at low temperature. This behaviour is the same as the behaviour of the degenerate two-charge state system. However, due to the additional second-order type transitions to the two excited states, which also generates the Kondo spin coupling behaviour, the effective Kondo coupling is larger, the Kondo scale is as a result larger, and the RG flow occurs at a significantly higher temperature than that of the two-charge state system at the same coupling strength. For example, when the coupling $t/D = 0.1$, the transition $S_{\text{imp}} = \ln 4 \to \ln\sqrt{3}$ occurs at $T/D \sim 10^{-8}$ for the four-charge state system (the cyan line of Figure 5.30) whereas it occurs at $T/D \sim 10^{-10}$ for the degenerate two-charge state system (the red line of Figure 5.8).

Finally, when the coupling is very large, the states $\{|\chi_i\rangle\}$, equation (5.2.19)–(5.2.20), which are doubly degenerate are formed and the impurity entropy starts off at $\ln 2$ and flows towards the NFL value of $\ln\sqrt{3}$. As we mentioned above, in this system, the effective spin coupling is a result of the first-order contribution

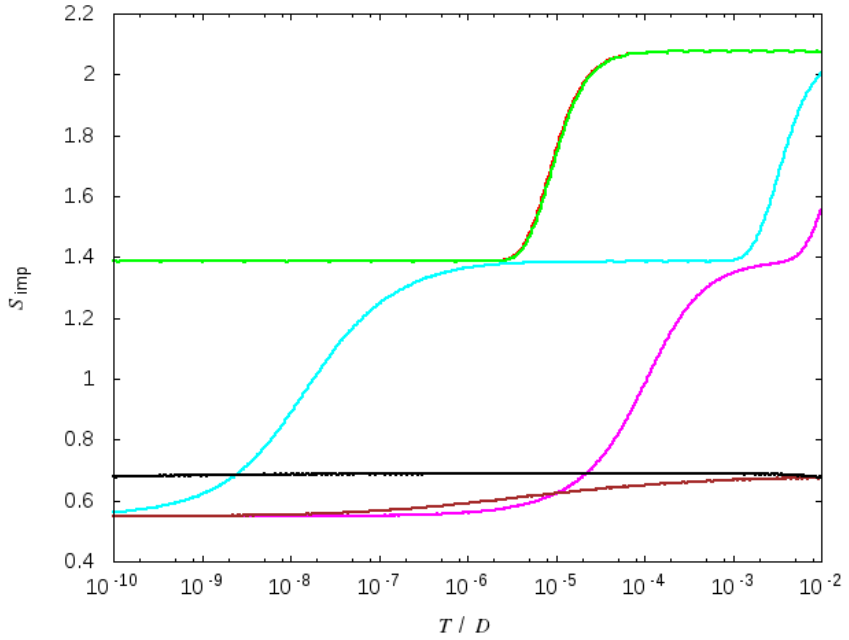

Figure 5.30: Temperature dependence of the Impurity entropy of the four-charge state Majorana device, where the energy gap $|\varepsilon|/D = 2 \times 10^{-5}$ and the coupling $t/D = 10^{-5}$ (red, underneath the green line), 10^{-3} (green), 10^{-2} (blue), 0.1 (cyan), 0.2 (magenta), 0.5 (brown), and 1 (black). There are three types of RG flows present here. The first one, the flow from $\ln 8$ to $\ln 4$ where the two excited states are projected out, occurs at $T \sim |\varepsilon|$ when the coupling $(t/D)^2 < |\varepsilon|/D$ depending on which is bigger. When the coupling is strong enough, we observe the second type of flow from $\ln 4$ to the NFL value of $\ln \sqrt{3}$. When the coupling becomes very strong, a new ground state is formed from the two ground states and its entropy is reduced to $\ln 2$ even at high temperature, and eventually flows to the NFL fixed point.

from the degenerate ground states and the second-order virtual transitions to excited states. Since the Kondo scale in the large-t regime of the degenerate two-charge state system is $T_\mathrm{K} \sim \mathrm{e}^{-ct}$ and we also know that for the general (non-degenerate) two-charge state system in large-t limit, increasing the coupling t also decreases the Kondo temperature (Section 5.2.4), the Kondo scale of this system in this region should be smaller than that of the degenerate two-charge state system. For instance, when the coupling $t/D = 1$, the Kondo scale T_K

is below 10^{-10} for the four-charge state system (the black line of Figure 5.30) whereas $T_\mathrm{k}/D \sim 10^{-6}$ for the degenerate two-charge state system (the magenta line of Figure 5.8).

We may therefore conclude that the physics of this system is characterised mainly by the degenerate ground states, resulting in the behaviour of the degenerate two-charge state system. This occurs because the coupling between the two ground states is of first-order nature. The transitions to the excited states which are of second-order nature are less important, but do serve to increase the effective coupling constant of the system. This nonetheless may be relevant when producing a real topological Kondo device with an experimentally observable Kondo scale. In the next section, we shall study the system where the ground states are not required to be degenerate and we are then able to study effectively the full low-energy system that is generated by the charging energy Hamiltonian.

5.4.2 Asymmetric System

In the rest of this chapter, we will study the four-charge state model, in which the requirement that $\delta = 0$ is no longer enforced, resulting in non-zero $\Delta\varepsilon$. In addition, evidently from the equations (5.4.2)–(5.4.3), the sizes of the two energy gaps are not equal. Nonetheless, if we keep to small values of δ, then the two energy gaps will be of very similar sizes. Hence, we will investigate the asymmetric four-charge state system with non-zero $\Delta\varepsilon$, which we refer to as either the energy difference or the asymmetry parameter, but equal energy gaps $|\varepsilon| = |\varepsilon'|$.

5.4.2.1 Decoupled Limit

In this limit, the impurity entropy of the system can be calculated:

$$S_\mathrm{imp} = \ln 2 + \ln Z + \frac{1}{T}\frac{\varepsilon\,\mathrm{e}^{-\varepsilon/T} + (\varepsilon+\Delta\varepsilon)\,\mathrm{e}^{-(\varepsilon+\Delta\varepsilon)/T} + \Delta\varepsilon\,\mathrm{e}^{-\Delta\varepsilon/T}}{Z}, \tag{5.4.7}$$

where Z the partition function is

$$Z = 1 + \mathrm{e}^{-\varepsilon/T} + \mathrm{e}^{-(\varepsilon+\Delta\varepsilon)/T} + \mathrm{e}^{-\Delta\varepsilon/T}, \tag{5.4.8}$$

and the factor of $\ln 2$ is a result of the Majorana degeneracy as usual. The NRG results agree with this analytical formula as shown in Figure 5.31.

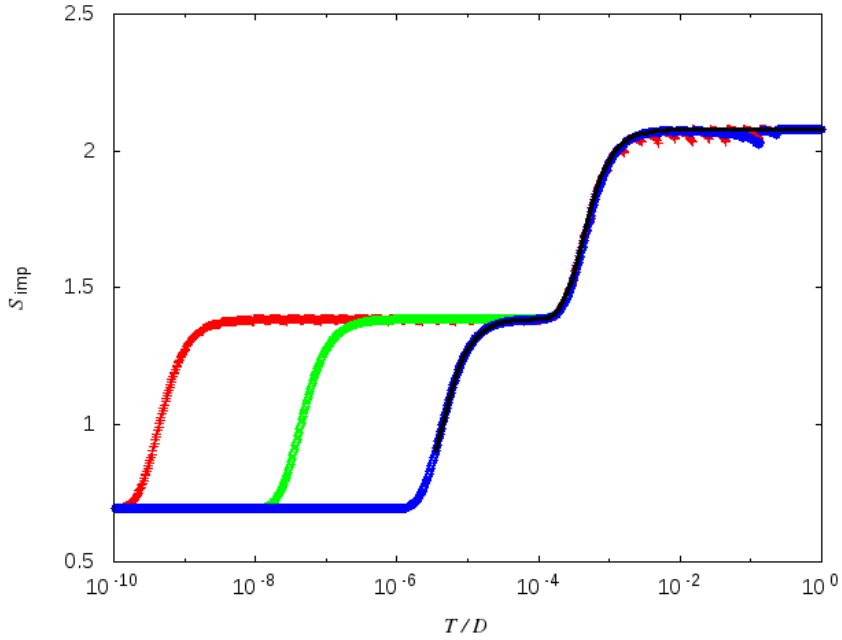

Figure 5.31: Temperature dependence of the Impurity entropy of the asymmetric four-charge state Majorana device in the decoupled limit. In this case, we fix the energy gap $|\varepsilon|/D = 10^{-3}$ and vary the asymmetry parameter $\Delta\varepsilon/D = 10^{-9}$ (red), 10^{-7} (green), and 10^{-5} (blue). The NRG results agree with the equation (5.4.7) as is shown in the case of $\Delta\varepsilon/D = 10^{-5}$ (black line).

At high temperature, the impurity entropy takes the value of $\ln 8$ due to the fact that all four states in the superconductor, each of which is coupled to two Majorana states with the same parity, are accessible. When the temperature is lowered so that it is smaller than the energy gap, the entropy flows to $\ln 4$, because the empty and the triply occupied states become energetically inaccessible. As before, the transition occurs at $T \sim |\varepsilon|$. Finally, upon further lowering the temperature until it is less than the scale of the asymmetry parameter, even the doubly occupied state becomes energetically inaccessible and the entropy is reduced to $\ln 2$ where only the degeneracy in the Majorana sector remains. The second transition occurs at the temperature scale $T \sim \Delta\varepsilon$ expectedly.

This RG flow pattern (Figure 5.31) arises in the case where the asymmetry parameter $\Delta\varepsilon$ is smaller than the energy gap. We in principle can of course investigate the other case where the asymmetry parameter is bigger. However,

since this limit cannot be realised in the charging energy Hamiltonian (2.3.3), we will not study it.

5.4.2.2 Large-Energy Gap Limit

Next, we move on to the large-energy gap limit. When we studied the symmetric system (Section 5.4.1.2), we learned that its physics is dominated by the degenerate ground states because the transitions between them by the Hamiltonian are first order in the ground-state subspace whereas the transitions to the excited states are second order and hence are much less important. In this case, we can therefore expect the physics of the system to be dominated by the two lowest energy states and the behaviour of the system be similar to that of the general (not large energy gap) two-charge state system (Section 5.2.4).

In order to confirm this hypothesis, we calculate the impurity entropy as a function of temperature in the limit where the energy gap is large, $|\varepsilon|/D = 20$ and 50, and we keep the asymmetry parameter small at $\Delta\varepsilon/D = 10^{-5}$. In comparison to the results of the two-charge state device with the energy gap 10^{-5} (Figure 5.11), whereas there is only a slight discrepancy in the case of the smaller energy gap $|\varepsilon|/D = 20$ when the coupling t is small (Figure 5.32), if $|\varepsilon|/D = 50$, the impurity entropy curve is visually superimposable onto the results of the two-charge state system (not shown). The discrepancy is a result of the virtual second-order transitions to the N and $N + 3$ charge states. Hence, we conclude that the physics in this regime is dominated by the physics of the two low-energy states. The transitions to the other two energy levels, since they are very high in energy and are of second-order nature, do not affect much of the physics in this regime.

5.4.2.3 Lifting the Constraints

Finally, we lift the large-energy gap constraint on the system and study the asymmetric system in general. Quite similar to the previous case, we also expect the behaviour of the system to be dominated by the two ground states as well, especially at low temperature. In order to facilitate the comparison between this system and the two-charge state system, we shall set the asymmetric parameter

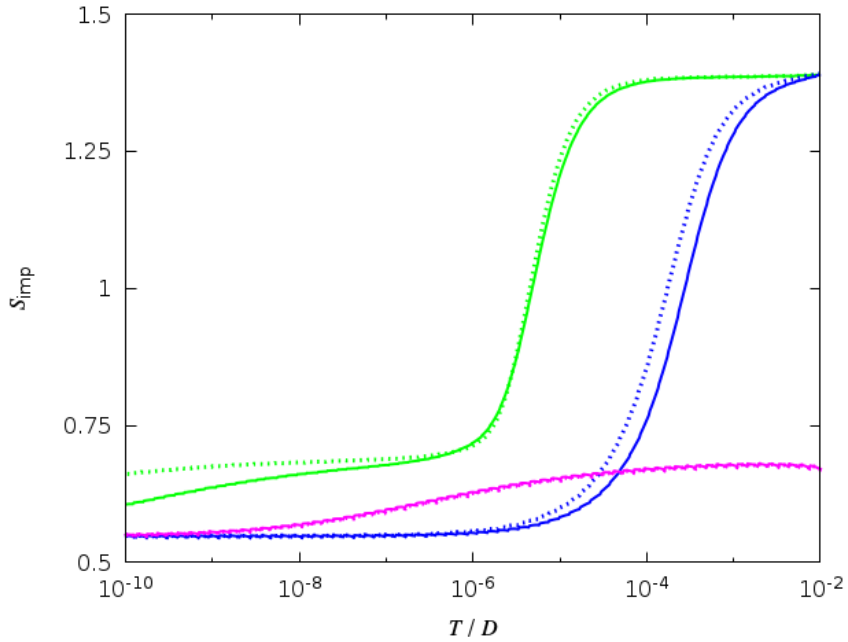

Figure 5.32: Temperature dependence of the Impurity entropy of the asymmetric four-charge state Majorana device, with large energy gap $|\varepsilon|/D = 20$ and the asymmetric parameter $\Delta\varepsilon/D = 10^{-5}$. Specifically, we show the results (solid lines) when the coupling strength t/D is 0.2 (green), 0.3 (blue), and 1 (magenta), in comparison to the results of the two-charge state device when its energy gap is 10^{-5} (dotted lines). When t is small, there is a small difference between the two systems. When t is large, the results are visually the same.

$\Delta\varepsilon$ to be of magnitude $10^{-5}D$, so that it can be directly compared with the two-charge state system with the gap of that same size (Figure 5.11). The energy gap is set a large value $|\varepsilon|/D = 10^{-3}$.

The impurity entropy calculated from NRG for this system is shown Figure 5.33. When the coupling is very weak $t/D < 0.1$, we observe two types of RG flows: one from $\ln 8 \to \ln 4$ at $T \sim |\varepsilon|$ when the high-energy empty and triply occupied states are projected out, and the other from $\ln 4 \to \ln 2$ at $T \sim \Delta\varepsilon$ when even the doubly occupied state becomes energetically inaccessible and is also projected out. The second RG flow is the same type of flow found in the two-charge state system. When the coupling is increased so that $(t/D)^2 > |\varepsilon|/D$, the first RG flow occurs then at $T/D \sim (t/D)^2$.

In the intermediate-t range, $0.1 < t/D < 0.5$, the first flow will happen at the energy scale $T/D > (t/D)^2$. In addition, we observe the NFL behaviour at very low temperature. In this regime, compared to the results of the two-charge state system, the temperature at which we observe the flow to $\ln\sqrt{3}$ is higher since additional transitions to the excited states are also of Kondo spin nature and effectively contributes to the additional coupling strength; since $T^* \sim \mathrm{e}^{-c/J}$, the increasing effective coupling J increases T^*.

When the coupling t is large, $t/D > 0.5$, just as in the two-charge state system, the duality behaviour is observed here. Moreover, for the same reason, in this regime, the effective coupling strength is greater than that of its two-charge state counterpart, and since $T_\mathrm{K} \sim \mathrm{e}^{-ct}$ in this region, the transition to the NFL fixed point occurs at the energy scale far below that of its two-charge state counterpart.

5.5 Summary

We close this chapter by summarising what we have learned from studying the Majorana device without performing the low-energy transformation. First of all, we know that the topological Kondo effect, or the physics of the spin model that we have previously studied, can be captured by modelling the superconducting island as a system as simple as the two-charge state system. In the large-energy gap limit, the two-charge state system indeed exhibits the same behaviour as that of the spin model, and topological Kondo effect can be observed both at small-t coupling , where the effective spin coupling constant $J \sim (\frac{t^2}{|\varepsilon|})^2\,\mathrm{e}^{-a|\varepsilon|/t^2}$, and also at large-$t$ coupling, where the effective spin coupling constant becomes $J \sim \frac{1}{t^4}\,\mathrm{e}^{-bt^2}$. The duality $J \leftrightarrow \frac{1}{J}$ behaviour is also captured by this system. It appears nonetheless that the ground state of the superconducting sector must be non-degenerate for the topological Kondo effect to be observed at moderate t coupling as is seen when we study the degenerate models.

When we include an additional charge state to the model system and study the three-charge state system, we learn that the topological Kondo effect is still observed in this model system. However, the crucial difference between this model system and the two-charge state system is the fact that the duality behaviour is no longer observed at large coupling t. Nevertheless, due to the fact that there is an

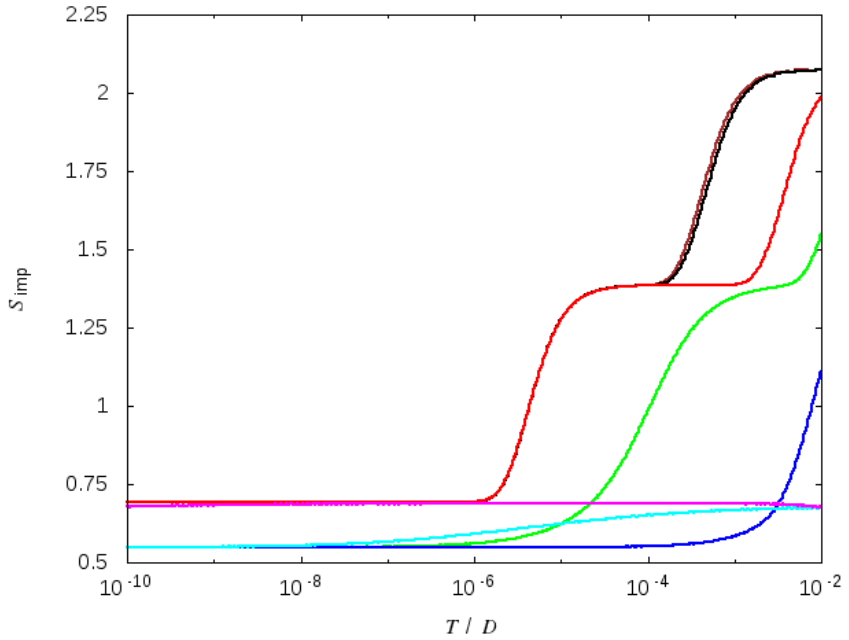

Figure 5.33: Temperature dependence of the Impurity entropy of the asymmetric four-charge state Majorana device, with the energy gap $|\varepsilon|/D = 10^{-3}$ and the asymmetric parameter $\Delta\varepsilon/D = 10^{-5}$. The coupling strength t/D is varied from 10^{-3} (brown), 10^{-2} (black), 0.1 (red), 0.2 (green), 0.3 (blue), 0.5 (cyan), 1 (magenta). The qualitative behaviour of this system should be similar to that of the two-charge state system with the gap size of $10^{-5}D$, so we can compare the results in this figure with those in Figure 5.11. When t is very small, there is an additional flow of the impurity entropy at high temperature from $\ln 8$ due to the additional two high-energy (N and $N+3$) states. In the intermediate-t regime, the results are the same except that the temperature scale of the crossover for this system is higher than that of the two-charge state system due to the additional contribution from the virtual transitions to the other two high-energy states. In the large-t regime, the duality is observed as expected, but the Kondo temperature is far smaller than that of the two-charge state system since stronger effective couping implies lower Kondo temperature in this regime.

additional energy level for the second-order virtual excitations, the spin coupling J is effectively larger than that of the two-charge state system with equal coupling t; hence, topological Kondo effect can be observed at higher temperature given the same coupling strength t.

Finally, we study the four-charge state system, a model in which it is possible to have doubly degenerate ground states, where it is possible for each of them to have their own virtual excitations. Since this system has both the ground state degeneracy and also the possibility for virtual excitations, the behaviour of the system is a combination of the two and the duality is once again observed. However, as mentioned before, the topological Kondo effect can be observed at moderate t only if the ground-state degeneracy is broken. Thus, the topological Kondo effect in this case is observed only at large t coupling. Even for the asymmetric model where the ground states are not degenerate, a sufficiently large energy gap is still required for the topological Kondo effect to be observed.

Now that we have understood the behaviour of the three-lead Majorana device, both its effective low-energy spin model and the model in which superconducting island is viewed as a collection of charge states, we extend the device to include the fourth conduction electron lead.

6

Addition of the Fourth Lead

In this final chapter, we attach an additional conduction electron lead to the Majorana device. Using the same approach that we used to study the spin model (Chapter 3) and the level models (Chapter 5) of the three-lead Majorana device, we shall study this four-lead device by first deriving the low-energy effective Hamiltonian which turns out to be another spin Hamiltonian, specifically it is the two-channel Kondo model [78], which has been proposed initially as a model that takes into account the internal orbital structure of the impurity [55], and is a subject of extensive studies both theoretically via a variety of different methods such as Abelian bosonisation [109], large-n expansion [110, 111], NRG [106, 112, 113, 114, 115], Bethe ansatz [116, 117], CFT [52], and also experimentally [57, 58]. The thermodynamic properties of the two-channel Kondo model have been well studied and will be confirmed. Its conductance has also been calculated, but for the same reason as in the case of the three-lead Majorana device (Section 3.2.3), the temperature dependence of the conductance of this device is different from the standard $\sqrt{T}$ signature of the two-channel Kondo model [78]. And whilst the asymptotic low-temperature behaviour of the conductance of the N-lead Majorana device has already been derived, we calculate the full crossover curve for the 4-lead device using NRG. Afterwards, we shall study the full Hamiltonian by modelling the charging energy part of the superconducting island as a two-charge state system, analogous to what we did for the three-lead device (Section 5.2).

The Hamiltonian (2.3.1) as is introduced in Section 2.3 is the Hamiltonian of the Majorana device. As before, if we only keep the leading-order terms and drop all the exponentially-small terms (non-local couplings between the Majoranas and the non-local leads, $t_{ij}, i \neq j$, and also between the Majorana themselves, H_{M}), it then takes the form

$$H = H_{\mathrm{leads}} + H_{\mathrm{c}} + H_{\mathrm{t}}, \tag{6.0.1}$$

where $H_{\mathrm{leads}} = \sum_{ki} \varepsilon_k a_{ki}^\dagger a_{ki}$ is the enery of the free spinless conduction electron lead i, $H_{\mathrm{c}} = E_{\mathrm{c}} \left(N - \frac{q}{e}\right)^2$ is the charging energy of the superconducting island, and $H_{\mathrm{t}} = \sum_i t_{ii} \gamma_i \psi_i \mathrm{e}^{\mathrm{i}\phi/2} + \mathrm{adj.}$ is the tunnelling coupling between the Majorana and the lead.

6.1 The Low-Energy Spin Behaviour

6.1.1 The Two-Channel Kondo Hamiltonian

As in Chapter 3, we study first the low-energy behaviour of the system by deriving its low-energy effective Hamiltonian. Since the method used in Section 3.1 still works here, we end up with the following effective Hamiltonian:

$$H_{\mathrm{eff}} = H_{\mathrm{leads}} + \sum_{i \neq k} \frac{2 t_{ii}^* t_{jj}}{E_{\mathrm{c}}} \gamma_j \gamma_i \psi_i^\dagger \psi_j. \tag{6.1.1}$$

Knowing that the low-energy effective model of the Majorana device is a Kondo spin model, we shall attempt to rewrite the above Hamiltonian into a spin Hamiltonian. Consider the simplest isotropic case where all the coupling constants are equal. A set of spin-$\frac{1}{2}$ operators can be formed from the first three Majoranas as before, $S_\alpha = -\frac{\mathrm{i}}{4} \sum_{ij} \epsilon_{\alpha ij} \gamma_i \gamma_j$, but we can also use the last Majorana as well: $S_\alpha = -\mathrm{i}\gamma_4 \gamma_\alpha$ [5]. If we now relabel the coupling constant $J = \frac{4|t^2|}{E_{\mathrm{c}}}$, the second term of the Hamiltonian can be written as

$$\begin{aligned} H_{\mathrm{K}} = J \Big\{ \quad S_z \quad & \left(\psi_2^\dagger \psi_1 - \psi_1^\dagger \psi_2 + \psi_3^\dagger \psi_4 - \psi_4^\dagger \psi_3\right) + \\ \left(S^+ - S^-\right) & \left(\psi_1^\dagger \psi_3 - \psi_3^\dagger \psi_1 + \psi_2^\dagger \psi_4 - \psi_4^\dagger \psi_2\right) + \\ \mathrm{i}\left(S^+ + S^-\right) & \left(\psi_1^\dagger \psi_4 - \psi_4^\dagger \psi_1 + \psi_3^\dagger \psi_2 - \psi_2^\dagger \psi_3\right) \Big\}, \end{aligned} \tag{6.1.2}$$

where as usual, the raising and lowering operators are defined via $S^{\pm} = S_x + \mathrm{i}S_y$. Furthermore, we perform the following transformation, which is analogous to equation(3.2.2–3.2.4):

$$\phi_{1,2} = \frac{1}{\sqrt{2}}(+\psi_1 \pm \mathrm{i}\psi_2), \tag{6.1.3}$$

$$\phi_{3,4} = \frac{1}{\sqrt{2}}(\pm\psi_3 + \mathrm{i}\psi_4). \tag{6.1.4}$$

We then obtain the following Hamiltonian

$$\begin{aligned} H_{\text{eff}} = \sum_{kj} \varepsilon_k c^{\dagger}_{k,j} c_{k,j} + J\Big\{ & S_z \left(\phi^{\dagger}_3\phi_3 - \phi^{\dagger}_1\phi_1 + \phi^{\dagger}_2\phi_2 - \phi^{\dagger}_4\phi_4 \right) \\ & + S^{+} \left(\phi^{\dagger}_1\phi_3 + \phi^{\dagger}_4\phi_2 \right) + S^{-} \left(\phi^{\dagger}_3\phi_1 + \phi^{\dagger}_2\phi_4 \right) \Big\}. \end{aligned} \tag{6.1.5}$$

Since each of the ϕ operator pair 1, 3 and 2,4 form a spin-$\frac{1}{2}$ object, in particular, $2 \equiv 3 \equiv \uparrow$ and $1 \equiv 4 \equiv \downarrow$ whereas $I_z = \frac{1}{2}\left(\phi^{\dagger}_{\uparrow}\phi_{\uparrow} - \phi^{\dagger}_{\downarrow}\phi_{\downarrow} \right)$ and $I^{-} = \phi^{\dagger}_{\downarrow}\phi_{\uparrow}$, the effective Hamiltonian then takes the form

$$\begin{aligned} H_{\text{eff}} &= \sum_{kj} \varepsilon_k c^{\dagger}_{k,j} c_{k,j} + J\Big\{ 2S_z \left(I_{1z} + I_{2z} \right) + S^{+} \left(I^{-}_1 + I^{-}_2 \right) + S^{-} \left(I^{+}_1 + I^{+}_2 \right) \Big\} \\ &= \sum_{kj} \varepsilon_k c^{\dagger}_{k,j} c_{k,j} + 2J\mathbf{S} \cdot \left(\mathbf{I}_1 + \mathbf{I}_2 \right), \end{aligned} \tag{6.1.6}$$

which is exactly the two-channel Kondo Hamiltonian, agreeing with what Béri proposed for the 4-lead system using the results of a quantum Brownian model [78].

In implementing the NRG code, we use the Hamiltonian (6.1.5), which consists of four spinless electron leads being coupled the a spin-$\frac{1}{2}$ impurity.

6.1.2 Thermodynamics

Knowing that this is the two-channel Kondo model, since the impurity is a spin-$\frac{1}{2}$, we expect that the impurity entropy take the value of $\ln 2$ at high temperature. Furthermore, since the impurity spin is less than the maximum value of the spin of the conduction electrons, $\frac{n}{2} = 1 > \frac{1}{2}$, the impurity is overscreened and the non-Fermi liquid behaviour can be observed at low temperature. In particular, the zero-temperature value of the impurity entropy can be calculated from equation

(2.6.10): $S_{\text{imp}}(0) = \ln\sqrt{2}$ [92, 93]. We use the NRG technique to calculate the impurity entropy of this spin system, and as is shown in the left panel of Figure 6.1, the two limiting values of the impurity entropy are confirmed.

In addition, the low-temperature asymptote of the impurity entropy is predicted to take the form of the equation (2.6.11): $S_{\text{imp}}(T) = S_{\text{imp}}(0)+aT(1-b\ln T)$, for the two-channel ($n = 2$) Kondo model [52], in agreement with our results calculated from NRG (left panel of Figure 6.1). Similarly, the impurity spin susceptibility $T\chi$ flows from the high-temperature free-spin-$\frac{1}{2}$ value of $\frac{1}{4}$ to the NFL value at 0, with the same low-temperature asymptote: $T\chi_{\text{imp}} \sim T(1 - d\ln T)$ [52], in agreement with NRG as well (right panel of Figure 6.1).

We then look at the dependence on the coupling strength J of the Kondo temperature, which we now take to be the temperature at which the impurity entropy is at the midpoint between the free-spin and NFL values: $S_{\text{imp}}(T_{\text{K}}) = \frac{1}{2}(\ln 2 + \ln\sqrt{2}) \approx 0.52$. We found that the NRG results agree with the with the equation (2.5.37) with $n = 2$:

$$T_{\text{K}}/D \sim \rho J\, \mathrm{e}^{-1/\rho J}. \tag{6.1.7}$$

6.1.3 Linear Conductance

Finally, we consider the linear conductance which is a dynamic property that is experimentally relevant. Equation (2.6.32) relates the conductance tensor $G_{ij}(\omega)$ to the imaginary part of the spectral function $K''_{ij}(\omega)$, which can be calculated when the operators $\dot{N}_i$ are known via equation (2.6.27); therefore, we first calculate such operators. As in section 3.2.3, we represent the number operators in the physical basis by $N_i = a^\dagger_{ki}a_{ki}$ and those in the transformed basis by $\mathcal{N}_j = c^\dagger_{k,j}c_{k,j}$. We choose to calculate $\dot{N}_i$ as they can be physically interpreted directly, but express them in the transformed basis because these are the operators that are

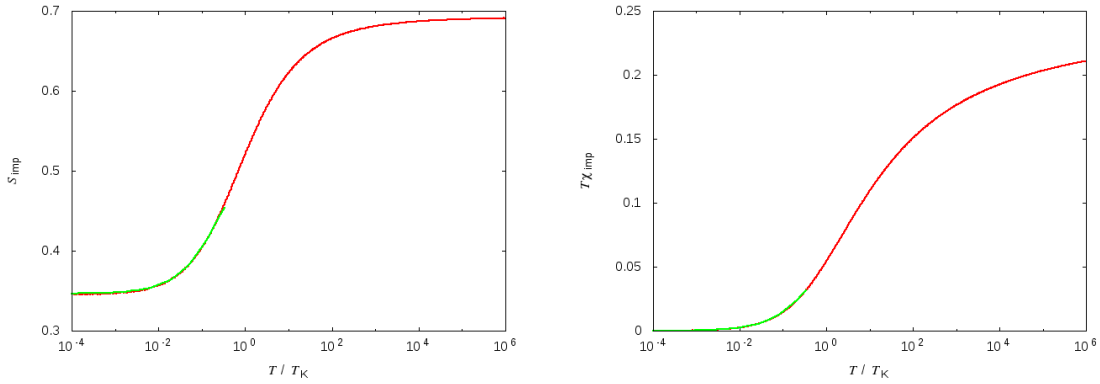

Figure 6.1: The universal temperature dependence of the thermodynamics for the effective isotropic spin model of the Majorana device with four conduction electron leads attached. (left) The impurity entropy $S_{\rm imp}$ (red line) showing the RG flow from the free spin value of $\ln 2$ to the two-channel Kondo NFL value of $\ln\sqrt{2} \approx 0.35$, with the low-temperature asymptote: $T(1 - b \ln T)$ (green line). (right) The impurity spin susceptibility $T\chi_{\rm imp}$ (red line) following the same crossover with the asymptote: $T(1 - d \ln T)$ (green line).

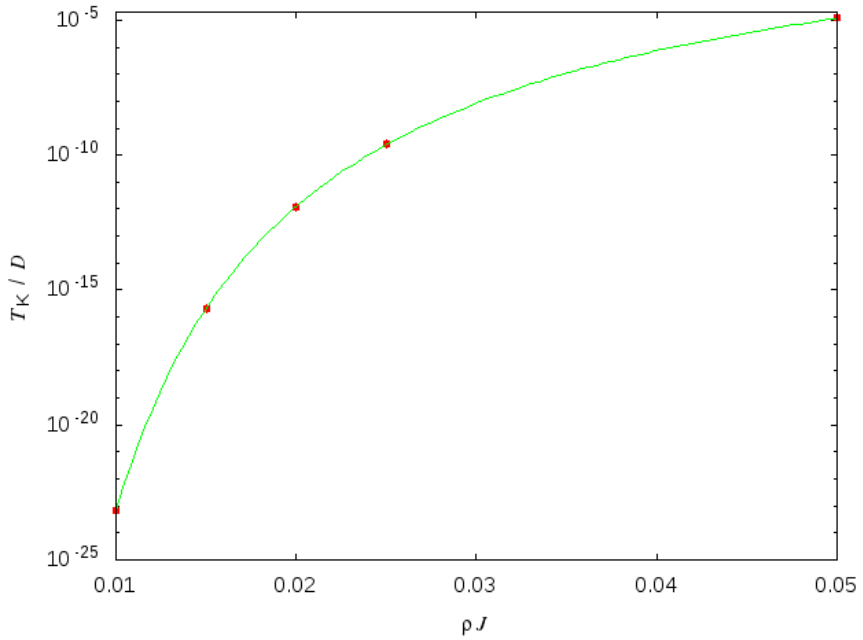

Figure 6.2: The dependence of the Kondo temperature $T_{\rm K}$ on the coupling J for the effective isotropic spin model of the 4-lead Majorana device. The NRG results (red dots) agree with the analytical relation (6.1.7) (green line).

being used in the NRG code:

$$\begin{aligned}
\mathrm{i}\hbar\dot{N}_1 = +\frac{\lambda}{2}\Big\{ & S^+\left[\left(\phi_1^\dagger+\phi_2^\dagger\right)\phi_3-\phi_4^\dagger\left(\phi_1+\phi_2\right)\right]+S^-\left[\left(\phi_1^\dagger+\phi_2^\dagger\right)\phi_4-\phi_3^\dagger\left(\phi_1+\phi_2\right)\right] \\
& +2S^z\left[\phi_1^\dagger\phi_2-\phi_2^\dagger\phi_1\right]\Big\}, \qquad (6.1.8)\\
\mathrm{i}\hbar\dot{N}_2 = +\frac{\lambda}{2}\Big\{ & S^+\left[\left(\phi_1^\dagger-\phi_2^\dagger\right)\phi_3+\phi_4^\dagger\left(\phi_1-\phi_2\right)\right]-S^-\left[\left(\phi_1^\dagger-\phi_2^\dagger\right)\phi_4+\phi_3^\dagger\left(\phi_1-\phi_2\right)\right] \\
& -2S^z\left[\phi_1^\dagger\phi_2-\phi_2^\dagger\phi_1\right]\Big\}, \qquad (6.1.9)\\
\mathrm{i}\hbar\dot{N}_3 = -\frac{\lambda}{2}\Big\{ & S^+\left[\left(\phi_3^\dagger-\phi_4^\dagger\right)\phi_2+\phi_1^\dagger\left(\phi_3-\phi_4\right)\right]-S^-\left[\left(\phi_3^\dagger-\phi_4^\dagger\right)\phi_1+\phi_2^\dagger\left(\phi_3-\phi_4\right)\right] \\
& -2S^z\left[\phi_3^\dagger\phi_4-\phi_4^\dagger\phi_3\right]\Big\}, \qquad (6.1.10)\\
\mathrm{i}\hbar\dot{N}_4 = +\frac{\lambda}{2}\Big\{ & S^+\left[\left(\phi_3^\dagger+\phi_4^\dagger\right)\phi_2-\phi_1^\dagger\left(\phi_3+\phi_4\right)\right]+S^-\left[\left(\phi_3^\dagger+\phi_4^\dagger\right)\phi_1-\phi_2^\dagger\left(\phi_3+\phi_4\right)\right] \\
& -2S^z\left[\phi_3^\dagger\phi_4-\phi_4^\dagger\phi_3\right]\Big\}. \qquad (6.1.11)
\end{aligned}$$

As expected, $\sum_i \dot{N}_i = 0$, which is the current conservation. In terms of the conductance tensors, this is $\sum_i G_{ik}(\omega) = 0$ for any k. The isotropy condition gives $G_{ik}(\omega) = G_{jk}(\omega)$ when $i, j \neq k$. Combining the two, we then have

$$-\frac{1}{3}G_{ii}(\omega) = G_{ik}(\omega). \qquad (6.1.12)$$

Figure 6.3 shows the frequency dependence of both the diagonal and off-diagonal elements of the zero-temperature conductance tensors, where we arbitrarily choose $G_{11}(\omega)$ to represent the diagonal elements and $G_{12}(\omega)$ the off-diagonal elements. The relation (6.1.12) above is confirmed at all frequencies and the diagonal elements are negative as expected (Section 2.6.3). Furthermore, the zero-frequency values are observed to be $G_{ii}(\omega = 0) = -\frac{3}{2}$ and $G_{ik}(\omega = 0) = \frac{1}{2}$. Similar to the thermodynamics of the system, clearly the conductance of this system is not the same as that of the three-lead device. Béri has generalised the calculations of Nayak et al [118], Oshikawa et al [119], and Fu [62] and found that the zero-temperature values of the conductance of the Majorana device take the form [78]:

$$G_{ik}(0) = 2\frac{e^2}{h}\left(\frac{1}{N}-\delta_{ik}\right). \qquad (6.1.13)$$

This equation then explains both of the zero-frequency zero-temperature values in our case with $N = 4$ above and also generates the correct zero-temperature

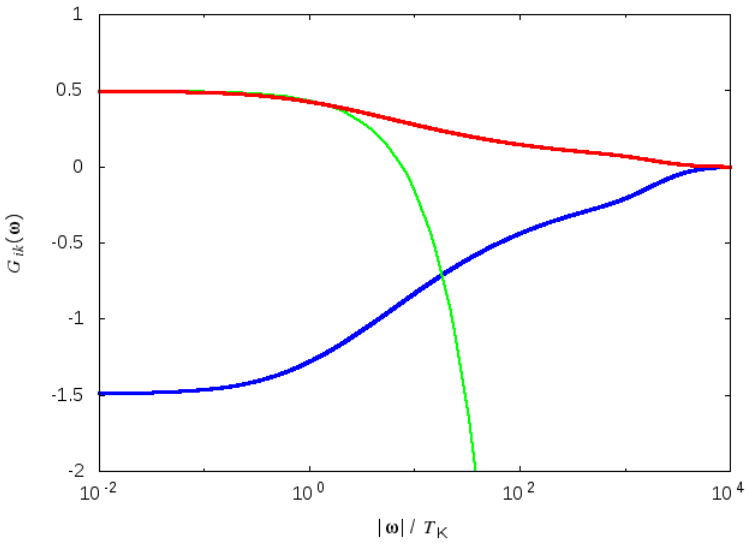

Figure 6.3: The frequency dependence of the zero-temperature conductance tensors G_{ij} for the effective isotropic spin model of the Majorana device with four conduction electron leads attached, both for the non-diagonal component $G_{ik}, i \neq k$ (red line) and the diagonal component G_{ii} (blue line). $G_{ik}(\omega) = -\frac{1}{3}G_{ii}(\omega)$ as expected. At low temperature, $G_{ik}(|\omega|/T_\mathrm{K})$ is linear in frequency (green line) in agreement with the NRG results.

values of the three-lead device studied earlier in Chapter 3 and 4. Moreover, using the same argument that is given in Section 3.2.3 for the three-lead device, that the first-order correction to the conductance vanishes by symmetry, and the second-order correction is of the order $2\Delta - 2$, where $\Delta = 2(N-1)/N$ [78], we expect the leading-order correction to the conductance for this device to be linear. Indeed, we can confirm that the asymptotic behaviour of the non-diagonal conductance calculated from NRG (Figure 6.3) is of the form

$$G_{ik}(\omega; T = 0) = G_{ik}(0,0) - \frac{\omega}{T_\mathrm{K}}, \tag{6.1.14}$$

and the correction is indeed linear in frequency.

Now that we understand the basic effective low-temperature spin behaviour of the Majorana device with four conduction electron leads attached to the superconducting island, we will study the model without performing the low-temperature projection, but thinking of the superconductor as an orbital with an energy level available to occupy up to one spinless electron.

6.2 Four-Lead Two-Charge State System

In this section, we shall investigate the superconducting island attached to four-lead conduction electrons without the low-energy projection. As in the case of the three-lead device (Section 5.2), we model the superconducting Hamiltonian simply as a two-charge state system, $H_{\mathrm{SC}} = \varepsilon n$, where we have chosen the occupied state to be lower in energy than the empty state, i.e., $\varepsilon < 0$.

In order to implement the NRG codes for this model, as in the case of the three-lead device (Section 5.1), we change the Majorana operators into the standard Dirac fermion operators:

$$f = \frac{1}{2}\left(\gamma_1 + \mathrm{i}\gamma_2\right), \tag{6.2.1}$$

$$f' = \frac{1}{2}\left(\gamma_3 + \mathrm{i}\gamma_4\right). \tag{6.2.2}$$

In addition, to avoid working with complex Hamiltonian matrix elements, we assume the isotropic symmetry $t_i = t$ and whilst we use the same transformations for the first two lead operators

$$\phi_1 = \frac{1}{\sqrt{2}}(\psi_1 + \mathrm{i}\psi_2), \tag{6.2.3}$$

$$\phi_2 = \frac{1}{\sqrt{2}}(\psi_1 - \mathrm{i}\psi_2), \tag{6.2.4}$$

instead of identity for the third lead operators, since both lead 3 and 4 are now coupled to the Majorana fermions, we make the equivalent transformations to these two leads:

$$\phi_3 = \frac{1}{\sqrt{2}}(\psi_3 + \mathrm{i}\psi_4), \tag{6.2.5}$$

$$\phi_4 = \frac{1}{\sqrt{2}}(\psi_3 - \mathrm{i}\psi_4). \tag{6.2.6}$$

The tunnelling Hamiltonian then becomes

$$H_{\mathrm{t}} = \sqrt{2}td^{\dagger}\left\{\left(f^{\dagger}\phi_1 + f\phi_2\right) + \left(f'^{\dagger}\phi_3 + f'\phi_4\right)\right\} + \mathrm{adj.} \tag{6.2.7}$$

Finally, similar to the case of three-lead model, we remove the states with incorrect parity by adding the fictitious energy (5.2.4).

6.2.1 Decoupled Limit

We first study the system in the decoupled limit where the impurity entropy is analytically found to be

$$S_{\text{imp}} = \ln 2 + \ln\left(1 + \mathrm{e}^{-\varepsilon/T}\right) + \frac{\varepsilon}{T}\frac{\mathrm{e}^{-\varepsilon/T}}{1 + \mathrm{e}^{-\varepsilon/T}}, \tag{6.2.8}$$

which is identical to that of the two-charge state three-lead device in the decoupled limit (Section 5.2.1), since the superconducting and the Majorana structures of the two models are identical.

The NRG results are shown in Figure 6.4, which, in comparison to the results of the two-charge state three-lead device (Figure 5.2), has a similar flow pattern with the same crossover taking place at the same temperature scale $T^* \sim |\varepsilon|$. However, it is clear that even when the NRG calculations are performed with the z averaging, if we keep the same number of states per iteration ($N_s = 2000$ in

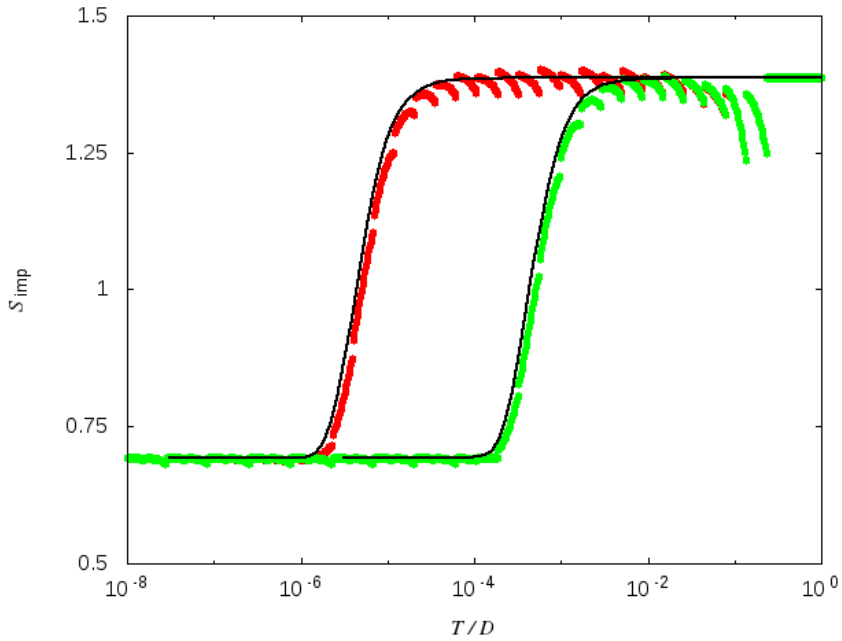

Figure 6.4: Impurity entropy as a function of temperature of the four-lead two-charge state Majorana device in the decoupled limit. The results from NRG is shown, in the case of $-\varepsilon/D = 10^{-5}$ (red) and 10^{-3} (green) against the analytical results (black lines) from the equation (6.2.8).

both calculations), the results obtained for the four-lead system – in addition to taking more computing time – show more oscillations. This is due to the fact that the size of the Hilbert space in each iteration is twice the size of that of the three-lead system; more computing time is required to diagonalise such matrices in addition to the fact that more states need to be retained to reach the same level of accuracy. In this section, the results for the calculations with the same N_s as in the three-lead systems are shown to visually reflect that more resources are required for the calculations in this system. In the next section, in calculating the thermodynamic properties of the system, we will increase the number of states $N_s \to 4000$ and in calculating dynamics, we increase $N_s \to 6000$ and this is where we reach the computing limit given the resources available.

6.2.2 Large-Energy Gap Limit

We now increase the size of the energy gap so that it is much larger than the coupling strength, in which case we expect that the low-temperature behaviour of the model can be described by the spin model studied in the previous section. We choose the coupling strength to be the same value as that we chose when we studied the two-charge state three-lead model, $|\varepsilon|/D = 10$.

The impurity entropy calculated by NRG is shown in Figure 6.5. Since the enery gap is large, the empty superconducting state is energetically unfavourable and is projected out very quickly. There is a RG flow from the high temperature where $S_{\text{imp}} = \ln 2$, whose superconducting configuration is occupied and the entropy is a result of the odd configuration of the Majoranas, to the NFL value $S_{\text{imp}} = \ln \sqrt{2}$, which is exactly the behaviour of the low-temperature effective spin model (of the two-channel Kondo type) studied earlier. The crossover curves are confirmed to be the universal curve.

Another feature that can be seen quite clearly in the figure is the oscillations in the curve. Even with the z averaging and the increased number of states retained at each iteration $N_s = 2000 \to 4000$, it is still insufficient for the oscillations to be visually dampened. As will be explained below, the calculations with $N_s = 6000$ can be achieved but with difficulty and we cannot perform the NRG calculations to very low temperature.

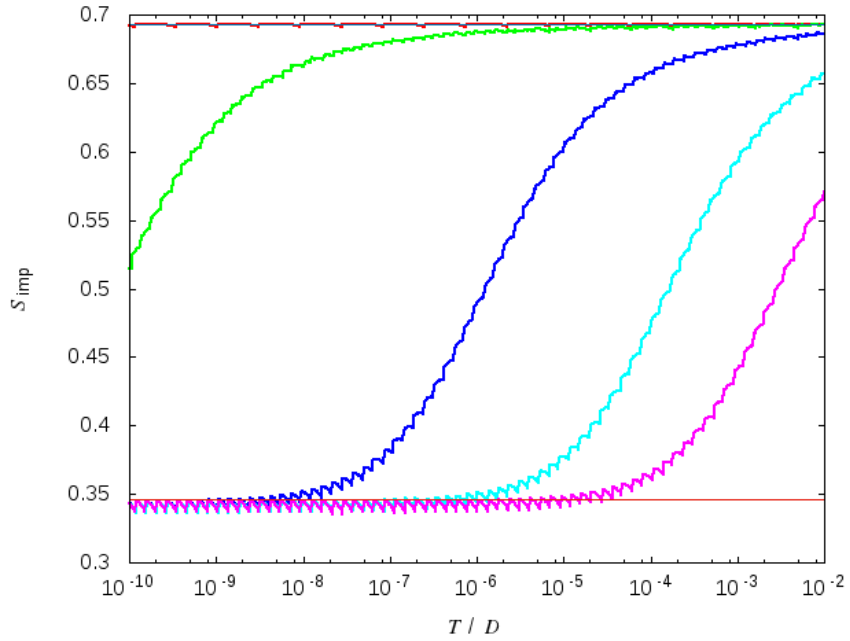

Figure 6.5: Temperature dependence of the impurity entropy of the four-lead Majorana device in the large-energy gap limit with $|\varepsilon|/D = 10$ and the coupling strengths $t = 0.5$(red), 0.75(green), 1(blue), 1.25(cyan), and 1.5(magenta). The entropy flows from the high-temperature value of $\ln 2$ to the two-channel Kondo NFL value of $\ln\sqrt{2}$. These crossover curves are exactly the universal crossover of the effective spin model (Figure 6.1, left panel).

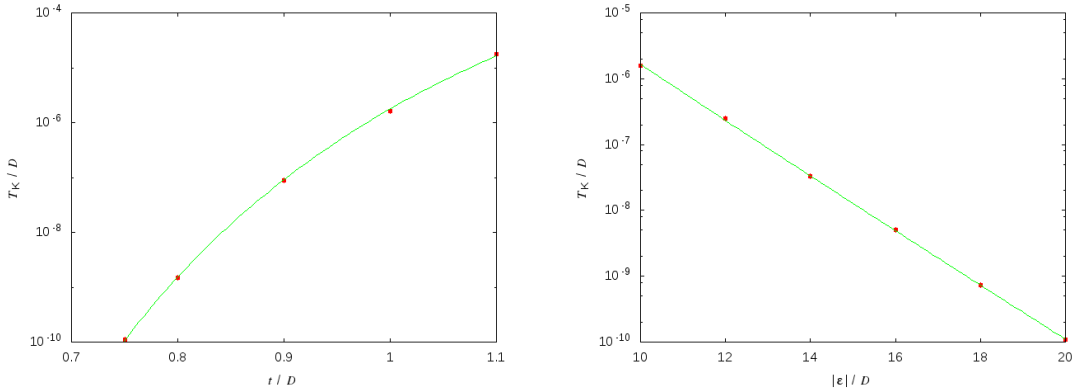

Figure 6.6: The dependence of the Kondo temperature T_K on the coupling strength t when the energy gap is kept constant at $|\varepsilon|/D = 10$ (left) and on the energy gap $|\varepsilon|$ when the coupling is kept constant at $t/D = 1$ (right) of the four-lead Majorana device in the large-energy gap limit. The data from NRG calculations (red circles) agree very well with the predicted relation (green lines), equation (6.2.9).

We then study the dependence of the Kondo temperature on the coupling constant and the energy gap. We know from the study of the spin model that dependence is described by the equation (6.1.7). In addition, we also know that the second-order excitation generates the effective coupling of strength $J \sim t^2/|\varepsilon|$, we then expect the dependence of the Kondo temperature on the coupling and the energy gap to be

$$T_{\mathrm{K}}/D \sim \frac{t^2}{|\varepsilon|}\,\mathrm{e}^{-k|\varepsilon|/t^2}. \tag{6.2.9}$$

The two dependences are confirmed as shown separately in Figure 6.6, where we show that $T_{\mathrm{K}} \sim t^2\,\mathrm{e}^{-c_1/t^2}$ when the energy gap is kept constant at $-\varepsilon/D = 10$ in the left panel and that $T_{\mathrm{K}} \sim \frac{1}{|\varepsilon|}\,\mathrm{e}^{-c_2|\varepsilon|}$ when the coupling constant is kept constant at $t/D = 1$ in the right panel.

Finally, we also calculate the zero-temperature linear conductance tensor of the model. As before, we need the expression for $\mathrm{i}\hbar\dot{N}_i$, where N_i are the number operators in the physical basis, but written in terms of the NRG-basis operators:

$$\mathrm{i}\hbar\dot{N}_1 = \frac{t}{2}\left\{\left(\phi_1^\dagger + \phi_2^\dagger\right)\left(f + f^\dagger\right)d - d^\dagger\left(f + f^\dagger\right)\left(\phi_1 + \phi_2\right)\right\}, \tag{6.2.10}$$

$$\mathrm{i}\hbar\dot{N}_2 = \frac{t}{2}\left\{\left(\phi_1^\dagger - \phi_2^\dagger\right)\left(f - f^\dagger\right)d + d^\dagger\left(f - f^\dagger\right)\left(\phi_1 - \phi_2\right)\right\}, \tag{6.2.11}$$

$$\mathrm{i}\hbar\dot{N}_3 = \frac{t}{2}\left\{\left(\phi_3^\dagger + \phi_4^\dagger\right)\left(f' + f'^\dagger\right)d - d^\dagger\left(f' + f'^\dagger\right)\left(\phi_3 + \phi_4\right)\right\}, \tag{6.2.12}$$

$$\mathrm{i}\hbar\dot{N}_4 = \frac{t}{2}\left\{\left(\phi_3^\dagger - \phi_4^\dagger\right)\left(f' - f'^\dagger\right)d + d^\dagger\left(f' - f'^\dagger\right)\left(\phi_3 - \phi_4\right)\right\}. \tag{6.2.13}$$

The frequency dependence of the zero-temperature conductance calculated from NRG is shown in Figure 6.7 (red line) for the calculation with 6000 states retained in each iteration. The result obtained in this case is similar to but visibly different from that of the spin model (black line). We suspect that this is due to the number of states kept in each iteration is insufficient; nevertheless, with the computing resources that we have, we cannot increase it any more. Increasing the number of leads attached to the superconductor to four requires an exponential increase of the computing resources and we can no longer calculate the dynamic properties of this model as accurately as before. In particular, given the computing resources of 32 GB of memory and 400 GB of hard disk available, the conductance calculations with $N_s = 6000$ can be performed with the maximum of 36 NRG iterations which is equivalent to $T/D \sim 10^{-8}$. Furthermore, the

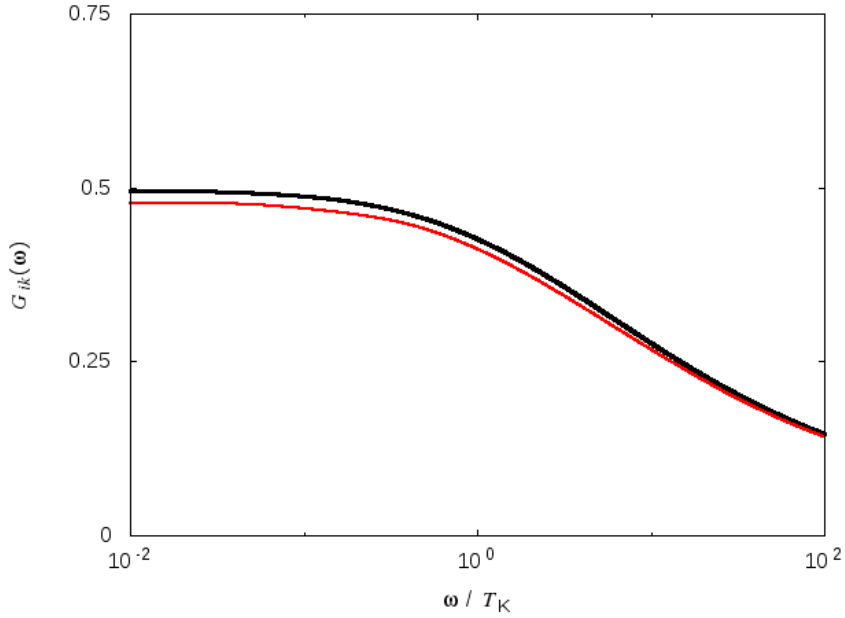

Figure 6.7: The frequency dependence of the zero-temperature non-diagonal conductance tensor G_{ik} of the Majorana device (black line) in comparison with the result of the spin model (black line) as is shown earlier in Figure 6.3. In this case, the results are visibly different and we suspect that this is due to the number of states kept in each NRG iteration is insufficient for the level model.

calculations cannot be performed with more states retained as the Hilbert space will be too large for the codes to handle given the size of the memory available. Although it is inconclusive from the conductance results that this model possesses the same low-temperature properties as the spin model, the thermodynamic results do suggest that such is the case.

We may conclude that the level model in the large-energy gap limit does behave in the same way as the spin model as expected and leave the study of both models in the more general case where the isotropy symmetry condition is lifted as future work.

7

Summary

In this thesis, we have undertaken a detailed theoretical study of the topological Kondo effects in the Majorana devices to confirm and develop the initial proposal of Benjamin Béri [41].

First, we studied the minimal device which requires three conduction leads to be connected to the superconducting island. Following Béri's argument, in chapter 3, we rederived the low-energy effective model and showed that indeed it is a spin model, in particular, it comprises a spin-$\frac{1}{2}$ impurity which is realised from the Majorana fermions, coupled to spin-1 conduction electrons which are formed from the three channels of spinless lead electrons. We then use Numerical Renormalisation Group to study thermodynamics, t matrices, and the conductance tensors of this model with the isotropic symmetry constraint. We confirmed that the low-temperature thermodynamics of this model is very similar to that of the four-channel Kondo model, an interesting properties of which is the residual non-zero impurity entropy of the value $\ln \sqrt{3}$ regardless of whether the spin coupling is isotropic or not. Furthermore, we also confirmed that the asymptotic behaviour of the Kondo temperature and the spin susceptibility of the model take the same form of that of the four-channel Kondo model as expected. The dynamics of the model, nevertheless, is distinctly different, for instance, the zero-frequency value of the scattering t matrix of the 4-channel Kondo model is predicted by CFT to be ≈ 0.21 whereas that of our system is found to be 0.5. As for the conductance, in addition to confirming the asymptotic behaviour that was calculated by Béri via CFT, we used NRG to calculate the full crossover curve, confirming that despite

the similar thermodynamics, the dynamic properties of these models are different since the actual conduction channels of the two models are different: there is only a single channel of spin-1 electrons in our model whereas there are 4 channels of spin-$\frac{1}{2}$ electrons in the 4-channel Kondo models.

We then lowered the symmetry constraint of the model from the full isotropy to the axial symmetry, where we allowed the longitudinal coupling constant to be different from the transverse coupling constant. First of all, we confirmed that the non-Fermi liquid properties are robust against this type of symmetry breaking, thus, making the prospect of experimentally observing the topological Kondo effect more likely. Then we investigated in details the Kondo temperature of this system. When the transverse coupling constant is small, Béri's has shown that the scaling equations of this model is the same as that of a single-channel model; we confirmed that the Kondo temperature of our system is of the same form as that of the anisotropic single-channel Kondo model. When the transverse coupling constant is large, however, we used Bosonisation to show that there exists a mapping between the large and the small transverse coupling constants for a system at a fixed longitudinal coupling constant. This result then implies that despite the similar nature of the fixed points of our model and the 4-channel Kondo model, the phase diagrams of the two systems are in fact very different: there are two Kosterlitz–Thouless lines separating between the ferromagnetic and antiferromagnetic domains in the 4-channel Kondo model, but only one in our system – the disappearance of the other Kosterlitz–Thouless line is due to the duality. Finally, we calculated the dynamics of the model, which once again confirmed the robustness of the low-temperature NFL behaviour against the anisotropy.

In chapter 4, we confirmed that the exponentially small long-range couplings between the Majoranas or those between the Majorana and the conduction electrons on different leads, which can be expressed as another type of anisotropy parameterised by δ, and an effective Zeeman magnetic field in the context of Kondo model, render the non-Fermi liquid fixed point unstable at low temperature. The RG of the system flows to the strong-coupling fixed point where it becomes a standard Fermi liquid and there is no longer any residual impurity entropy. Nevertheless, if the anisotropy parameter $\delta \ll J$ the spin coupling constant, the temperature scale at which the RG of the system flows to the NFL

fixed point T_{K}, will be sufficiently separated from the temperature scale at which the RG flows to the strong-coupling fixed point T^*_{FL}, and the non-Fermi liquid properties can still be observed in the intermediate temperature scale. This scale separation can be observed both in thermodynamics and dynamics of the model. Furthermore, we have studied the effect of the Zeeman field in details and found that indeed the field produces the same effect as that of the anisotropy, rendering the non-Fermi liquid fixed point unstable, and forcing the system to become a Fermi liquid at low temperature, though magnitude of the field required for such an observation is much lower than that of the anisotropy. This behaviour can be seen very clearly in the thermodynamics and the conductance of the system. Whilst at first sight, it appears that the t matrices of the two systems are very different; however, we have also shown that in fact the two are closer related to each other and are different from the other simply by a factor of the imaginary unit i.

In the second half of chapter 4, we went back to the original spin coupling model, once again ignored all the small perturbations as we had done before in chapter 3, and studied the system where we no longer imposed any symmetry requirements. We confirmed that the non-Fermi liquid properties of the system are robust against the anisotropy of the couplings in general. We then investigated the dependence of the Kondo scale on the three coupling constants in details and found that the duality behaviour can still be observed. Finally, we compared the Kondo temperatures obtained from NRG to those obtained from solving the scaling equations and found that the results agree very well in the region where the coupling constant is less than 1, which is to be expected since the scaling equations are obtained from perturbation theory which breaks down when the coupling is greater than 1.

In addition to studying the low-temperature effective spin behaviour of the device, in chapter 5, we attempted to study it, without performing the low-temperature projection as had been done in chapter 3, by modelling the superconducting island as a dot with a few energy levels available so that its energy spectrum is the same as that which is described by the charging energy term on the original Hamiltonian. In this case, the Hamiltonian of the system is an

Anderson-type model which can be investigated by the Numerical Renormalisation Group. We studied a few different configurations of the energy levels on the superconductor and also in a few different limits. Due to the charging energy term of the Hamiltonian, it is meaningful to discuss a state with a specific charge. In particular, we started with the simplest configuration, when the dot only has two energetically accessible charge states, and increased it to the maximum of four charge states later. To systematically investigate each configuration of the superconducting dot, we started by considering the decoupled limit, where the impurity entropy can be analytically calculated and confirmed that the results calculated from NRG agree with this. We then considered the large-energy gap low-temperature limit – the condition in which we had assumed in deriving the effective spin model in chapter 3 – and we found that indeed, the device behaves in the same manner as the spin model and the non-Fermi liquid properties are preserved; in fact, it turns out that this is common to all configurations of the dot, which is to be expected. Similarly, the duality behaviour between the large and small coupling constant regimes are also observed. Afterwards, we studied another extreme limit of the superconducting configuration, the doubly degenerate limit, where the two charge states are of the same energy. It was found that the coupling is required to be as large as $0.1D$ before the impurity entropy drops to the NFL fixed point value of $\ln\sqrt{3}$ at the temperature scale above $10^{-10}D$ and this flow is not universal. Nevertheless, once the coupling constant is much larger, the spin behaviour and the universal flow of the impurity entropy from $\ln 2$ to $\ln\sqrt{3}$ is recovered. This behaviour can be explained by using perturbation theory in the large-t limit, where we have found that the effective Hamiltonian is indeed the spin Hamiltonian. Finally, we studied the behaviour of the device without imposing any constraints on the system, where we have found mixed behaviour ranging from the regime where the device is effectively decoupled (very small t), to the regime where the device is effectively degenerate, and finally to the large-t regime, where the flow to NFL fixed point is observed.

We then increased the number of accessible charge states to three, considered first the case where the energy spectrum was symmetric, and followed the same sequence of the investigation as had been done earlier. We confirmed that thermodynamics of the model in the decoupled limit agreed with the analytical

results. In the large-energy gap limit, however, we found that the behaviour of the system was not entirely what was expected. Whereas the low-temperature residual entropy is still the NFL $\ln\sqrt{3}$ value and the crossover curve is the universal spin crossover, the duality disappears: regardless of how large we increase the coupling constant, the Kondo temperature never decreases. The same behaviour is also observed when all three energy levels are degenerate, in which case we used the perturbation theory to study the system in the large-t limit. Since the effective Hamiltonian generated from the second-order virtual transitions is not a spin-$\frac{1}{2}$ impurity model coupled to spin-1 conduction electrons, the arguments we used to prove the duality in the spin model before do not apply and thus the duality is not to be expected in this model. Nonetheless, in the intermediate range of the coupling constants, the standard universal spin crossover can be observed. Upon lifting the constraint, we found as before that the system has mixed behaviour. In the asymmetric system, after confirming the results in the decoupled limit with the analytical relations, we found that in the large-energy gap limit, the universal spin behaviour is recovered with the new effective coupling constant being the sum of the effective coupling constants of each of the two levels. In general, depending on the relative size of the coupling constant and the two energy gaps, we may observe the flow of the impurity entropy from $\ln 6$ to $\ln 4$ then to $\ln 2$ or a direct flow from $\ln 6$ to $\ln 2$ in the small-t region, a feature that is of the decoupled limit. When the coupling is large enough, the flow towards the NFL fixed point value of $\ln\sqrt{3}$ is observed.

In the last section of chapter 5, we studied the four-charge state system, which we believed to be a model that should capture all the low-energy features of the energy spectrum that is generated by the original charging energy Hamiltonian since it is possible to have doubly degenerate ground states, where each charge state can be virtually transitioned to the adjacent charge state. In the symmetric system, after having confirmed with the analytical results in the decoupled limit, we have found that effectively the behaviour of the system can be understood as a combination of the properties of the two-charge state systems since this system is basically composed of two two-level systems whose ground state is tunnel coupled to each other, which in turn is effectively the degenerate two-level system studied previously. In fact, we have found that the physics of this system is principally

governed by the latter because the effective model that arises from the transitions within the ground-state manifold is of first-order nature whereas those from the transitions from the ground-state manifold to the remaining two excited states are of second-order nature. Furthermore, once again the duality behaviour between the small coupling and large coupling regimes are recovered; after all, this system does contain a degenerate pair of charge states, which have been found earlier to show duality. In the case of the asymmetric system, it turns out that the physics can be understood mainly by considering the effective model that arises from two lowest energy states; the other two states only serve to change the minor details of the system, e.g., the exact value of the Kondo temperature. We close this chapter by making a remark of a feature that is common to all configurations of the dot: it appears that in order for the topological Kondo effect to be observed at a moderate t coupling, the ground state degeneracy must be broken. Otherwise, the physics of the system will be governed by the transitions between the degenerate ground states, resulting in the $\ln 4 \to \ln \sqrt{3}$ flow which is not the universal RG flow of spin model.

Finally, we extend the two models to the case where an additional conduction lead is attached to the superconducting island in chapter 6. Following Béri, we have confirmed that the low-energy effective Hamiltonian of the four-lead Majorana device is the two-channel Kondo Hamiltonian. Due to the required computing resources that is increased for the calculations of this system, we content ourselves to study only the simplest limit: the model with isotropic symmetry constraint. We used NRG to calculate and confirm that the thermodynamics of this model is indeed what is expected of the two-channel Kondo model, for instance, the residual low-temperature impurity entropy of $\ln \sqrt{2}$. We have also used NRG to calculate the full crossover conductance curve and verified that our results agree with the zero-temperature values and the asymptotic behaviour proposed by Béri. Furthermore, we studied the simple two-charge state model in the large-energy gap limit and found that its low-energy thermodynamics indeed is captured by the spin model. We have also attempted to calculate a full crossover conductance curve of the model, however, due to the required computing resources, the calculations were met with difficulties and we could not obtain results that agree exactly with the spin model.

Much work can be extended to the studies in this thesis, in particular we have not included any exponentially small perturbations, that arise from the long-range coupling between the Majoranas or between the Majorana and the conduction electrons in different leads, in the studies of chapter 5. Similar to the results seen in chapter 3, it is possible that these perturbations will destroy the low-temperature NFL behaviour. We may also study how the different superconducting configurations will affect this destablisation. Even more so in chapter 6, once more computing resources are available, we could expand the investigation of the system to fully include the accurate calculations of the conductance and the t matrices. We will also include the exponentially small perturbations and see how they destablise the NFL fixed point at low temperature. Finally, we could extend the superconducting dot model to include many more accessible energy levels in order to learn how they affect the behaviour of the system and we would include the exponentially small perturbations that could destablise the NFL behaviour of the system as well.

References

[1] D. Csontos. Exotic matter. *Nature*, 464, 175 (2010).

[2] P. W. Anderson. More is different. *Science*, 177, 393 (1972).

[3] F. Wilczek. Majorana returns. *Nat. Phys.*, 5, 614 (2009).

[4] P. B. Pal. Dirac, Majorana, and Weyl fermions. *Am. J. Phys.*, 79, 485 (2011).

[5] M. Leijnse and K. Flensberg. Introduction to topological superconductivity and Majorana fermions. *Semicond. Sci. Technol.*, 27, 124003 (2012).

[6] C. Beenakker. Search for Majorana fermions in superconductors. *Annu. Rev. Cond. Mat. Phys.*, 4, 113 (2013).

[7] M. Srednicki. *Quantum Field Theory.* Cambridge University Press (2007).

[8] P. A. M. Dirac. The Quantum Theory of the Electron. *Proc. R. Soc. Lond. A*, 117, 610 (1928).

[9] P. A. M. Dirac. On the Annihilation of Electrons and Protons. *Mathematical Proceedings of the Cambridge Philosophical Society*, 26, 361375 (1930).

[10] P. A. M. Dirac. Note on Exchange Phenomena in the Thomas Atom. *Mathematical Proceedings of the Cambridge Philosophical Society*, 26, 376385 (1930).

[11] H. Weyl. Gravitation and the Electron. *Proc. Natl. Acad. Sci. U. S. A.*, 15, 323 (1929).

[12] L. M. Brown. The idea of the neutrino. *Phys. Today*, 31, 23 (1978).

[13] J. F. Annett. *Superconductivity, Superfluids, and Condensates.* Oxford University Press (2004).

[14] J. Alicea. New directions in the pursuit of Majorana fermions in solid state systems. *Rep. Prog. Phys.*, 75, 076501 (2012).

[15] A. Y. Kitaev. Unpaired Majorana fermions in quantum wires. *Phys. Usp.*, 44, 131 (2001).

[16] J. Nilsson, A. R. Akhmerov, and C. W. J. Beenakker. Splitting of a Cooper Pair by a Pair of Majorana Bound States. *Phys. Rev. Lett.*, 101, 120403 (2008).

[17] J. Linder, Y. Tanaka, T. Yokoyama, A. Sudbø, and N. Nagaosa. Unconventional Superconductivity on a Topological Insulator. *Phys. Rev. Lett.*, 104, 067001 (2010).

[18] L. Fu and C. L. Kane. Superconducting Proximity Effect and Majorana Fermions at the Surface of a Topological Insulator. *Phys. Rev. Lett.*, 100, 096407 (2008).

[19] L. Fu and C. L. Kane. Josephson current and noise at a superconductor / quantum-spin-Hall-insulator / superconductor junction. *Phys. Rev. B*, 79, 161408 (2009).

[20] P. G. de Gennes. Boundary Effects in Superconductors. *Rev. Mod. Phys.*, 36, 225 (1964).

[21] Y.-J. Doh, J. A. van Dam, A. L. Roest, E. P. A. M. Bakkers, L. P. Kouwenhoven, and S. De Franceschi. Tunable Supercurrent Through Semiconductor Nanowires. *Science*, 309, 272 (2005).

[22] J. A. van Dam, Y. V. Nazarov, E. P. A. M. Bakkers, S. De Franceschi, and L. P. Kouwenhoven. Supercurrent reversal in quantum dots. *Nature*, 442, 667 (2006).

[23] R. M. Lutchyn, J. D. Sau, and S. Das Sarma. Majorana Fermions and a Topological Phase Transition in Semiconductor-Superconductor Heterostructures. *Phys. Rev. Lett.*, 105, 077001 (2010).

[24] Y. Oreg, G. Refael, and F. von Oppen. Helical Liquids and Majorana Bound States in Quantum Wires. *Phys. Rev. Lett.*, 105, 177002 (2010).

[25] A. Cook and M. Franz. Majorana fermions in a topological-insulator nanowire proximity-coupled to an *s*-wave superconductor. *Phys. Rev. B*, 84, 201105 (2011).

[26] G. Moore and N. Read. Nonabelions in the fractional quantum hall effect. *Nucl. Phys. B*, 360, 362 (1991).

[27] N. Read and D. Green. Paired states of fermions in two dimensions with breaking of parity and time-reversal symmetries and the fractional quantum Hall effect. *Phys. Rev. B*, 61, 10267 (2000).

[28] S. Das Sarma, C. Nayak, and S. Tewari. Proposal to stabilize and detect half-quantum vortices in strontium ruthenate thin films: Non-Abelian braiding statistics of vortices in a $p_x + ip_y$ superconductor. *Phys. Rev. B*, 73, 220502 (2006).

[29] J. Jang, D. G. Ferguson, V. Vakaryuk, R. Budakian, S. B. Chung, P. M. Goldbart, and Y. Maeno. Observation of Half-Height Magnetization Steps in Sr2RuO4. *Science*, 331, 186 (2011).

[30] M. Z. Hasan and C. L. Kane. *Colloquium* : Topological insulators. *Rev. Mod. Phys.*, 82, 3045 (2010).

[31] J. E. Moore. The birth of topological insulators. *Nature*, 464, 194 (2010).

[32] T. L. Hughes. Majorana fermions inch closer to reality. *Physics*, 4, 67 (2011).

[33] P. Hosur, P. Ghaemi, R. S. K. Mong, and A. Vishwanath. Majorana Modes at the Ends of Superconductor Vortices in Doped Topological Insulators. *Phys. Rev. Lett.*, 107, 097001 (2011).

[34] X.-L. Qi and S.-C. Zhang. Topological insulators and superconductors. *Rev. Mod. Phys.*, 83, 1057 (2011).

[35] J. D. Sau, R. M. Lutchyn, S. Tewari, and S. Das Sarma. Generic New Platform for Topological Quantum Computation Using Semiconductor Heterostructures. *Phys. Rev. Lett.*, 104, 040502 (2010).

[36] X.-L. Qi, T. L. Hughes, and S.-C. Zhang. Chiral topological superconductor from the quantum Hall state. *Phys. Rev. B*, 82, 184516 (2010).

[37] A. Ii, K. Yada, M. Sato, and Y. Tanaka. Theory of edge states in a quantum anomalous Hall insulator/spin-singlet s-wave superconductor hybrid system. *Phys. Rev. B*, 83, 224524 (2011).

[38] A. Stern. Non-Abelian states of matter. *Nature*, 464, 187 (2010).

[39] C. Nayak, S. H. Simon, A. Stern, M. Freedman, and S. Das Sarma. Non-Abelian anyons and topological quantum computation. *Rev. Mod. Phys.*, 80, 1083 (2008).

[40] S. M. Albrecht, A. P. Higginbotham, M. Madsen, F. Kuemmeth, T. S. Jespersen, J. Nygård, P. Krogstrup, and C. M. Marcus. Exponential protection of zero modes in Majorana islands. *Nature*, 531, 206 (2016).

[41] B. Béri and N. R. Cooper. Topological Kondo Effect with Majorana Fermions. *Phys. Rev. Lett.*, 109, 156803 (2012).

[42] L. Kouwenhoven and L. Glazman. Revival of the Kondo effect. *Phys. World*, 14, 33 (2001).

[43] J. Kondo. Resistance Minimum in Dilute Magnetic Alloys. *Prog. Theor. Phys.*, 32, 37 (1964).

[44] P. W. Anderson. A poor man's derivation of scaling laws for the Kondo problem. *J. Phys. C: Solid St. Phys.*, 3, 2436 (1970).

[45] K. G. Wilson. The renormalization group: Critical phenomena and the Kondo problem. *Rev. Mod. Phys.*, 47, 773 (1975).

[46] H. R. Krishna-murthy, J. W. Wilkins, and K. G. Wilson. Renormalization-group approach to the Anderson model of dilute magnetic alloys. I. Static properties for the symmetric case. *Phys. Rev. B*, 21, 1003 (1980).

[47] H. R. Krishna-murthy, J. W. Wilkins, and K. G. Wilson. Renormalization-group approach to the Anderson model of dilute magnetic alloys. II. Static properties for the asymmetric case. *Phys. Rev. B*, 21, 1044 (1980).

[48] R. Bulla, T. A. Costi, and T. Pruschke. Numerical renormalization group method for quantum impurity systems. *Rev. Mod. Phys.*, 80, 395 (2008).

[49] P. Nozières. A "fermi-liquid" description of the Kondo problem at low temperatures. *J. Low Temp. Phys.*, 17, 31 (1974).

[50] N. Andrei. Diagonalization of the Kondo Hamiltonian. *Phys. Rev. Lett.*, 45, 379 (1980).

[51] P. B. Wiegmann. Exact solution of s-d exchange model at T = 0. *J. Exp. Theor. Phys.*, 31, 364 (1980).

[52] I. Affleck and A. W. Ludwig. Critical theory of overscreened Kondo fixed points. *Nucl. Phys. B*, 360, 641 (1991).

[53] I. Affleck. Conformal Field Theory Approach to the Kondo Effect. *Acta Phys. Pol. B*, 12, 1869 (1995).

[54] P. W. Anderson. Localized Magnetic States in Metals. *Phys. Rev.*, 124, 41 (1961).

[55] P. Nozières and A. Blandin. Kondo effect in real metals. *J. Phys. France*, 41, 193 (1980).

[56] M. Pustilnik and L. Glazman. Kondo effect in quantum dots. *J. Phys.: Condens. Matter*, 16, R513 (2004).

[57] R. M. Potok, I. G. Rau, H. Shtrikman, Y. Oreg, and D. Goldhaber-Gordon. Observation of the two-channel Kondo effect. *Nature*, 446, 167 (2007).

[58] A. J. Keller, L. Peeters, C. P. Moca, I. Weymann, D. Mahalu, V. Umansky, G. Zarand, and D. Goldhaber-Gordon. Universal Fermi liquid crossover and quantum criticality in a mesoscopic system. *Nature*, 526, 237 (2015). Letter.

[59] A. Golub, I. Kuzmenko, and Y. Avishai. Kondo Correlations and Majorana Bound States in a Metal to Quantum-Dot to Topological-Superconductor Junction. *Phys. Rev. Lett.*, 107, 176802 (2011).

[60] M. Lee, J. S. Lim, and R. López. Kondo effect in a quantum dot side-coupled to a topological superconductor. *Phys. Rev. B*, 87, 241402 (2013).

[61] M. Cheng, M. Becker, B. Bauer, and R. M. Lutchyn. Interplay between Kondo and Majorana Interactions in Quantum Dots. *Phys. Rev. X*, 4, 031051 (2014).

[62] L. Fu. Electron Teleportation via Majorana Bound States in a Mesoscopic Superconductor. *Phys. Rev. Lett.*, 104, 056402 (2010).

[63] A. Zazunov, A. L. Yeyati, and R. Egger. Coulomb blockade of Majorana-fermion-induced transport. *Phys. Rev. B*, 84, 165440 (2011).

[64] B. van Heck, R. M. Lutchyn, and L. I. Glazman. Conductance of a proximitized nanowire in the Coulomb blockade regime. *Phys. Rev. B*, 93, 235431 (2016).

[65] A. Golub and E. Grosfeld. Charge resistance in a Majorana *RC* circuit. *Phys. Rev. B*, 86, 241105 (2012).

[66] M. Lee and M.-S. Choi. Quantum Resistor-Capacitor Circuit with Majorana Fermion Modes in a Chiral Topological Superconductor. *Phys. Rev. Lett.*, 113, 076801 (2014).

[67] E. Eriksson, A. Nava, C. Mora, and R. Egger. Tunneling spectroscopy of Majorana-Kondo devices. *Phys. Rev. B*, 90, 245417 (2014).

[68] F. Buccheri, G. D. Bruce, A. Trombettoni, D. Cassettari, H. Babujian, V. E. Korepin, and P. Sodano. Holographic optical traps for atom-based topological Kondo devices. *New J. Phys.*, 18, 075012 (2016).

[69] A. Hewson. *The Kondo Problem to Heavy Fermions*. Cambridge University Press (1997).

[70] M. Fabrizio and A. O. Gogolin. Toulouse limit for the overscreened four-channel Kondo problem. *Phys. Rev. B*, 50, 17732 (1994).

[71] A. M. Sengupta and Y. B. Kim. Overscreened single-channel Kondo problem. *Phys. Rev. B*, 54, 14918 (1996).

[72] M. R. Galpin, A. K. Mitchell, J. Temaismithi, D. E. Logan, B. Béri, and N. R. Cooper. Conductance fingerprint of Majorana fermions in the topological Kondo effect. *Phys. Rev. B*, 89, 045143 (2014).

[73] A. Zazunov, P. Sodano, and R. Egger. Even-odd parity effects in Majorana junctions. *New J. Phys.*, 15, 035033 (2013).

[74] A. Altland and R. Egger. Multiterminal Coulomb-Majorana Junction. *Phys. Rev. Lett.*, 110, 196401 (2013).

[75] A. Zazunov, A. Altland, and R. Egger. Transport properties of the Coulomb-Majorana junction. *New J. Phys.*, 16, 015010 (2014).

[76] A. M. Tsvelik. Majorana Fermion Realization of a Two-Channel Kondo Effect in a Junction of Three Quantum Ising Chains. *Phys. Rev. Lett.*, 110, 147202 (2013).

[77] N. Cramp and A. Trombettoni. Quantum spins on star graphs and the Kondo model. *Nuclear Physics B*, 871, 526 (2013).

[78] B. Béri. Majorana-Klein Hybridization in Topological Superconductor Junctions. *Phys. Rev. Lett.*, 110, 216803 (2013).

[79] A. Altland, B. Béri, R. Egger, and A. M. Tsvelik. Bethe ansatz solution of the topological Kondo model. *J Phys A: Math Theor*, 47, 265001 (2014).

[80] A. Altland, B. Béri, R. Egger, and A. M. Tsvelik. Multichannel Kondo Impurity Dynamics in a Majorana Device. *Phys. Rev. Lett.*, 113, 076401 (2014).

[81] E. Eriksson, C. Mora, A. Zazunov, and R. Egger. Non-Fermi-Liquid Manifold in a Majorana Device. *Phys. Rev. Lett.*, 113, 076404 (2014).

[82] S. Plugge, A. Zazunov, E. Eriksson, A. M. Tsvelik, and R. Egger. Kondo physics from quasiparticle poisoning in Majorana devices. *Phys. Rev. B*, 93, 104524 (2016).

[83] M. Franz. Race for Majorana fermions. *Physics*, 3, 24 (2010).

[84] R. F. Service. Search for Majorana Fermions Nearing Success at Last? *Science*, 332, 193 (2011).

[85] A. Kitaev. Fault-tolerant quantum computation by anyons. *Ann. Phys.*, 303, 2 (2003).

[86] R. K. Pathria and P. D. Beale. *Statistical Mechanics*. Academic Press, 3rd edition (2011).

[87] A. Altland and B. D. Simons. *Condensed Matter Field Theory*. Cambridge University Press, 2nd edition (2010).

[88] S. Nah. *Kondo temperature of a quantum dot*. Ph.D. thesis, Georgia Institute of Technology (2011).

[89] D. M. Cragg, P. Lloyd, and P. Nozieres. On the ground states of some s-d exchange Kondo Hamiltonians. *J. Phys. C*, 13, 803 (1980).

[90] W. C. Oliveira and L. N. Oliveira. Generalized numerical renormalization-group method to calculate the thermodynamical properties of impurities in metals. *Phys. Rev. B*, 49, 11986 (1994).

[91] V. L. Campo and L. N. Oliveira. Alternative discretization in the numerical renormalization-group method. *Phys. Rev. B*, 72, 104432 (2005).

[92] A. M. Tsvelick. The thermodynamics of multichannel Kondo problem. *J. Phys. C*, 18, 159 (1985).

[93] I. Affleck and A. W. W. Ludwig. Universal noninteger "ground-state degeneracy" in critical quantum systems. *Phys. Rev. Lett.*, 67, 161 (1991).

[94] A. Weichselbaum and J. von Delft. Sum-Rule Conserving Spectral Functions from the Numerical Renormalization Group. *Phys. Rev. Lett.*, 99, 076402 (2007).

[95] R. Peters, T. Pruschke, and F. B. Anders. Numerical renormalization group approach to Green's functions for quantum impurity models. *Phys. Rev. B*, 74, 245114 (2006).

[96] I. Affleck and A. W. W. Ludwig. Exact conformal-field-theory results on the multichannel Kondo effect: Single-fermion Green's function, self-energy, and resistivity. *Phys. Rev. B*, 48, 7297 (1993).

[97] W. Izumida, O. Sakai, and Y. Shimizu. Many Body Effects on Electron Tunneling through Quantum Dots in an Aharonov-Bohm Circuit. *J. Phys. Soc. Jpn.*, 66, 717 (1997).

[98] P. Phillips. *Advanced Solid State Physics*. Cambridge University Press (2012).

[99] N. L. Dickens and D. E. Logan. On the scaling spectrum of the Anderson impurity model. *J. Phys.: Condens. Matter*, 13, 4505 (2001).

[100] P. W. Anderson, G. Yuval, and D. R. Hamann. Exact Results in the Kondo Problem. II. Scaling Theory, Qualitatively Correct Solution, and Some New Results on One-Dimensional Classical Statistical Models. *Phys. Rev. B*, 1, 4464 (1970).

[101] R. Žitko, R. Peters, and T. Pruschke. Properties of anisotropic magnetic impurities on surfaces. *Phys. Rev. B*, 78, 224404 (2008).

[102] R. Shankar. Bosonization: How to Make It Work for You in Condensed Matter. *Acta Phys. Pol. B*, 26, 1835 (1995).

[103] J. von Delft and H. Schöller. Bosonization for beginners — refermionization for experts. *Ann. Physik*, 7, 225 (1998).

[104] D. Sénéchal. *An Introduction to Bosonization*, Springer New York, New York, NY, pages 139–186 (2004).

[105] A. Schiller and L. De Leo. Phase diagram of the anisotropic multichannel Kondo Hamiltonian revisited. *Phys. Rev. B*, 77, 075114 (2008).

[106] E. Sela, A. K. Mitchell, and L. Fritz. Exact Crossover Green Function in the Two-Channel and Two-Impurity Kondo Models. *Phys. Rev. Lett.*, 106, 147202 (2011).

[107] M. Pustilnik, L. Borda, L. I. Glazman, and J. von Delft. Quantum phase transition in a two-channel-Kondo quantum dot device. *Phys. Rev. B*, 69, 115316 (2004).

[108] G. G. Claude Cohen-Tannoudji, Jacques Dupont-Roc. *Atom-Photon Interactions: Basic Processes and Applications*. Wiley (1998).

[109] V. J. Emery and S. Kivelson. Mapping of the two-channel Kondo problem to a resonant-level model. *Phys. Rev. B*, 46, 10812 (1992).

[110] J. Gan, N. Andrei, and P. Coleman. Perturbative approach to the non-Fermi-liquid fixed point of the overscreened Kondo problem. *Phys. Rev. Lett.*, 70, 686 (1993).

[111] D. L. Cox and A. E. Ruckenstein. Spin-flavor separation and non-Fermi-liquid behavior in the multichannel Kondo problem: A large-N approach. *Phys. Rev. Lett.*, 71, 1613 (1993).

[112] S. Yotsuhashi and H. Maebashi. Crossover Temperature from Non-Fermi Liquid to Fermi Liquid Behavior in Two Types of Impurity Kondo Model. *J. Phys. Soc. Jpn.*, 71, 1705 (2002).

[113] A. I. Tóth, L. Borda, J. von Delft, and G. Zaránd. Dynamical conductance in the two-channel Kondo regime of a double dot system. *Phys. Rev. B*, 76, 155318 (2007).

[114] A. I. Tóth and G. Zaránd. Dynamical correlations in the spin-half two-channel Kondo model. *Phys. Rev. B*, 78, 165130 (2008).

[115] A. K. Mitchell and E. Sela. Universal low-temperature crossover in two-channel Kondo models. *Phys. Rev. B*, 85, 235127 (2012).

[116] N. Andrei and C. Destri. Solution of the Multichannel Kondo Problem. *Phys. Rev. Lett.*, 52, 364 (1984).

[117] A. Tsvelick and P. Wiegmann. Solution of then-channel Kondo problem (scaling and integrability). *Z. Phys. B*, 54, 201 (1984).

[118] C. Nayak, M. P. A. Fisher, A. W. W. Ludwig, and H. H. Lin. Resonant multilead point-contact tunneling. *Phys. Rev. B*, 59, 15694 (1999).

[119] M. Oshikawa, C. Chamon, and I. Affleck. Junctions of three quantum wires. *Journal of Statistical Mechanics: Theory and Experiment*, 2006, P02008 (2006).